ABSTRACT

Title of dissertation: IMPACT LOAD MODEL ANALYSIS ON THE VEHICLE-TO-PIER COLLISION

Xu, Chaoran, Doctor of Philosophy, 2019

Dissertation directed by: Professor Chung C. Fu
Department of Civil and Environmental Engineering

As the key member of the bridge substructure, the pier is always the most concerned part under variety of hazards, among which the vehicle-induced impact is a rare but an extreme load hazard that may result in significant structural damage, even full failure of the bridge pier. This study overviewed the previous studies in vehicle-to-pier collision and found the design in AASHTO code conservative.

Based on the explicit finite elemental method, the sensitivities to the impact load values of different parameters of bridges and vehicles are analyzed by LS-DYNA@. The impact load is the most sensitive among various parameters, including impact velocity, concrete strength, pier diameter, pier length, impact height, axial force, and cargo mass.

Two simplified impact load models are suggested for improvement of the design values of the impact load: the simplified mass-spring model and response surface model. The simplified mass-spring model is applied to the explicit analyses on reduced vibration system to obtain the impact load following appropriate assumption. On the other hand, the response surface model is based on mathematic experiment with large quantities of data to find fitting function of the impact load according to the variation of the sensitive parameters. Both methods can give approximate solution for the dynamic peak impact

load and the static equivalent impact load. Comparatively, the response surface model is more efficient in design by giving the function of the impact load.

The reliability of the pier under the impact load has been analyzed based on Monte-Carlo simulation and response surface model. For light-weight and medium-weight trucks induced impact events, the failure probability of the pier could be controlled to a very low level (i.e. 0.137%, reliability index equal to 3) by appropriately increasing the resistance of the pier. For the heavy truck induced impact load, the most efficient way to reduce the failure probability is to limit the impact velocities, while the cost for increasing the resistance of the pier is uneconomic.

In conclusion, the suggested simplified impact load model based on the parametric study could be applied to future analyses and designs for the truck-to-pier impact hazard.

IMPACT LOAD MODEL ANALYSIS ON THE VEHICLE-TO-PIER COLLISION

by

Xu, Chaoran

Dissertation submitted to the Faculty of the Graduate School of the
University of Maryland, College Park in partial fulfillment
of the requirements for the degree of
Doctor of Philosophy
2019

Advisory Committee:

Professor Fu, Chung C. , Chair
Professor Amde, Amde M.
Professor Aggour, M. Sherif
Professor Zhang, Yunfeng
Professor Lee, Sung , Dean's Representative

Acknowledgements

For the completion of the dissertation, I have received a great deal of assistance and support from many people. Without their helps, it is impossible for me to finish this work

First, I would thank my academic supervisor and advisor Dr. Chung C. Fu. In the five-year study in University of Maryland, Dr. Fu engaged himself in training me as an excellent Ph.D. student. I was offered great opportunities by joining the Best Center as his research assistant. Under his guide, I participated in varieties of research projects. It is also Dr. Fu who gave me the hints of the dissertation topic. Dr. Fu's academic inspiration and dedication lighted up my way to achieve Ph.D. degree. Without Dr. Fu, there would be no this dissertation.

Second, my dissertation committee members (Dr. Made, Dr. Aggour, Dr. Zhang and Dr. Lee) gave me invaluable suggestions on my dissertation. Their experiences and unique comments helped me improve my dissertation a lot.

Besides, my research teammates (Gengwen Zhao, Yunchao Ye, Yifan Zhu, Kuang-yuan Hou and Xinya Liu) in Best Center gave me great support and help in my study. Thanks to these best teammates, my academic life become so colorful and warm. It was also the discussions and advices from my teammates that solved a lot of technical issues in the dissertation.

At last, I would pay my deepest gratitude to my families. Their love and endless support always gives me the power to step out of depression. They always stand with me to overcome all the difficulties.

Table of Contents

List of Figures

List of Tables

Chapter 1 Introduction

1.1 Background

As the key member of the bridge substructure, the bridge pier is always the most concerned part under variety of hazards. A vehicle collision with a pier is such an extreme-loading hazard, which may be rare, but may result in significant structural damage, even full failure and collapse of the whole bridge during the lifespan of the bridge.

Harik et al. (1990) collected the data of bridge failures in the United State from 1951 through 1988. It was found that the vehicle collision had caused serious structural failures including partial collapses and total collapses. Only in Kentucky, five (5) full-collapse failures and two (2) partial-collapse failures were caused by trucks or cars colliding with the structures for 35 bridge failures in total. And throughout the United States, 42 of the 79 failures are due to collision. For the collision-induced failures, 36 are due to the direct impact involving ships, trucks, and trains, and others are due to the second hazard after collision, such as the exploding and blasting.

Wardhana and Hadipriono (2003) conducted a similar study of over 500 failure events of bridges from 1989 to 2000. The study shows that failures took place primarily during the service life of the bridges. Flood/scour, collision and overload are the leading causes of bridge failures, of which 11.7% (59 of 503) are due to the collision involving vehicles, vessels, trains, et al.

More recently, the technical report MCEER-13-0008 (Lee, et al., 2013) summarized the total 1062 bridge failures after 1980 in the United States. The report shows that bridges are ranked in second vulnerable to collision (113 failures) after scour (121 failures), as

shown in Table 1-1. And the number of failures caused by earthquake, always mentioned for the extreme event, is much fewer with the total 16 failures.

The following recent vehicle-collision events show the significant damage to the bridge due to the impact load, which not only led to structural failures but also traffic disruptions.

Table 1-1 Bridge failures from 1980 to 2013

Causes of Failure	Failure Types		
	Total Collapse	Partial Collapse	Distress
Design Error	38%(8)	52%(11)	10%(2)
Lack of Maintenance	67%(2)	33%(1)	0%(0)
Deficiency in Construction	32%(10)	65%(20)	3%(1)
Material Defect	23%(3)	46%(6)	31%(4)
Earthquake	38%(6)	63%(10)	0%(0)
Scour	50%(61)	50%(60)	0%(0)
Flood	75%(83)	25%(27)	0%(0)
Collision	39%(44)	60%(68)	1%(1)
Environmental Degradation	29%(12)	69%(29)	2%(1)
Overload	76%(71)	24%(23)	0%(0)
Fire	50%(12)	50%(12)	0%(0)
Wind	78%(35)	22%(10)	0%(0)

A truck crashed into a bride pier that carries a county road over I-90 near Worthington rests on its side following the June 2, 2003, incident. The driver and passenger suffered minor injuries. The pier shows obvious shear failure at the location of impact and at the connection with the bent cap, as shown in Figure 1-1. Bridge and highway maintenance crews used concrete box culverts, steel bridge beams and five-inch timbers to stabilize the pier and support the bridge deck. And repair work took months to replace the damaged pier.

Figure 1-1 Bridge pier damage resulting from the truck crash

On July 7, 2005, a truck-tractor-trailer loaded with an unknown load crashed into a bridge pier on IH-35 in Red Oak, Texas. This bridge is located on US-77 and carries traffic over IH-35. This vehicle, which was speeding in excess of 60 mph, impacted the northernmost 30-inch diameter pier of the center 3-pier bent located in the median of IH-35. The collision with the pier caused shear failure in the 30-inch diameter pier. The bridge did not collapse as a result of impact.

Figure 1-2 Shear failure near the connection of the pier and the cap

On May 30, 2007, a truck-tractor-trailer loaded with home building products crashed into a bridge pier on IH-45 about 3 miles east of Corsicana, Texas. This bridge is located on Roane Road and carries traffic over IH-45. This vehicle impacted the northernmost 30-

inch diameter pier of the center 2-pier bent located in the median of IH-45. The collision with the pier caused severe cracking in the 30-inch diameter pier, as shown in Figure 1-3. The weight of the vehicle and payload was approximately at 80,000 lb, and the impact speed was approximately 60 mph.

Figure 1-3 Transverse crack caused by the impact

On 15 August 2007 at around 3:00 a.m., a semi-truck, carrying 55-gallon drums of sodium hypochlorite, was westbound on I-70 when the driver lost control then overcorrected twice, and crashed into a concrete bridge pillar on the north edge of Grand Junction. Two truckers were killed in this accident. The truck tore out 75 feet of guardrail before the impact. The impact force led to large shear force which caused shear failure at the connection of the bent cap and the pier that carries Road 26.5, as shown Figure 1-4. Colorado DOT cost around $286,000 to repair the undermined bridge.

Figure 1-4 Shear failure at top of the pier

On 22 May 2011 at around 3:00 a.m., a tractor-trailer carrying newspapers and magazines was traveling northbound on I-85 near Gaffney, SC, when it struck the pier of the SC Highway 150 overpass. The force of the collision destroyed the impacted column and half of the bent cap while also damaging the other two columns and resulting in the sagging of the superstructure spans. The destruction caused by the collision is shown in Figure 1-5. I-85 northbound traffic resumed 52 hours following the accident, after the damaged section of the overpass was demolished. The whole overpass was later replaced with an entirely new bridge. The replacement work, which cost $3.4 million, was finished 152 days after the accident occurred. The roadway was reopened on SC Highway 150 on 21 October 2011.

Figure 1-5 Tractor-trailer collision with the SC Highway 150 Bridge over I-85

On 11 June 2012 at around 4:00 p.m., a tractor-trailer carrying various electronics was traveling westbound on I-30 in Dallas, TX, when the driver supposedly fell asleep at the wheel and crashed into the bridge support columns of the Dolphin Road overpass. The force of the impact was so great that the cab of the tractor and a portion of the trailer were split in half. The impact, shown in Figure 1-6, resulted in a shear failure to the easternmost pier, requiring emergency repairs to be conducted to stabilize the overpass. The highway was shut down for over 15 hours and the repairs to the bridge took about a week.

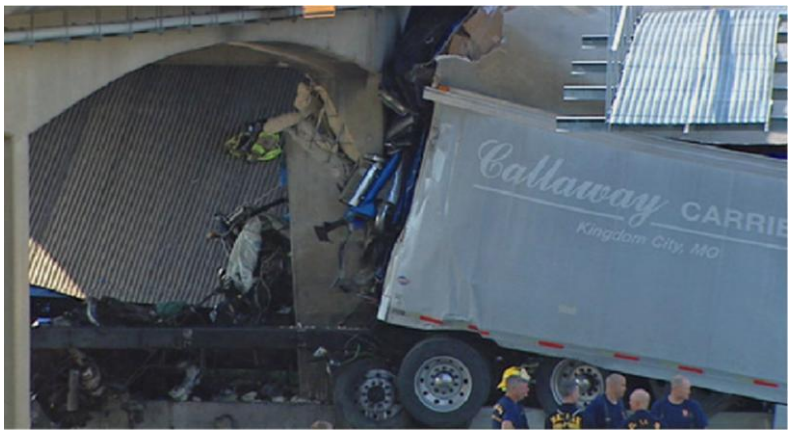

Figure 1-6 Tractor-trailer collision with the I-30 Bridge over Dolphin Road

On March 9, 2018, a tractor-trailer lost control and ran off the westbound lanes. The truck smashed into the pier supporting the Four Holes Swamp Road Bridge. Shear failure was observed at the bottom and the top of the pier as well as at the bent cap. All westbound lanes of I-26 and the Four Holes Road overpass were closed following the crash. The damaged bridge was demolished to ensure the safety of traffic on I-26 before reopening. SCDOT has plans to replace the bridge. The accident remains under investigation.

Figure 1-7 Tractor-trailer collision with the pier on I-26, which was torn down after then

Except for the crash incidents shown above, there were still other collision events, which also yielded serious structural damages. Therefore, it is necessary to take overall studies on the failure behaviors of the bridge piers caused by vehicle-induced impact load, and to give a more sufficient design criterion of the pier under vehicle impact.

1.2 Literature Review

According to the most recent report from US DOT Federal Highway Administration, there are 614,387 bridges, of which the number in good condition is only 291,412, by highway system in the United States till the end of 2016. For bridges need maintenance and repairing there are 48,559 in poor condition, about 8% of the total number. Only in Maryland, there are 308 called Structurally Deficient (SD) bridges. These structurally deficient bridges demand immediate maintenance, rehabilitation or reconstruction to

ensure their performance can fulfil the heavy daily traffic task. The report indicates that large quantities of bridges cannot meet the design requirement today, so does the impact design. Many technique reports and research papers have been posted, and engaged into the field of studying impact design. To summarize the current state of the design and study of the impact mechanism between a vehicle and a bridge pier, following literatures are preliminarily reviewed.

1.2.1 AASHTO Load Resistance and Factor Design (LRFD)

The American Association of State Highway and Transportation Officials has long history after including the impact design into the code, and also makes adjustment to the impact load to fit the increasing truck weight and speed.

For AASHTO LRFD 4th edition (2007), the article 3.6.5.2 specifies that, without the protection in article 3.6.5.1, the abutments and piers located within a distance of 30ft to the edge of roadway, or within a distance of 50ft to the centerline of a railway track, shall be designed for an equivalent static force of 400kip, which is assumed to act in any direction in a horizontal plane, at a distance of 4 ft. above the ground, based on the information from full-scale crash tests of barriers for redirecting 80-kip tractor trailers and from analysis of other truck collisions.

For the latest LRFD code (8th edition, 2017), the equivalent load has been adjusted to 600kips for the vehicle impact, and the location to apply the load is moved to 5ft. above the ground. The orientation of impact is assumed to act in the direction of zero to 15 degrees with the edge of the pavement in a horizontal plane. This revision is based on the latest crash tests of rigid columns impacted by 80-kip tractor trailers at 50 mph (Buth et al., 2011).

Field observation indicates shear failures are the primary mode of failure for individual columns and columns that are 30in. in diameter and smaller are the most vulnerable.

However, the impact load specified in the code is still general compared with the force induced by ship collision in article 3.14.8. The ship collision force clearly states the relationship with the mass and the velocity of a vessel:

$$P_s = 8.15V\sqrt{DWT} \qquad \text{Eq. 1-1}$$

Where P_s is the equivalent static vessel impact force; DWT is the deadweight tonnage of vessel; V is the impact velocity.

From the specification about the ship collision force, the current vehicle collision force cannot present the relationship with the speed and mass of the vehicle. Furthermore, due to the process of impact is a result of complicated coupling of two systems. Any parameter change of one system will lead to a different result of impact load. The mass and stiffness contribution of both superstructure and substructure should be taken into consideration to give a more convincing result.

In code ASCE7-10, although no impact load for pier is specified, an equivalent static horizontal on barrier system with 6000 lbf is listed in Chapter 4.5.3. However, this value is much lower than the specification of the AASHTO LRFD specification.

The Annex B of European code Part 1-1 gives the impact of a vehicle on a barrier within 1.5m range as:

$$F = 0.5mv^2/(\delta_c + \delta_b) \qquad \text{Eq. 1-2}$$

Where m is the gross mass (kg) of the vehicle; v is the velocity (m/s) of the vehicle normal to the barrier; δ_c is the deformation (mm) of the vehicle; δ_b is the deformation mm) of the barrier. For weight of vehicles not exceeding 2500kg, when applying this equation,

following values could be used to determine the force F: m=1500kg, v=4.5m/s, δ_c=100mm. For rigid collision, the δ_b could take the value of zero. F then takes value 152kN (34.2 kips) which is also much smaller than the specification in the AASHTO.

The part 1-7 of the European code gives an equivalent static impact load up to 1000 kN (225kips) in the direction parallel, and 500kN(112.5kips) normal to the orientation of the road adjacent to the pier. This value is closer to the AASHTO value but still underestimated. Annex C suggested an alternative method to evaluate the impact load by the equation:

$$F = v\sqrt{km} \qquad \text{Eq. 1-3}$$

Where v is the impact velocity; k is the equivalent elastic stiffness of the object; m is the mass of the colliding object. This equation gives more reasonable estimation of the impact according to Ferrer's study (2010).

Therefore, there is demand to give the study involving the truck weight, velocity and properties of pier in detail to generalize an equation of collision load including these parameters.

1.2.2 Experiment study

National Highway Traffic Safety Administration (NHTSA) had conducted series of full-scale tests to investigate the properties of different vehicles in a crash. For example, the Chevrolet C1500 Silverado pickup truck was tested by crashing into a rigid war at the speed of 35mph in 1998. (Test Number 2809). Honda Accord was tested at speed of 35.1 mph in 2017 for new car safety evaluation (Test number 10191). The data of all these tests is accessible on the website of NHTSA Vehicle Crash Test Database. Although these tests only involve tests of vehicle with rigid wall, the data was applied to build and modify the

vehicle finite element model. The refined vehicle model provides the way to accurately simulate the process of impact during collision.

Kishi et al. (2002) designed a falling-weight impact tests to establish a rational impact-resistant design procedure of shear failure-type reinforced concrete (RC) beams. Twenty-seven simply supported rectangular RC beams without shear rebar were used. All RC beams were of 150mm width and 250mm depth in cross section, with variables including rebar and shear-span ratios. The free-dropping steel hammer weighed 300kg with a spherical striking face. During the test, only a few vertical flexural cracks developed at the low impact velocity, V=1m/s. A severe diagonal crack was developed in the case of V=3m/s. Keeping increasing the impact velocity to V=5m/s, the RC beam was split into three parts due to severe diagonal cracks. Empirical equation for required static shear capacity was developed with a maximum reaction force equal to one and a half times of the required static shear capacity. And the beam would absorb 60% of initial kinematic energy during the impact.

Saatci and Vecchio (2009) had free dropping tests on eight reinforced concrete beams and static tests on four reinforced concrete beams with different stirrup spaces and drop masses. All specimens, regardless of their shear capacity, developed severe diagonal shear cracks, as shown in Figure 1-8, even if the member is flexure-critical under static load conditions. Specimens with higher shear capacity were able to sustain more impacts and absorb more energy, whereas the ones with lower shear capacity suffered extensive damage under the same or smaller impact loads. The highly dynamic nature of the responses lead to the resistance of impact forces from the inertia of the specimens at the initial stages of response specimens, before the forces reached the supports.

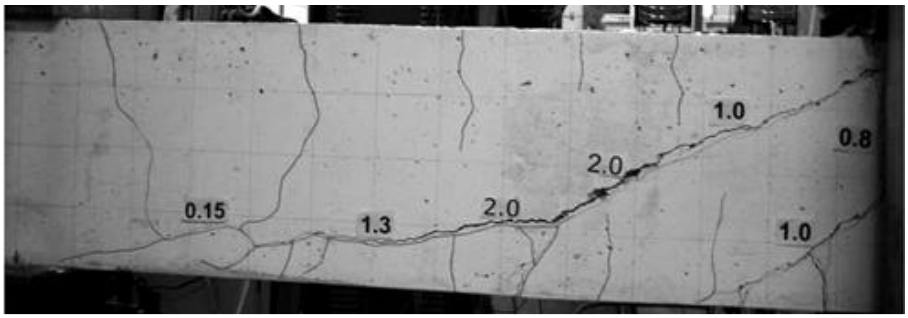

Figure 1-8 Diagonal shear cracks during the impact test

Fujikake et al. (2009) conducted a very detailed experiment about a rigid hammer freely dropping onto a concrete beam. Twelve specimens of RC beams with different amount of longitudinal reinforcement were investigated to study the impact response corresponding to the different impact velocities. The striking head of the drop hammer had a hemispherical tip with a 90-mm radius and a mass of 400 kg. The dropping height ranged from 0.15 to 1.20 m to realize different impact velocity. An analytic model of a two-degree-of-freedom mass-spring-damper system was developed to evaluate the response of reinforced concrete beam, and was compared with the experimental result, as illustrated in Figure 1-9. A perfectly plastic collision was assumed between the hammer and the beam (Suzuki et al. 1996). The contact spring was assumed based on Hertz's contact theory. And the damping coefficients c_1 is assumed to be 0, while c_2 is assumed as:

$$c_2 = \sqrt{\frac{m_1 m_2}{m_1 + m_2} k_2} \qquad \text{Eq. 1-4}$$

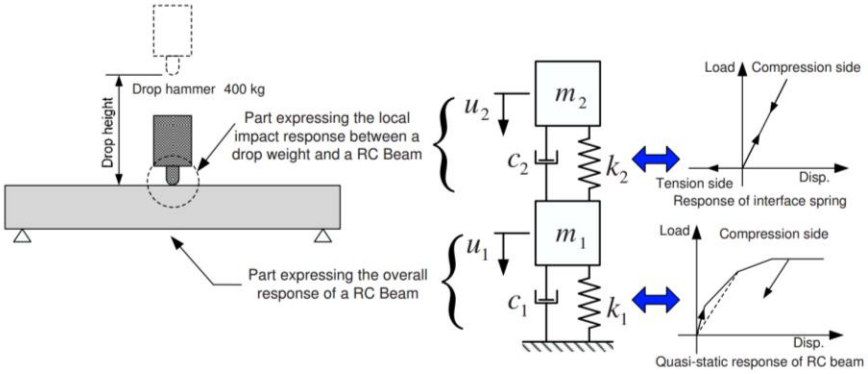

Figure 1-9 Two-degree-of-freedom mass-spring-damper system model

Based on the result, with the comparatively higher amounts of longitudinal reinforcement, the RC beam exhibited not only the overall flexural failure, but also local failure located near impact loading point due to the large impact from the loading acting on a single point. The analytical model was shown to be in good agreement with the experimental mid-span deflection when the RC beams exhibited only an overall flexural failure.

Buth et al. (2011) conducted a full-scale crash test of truck running into a bridge pier shaft with 36 in. in diameter and 14 ft. in height, as shown in Figure 1-10. The trucks were van-type semi-tractor-trailers ballasted with bags of sand on pallets with the weight around 80,000lb. Impact speed was nominally 50mph. The test result has been filtered with 0.05-sec average values of responses, and the 0.05-sec average data is close to the equivalent static result. Two peak impact loads were observed during the test. One is due to collision between the engine of tractor and the pier, and the other is due to impact induced by the trailer. Based on the test result, revision of the AASHTO LRFD code was made, by changing the equivalent static force of 400 kips to 600 kips for vehicle collision force. Meanwhile, the location of impact was moved upward from 4ft. to 5ft. above ground.

Figure 1-10 Full-scale tractor-trailer-to-pier crash test

Deng et al. (2012) carried out an experiment to study the dynamic behavior of concrete-filled circular Steel tubes under high-Strain Rate Impact Loading. Nine simply supported circular steel concrete-filled tubes (CFTs), two circular steel posttensioned concrete-filled tubes (PTCFTs), and one circular steel fiber–reinforced concrete-filled tube (FRCFT) had been tested in an instrumented drop-weight impact facility. Four damage modes were observed in the test, including no crack, crack at the bottom, crack up to lower half of the circumference, and rupture. The structural response of the beam is predominantly flexural rather than shear within the plateau. Failure in the steel tubes was commonly tensile facture or rupture along the circumference. Concrete core in the impact area commonly crushed under compression and cracked under tension. The use of prestressing strands and steel fibers significantly restrained tension cracks in the concrete by comparing the result of PTCFT and FRCFT specimens with CFT specimens.

Chen et al. (2016) developed a scaled equivalent truck frame based on the F800 Ford single unit truck. The scaled equivalent frame was comprised of two steel blocks mounted on a steel frame. The first block represented the engine, clutch, and transmission, while the second represented the cargo. The supporting frame was made up of steel channel members with similar properties to the chassis of the truck. The frame

was designed to strike at mid span of three RC columns vertically. The three specimens of RC column had a diameter of 333mm. There were total 16 longitudinal reinforcements with diameter 8mm, and stirrups with diameter of 6.5mm were spaced at 333mm. The impact speeds ranged from 10.4 to 13.9m/s, and the truck frames had masses from 451 to 1026kg. The test result was compared with the finite element analysis of a full-scale collision between the F800 truck and the pier. The study shows that the equivalent truck frame could provide a similar impact result as the full-scale truck. The dynamic response of the test kept a good agreement with the response from finite element analysis. The failure model exhibits obvious shear behavior near the impact point, as shown in Figure 1-11.

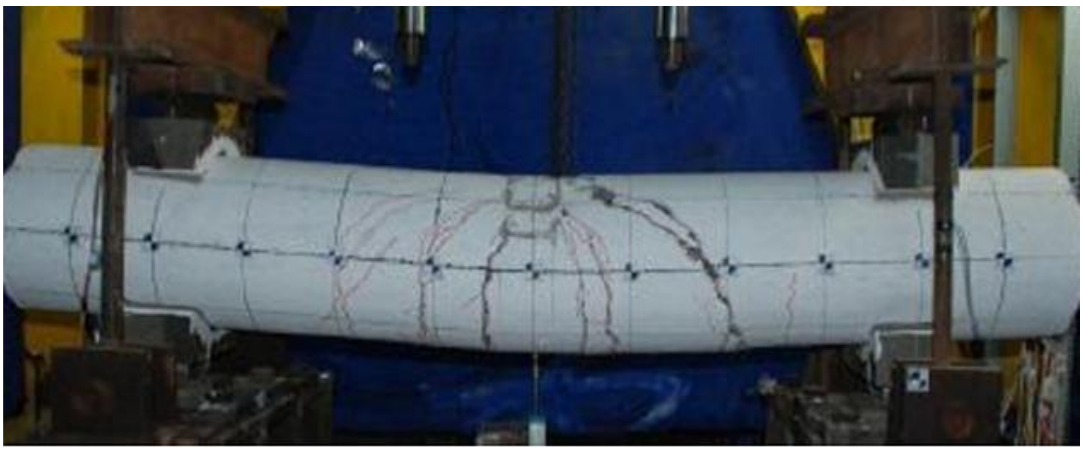

Figure 1-11 Impact Tests of Model RC Columns by an equivalent truck frame

Demartino (2017) conducted an experimental investigation on the behavior of shear-deficient reinforced circular RC columns of 330 mm diameter and 1700mm height under lateral-impact loading. A total of 10 specimens (five for each type with different hoop spacing) were tested under a lateral rigid-hammer impact at different impact velocities (2.25, 3 and 4.5 m/s) and boundary conditions (cantilever and fixed-simply-supported). Two phases during impact were observed. In the first phase, a large peak value

characterized as a large impulse is observed. This sudden increase occurred to obtain deceleration of the test truck and local acceleration of the RC column, to make them acquire a common velocity and move together. The impact force was mainly governed by the inertia of the RC column. In the second phase, impact force died down, and the reduction is proportional to the damage and loss of stiffness of the column. In all tests, the post-impact condition revealed a brittle shear-type damage characterized by one main diagonal crack starting from the base of the column to the impact point. The shear damage could be reduced by increasing the transverse reinforcement ratio. Some flexural cracks were found behind the impact point

1.2.3 Numerical study

El-Tawil (2004) studied the dynamic performance of a single pier with either rectangular or circular section subjected to the impact from Chevrolet C2500 and F800 Ford single unit truck. The dimension of the rectangular section was 4.75 ft. x 4.5ft, while the circular section had a diameter of 3.5ft. Two lines of beam elements were applied to the simulation of the superstructure. Compression-only soil spring was used to realize the soil-pile interaction. All materials of pier were assumed linear elastic. The study involves a sensitive study about the coefficient of friction (COF) between two contact faces. It was found that increasing COF to 0.6 would lead to one and a half times of contact force, compared with the result of COF equal to 0.3. But lower COF would have no large influence on the contact force. It was found the equivalent static impact force of C2500 pickup truck lied bellow the AASHTO code with 400kips. But the impact load of F800 single unit truck had far exceeded the design force. A 50-ms average was used to obtain the equivalent static force for design demand.

Consolazio and Cowan (2005) built a 3D model of double-column pier with the bent, the foot and piles. A simplified model, containing SDOF barge system coupled with MDOF pier system, was suggested, and its result was compared with the finite element solution. An exponentially decaying historical averaging process is used to compute damped increments of barge impact force. The study shows pier column shape and overall pier stiffness have been found to have only marginal influence on the sustained impact forces generated. And mass may not necessarily impose significant additional structural demand on the pier due to additional kinetic impact energy dissipated during the through increased plastic barge deformation. The suggested simplified method can efficiently evaluate the dynamic force.

Ferrer (2010) had a simulation of collision between C2500 pickup truck and H-shape column. The simulation results showed that the static load equivalent to an impact was strongly dependent on the speed of the impacting vehicle. Changes in the mass of the vehicle did not significantly affect the equivalent static loads obtained. And it was found that the indication given in Annex C of EUROCODE 1 was close to the results obtained in this study and are on the safe side, whereas the loads proposed in part 1.1 Annex B and Part 1.7 were both less than obtained values in this study.

Buth (2010) simulated the collision events of a single unit truck weighing 65,000lb and a tractor trailer weighing 80,000lb crashing into a rigid circular pier. It was found with larger pier diameter, the impact force will be reduced, although the decrease is limited (15% lower with twice of the diameter). Rigid ballast in the cargo and higher impact velocity would increase the impact force. The impact force averaged in 50ms is useful to predict the design load.

Liu (2012) started from simulating the impact test of Fujikake et al. (2009). The F800 truck model developed by National Crash Analysis Center for crash simulation with the concrete barrier (2005) was adopted to realize the collision simulation between a median-weight truck and a square pier. The truck was set to strike the pier with an angle of 20 °. The impact velocity and the pier size were selected for parametric study. 12 cases are included in total with the pier size ranging from 3ft. to 4ft., and the impact velocity ranging from 30mph to 70mph. With the increase of impact velocity, the pier cracked at the height of impact, then the pier concrete spalled near the connection with the cap, at last the pier failed due to combination of moment and shear, as shown in Figure 1-12. A crack also developed in the cap near the connection of the second pier for a high impact velocity. It was also found that the impact force is largely independent of the pier size and mainly depends on impact (approach) velocity and weight of the truck. For higher speed, the impact between cargo and pier yielded larger impact force, while the head impact resulted in peak load for lower speed due to dying down of the velocity before the secondary impact with cargo. A steel jacket can effectively improve the performance of pier under impact load. With full composite jacket under 70mph impact velocity, only minor damages were casted onto the pier.

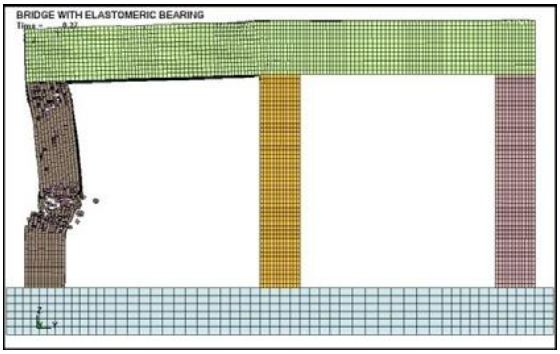

Figure 1-12 Behavior of bridge piers during vehicular impacts

Mohammed (2012) investigated the behavior of a single hammer head pier column under impact load induced by the C2500 pickup truck and F800 single unit truck. In the finite element analysis, 20 specimens with different concrete strengths, impact velocities, and section aspect ratio, were analyzed. Damage scale factor was employed as the index of current failure state and given as a function of effective plastic strain. A regression analysis was performed based on 20 cases to give the function between the damage scale factor and effective plastic strain. Deployable honeycomb energy absorbers with different shapes were designed and compared as an efficient way to reduce peak compressive stress during impact.

Gomez (2014) performed a parametric study on a F800 single unit truck crash into a circular pier with 900mm diameter. The pier is modeled with concrete footing, concrete piles as well as soil springs. The parameters for parametric study include the diameter of section, the spacing of hoop and the impact velocity. The displacement of the pier, shear force and moment at each section, and the dynamic impact force were investigated for each load case. It was shown that as the stiffness of the piers increased, there was an increase in peak dynamic impact forces, a decrease in lateral displacements, and an increased resistance to shear and moment stress. Increasing pier diameter, using a multi-pier bent, or decreasing hoop spacing all led to increased stiffness of the bridge piers. Vehicle impact velocity has a significant effect on the amount of kinetic energy that must be absorbed by the pier and colliding vehicle. The damage ratios, calculated by dividing the peak dynamic impact force by the shear capacity of the pier, can be used to design bridge piers for specific damage states resulting from vehicle collisions.

Abdelkarim et al. (2016) studied the performance of hollow-core FRP–concrete–steel bridge columns subjected to vehicle collision. The effects of 14 parameters of 34 columns were investigated: Concrete material model, concrete compressive strength, Material strain rate, Column height-to-diameter ratio, Column diameter, The FRP confinement ratio, Diameter-to-thickness ratio of the inner steel tube, Column void ratio, Embedded length-to-diameter ratio, Steel tube in-filled foam, Column top boundary condition, Axial load level, Vehicle velocity, and Vehicle mass on the behavior of HC-FCS columns. The main resistance of the HC-FCS columns came from the inner steel tube. The elastic properties can be used, for simplicity, to design the HC-FCS columns under vehicle collision. The peak dynamic force of the HC-FCS column was lower than that of the RC column. An equation $60\sqrt{KE}$ was used for estimating the equivalent static force, where KE is the kinetic energy of the vehicle.

Chen (2016) ran finite-element simulations to investigate the structural demands generated by a F800 colliding with a bridge pier. A F800 single unit truck was selected for collision simulation with a circular and a square. Cases with the different impact speed and weight were studied. The simulation data showed that truck weight alone is not directly correlated with the peak force delivered to the bridge pier while impact velocity, structural characteristics of the colliding truck, and the geometry and properties of the pier itself all play a significant role. Besides, the study employed a reduced coupled mass-spring-damper (CMSD) system, as shown in Figure 1-13, to analytically solve the impact force. The force-displacement diagrams of the equivalent springs were obtained by fitting the force-displacement relationship of the assumed spring with the impact force-displacement diagram.

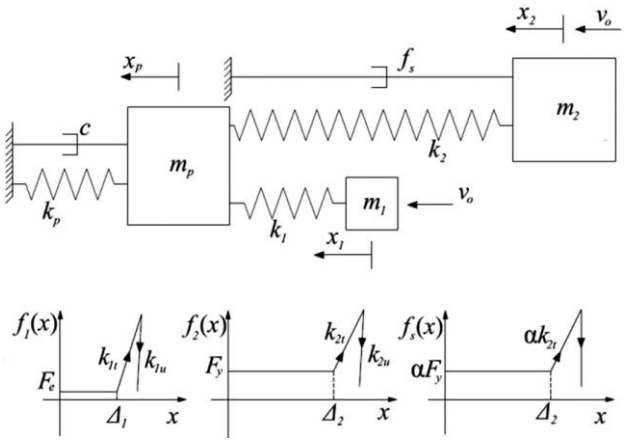

Figure 1-13 Simplified analytic model for the impact coupling

Do et al. (2018) had a numerical simulation of the F800 single unit truck crashing into a square-shape pier. The pier was modeled with the superstructure, a concrete box girder, as well as the concrete footing. 14 cases were compared involving the parameters: engine mass, vehicle mass, velocity. 6 extra cases were used to investigate the influence of different simplification of superstructure. The simplified models of superstructure included uniformly-distributed-load model, lumped mass model, and beam model. With the increase of vehicle speed, the failure models changed from local damage, to flexural cracking, then to shear cracking. Shear crack firstly appeared near the connection of the cap, and then appeared near the foot with the increase of the kinetic energy of engine. Finally, punching shear would take place. It was also found that the impact force causes a considerable increase of the axial force which should be taken into consideration in the design. All three simplified models can well predict the impact force, whereas the beam model and the lumped mass model can get good results of displacement that is close to the 3D full-scale model.

Cao et al. (2019) had a numerical simulation of the tractor-trailer truck impacting on a pier with different the dimension and the shape. Three main sources of impact demand

were identified: bumper, engine, and trailer. Each was shown to deliver a spike in the applied impact force. The engine impact induced the highest peak dynamic force, which was also closely associated with the impact speed. Shear failure was found to be the typical failure mode of the bridge pier, as was observed in numerous actual accidents. It was also found that the demands could be underestimated for trucks moving at speeds in excess of 80 km/h following the recommendation of the AASHTO LRFD bridge design specification. Based on the numerical simulation results, a simplified pulse demand model for bridge pier design against heavy truck impact. The main variables of the model were pier dimensions, impact speed, and truck weight. The simplified model can well simulate the impact load induced by tractor-semitrailer truck.

1.3 Summary

From the previous experimental studies, the impact load is more likely to yield shear failure which caused by the large impulse of the first stage that makes the rigid body and the beam or column move together. When there is enough shear resistance, flexure failure could also occur due to the tensile failure of the concrete. It also refers that most of impact tests are still based on the scaled and simplified model. The impact force could exhibit good result for the contact between a rigid body and a beam or column. However, due to the very complex coupling system of vehicle itself, impact tests involving rigid-body contact is hard to reflect the true relation. Because it is infeasible to run an experiment with many cases with full-scaled piers and real trucks, the numerical analysis is more preferred in studying the full-scale impact between the truck and the pier. Due to the limitation of the experimental study, researchers turn to computational simulation for the impact-load study.

The contact problem raises very requirement to ensure the accuracy of the simulation, which requires very small-time step and fine mesh. In the recent 10 years, with the explosive development of the performance of computer and the wide application of explicit dynamic, finite element analysis becomes a very useful tool to carry on the study of vehicle collision issues, which involving large amounts of nonlinear calculation. National Highway Traffic Safety Administration along with the National Crash Analysis Center has devoted large efforts to develop vehicle model based on large quantities of material and rigid impact tests, which guarantees the precision of vehicle model containing thousands of parts with different properties, in the collision tests. Many researches have conducted the FEM analysis based on these vehicle models. Most of these studies show strong shear failures during the impact analysis, especially for a vehicle with large kinetic energy. It was also found that the vehicular impact load had different sensitivities towards different property of vehicles and piers. But the concerned properties of each study were circumscribed. For instance, the simulation of collision between heavy-weight truck and pier is still insufficient, where most of simulations are for light-weight (pickup truck) and median-weight (single unit) vehicle. Therefore, more comprehensive study is needed.

Furthermore, both the experimental and computational studies illustrated that the impact loads specified in codes had a limitation in reveal the relationship between the parameters of the vehicle and the pier. Some of worthy analytic methods based on numerical simulation are proposed to better reflect the real condition of the impact load, but same as the FEM, these methods only comprise of few parameters.

Chapter 2 Theoretical foundation

2.1 Dynamic System

For a single-degree-of-freedom (SDOF) system as shown in Figure 2-1, the equation of motion can be described by the well-known equation of motion:

$$m\ddot{v}(t) + c\dot{v}(t) + kv(t) = p(t) \qquad \text{Eq. 2-1}$$

Where m is the mass; c is the damping coefficient; k is the stiffness of spring; p is the external force acting on the force; v is the displacement of the mass point.

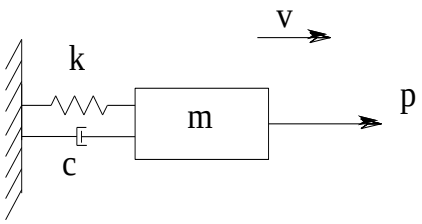

Figure 2-1 SDOF system

For multi-degree-of-freedom system, the Eq. 2-1 could be written as

$$\boldsymbol{M}\ddot{\boldsymbol{V}}(t) + \boldsymbol{C}\dot{\boldsymbol{V}}(t) + \boldsymbol{K}\boldsymbol{V}(t) = \boldsymbol{P}(t) \qquad \text{Eq. 2-2}$$

Where $\boldsymbol{M}$ is the mass matrix; $\boldsymbol{C}$ is the damping coefficient matrix; $\boldsymbol{K}$ is the stiffness matrix; $\boldsymbol{P}$ is the external force vector; $\boldsymbol{V}$ is the displacement vector.

The issue of a vehicle colliding with a pier is actually a very complicated coupling system with millions degree of freedom. This system can be divided into two major subsystems: 1) vehicle system; 2) pier system.

The vehicle system itself is a very complicated coupling system, which contains many components constrained together with welds, bolts, gears, etc. During the collision event, part by part, internal contact will be formed because of deformation and yielding. And the components of vehicle that have contacted with the pier were coupled with pier

with the contact stiffness and contact damping. Although to accurately and completely describe the motion of the equation of such a complex system is almost impossible, a diagram of a simplified coupling system can be shown in Figure 2-2.

As shown in Figure 2-2, k_{jk} and c_{jk} means the stiffness and damping between the jth and the kth degree of freedom. Degrees of freedom numbered, with 1, 2, 3, etc., were coupled with degrees of freedom of pier, named p_l, p_m, p_n, etc., through contact. And the impact force can be expressed as:

$$P_I = k_{1pl}\Delta_{1pl} + k_{2pm}\Delta_{2pm} + k_{3pn}\Delta_{3pn} + \cdots \quad \text{Eq. 2-3}$$

Where Δ_{1pl} is the relative displacement between degree of freedom 1 and p_l

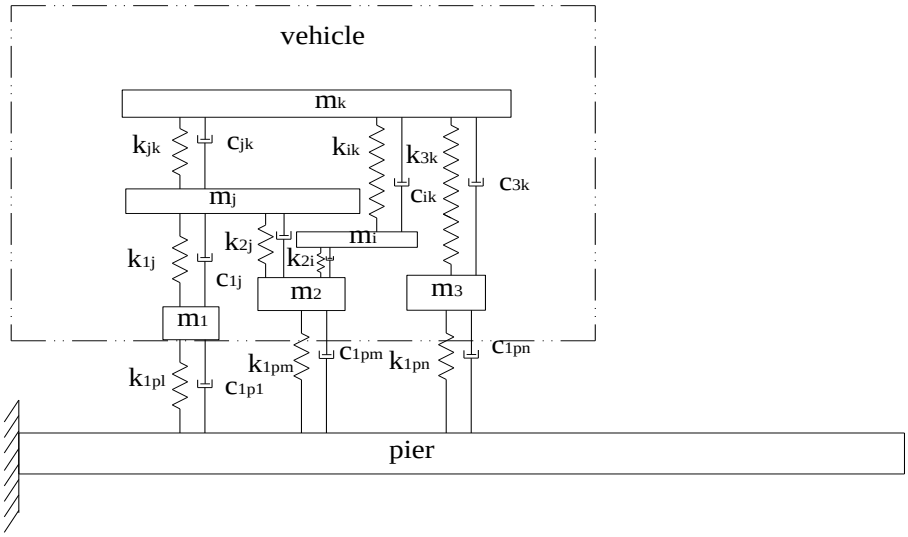

Figure 2-2 Simplified vehicle-to-pier coupling system

2.2 Contact Theory

The common way to solve the contact problem is to get the contact stiffness in order to couple to contact node as shown in part 2.1. The contact theory will be introduced in this section as the theoretical background for FEM based contact simulation.

2.2.1 Hertzian contact theory

Hertzian contact theory was first put forward by Heinrich Hertz in 1882 with the publication of the paper "On the contact of elastic solids". In the drop hammer test of Fujikake (2009), the Hertzian method was applied and well estimated the contact force, which proved the effectiveness in predicting the impact force between rigid-to-deformable collisions. For a rigid sphere in contact with an elastic half-space as shown in Figure 2-3 (Popov, 2010), The contact radius could be calculated by:

$$a = \sqrt{Rd} \qquad \text{Eq. 2-4}$$

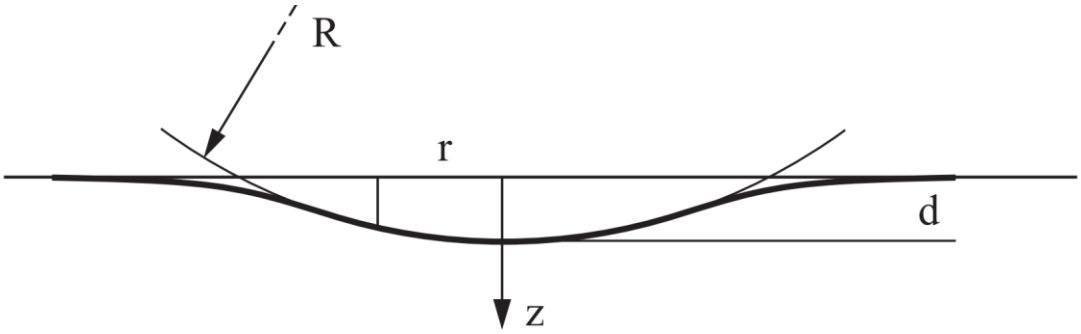

Figure 2-3 Deformation of surface during Hertzian contact

Following the assumption, there is:

$$u_z = d - \frac{r^2}{2R} \qquad \text{Eq. 2-5}$$

$$p = p_0 \left(1 - \frac{r^2}{a^2}\right)^{-1/2} \qquad \text{Eq. 2-6}$$

where u_z is the vertical displacement, and p is the distributed pressure at the location of radius r. For the maximum pressure, there is:

$$p_0 = \frac{2}{\pi} E^* \left(\frac{d}{R}\right)^{1/2} \qquad \text{Eq. 2-7}$$

So the impact force can be obtained through:

$$F = \frac{2}{3} p_0 \pi a^2 \quad \text{Eq. 2-8}$$

$$F = \frac{4}{3} E^* R^{1/2} d^{3/2} \quad \text{Eq. 2-9}$$

where for two curved surfaces, there is:

$$\frac{1}{E^*} = \frac{1-\nu_1^2}{E_1} + \frac{1-\nu_2^2}{E_2} \quad \text{Eq. 2-10}$$

$$\frac{1}{R} = \frac{1}{R_1} + \frac{1}{R_2} \quad \text{Eq. 2-11}$$

Despite of a famous and commonly used method to estimate the contact stiffness and force, there are several assumptions that limit the application of the Hertzian theory when taking the application in the crash simulation:

1. The strains of two contact parts should be located within the elastic limit.
2. The surfaces are continuous and non-conforming (implying that the area of contact is much smaller than the characteristic dimensions of the contacting bodies).
3. Each body can be considered an elastic half-space.
4. The surfaces are frictionless.

For crash analysis, the large impact load will force both the vehicle and pier into plastic state, and friction exists between two impact surfaces. Furthermore, it is hard to determine whether the contact surface of vehicle can be treated as half-space.

2.2.2 Penalty method

Another well-known method often applied in finite element analysis of contact problem is the penalty approach, which is also adopted by LS-DYNA (Peter Wriggers, 2002). Starting with the point-mass-spring system at a specific time t (Figure 2-4), where u is the distance from origin to the impact surface, h is total displacement, and c(u) is the penetration displacement. Assuming due to penetration into the contact surface, a spring

with the penalty stiffness k_c, also known as the penalty parameter, reacted onto the point mass to constrain its penetration.

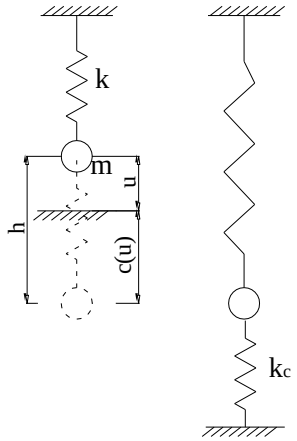

Figure 2-4 Penalty spring and its mechanism

Figure 2-4 shows a point-mass supported by a spring and a penalty spring due to the penalty term. With virtual work, there is:

$$ku\delta u - mg\delta u - k_c c(u)\delta u = 0 \qquad \text{Eq. 2-12}$$

from which, there is the solution

$$u = (mg + k_c h)/(k + k_c) \qquad \text{Eq. 2-13}$$

The value of the penetration depending on the penalty parameter can be obtained as:

$$c(u) = h - u = \frac{kh - mg}{k + k_c} \qquad \text{Eq. 2-14}$$

Hence, the two limiting cases can be distinguished in the penalty method:

$k_c \to \infty \Rightarrow u - h \to 0$, which means that one approaches the correct solution for very large penalty parameters, and hence only very small penetration occurs.

$k_c \to 0$ represents the unconstrained solution, and thus is valid for inactive constraints. In the case of contact, a solution with a very small penalty parameter leads to a high penetration.

The reaction force for a penalty method is computed from

$$R_N = k_c c(u) = \frac{k_c}{k+k_c}(kh - mg) \quad \text{Eq. 2-15}$$

2.2.3 Contact in LS-DYNA

From section 2.2.2, how to determine the k_c is important in the contact simulation. In LS-DYNA, when a slave node is penetrating a master segment, the penalty stiffness will be added to this slave node, as shown in Figure 2-5. Two methods are provided in LS-DYNA for the calculation of the penalty stiffness.

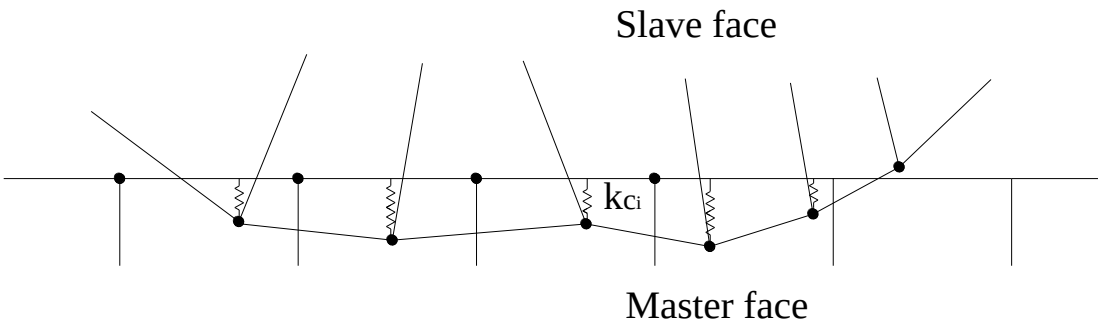

Figure 2-5 Contact springs reacted on the slave nodes

1) Standard penalty formulation

For solid element

$$k_c = \frac{f_s \times Area^2 \times K}{Volume} \quad \text{Eq. 2-16}$$

For shell element

$$k_c = \frac{f_s \times Area \times K}{\max(shell\ diagonal)} \quad \text{Eq. 2-17}$$

Where K is the bulk modulus of contacted element, Area is the face constrains the slave node. For homogenous isotropic materials,

$$K = \frac{\mathrm{E}}{3(1-2v)} \quad \text{Eq. 2-18}$$

where E is the Young's modulus; v is the Poisson's ratio. K can be taken as either the value of the master segment or the slave node.

When the stiffness of the master segment is very different from the stiffness of the slave node, for example, a steel ball impacting a foam bulk, it is very had to use the equation to determine the accurate contact stiffness.

2) Soft Constraint penalty Formulation

To solve the deficiency of the standard penalty formulation, soft constraint penalty formulation is given as:

$$k_{cs}(t) = SOFSCL \cdot \frac{m}{\Delta t^2} \quad \text{Eq. 2-19}$$

where m is the nodal mass, and Δt is the time step. The contact stiffness is to be taken as the maximum stiffness from equation k_{cs} and k_c:

$$k = \max\{k_{cs}, k_c\} \quad \text{Eq. 2-20}$$

The equation shows that the soft constraint formulation is directly related to the time step. With large time step, the stiffness will be taken place of by the standard simulation. Although the standard simulation contains no variable of the time step, large time step will induce large penetration, which may contract the real condition.

2.3 Explicit Dynamics

For complex MDOF system, analytical solution of the equation of motion is usually not possible. Such problems can be tackled by numerical time-stepping methods for integration of differential equation. Researchers have suggested several methods, which can be categorized into implicit method and explicit method. The LS-DYNA takes Nemark-β for the implicit analysis and Central difference method for the explicit analysis.

2.3.1 Implicit method

For the implicit structural dynamics problem, from Eq. 2-2, there is

$$\boldsymbol{M}\underline{\ddot{u}}^{n+1} + \boldsymbol{D}\underline{\dot{u}}^{n+1} + \boldsymbol{K_t}\underline{u}^{n+1} = \underline{P}^{n+1} \quad \text{Eq. 2-21}$$

Eq. 2-21 is solved by the unconditionally stable, one-step, Nemark-β time integration scheme in the following:

$$\underline{\dot{u}}^{n+1} = \underline{\dot{u}}^{n} + \Delta t(1-\gamma)\underline{\ddot{u}}^{n} + \gamma\Delta t\underline{\ddot{u}}^{n+1} \quad \text{Eq. 2-22}$$

$$\underline{\ddot{u}}^{n+1} = \frac{\underline{u}^{n+1}-\underline{u}^{n}}{\beta\Delta t^2} - \frac{\underline{\ddot{u}}^{n}}{\beta\Delta t} - \frac{1}{\beta}(\frac{1}{2}-\beta)\underline{\ddot{u}}^{n} \quad \text{Eq. 2-23}$$

The increments can be written as:

$$\Delta\underline{u}^{n} = \underline{u}^{n+1} - \underline{u}^{n} \quad \Delta\underline{\dot{u}}^{n} = \underline{\dot{u}}^{n+1} - \underline{\dot{u}}^{n} \quad \Delta\underline{\ddot{u}}^{n} = \underline{\ddot{u}}^{n+1} - \underline{\ddot{u}}^{n} \quad \text{Eq. 2-24}$$

$$\Delta\underline{P} = \underline{P}^{n+1} - \underline{P}^{n} \quad \text{Eq. 2-25}$$

Eq. 2-22 and Eq. 2-23 can be rewritten as

$$\Delta\underline{\dot{u}}^{n} = \Delta t\underline{\ddot{u}}^{n} + (\gamma\Delta t)\Delta\underline{\ddot{u}}^{n} \quad \text{Eq. 2-26}$$

$$\Delta\underline{u}^{n} = \Delta t\Delta\underline{\dot{u}}^{n} + \frac{(\Delta t)^2}{2}\underline{\ddot{u}}^{n} + \beta(\Delta t)^2\Delta\underline{\ddot{u}}^{n} \quad \text{Eq. 2-27}$$

Eq. 2-27 can be solved for

$$\Delta\underline{\ddot{u}}^{n} = \frac{\Delta\underline{u}^{n}}{\beta\Delta t^2} - \frac{\underline{\dot{u}}^{n}}{\beta\Delta t} - \frac{1}{2\beta}\underline{\ddot{u}}^{n} \quad \text{Eq. 2-28}$$

By substituting Eq.2.28 into Eq.2.26, there is:

$$\Delta\underline{\dot{u}}^{n} = \frac{\gamma}{\beta\Delta t}\Delta\underline{u}^{n} - \frac{\gamma}{\beta}\underline{\dot{u}}^{n} + \Delta t(1-\frac{\gamma}{2\beta})\underline{\ddot{u}}^{n} \quad \text{Eq. 2-29}$$

Then above two equations are substituted into the incremental equation of motion:

$$\boldsymbol{M}\Delta\underline{\ddot{u}}^{n} + \boldsymbol{D}\Delta\underline{\dot{u}}^{n} + \boldsymbol{K_t}\Delta\underline{u}^{n} = \Delta\underline{P}^{n} \quad \text{Eq. 2-30}$$

so that:

$$\boldsymbol{K_t}^{*}\Delta\underline{u}^{n} = \Delta\underline{P}^{n*} \quad \text{Eq. 2-31}$$

where

$$\boldsymbol{K_t}^* = \boldsymbol{K_t} + \frac{\gamma}{\beta \Delta t}\boldsymbol{D} + \frac{1}{\beta \Delta t^2}\boldsymbol{M} \quad \text{Eq. 2-32}$$

$$\Delta \underline{P}^{n*} = \Delta \underline{P}^n + \left(\frac{1}{\beta \Delta t} m + \frac{\gamma}{\beta} c\right) \underline{\dot{u}}^n + \left[\frac{1}{2\beta} m + \Delta t \left(\frac{\gamma}{2\beta} - 1\right) \boldsymbol{D}\right] \underline{\ddot{u}}^n \quad \text{Eq. 2-33}$$

1) For linear system

The incremental displacement is computed from:

$$\Delta \underline{u}^n = \boldsymbol{K_t}^{*-1} \Delta \underline{P}^{n*} \quad \text{Eq. 2-34}$$

Once $\Delta \underline{u}^n$ is known, $\Delta \underline{\dot{u}}^n$ and $\Delta \underline{\ddot{u}}^n$ can be computed based on Eq. 2-28 and Eq. 2-29, respectively, and $\underline{\ddot{u}}^{n+1}$ $\underline{\dot{u}}^{n+1}$ $\underline{u}^{n+1}$ can be calculated from Eq. 2-24.

Then the acceleration can also be obtained from the equation of motion at time i+1

$$\underline{\ddot{u}}^{n+1} = \boldsymbol{M}^{*-1}(\underline{P}^{n+1} - \boldsymbol{D}\underline{\dot{u}}^{n+1} - \boldsymbol{K_t}\underline{u}^{n+1}) \quad \text{Eq. 2-35}$$

Where Δt is the time step ; β and γ are the free parameters of integration. For a special case, $\beta = 1/4$ and $\gamma = 1/2$ make the method become the trapezoidal rule and energy conserving.

2) For nonlinear system

Iteration is required to approach the accurate result. Taken the modified Newton-Raphson iteration as the example, following steps are required for the $(n+1)^{th}$ time step.

The initialization of first iteration takes:

$$\underline{u}^{n+1}{}_0 = \underline{u}^n \quad \text{Eq. 2-36}$$

The initial true resisting force corresponding to the current tangent stiffness takes:

$$\underline{fs}^{n+1}{}_0 = \underline{fs}^n \quad \text{Eq. 2-37}$$

The residual force can be calculated as:

$$\Delta \underline{R}^{n+1}{}_{i+1} = \Delta \underline{R}^{n+1}{}_i - \Delta \underline{fs}^{n+1}{}_i \quad \text{Eq. 2-38}$$

And its initial value is

$$\Delta \underline{R}^{n+1}{}_0 = \Delta \underline{P}^{n*} \quad \text{Eq. 2-39}$$

The stiffness always takes the tangent stiffness of the stat point $\boldsymbol{K_t}^{*n+1}$

Then for the ith iteration:

$$\boldsymbol{K_t}^{*n+1} \Delta \underline{u}^{n+1}{}_i = \Delta \underline{R}^{n+1}{}_i \quad \text{Eq. 2-40}$$

The increment of displacement of the ith iteration $\Delta \underline{u}^{n+1}{}_i$ can be solved, and then is substituted into:

$$\underline{u}^{n+1}{}_i = \underline{u}^{n+1}{}_{i-1} + \Delta \underline{u}^{n+1}{}_i \quad \text{Eq. 2-41}$$

The increment of resisting force could be computed from:

$$\Delta \underline{fs}^{n+1}{}_i = \underline{fs}^{n+1}{}_i - \underline{fs}^{n+1}{}_{i-1} + (\boldsymbol{K_t}^{*n+1} - \boldsymbol{K_t}^{n+1})\, \Delta \underline{u}^{n+1}{}_i \quad \text{Eq. 2-42}$$

Then the residual force can be calculated as:

$$\Delta \underline{R}^{n+1}{}_{i+1} = \Delta \underline{R}^{n+1}{}_i - \Delta \underline{fs}^{n+1}{}_i \quad \text{Eq. 2-43}$$

The above steps will be repeated to meet the requirement of convergence at the jth iteration:

$$\frac{\Delta \underline{u}^{n+1}{}_j}{\Delta \underline{u}^{n+1}} < \epsilon \quad \text{Eq. 2-44}$$

where ϵ is the toleration of convergence.

Then $\Delta \underline{u}^{n+1}$ will be substituted back into Eq.2-26 and 2-27, for $\Delta \dot{\underline{u}}^{n}$ and $\Delta \ddot{\underline{u}}^{n}$. And then $\ddot{\underline{u}}^{n+1}$ $\dot{\underline{u}}^{n+1}$ $\underline{u}^{n+1}$ can also be obtained.

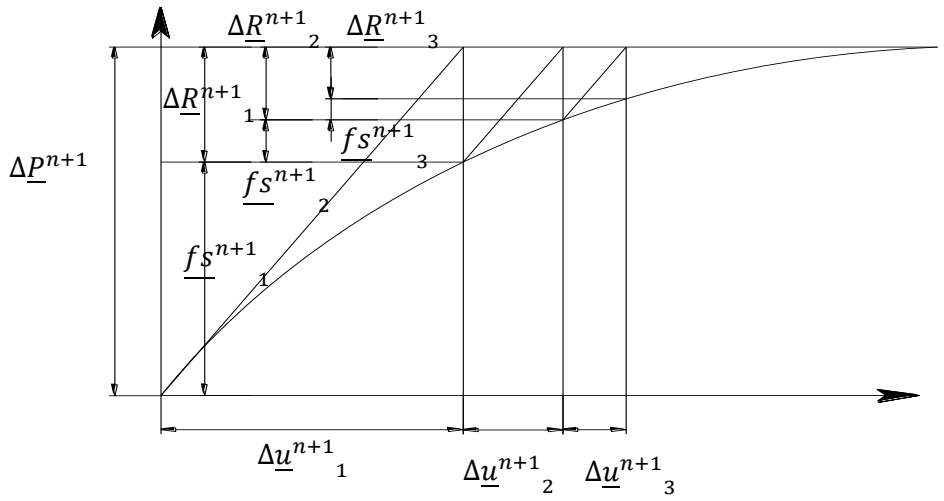

Figure 2-6 Nonlinear iterations

2.3.2 Explicit dynamic

Explicit dynamic analysis is conducted based on central difference method. We can design the algorithm of the explicit finite element method with the framework shown in the following process:

At the n[th] time step,

$$\dot{\underline{u}}^n = \frac{\underline{u}^{n-1}+\underline{u}^{n+1}}{2\Delta t} \qquad \ddot{\underline{u}}^n = \frac{\underline{u}^{n-1}-2\underline{u}^n+\underline{u}^{n+1}}{\Delta t^2} \qquad \text{Eq. 2-45}$$

So the equation of motion can be changed to:

$$\boldsymbol{M}\frac{\underline{u}^{n-1}-2\underline{u}^n+\underline{u}^{n+1}}{\Delta t^2} + \boldsymbol{D}\frac{\underline{u}^{n-1}+\underline{u}^{n+1}}{2\Delta t} + \boldsymbol{K_t}\underline{u}^n = \underline{P}^n \qquad \text{Eq. 2-46}$$

Transferring the known quantities to the right side, there is:

$$\boldsymbol{K_t}^*\underline{u}^{n+1} = \underline{P}^{n*} \qquad \text{Eq. 2-47}$$

$$\boldsymbol{K_t}^* = \frac{\boldsymbol{M}}{\Delta t^2} + \frac{\boldsymbol{D}}{\boldsymbol{2}\Delta t} \qquad \text{Eq. 2-48}$$

$$\underline{P}^{n^*} = \underline{P}^n - \left[\frac{\boldsymbol{M}}{\Delta t^2} - \frac{\boldsymbol{D}}{\boldsymbol{2}\Delta t}\right]\underline{u}^{n-1} - \left[\boldsymbol{K_t} - \frac{\boldsymbol{2M}}{\Delta t^2}\right]\underline{u}^n \qquad \text{Eq. 2-49}$$

$$\underline{u}^{n+1} = \boldsymbol{K_t}^{*\boldsymbol{-1}}\underline{P}^{n^*} \qquad \text{Eq. 2-50}$$

To avoid the instability of the solution which may cause blowing up of the result, it requires that:

$$\Delta t < \frac{2}{\omega_{max}} \qquad \text{Eq. 2-51}$$

where ω_{max} is the maximum circular frequency from the modal analysis. Besides, much smaller time step Δt should be taken even though the equation is satisfied to obtain accurate result.

The central difference method can be easily adopted for the solution of the nonlinear system by simply substituting the $\boldsymbol{K_t}$ with $\underline{fs}^n$, so that the only difference is

$$\underline{P}^{n^*} = \underline{P}^n - \left[\frac{\boldsymbol{M}}{\Delta t^2} - \frac{\boldsymbol{D}}{\boldsymbol{2}\Delta t}\right]\underline{u}^{n-1} - fs^n + \frac{\boldsymbol{2M}}{\Delta t^2}\underline{u}^n \qquad \text{Eq. 2-52}$$

By comparing the two methods, it shows that in nonlinear implicit analysis, solution of each step requires a series of trial solutions (iterations) to establish equilibrium within a certain tolerance. In explicit analysis, no iteration is required as the nodal accelerations are solved directly. Explicit analysis handles nonlinearities with relative ease as compared to implicit analysis, which includes the treatment of contact and material nonlinearities. But it should be noted that the requirement for maximum time step should be fulfilled, whereas the implicit method is unconditionally stable.

2.4 Hourglass Mode

For solid and shell elements in LS-DYNA during crash analysis, volume or area integration is carried out with Gaussian quadrature. g is the function defined over the volume:

$$\int g dv = \iiint g|\boldsymbol{J}| d\zeta d\eta d\xi \quad \text{Eq. 2-53}$$

which is approximated by

$$\sum_{i=1}^{n}\sum_{j=1}^{n}\sum_{k=1}^{n} g(\xi_i, \eta_j, \zeta_k)|\boldsymbol{J}| w_i w_j w_k \quad \text{Eq. 2-54}$$

where w_i, w_j, w_k are the weighing factors; $\boldsymbol{J}$ is the determinant of the Jacobian matrix. Usually one-point integration is chosen to cut down the calculation expense for the contact simulation. Besides, 8-point integration has another disadvantage in addition to cost. Fully integrated elements used in the solution of plasticity problems where Poisson's ratio approaches 0.5 lock up in the constant volume bending modes, which is known as the relative volume change:

$$\varepsilon_{xx} + \varepsilon_{yy} + \varepsilon_{zz} = \left(\sigma_{xx} + \sigma_{yy} + \sigma_{zz}\right)(1 - 2\nu)/E \quad \text{Eq. 2-55}$$

where Poisson's ratio ν is close to 0.5, the equation is equal to 0.

However, for one-point integration, there will be zero energy modes, which are also called hourglass modes. The four kinds of hourglass modes for one-point integrated solid element are shown in Figure 2-7.

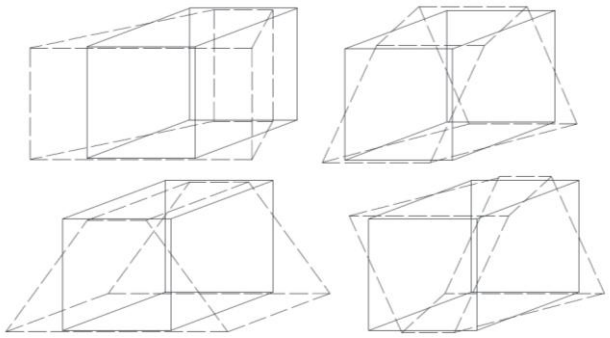

Figure 2-7 Hourglass modes for 8-node solid element

For one-point quadrature:

$$n = 1$$

$$w_i = w_j = w_k = 2$$

$$\xi_i = \eta_j = \zeta_k = 0$$

The shape function for the 8-node hexahedron is

$$\phi_i = \frac{1}{8}(1 + \xi\xi_i)(1 + \eta\eta_i)(1 + \zeta\zeta_i) \quad \text{Eq. 2-56}$$

An anti-symmetry property of the strain matrix will yield with:

$$\frac{\partial\phi_1}{\partial x_i} = -\frac{\partial\phi_7}{\partial x_i} \quad \frac{\partial\phi_3}{\partial x_i} = -\frac{\partial\phi_5}{\partial x_i} \quad \frac{\partial\phi_2}{\partial x_i} = -\frac{\partial\phi_8}{\partial x_i} \quad \frac{\partial\phi_4}{\partial x_i} = -\frac{\partial\phi_6}{\partial x_i} \quad \text{Eq. 2-57}$$

so that there is

$$\sum_{k=1}^{8} \frac{\partial\phi}{\partial x_i} \Gamma_{\alpha k} = 0 \quad \text{Eq. 2-58}$$

while the product of the shape vector with the nodal velocities

$$h_{i\alpha} = \sum_{k=1}^{8} \dot{x}_i^{\,k} \, \Gamma_{\alpha k} \quad \text{Eq. 2-59}$$

$$\mathrm{f}_{i\alpha} = a_h h_{i\alpha} \Gamma_{\alpha k} \quad \text{Eq. 2-60}$$

$$a_h = Q_{hg} \rho {v_e}^{2/3} \frac{c}{4} \quad \text{Eq. 2-61}$$

where v_e is the element volume; ρ is the density; c is the material sound speed; and Q_{hg} is a desirable constant to determine the magnitude of the resist force. In LS-DYNA, Q_{hg} is defined by the user. It should be noted that applying this force will also stiffen the element. Therefore Q_{hg} should be given a suitable value to prevent the hourglass model, but not yield an inaccurate result.

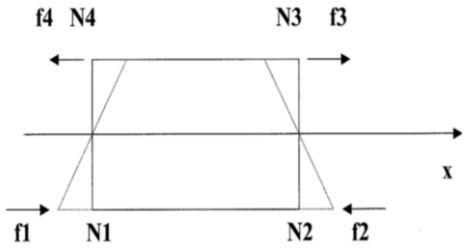

Figure 2-8 Resisting forces to prevent hourglass deformation

Chapter 3 Rigid-to-flexible-body impact

To get the accurate result of collision simulation between pier and vehicle, it is important to make sure the physical characteristics such as geometry, material properties, boundary conditions, and some extra parameters, such as the Hourglass coefficient, are set to the correct values, which can yield the solution reflecting the physical truth. The best way for the validation is to match the displacements and forces with experimental results. Since the process of vehicle colliding with pier is very complicated, the two coupled systems, the vehicle and the pier, are separated into two parts for validation purpose. This chapter will validate the pier model by the independent repeat verification of the experimental result of Fujikake et al. (2009) through the finite elemental simulation in LS-DYNA.

3.1 Original Experiment Setup

This original experiment tested a hammer dropping on a reinforced concrete beam with different heights. The dimension of the RC specimens as shown in Figure 3-1 are 259mm in depth, 150mm in width, and 1700 mm in length. The properties of the test RC beam specimens are listed in Table 3.1. The specimen S1616 included two top and two bottom longitudinal bars with diameter 16mm. The specimen S1322 included two top bars with diameter 13mm, and two bottom bars with diameter 22mm. The specimen D2222 included two top and two bottom bars with diameter 22mm. The yield strengths of D13, D16, and D22 were 397MPa, 426MPa, and 418 MPa, respectively. The transverse ties were spaced at 75mm along the beam with diameter 10mm. The aggregates had the maximum size of 10mm. All tests were performed within a period of four days after 70days of casting. The concrete compressive strength at the time of testing was 42MPa.

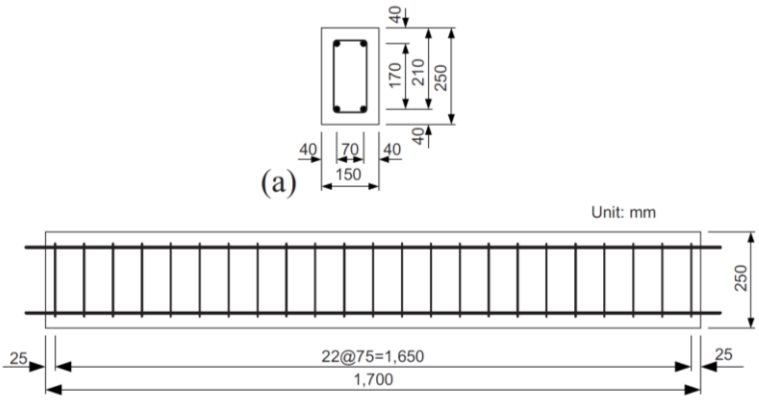

Figure 3-1 Dimension of RC beam specimens

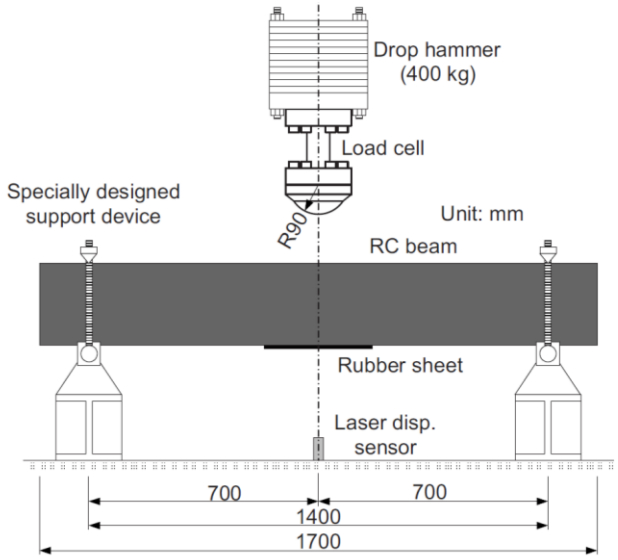

Figure 3-2 Configurations of the impact test

As shown in Figure 3-2, the drop hammer was dropped freely onto the top surface of the RC beam at mid-span from four different heights: 0.15m, 0.3m, 0.6m and 1.2m for S1616 beam specimens; 0.6, 0.6, 1.2 and 2.4m for S1322 and S2222 beam specimens, respectively. The hammer had a hemispherical head with a radius of 90mm. The total mass of the hammer was 400kg. The RC beam was supported by two specially designed devices, which allowed the beam to freely rotate, but unable to move transversely.

Table 3-1 Properties of the test RC beam specimens

Designation	Bending resistance $R_{M=4\ Mu/L}$ (kN)	Shear resistance $R_{S=2\ Vu}$ (kN)	R_S/R_M
S1616	91.1	232.0	2.55
S1322	162.2	245.4	1.51
S2222	162.6	245.4	1.51

3.2 Finite Element Modeling for the Independent Repeat Verification

To verification the original experimental result, the finite element software LS-DYNA is used in this study, due to its good performance in explicit dynamic simulation. To ensure the consistency of units, the input unit of length, time, stress, density, and force are in mm, sec, MPa and N, respectively.

3.2.1 Geometry

The finite element model of the beam is presented in Figure 3-3. The beam is broken into 46 parts: the concrete core and the concrete cover at mid span, at 1/4 span, and at support. The concrete is modeled with 8-node, constant stress, single-point integration solid hexahedron elements. The dimension of element in the longitudinal direction is 25mm. At each cross section, there are 32 elements for the concrete core, and 64 elements for the concrete cover.

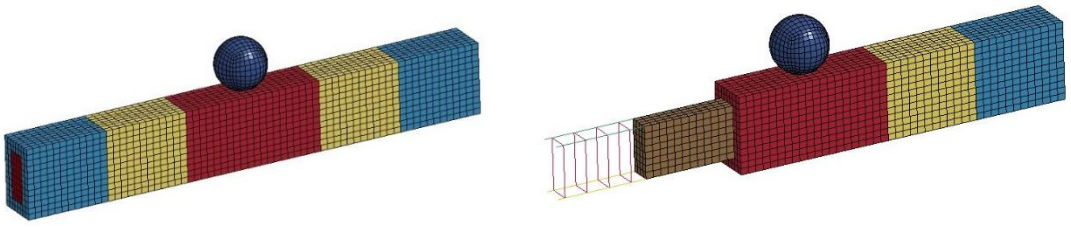

Figure 3-3 Finite element model of reinforcement concrete beam with drop hammer

The steel reinforcement is modeled with the beam element with two-node, Hughes-Liu with cross section integration, 2×2 Gaussian quadrature. The nodes of beam elements are merged with the nodes of concrete solid element, which allow the steel elements and concrete elements bonded together with no sliding.

The drop hammer is modeled with 8-node, constant stress, single-point integration solid elements. The drop hammer is simplified into a sphere with a 90mm radius.

The concrete part contains 6528 solid element elements. The longitudinal reinforcements have 272 elements, and the ties include 552 elements. For hammer, there are 5103 rigid elements. In total, the model includes 12455 elements and 16513 nodes. Figure 3.3 shows the mesh of the model.

3.2.2 Material

3.2.2.1 Concrete

The concrete of beam is modeled using material model 159. This material model is developed by Federal Highway Administration to predict the dynamic performance—both elastic deformation and failure—of concrete used in roadside safety structures when involved in a collision with a motor vehicle. (Murray, 2007).

Concrete is a composite material that consists primarily of aggregate and mortar. Its response is complex, ranging from brittle in the tensile and low confining pressure regimes to ductile at high confining pressure. The critical behaviors of concrete are shown below.

The elastic behavior of e concrete is isotropic before cracking, which means the concrete is assumed to be well mixed, vibrated, and not stratified. Young's modulus of concrete varies with concrete strength:

$$\mathrm{E} = \mathrm{E}_c \left(\frac{f'c}{10}\right)^{1/3} \quad \text{Eq. 3-1}$$

where E is the Young's modulus and $= 18275\mathrm{MPa}$ (which is the value of Young's modulus when $f'c = 10MPa$)

This equation is from Comité Euro-Internacional du Béton (CEB) - Federation for Prestressing (FIP) Model Code (1990). The shear and the bulk modulus can be obtained as well based on the equations:

$$\mathrm{G} = \frac{E}{2(1+v)} \quad \text{Eq. 3-2}$$

$$\mathrm{K} = \frac{E}{3(1-2v)} \quad \text{Eq. 3-3}$$

where v is the Poisson's ratio.

Alternatively, the ACI code 318 suggests the elastic modulus:

$$\mathrm{E}_c = 4700\sqrt{f'c}\ \mathrm{MPa} \quad \text{Eq. 3-4}$$

This formula gives Young's modulus that are within 9% of difference of those given by Eq. 3-1 based on report FHWA-HRT-05-062 (Murray 2007)

Concrete exhibits softening in the tensile and low to moderate compressive regimes. The damage formulation models both strains softening and modulus reduction. The damage formulation is based on the work of Simo and Ju (1987):

$$\sigma_{ij}^{d} = (1 - \mathrm{d})\sigma_{ij}^{vp} \quad \text{Eq. 3-5}$$

where d is a scalar damage parameter that transforms the stress tensor without damage, denoted σ_{ij}^{vp}, into the stress tensor with damage, denoted σ_{ij}^{d}. Thus, $1 - \mathrm{d}$ is a reduction factor whose value depends on the accumulation of damages. Damage to the concrete elements is tracked through ductile and brittle damage parameters. Ductile damage occurs when stress is applied to the element in compression. Brittle damage occurs when stress is

applied to the element in tension. The strain-stress relationship is shown in Figure 3-4. The concrete model has a mass density of 2,274 kg/m^3, an unconfined compressive strength of 42 MPa, and a maximum aggregate size of 10 mm. The element is set to erode after the maximum principle strain exceeds 0.1.

Concrete exhibits an increase in strength with increasing strain rate. A viscoelastic formulation is used to model an increase in strength of the elements with an increasing strain rate. CEB provides specifications for the DIF. However, the CEB specifications are not a good fit to the tensile data from Ross and Tedesco (1992). The material 159 gives default dynamic increase factor (DIF) curve, as shown in Figure 3-5 based on numerous calculations via a trial and error. This curve provides good fit to both the tension and compression data from Bischoff (1995) and Ross (1992).

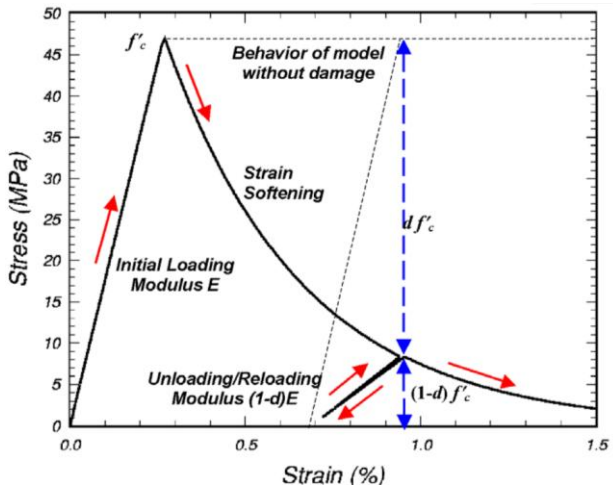

Figure 3-4 Strain-stress relationship of the concrete

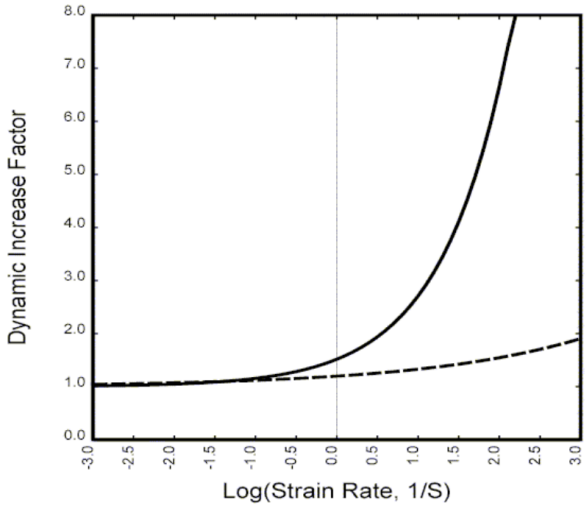

Figure 3-5 DIF related to the strain rate for the concrete

3.2.2.2 Steel reinforcement

The steel reinforcement material has applied material model 24, an elasto-plastic material model accounting for a stress-strain curve and strain rate dependency. Then, density of all reinforcement bars is 7850 kg/m^3. The elastic modulus is set to 200 GPa. The tangent modulus for the hardening stage is 1.5 GPa after the yield point reached. The yield stresses of the D10, D13, D16 and D22 are 295MPa, 397MPa, 426MPa and 418 MPa, respectively. The Poisson's ratio is assumed to be 0.3. The bilinear model for the steel reinforcement is shown in Figure 3-6.

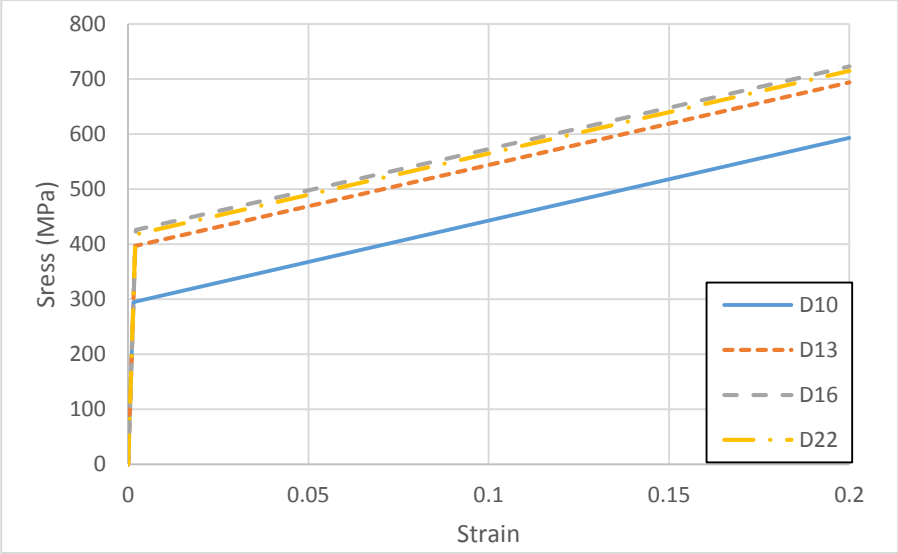

Figure 3-6 Strain-stress relationships of steel reinforcement bars

Malvar and Crawford (1998) collected data on dynamic tests conducted on steel reinforcement and proposed the following equations to determine the DIF of steel reinforcement:

$$\text{DIF} = \left(\frac{\dot{\varepsilon}}{10^{-4}}\right)^{\alpha} \quad \text{Eq. 3-6}$$

For yield stress, $\alpha = \alpha_{fy}$ is expressed as follows:

$$\alpha_{fy} = 0.074 - 0.040\frac{f_y}{414} \quad \text{Eq. 3-7}$$

For ultimate stress, $\alpha = \alpha_{fu}$ is expressed as follows:

$$\alpha_{fy} = 0.019 - 0.009\frac{f_u}{414} \quad \text{Eq. 3-8}$$

where f_y is the yield strength in MPa. These equations are valid for the steel material with yield stress between 290 MPa and 710 MPa, and for strain rates between 10^{-4} and 225 s^{-1}. The four curves of DIF corresponding to the strain rate are plotted in Figure 3-7.

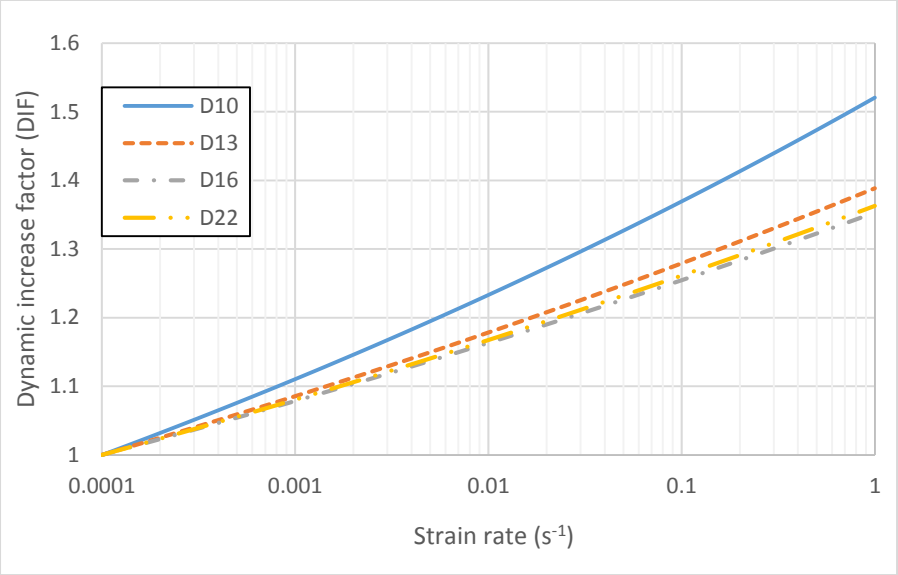

Figure 3-7 Dynamic increase factor for steel bars corresponding to the strain rate

3) Drop Hammer

The drop is assumed as a rigid steel ball, which modeled as material model 20. The elastic modulus of steel, 200GPa, and Poisson's ratio, 0.3, are assigned to the rigid elements, which are necessary for correct modeling the contact spring. The sphere representing the drop hammer has a radius of 90mm.

3.2.3 Modeling control

3.2.3.1 Boundary conditions

The nodes at the bottom of the beam, and 150mm away from the two ends, are restrained in the horizontal and vertical directions, which allow free rotation.

3.2.3.2 Initial Conditions and Loads

An initial velocity is applied to the drop hammer to account for the dropping height. The impact velocity is calculated based on theorem of kinetic energy:

$$v = \sqrt{2gh} \quad \text{Eq. 3-9}$$

where g is the acceleration of gravity (9.806 m/s^2); h is the free dropping height (m); v is the impact velocity (m/s). The corresponding impact velocities are 1.72, 2.43, 3.43, 4.85 and 6.86 m/s, corresponding to the dropping heights of 0.15, 0.30, 0.60, 1.20 and 2.40m, respectively.

The gravity is applied to the system as a body force corresponding to the acceleration 9.806m/s^3. A static implicit analysis is to be run before the explicit analysis to prescribe the initial deformation and stress for the beam to eliminate the dynamic response due to the gravity.

3.2.3.3 Contact

The automatic surface-to-surface contact is defined between the rigid drop hammer, and the beam. The rigid sphere is defined as the master part, and the beam is defined as the slave part. Friction in LS-DYNA is based on a Coulomb formulation:

$$f_s = \mu |f_n| \quad \text{Eq. 3-10}$$

where f_s is the frictional force; μ is the coefficient of friction; and f_n is the component of contact force normal to the contact surface. The coefficient of friction μ is defined based on the following equation:

$$\mu = \mu_d + (\mu_s - \mu_d) e^{-c|v|} \quad \text{Eq. 3-11}$$

Where μ_d is the dynamic coefficient of friction; μ_s is the static coefficient of friction; c is the exponential decay factor; v is the velocity. The static coefficient of friction and dynamic coefficient of friction are defined as 0.5 and 0.3, respectively. The exponential decay coefficient is 0.001 for velocity with unit in mm/s (1.0 for m/s). And the coefficient of friction at specific velocity is plotted in Figure 3-8.

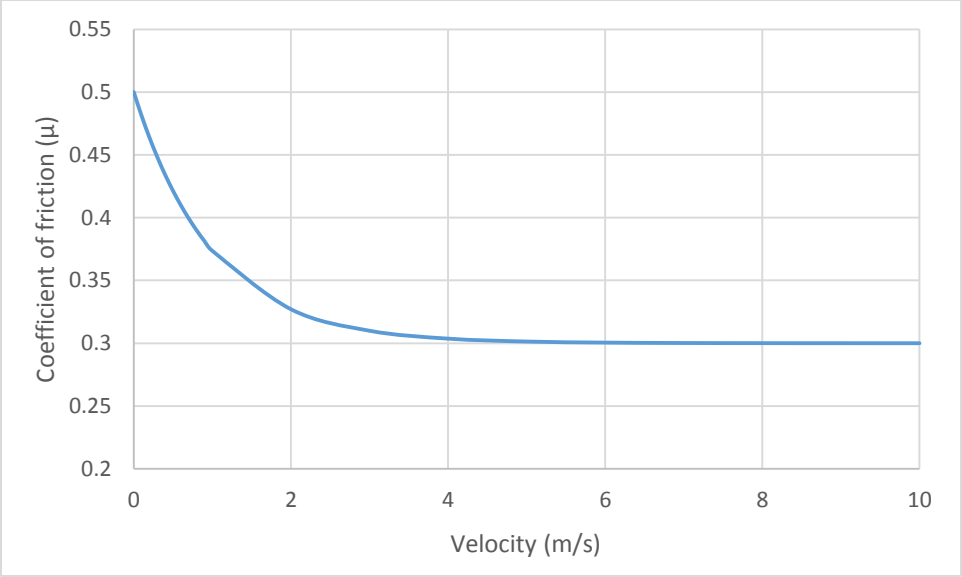

Figure 3-8 Exponential decay of Coefficient of friction

3.2.3.4 Solution control

A termination time of 0.035 seconds is selected, of which the time history can capture the impact and response from the drop hammer experiment. The initial time step is set to 10^{-6}s, which is enough to ensure the stability and accuracy of analysis, based on sensitive study of time steps from 10^{-5} to 10^{-7}.

Hourglass energy control is opened, which is based on the theory shown in section 2.4. To ensure the hourglass model is effectively restrained, the hourglass energy of the system should be less than 10% of the total energy of the whole system (Bala and Day, 2004). Viscous and stiffness hourglass control formulations generate hourglass forces proportional to the components of nodal velocity and displacement, respectively. Type 5, Flanagan-Belytschko with exact volume integration, hourglass control is a stiffness form algorithm and is used in this study to manage hourglass model in the drop hammer and vehicle impact simulations.

Due to the chosen of an appropriate hourglass coefficient will affect the obtained impact

force, a sensitive study has been performed to determine the hourglass coefficient. The S1322 bean with a drop height of 1.20 m is used to conduct this study.

The hourglass coefficient Q_h values ranged from the default value of 0.1 to 0.001 are studied. The impact forces of the different hourglass coefficients are shown in Figure 3-9. From the impact force, it can be illustrated that with the increase of the hourglass coefficient, the PDF changes little, but the impact force is larger for the higher constant, after the first peak of higher hourglass.

The hourglass energies corresponding to coefficient values of 0.1 and 0.001 are shown in Figure 3-10 and 3-11, respectively. From the two figures, it shows that larger hourglass coefficient will result in smaller hourglass energy, which means the hourglass model is better restrained. The ratios of hourglass to total energy for the hourglass coefficients equal to 0.1 and 0.001 are 3.1% and 15.6%, respectively. The ratio of the hourglass energy to the total energy is plotted in Figure 3-12. Figure 3-12 illustrates that, when hourglass coefficient reaches 0.003, the ratio of hourglass energy will be reduced to around 3% from the 15.6% corresponding to coefficient 0.001. Continuing increasing the hourglass coefficient has no further contribution to reducing energy ratio. Therefore, the hourglass coefficient in this study will take 0.01 for following analyses.

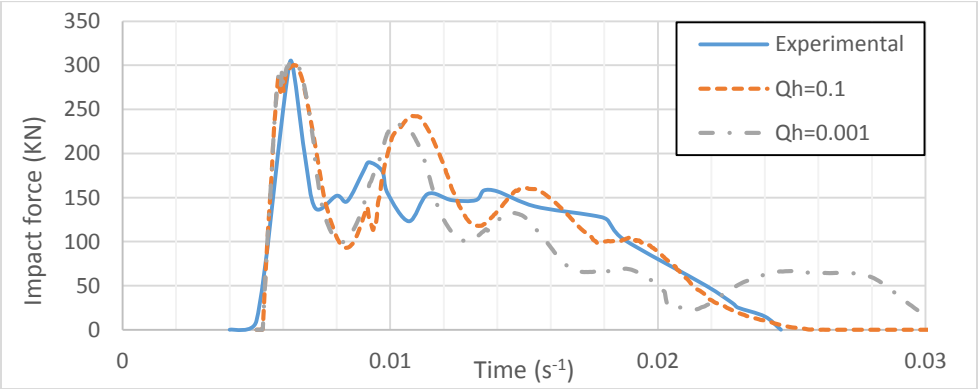

Figure 3-9 Impact force corresponding to different hourglass constant

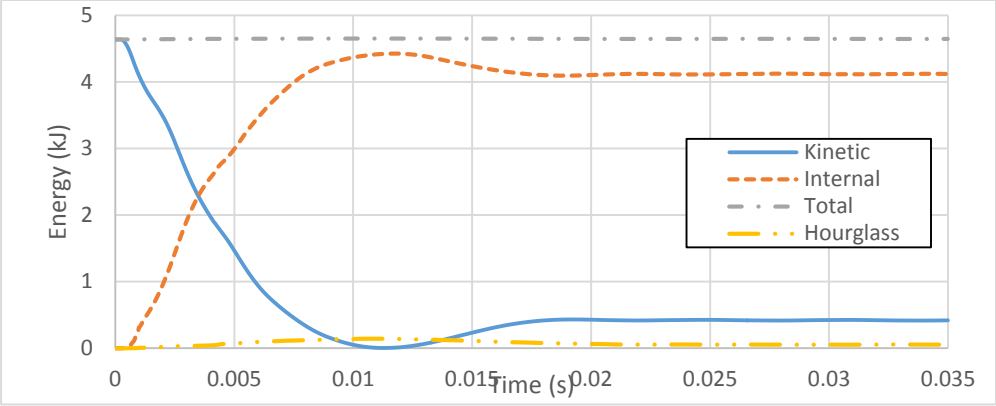

Figure 3-10 Hourglass energy corresponding to Q_h=0.1

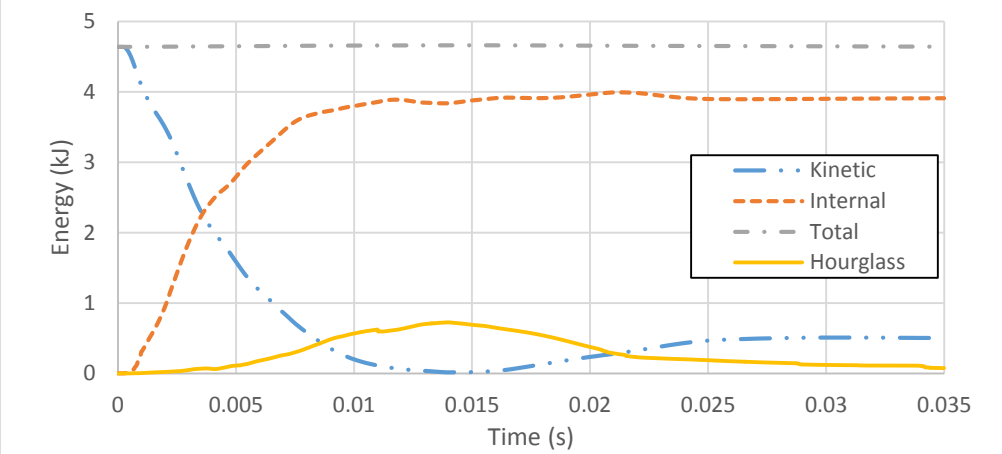

Figure 3-11 Hourglass energy corresponding to Q_h=0.001

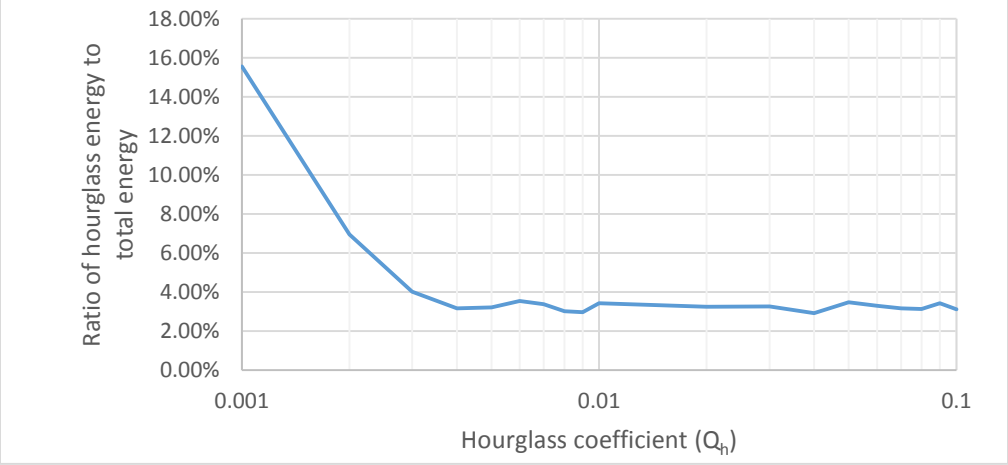

Figure 3-12 Ratio of hourglass energy to total energy

3.3 Simulation Result and Comparison

The experimental results reported by Fujikake et al. (2009) are compared with the mid-span deflection and impact forces from the analyses. The S1616, S1322, and S2222 beam experimental and analytical results are presented from Figures 3-13 to 3-15, respectively. The average differences for the peak values of impact load and mid-span displacement between the analytical and experimental results are 8.6% and 9.2%, respectively, which shows that the peak dynamic responses of FEM analyses match well with the experimental results.

It shows that with the increase of drop height, both the displacement and impact force increase due to faster impact speed of the hammer. From the time history of the impact force, the analytic curves keep in good agreement with the experimental curve for around the first peak response, which is also the maximum dynamic response yielded during the initial contact. For the second peak response, the value of the analytic curve is larger. For the displacement, although the peak values match each other well, the results of FEM analyses obviously die down faster than the experimental result. Almost for all the cases, the displacement of FEM analyses is slightly lower than the experimental result.

The crack profile is observed using the plastic strain contours (Mohammed 2011). The effective plastic strain is expressed as:

$$\xi_{eff}^{p} = \int_0^t \left(\frac{2}{3}\dot{\xi}_{ij}^{p}\dot{\xi}_{ij}^{p}\right)^{1/2} dt \qquad \text{Eq. 3-12}$$

$$\dot{\xi}_{ij}^{p} = \dot{\xi}_{ij} - \dot{\xi}_{ij}^{e} \qquad \text{Eq. 3-13}$$

where $\dot{\xi}_{ij}$, $\dot{\xi}_{ij}^{e}$, $\dot{\xi}_{ij}^{p}$ are the strain rate tensor, elastic strain tensor and plastic strain tensor, respectively.

The crack patterns are in good agreement with the experimental results. The crack profiles of the analytical and experimental results are displayed from Figures 3-16 to 3-18. The red area of contours shows the diagonal development of the cracks. For high-speed impact (drop height at 1.2m and 2.4m), the erosion at top of the beam occurs due to local compression yielding from contact force. The failure model shows a combination of shear failure and bending failure. For low impact velocity, the bending failure is more obvious, while for high-speed impact, the shear failure dominates.

3.4 Summary

Based on the comparison between the FEM results and experimental results, it can be concluded that the finite element model, with material models 24 and 159, can be applied to the simulation of the reinforcement concrete pier under the dynamic impact load from the vehicle. The automatic surface to surface contact algorithm can accurately capture the coupling characteristics between two impact objects. Flanagan-Belytschko stiffness hourglass control minimizes the hourglass deformation of under-integrated solid.

Table 3-2 Percentage error between the FEM result and experimental result

	S1616		S1322		S2222	
Dropping height (m)	F_I (kN)	D (mm)	F_I (kN)	D (mm)	F_I (kN)	D (mm)
0.15	17.3%	7.5%	-	-	-	-
0.30	16.7%	4.7%	16.1%	18.4%	5.5%	11.3%
0.60	6.0%	9.2%	3.8%	15.5%	3.4%	8.5%
1.20	3.0%	13.7%	2.0%	11.3%	4.5%	4.1%
2.40	-	-	15.0%	3.3%	9.9%	6.2%

Note: F_I=Impact force; D=displacement

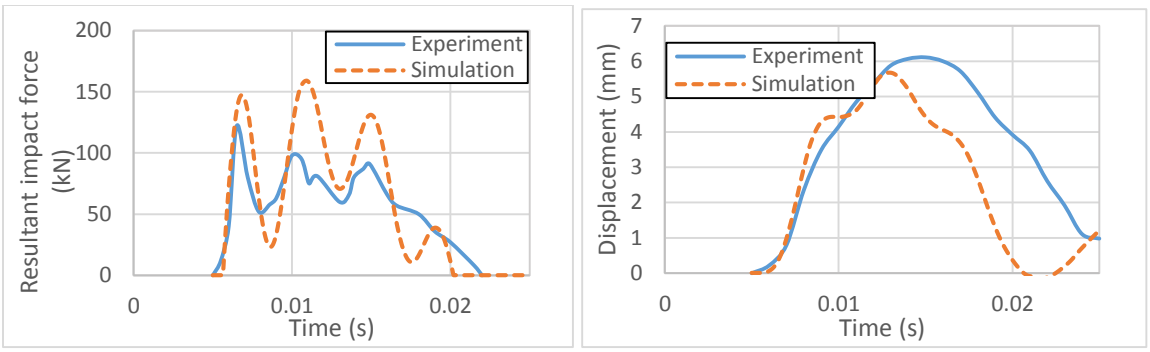

a) Drop height at 0.15m

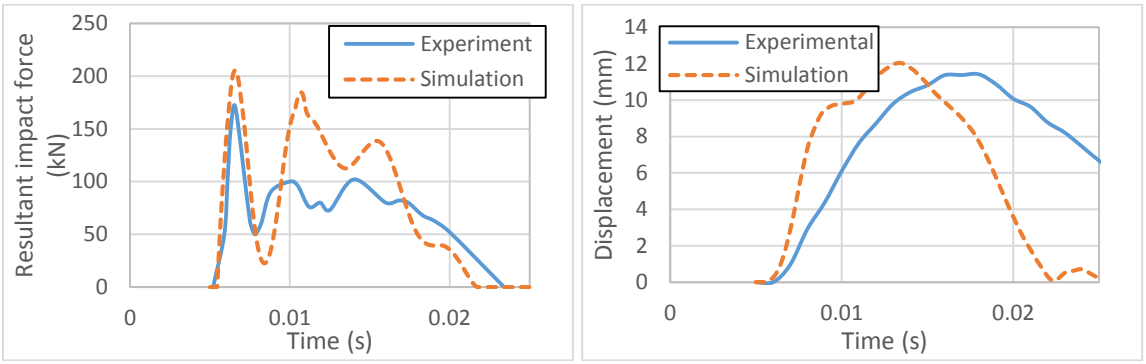

b) Drop height at 0.30m

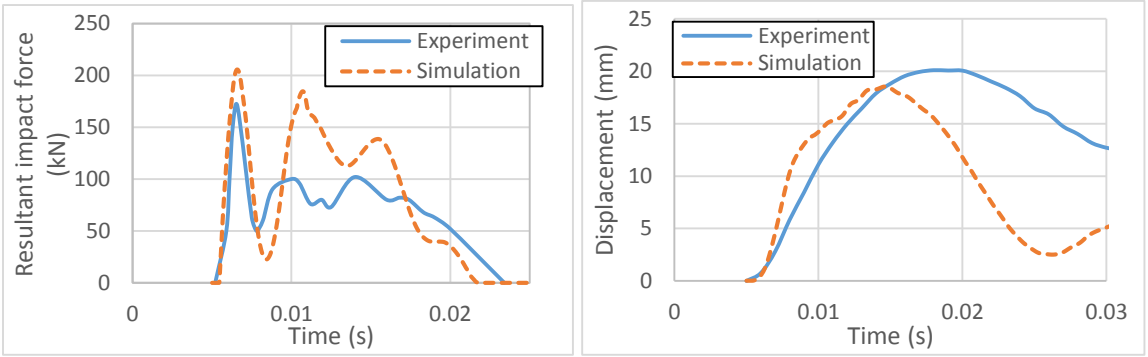

c) Drop height at 0.60m

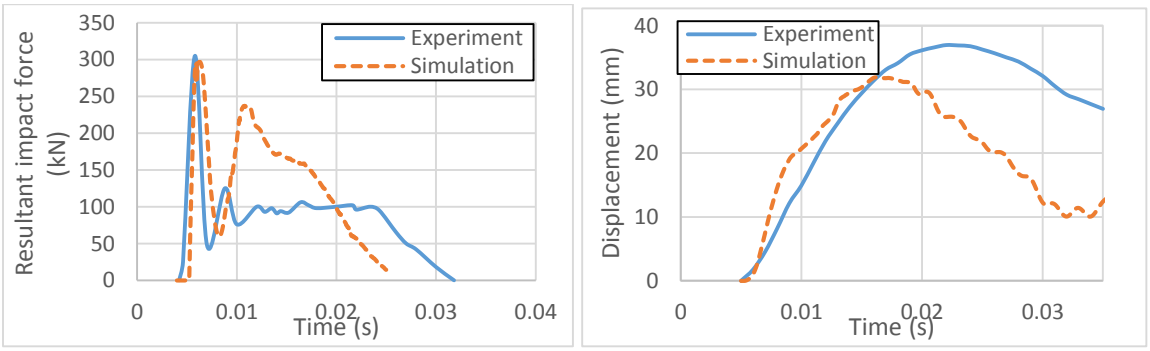

d) Drop height at 1.20m

Figure 3-13 Impact force and mid-span deflection for S1616 beam

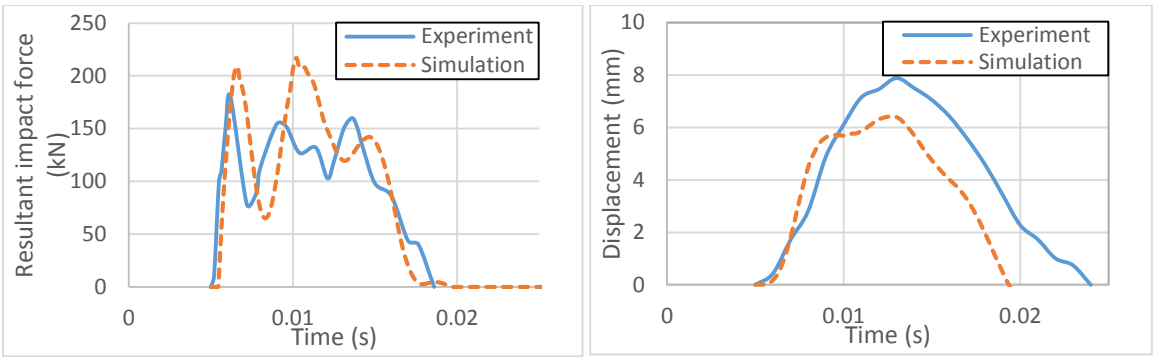

a) Drop height at 0.30m

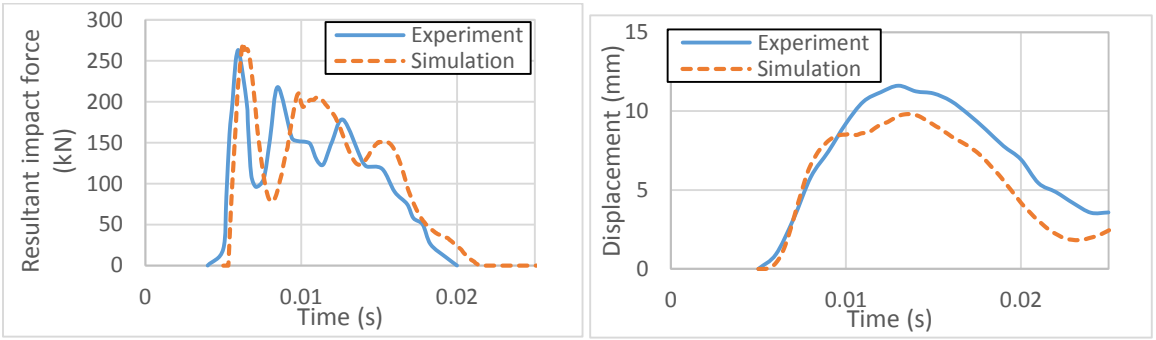

b) Drop height at 0.60m

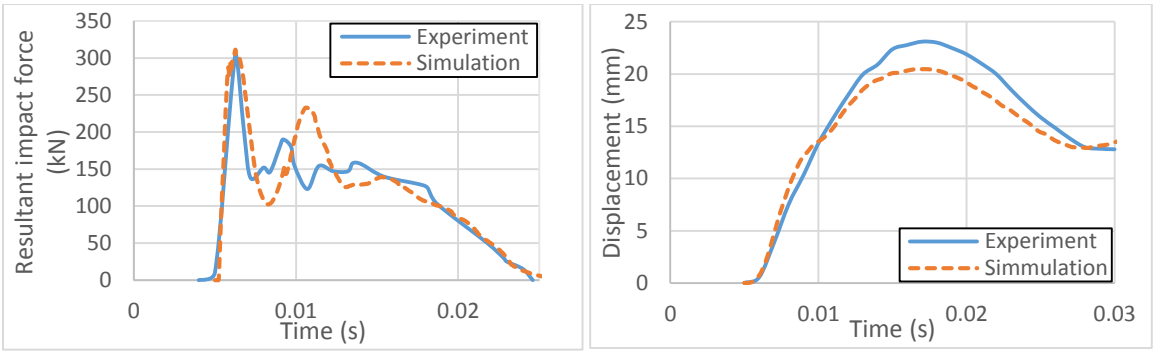

c) Drop height at 1.20m

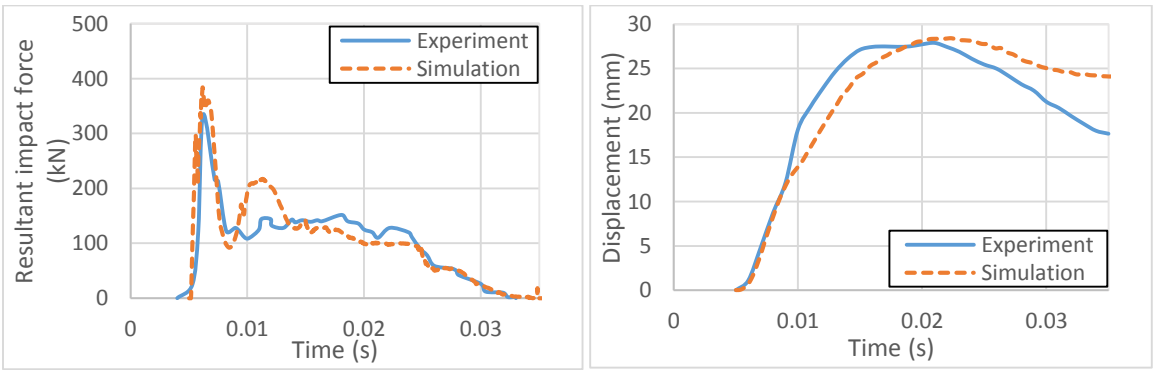

d) Drop height at 2.40m

Figure 3-14 Impact force and mid-span deflection for S1322 beam

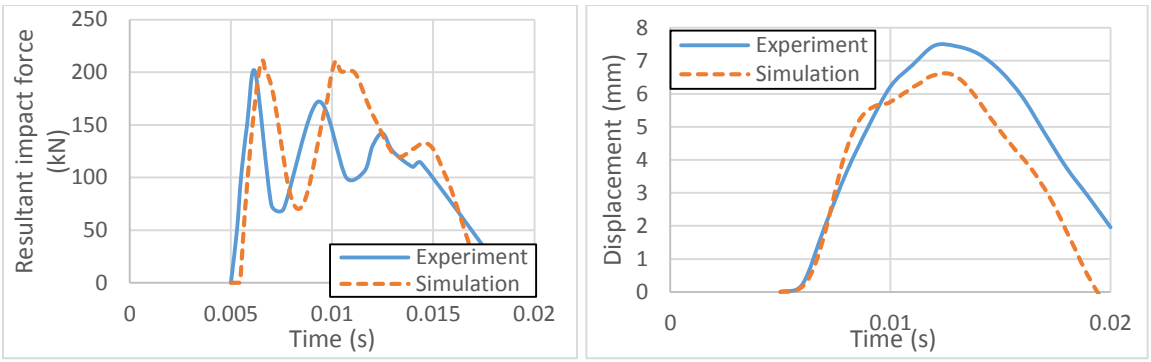

a) Drop height at 0.30m

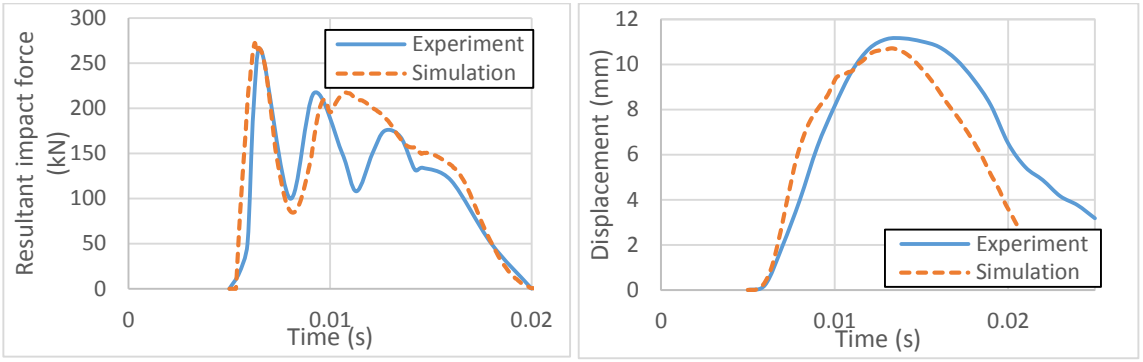

b) Drop height at 0.60m

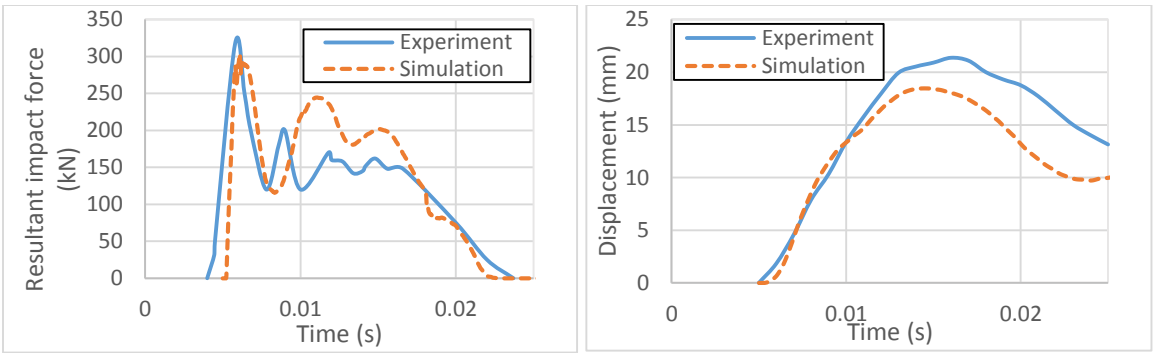

c) Drop height at 0.60m

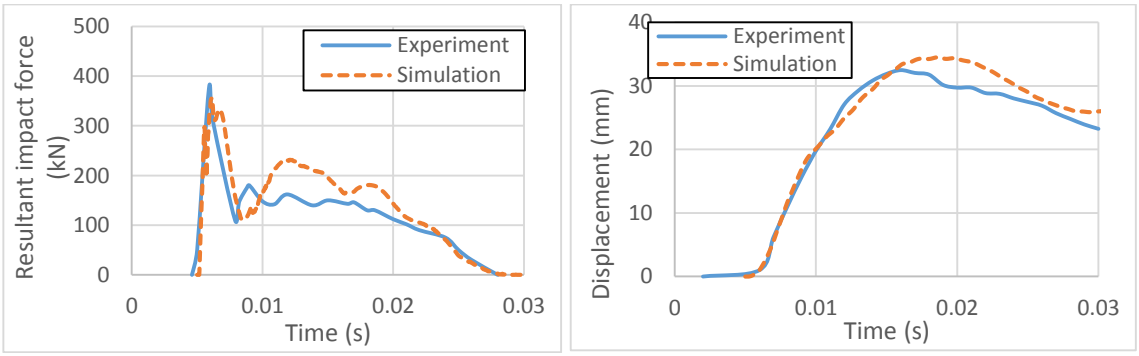

d) Drop height at 0.60m

Figure 3-15 Impact force and mid-span deflection for S2222 beam

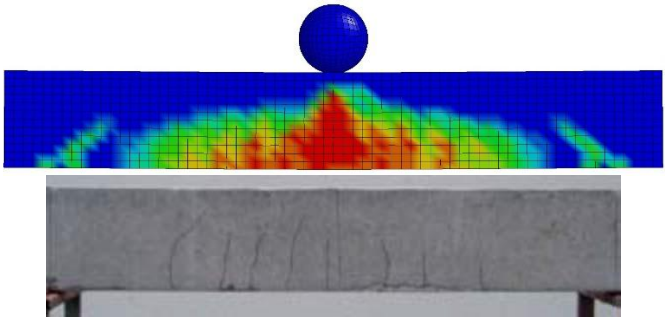

(a) Drop height at 0.15m

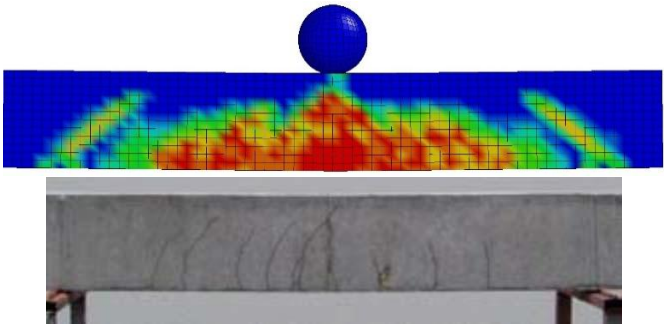

(b) Drop height at 0.3m

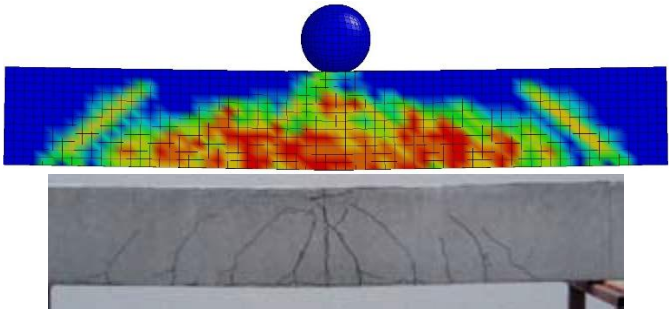

(c) Drop height at 0.6m

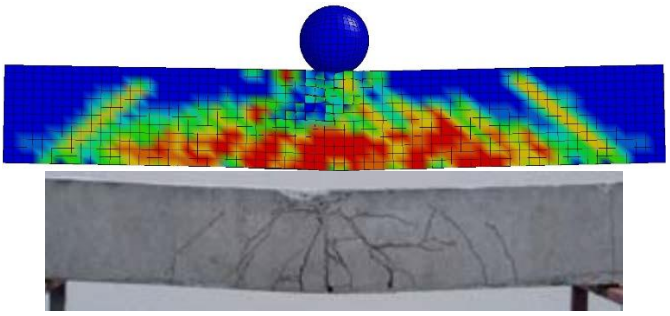

(d) Drop height at 1.2m

Figure 3-16 Plastic strain for specimen S1616

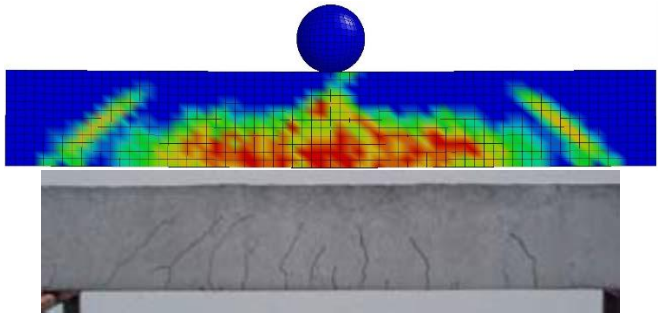

(a) Drop height at 0.3m

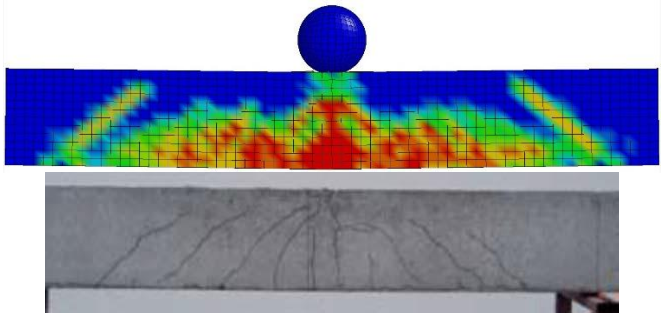

(b) Drop height at 0.6m

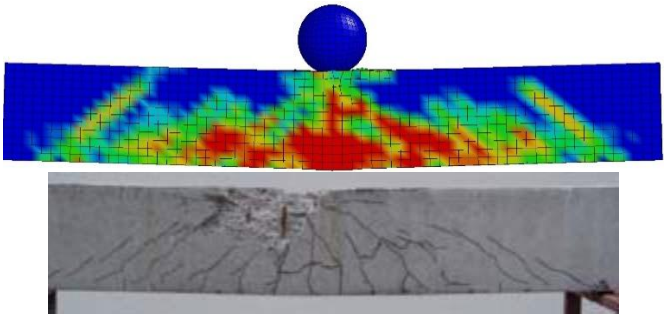

(c) Drop height at 1.2m

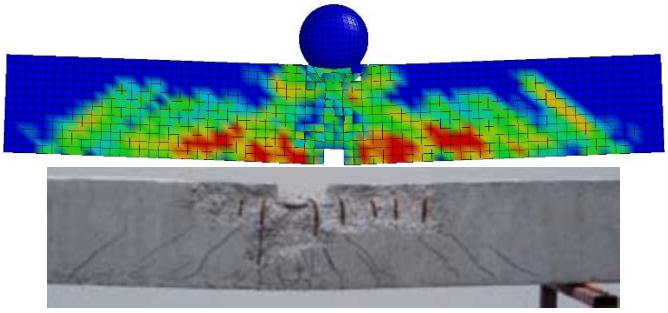

(d) Drop height at 2.4m

Figure 3-17 Plastic strain for specimen S1322

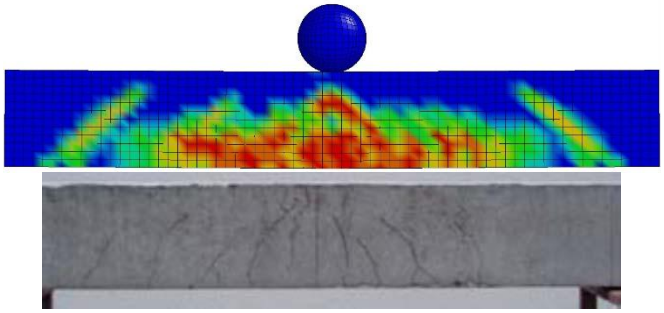

(a) Drop height at 0.3m

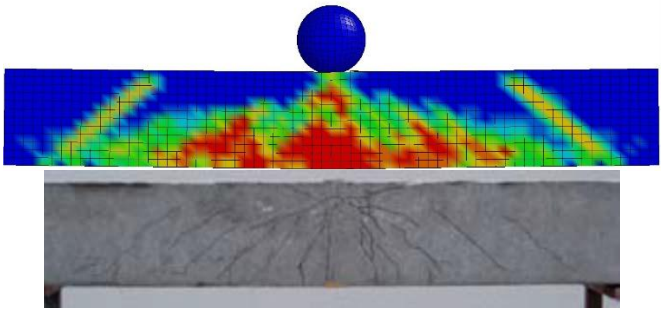

(b) Drop height at 0.6m

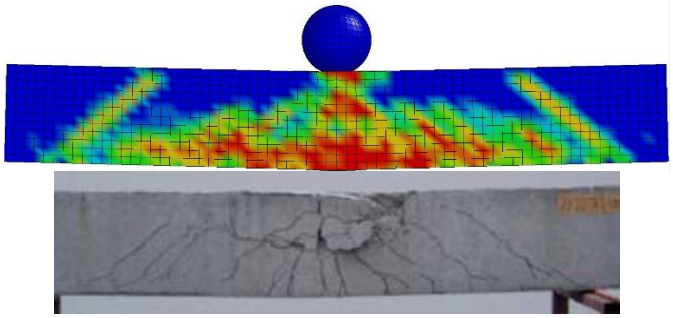

(c) Drop height at 1.2m

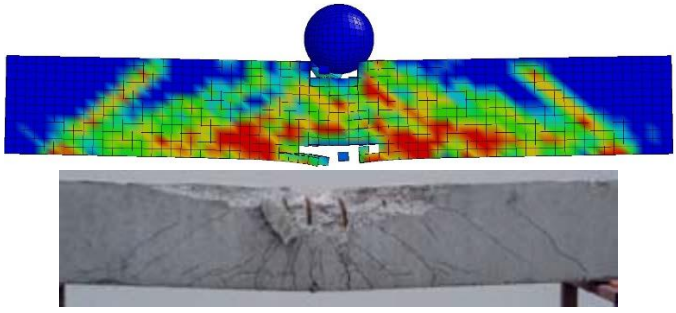

(d) Drop height at 2.4 m

Figure 3-18 Plastic strain for specimen S2222

Chapter 4 Vehicle-to-pier collision

To verify the impact feature able to be realized by finite element analysis between a vehicle and a bridge pier, the finite elemental simulation on the vehicle-to-pier collision is conducted and compared with existing researches.

4.1 Vehicle Models

For the coupling system consisting of a vehicle and a pier, the vehicle is much more intricate than the pier. That how the built model can reflect the characteristics of vehicle with thousands of members is a complicated technique and time-consuming work. National crash analysis center (NCAC), belonging to Federal Highway Administration, and the National Highway Traffic Safety Administration have devoted large effort into developing varieties of vehicle model, based on large quantities of vehicle-to-rigid-wall crash test. These vehicle models are widely used in crash simulation, involving car-to-car, car-to-barrier, car-to-pier collision, etc. Three trucks are selected in this study for vehicle-to-pier collision: the Chevrolet C2500 pickup truck, the F800 Ford single unit truck, and the tractor with 45ft semitrailer, as shown in Figure 4-1. The three types of truck are proposed here to represent the light-weight, medium-weight, and heavy-weight vehicles. For vehicles model, no further changes have been done about the physical properties of members, except for the mass of cargo, and the initial velocity. The number of elements and the total masses (including ballast) of three trucks are listed in Table 4-1. The kinetic energies for three trucks corresponding to different velocities are plotted in Figure 4-2.

Table 4-1 Properties of truck model

Truck type	Number of Elements	Mass (Mg)
C2500	10518	1.976
F800	35193	8.167
Tractor-trailer	373662	36.172

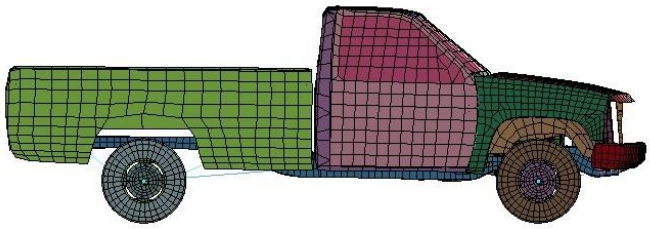

(a) Chevrolet C2500 pickup truck

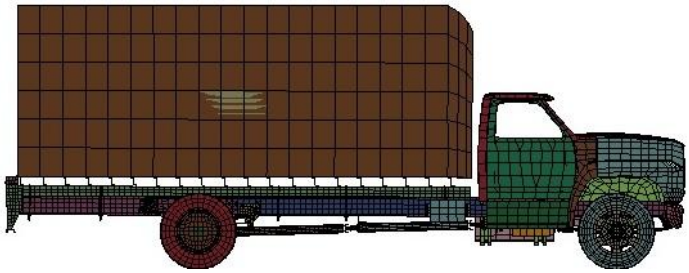

(b) Ford F800 single unit truck

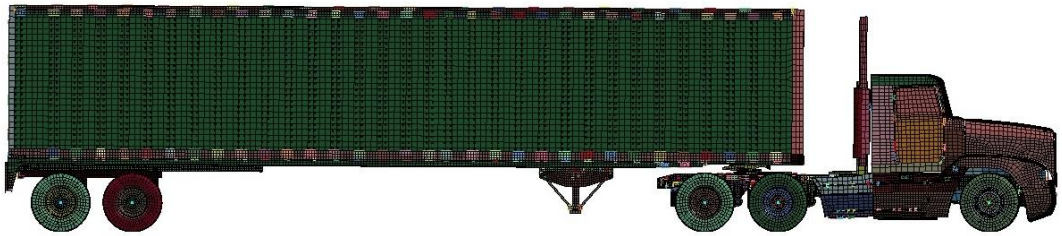

(c) Tractor, day cabin, with 45-ft semitrailer

Figure 4-1 Finite element model of trucks

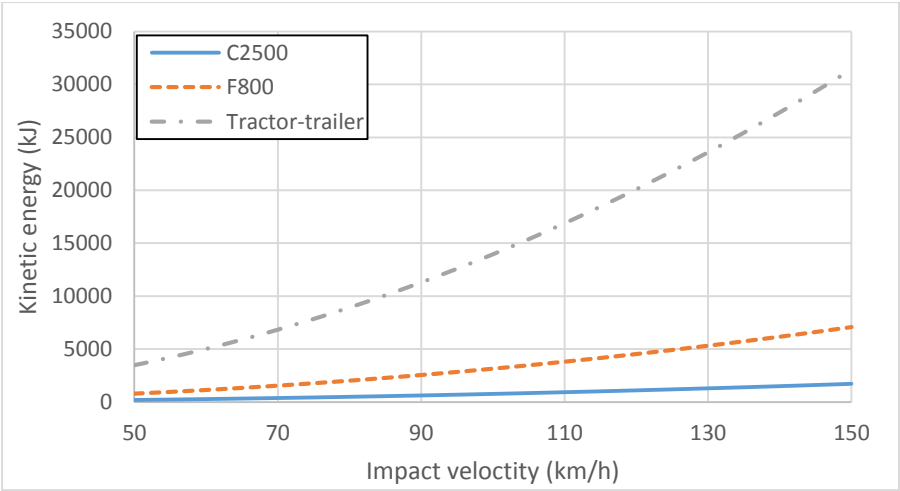

Figure 4-2 Kinetic energy versus impact velocity for the vehicle models

4.2 Vehicle Collision Validation

In order to validate the finite element model for three trucks with vehicle-to-pier collision simulation following existing studies are conducted, and the results are compared with the data from the original analysis or the experiment to verify the accuracy. The C2500 and F800 models are validated following the FDOT report (Project number BC355-6) by El-Tawil and Sherif (2004). Tractor trailer model is validated following the experiment in FHWA report 9-4973-2 by Buth et al. (2011).

4.2.1 Chevrolet C2500 Pickup Truck and Ford F800 Single Unit Truck

4.2.1.1 Modelling of the pier

The pier geometry follows the dimensions of "Pier II'" in the report BC355-6, as shown in Figure 4-3. Pier II is a reinforced concrete pier. It has a circular cross-section of 1075 mm (3' 6") diameter and a height of 9925 mm (29' 95/16"). The pier is modeled with a reinforced concrete pile cap with dimension 3300 mm x 2300 mm x1075 mm (10' x 7' x 3' 6") in diameter and embedded 830 mm (2' 6") into the ground, supported on six 450 mm (18") diameter prestressed concrete piles of 10000 mm length. 14#11 bars (35 mm diameter) and #5 (16 mm) diameter round hoop spaced at 5" (127 mm) are embedded in the pier concrete.

The superstructure of two parallel box girders sitting on the pier is modeled using beam elements. The geometric properties of each box girder are as follows:

$$A = 80133.0\ mm^2\ (124\ in^2)$$

$$I_{zz} = 2.798 \times 10^{10}\ mm^4\ (6.722 \times 10^4\ in^4)$$

$$I_{yy} = 8.340 \times 10^{10}\ mm^4\ (2.004 \times 10^5\ in^4)$$

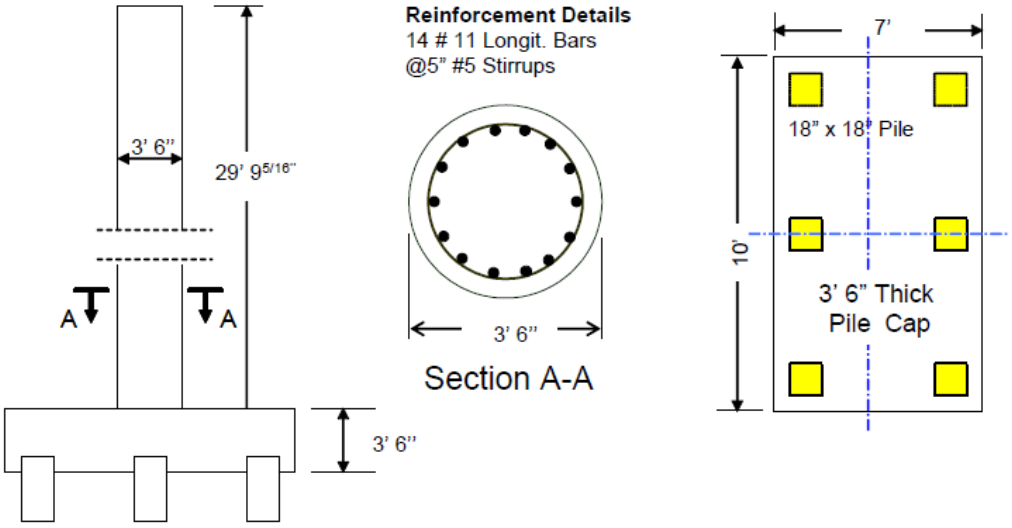

Figure 4-3 Details of the pier

Where z is the horizontal axis and y is the vertical axis. The composite section is transformed into equivalent steel section for the calculation. The girder consists of two spans with length 53,400 mm (175 ft) and 50,000 mm (165 ft), respectively, which are assumed to be pinned at their fat ends. Each span of a girder is modeled by 20 elastic beam elements. The beam is constrained with the node at top of the pier in translational degree of freedom.

The soil-pile interaction is modeled with elastic spring. The stiffness of springs was calculated using the approaches recommended by Greimann and wolde-Tinsae (1998) as shown in Table 4-2. The soil behind the pier is loose sand with the unit weight of 18kN/m^3.

The concrete and steel are all assumed to be elastic material following El-Tawil's study. The strain rate of steel follows the assumption in Chapter 3. The finite element model of the pier is shown in Figure 4-4.

Table 4-2 Parameters for soil springs

Parameter	Case	
	Clay	Sand
Lateral springs		
P_u	9 c_u B	$3\gamma Bk_p x$
k_h	67 c_u	$n_h x$
Vertical springs		
f_{max}(H-piles), klf	The least of $2(d+b_f)c_u$ $2(d+2b_f)c_a$ $2(dc_u+b_f c_a)$	$0.02N[2(d+2b_f)]$
f_{max}(others), klf	The lesser of I_gC_a I_gC_u	$0.04NI_g$
k_v	$10f_{max}/Z_c$	$10f_{max}/z_c$
Point spring		
q_{max} (ksf)	9cu	$8N_{corr}$
k_q	$10q_{max}/Z_c$	$10q_{max}/z_c$

Note: B=pile width; b_f=flange width (ft); c_a=adhesntion–between soil and pile=αc_u; c_u=undrained cohesion of the clay soil=97.0N+114(psf); d=section depth (ft); J=200 for loose sand, 600 for medium sand, 1500 for dense sand; I_g=gross perimeter of the pile (ft); $k_p=\tan^2(45°+\phi/2)$; N=average standard penetration blow; N_{corr}=N if N≤15, or N_{corr} =15+0.5(N-15) if N>15 (N=15 in this study); n_h=constant of subgrade reaction=$J_\gamma/1.35$; x= depth from the soil surface; z_c=relative displacement required to develop f_{max} or q_{max}, and z_c=0.4” for sand, 0.2” for clay; α=shear strength reduction factor; γ=effective unit soil weight; ϕ=angle of internal friction.

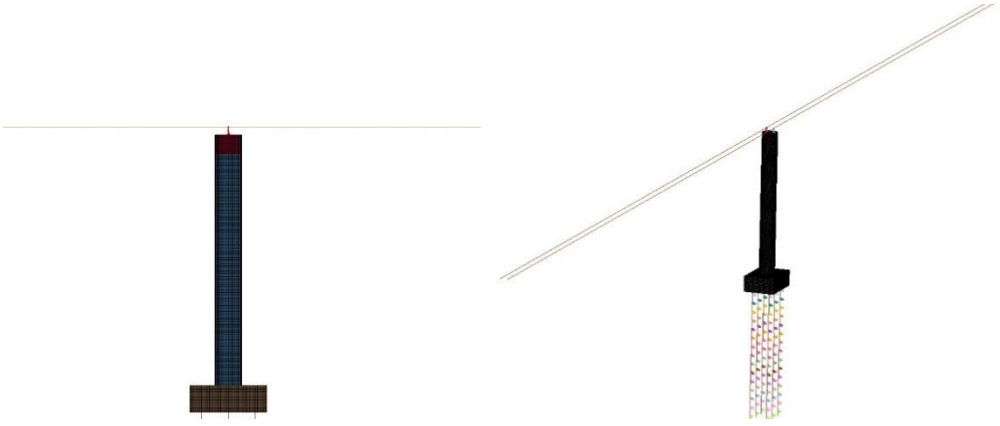

Figure 4-4 Finite element model of the pier

4.2.1.2 Analysis control

Vehicle impact simulations are conducted at four velocities: 55, 90, 110, and 135 km/h. The initial translational velocities are applied to the vehicles in the global x- direction (perpendicular to the plane of the bridge). Gravity is applied to the system as static implicit preload to eliminate the vibration due to gravity.

Automatic surface-to-surface contact is applied to the vehicle-to-pier collision. The master part, the truck, transfers its energy to the slave part, the pier, through contact. The static coefficient is set to 0.5, and the dynamic coefficient is set to 0.3, based on the study of El-Tawil (2005).

100ms is used as the termination time for each simulation which is enough to capture the peak impact force, which is mainly yielded by the contact between the engine and the pier. Hourglass is set to 0.01 based on the study in Chapter 3. The initial time step is set to 10-7 s. A time interval of 0.1ms is used for collection of data of resultant contact forces.

4.2.1.3 Result

1) Chevrolet C2500 pickup truck

The process of impact is shown in Figure 4-5, which depicts the analysis in this study reflects the similar progression of impact when the vehicle striking at the bridge pier. The resultant contact force at different impact velocities are plotted in Figure 4-6. The peak resultant impact forces at impact velocity, 55km/h, 90km/h, 110km/h, and 135 km/h, are 3633.7kN, 7658.9kN, 9778.6kN, and 11593.21kN, respectively. The peak resultant force all happen when the engine striking at the pier.

The comparison of the peak impact forces with the study of El-Tawil et al. (2004), Gomez (2014), Abdelkarim and El Gawady (2017) is made. It shows that the peak impact force is

close to the result obtained in the previous study. The vehicle model simulations are believed to match well with published reference and will be used for further study in the following chapters.

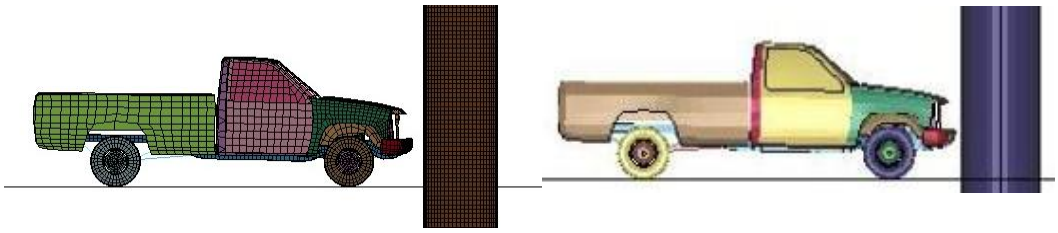

a) Time at 0.000 seconds

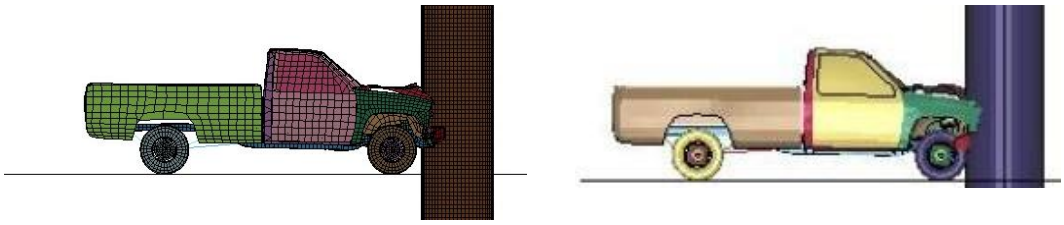

b) Time at 0.021 seconds

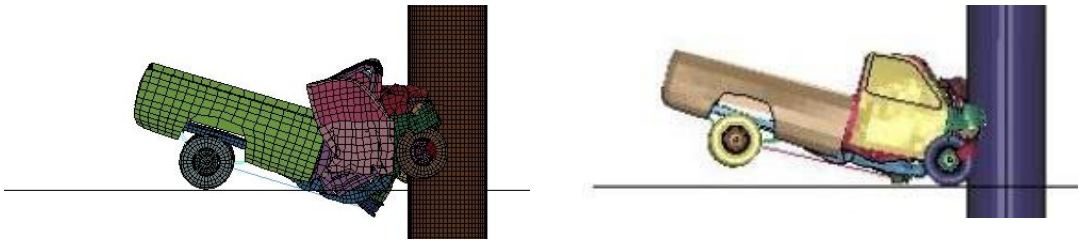

c) Time at 0.111 seconds

Figure 4-5 Progression of impact of C2500 pickup truck at 110 km/h comparing simulation results (left) with El-Tawil's (2004) results (right)

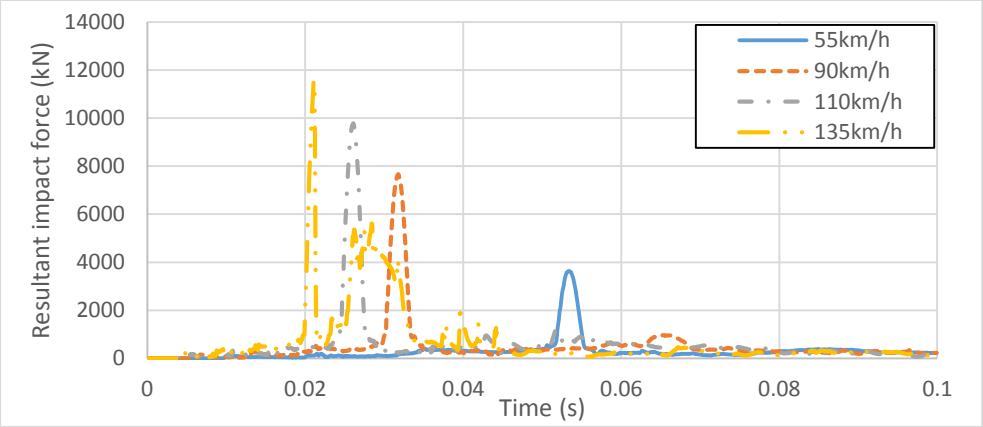

Figure 4-6 Resultant impact force for the C2500 pickup truck at various impact velocities

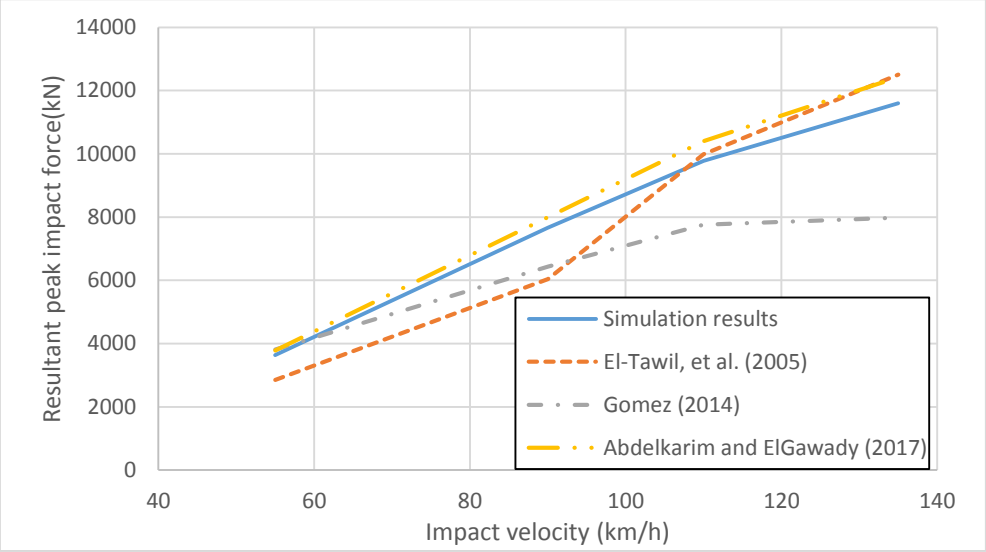

Figure 4-7 Comparison between the simulation results and the results published by El-Tawil et al. (2005), Gomez (2014) and Adelkarim (2017)

2) Ford F800 single unit truck

The process of impact is shown in Figure 4-8, which depicts the analysis in this study reflects the similar progression of impact when the vehicle striking at the bridge pier. The resultant contact forces at different impact velocities are plotted in Figure 4-9. The peak resultant impact forces at impact velocities, 55km/h, 90km/h, 110km/h, and 135 km/h, are

1858.8 kN, 8414.2kN, 11981.2kN, and 16958.3kN, respectively. The peak resultant forces all happened when the engine striking at the pier.

The comparison of the peak impact forces with the study of El-Tawil et al. (2004), Mohammed (2011) and Gomez (2014) was made. It shows that the peak impact force is close to the result obtained in the previous study. The vehicle model simulations are believed to match well with published reference and will be used for further study in following chapters.

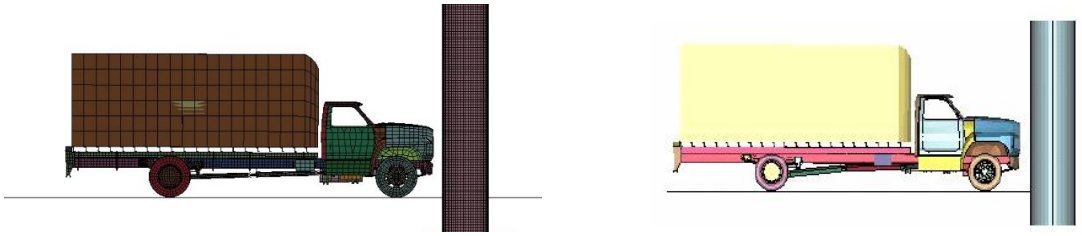

a) Time at 0.000 seconds

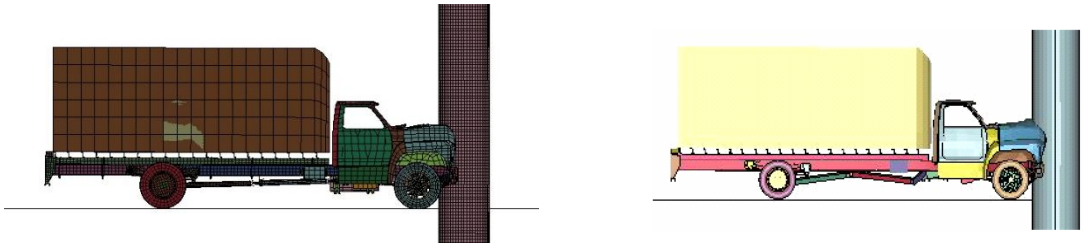

b) Time at 0.021 seconds

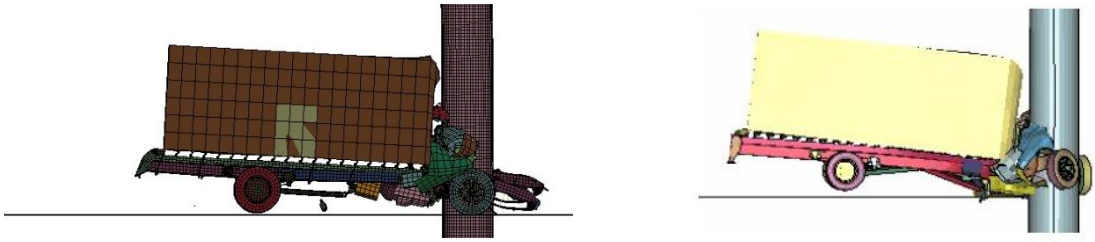

c) Time at 0.111 seconds

Figure 4-8 Progression of impact of F800 single unit truck at 110 km/h comparing simulation results (left) with El-Tawil's (2004) results (right)

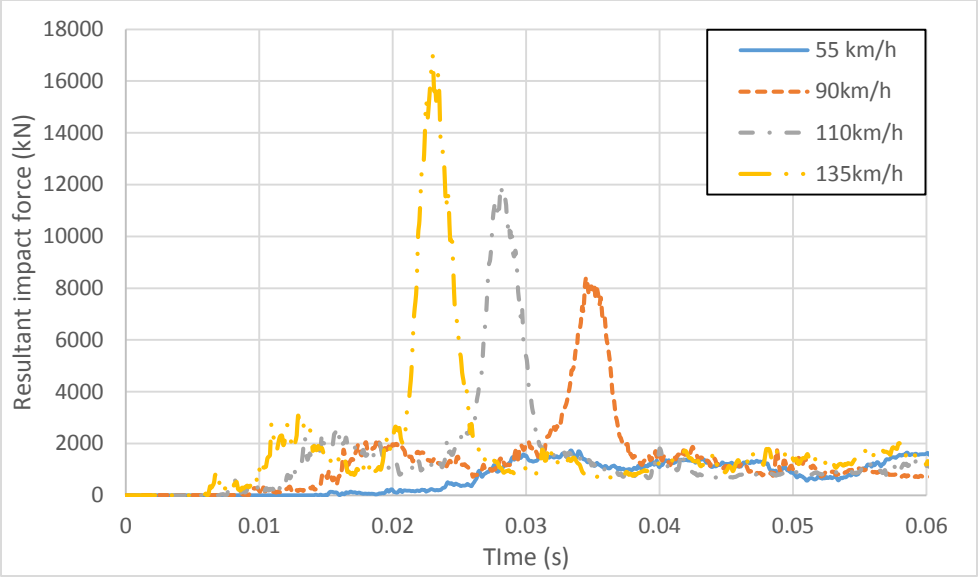

Figure 4-9 Resultant impact force for the F800 single unit truck at various impact velocities

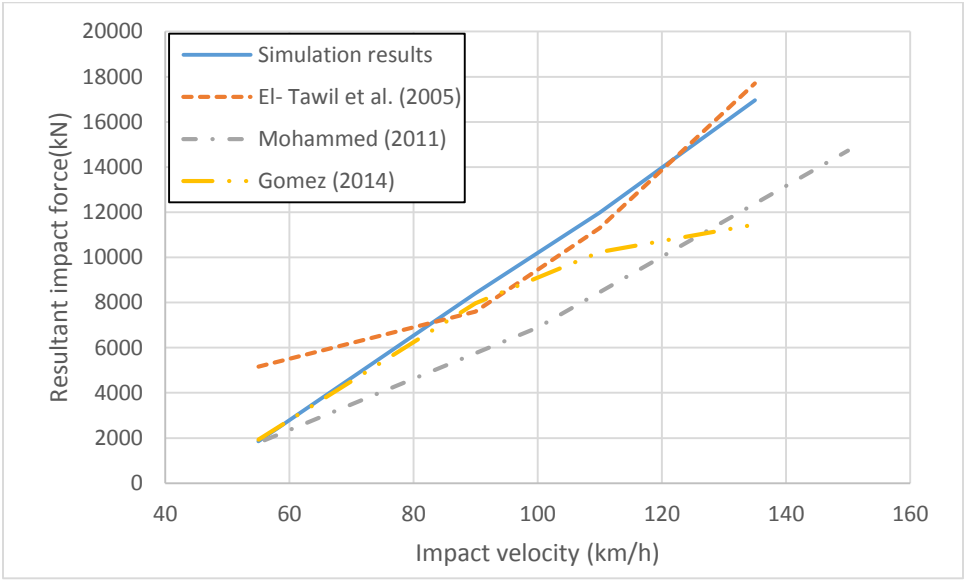

Figure 4-10 Comparison between the simulation results and the results published by El- Tawil et al. (2005), Mohammed (2011), Gomez (2014)

4.2.2 Tractor-semitrailer Truck

4.2.2.1 Finite element modeling

The tractor-semitrailer truck is validated by comparing the result of the FHWA report 9-4973-2 by Buth et al. (2011) Texas Department of Transportation, which involves

a full-scale tractor-trailer truck striking a specially designed pier. The photos for this experiment are shown in Figure 4-11. The experimental pier and the suggested simplified model are shown in Figure 4-12

Based on the suggested model for analysis in the report, a finite element model including the tractor-trailer truck, and the pier, is built in the LS-DYNA, as shown in Figure 4-13. The pier is concrete-filled circular steel pier has a height of 14ft, with diameter 36in. The thickness of the steel tube is 1in. The filled concrete has strength 5000psi (34.5MPa). The spring stiffness at the height 1ft, and at the height 13ft, are 165kip/in (28.98kN/mm) and 1137kip/in (199.1kN/mm). The steel material is modeled with bilinear model with tangent stiffness 1.5GPa in the hardening stage. The concrete is simulated by material model 159, which is used in Chapter 3.

Figure 4-11 Full-scale impact test of tractor-trailer truck colliding a pier (Buth, et al., 2011)

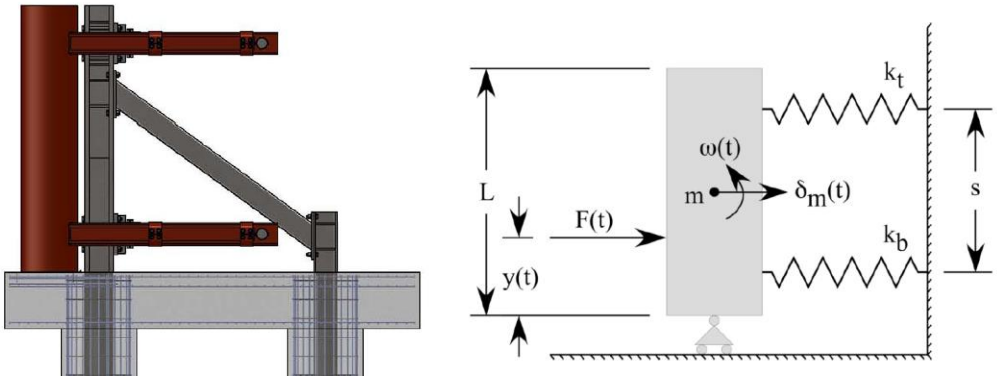

Figure 4-12 The experimental pier and the suggested simplified model for analysis.

Figure 4-13 the finite element model for the crash scenario

4.2.2.2 Results

1) Resultant impact force

The report suggested 50-ms average value of the dynamic force to get the equivalent static impact force. It shows that the 50-ms average value of resultant impact force matches well with the suggested 600kip impact force in this report, which is also adopted by the AASHTO LRFD bridge design specification, as shown in Figure 4-14.

The behavior of the impact force over the duration of the impact is comparable to the impact force time-history recorded during the experiment. The hourglass energy was observed to account for less than 10% of the total energy in the system; verifying the proper use of hourglass energy control. Overall the numerical analysis matches well with the experimental results.

2) Failure model

Bridge piers subjected to vehicle impact forces are typically found to have large shear and bending forces. Shear failure is the major mode of failure typically observed in the field where the shear force generated by the impact exceeds the shear capacity of the pier (Buth et al. 2010). This failure was also verified by the impact study of the C2500 vehicle striking into the pier. The plastic strain formed a 45-degree angle zone at the height

of impact. The failure modes of the column in the finite element model appear to be consistent with the observed failure modes of impacted columns.

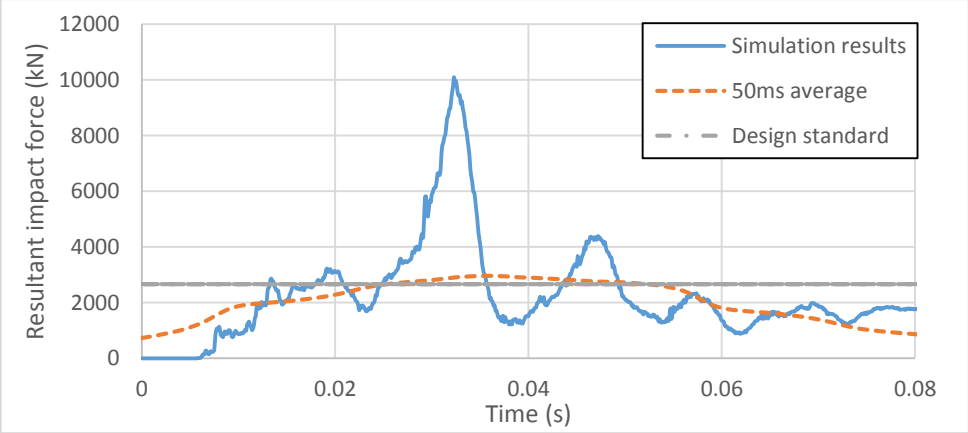

Figure 4-14 Filtered data for tractor-trailer impact

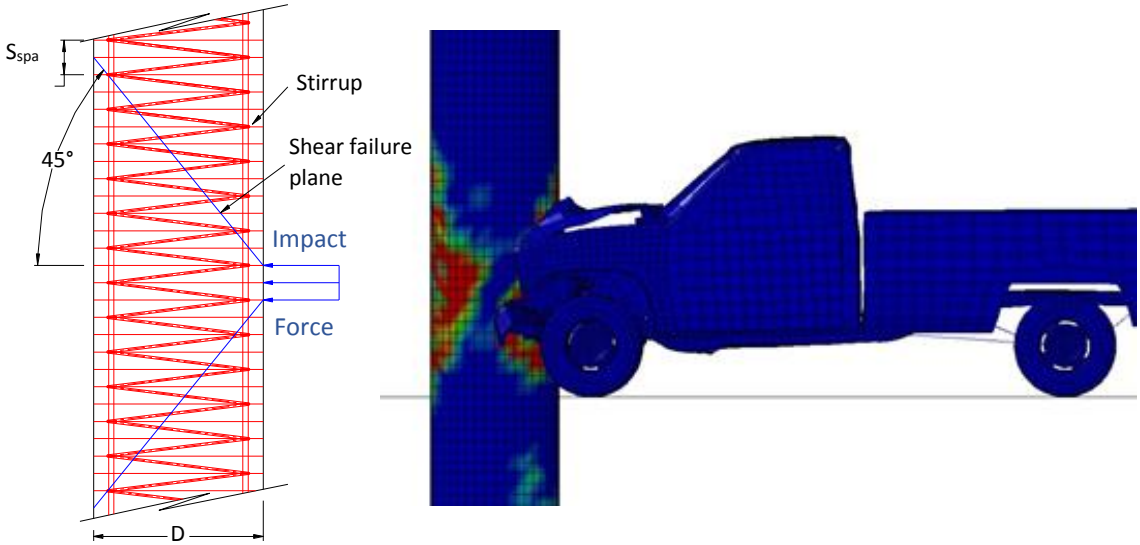

Figure 4-15 observed failure mechanism form impact force on bridge pier

4.3 Summary

This chapter ran simulations based on finite element model and experimental data in previous studies. The impact load maintains good consistency with the finite element analyses results of previous numerical studies by El-Tawil et al. (2005), Mohammed (2011), Buth (2011), Gomez (2014) and Adelkarim (2017). Compared with previous research data, the dynamic response matches well mutually with a same set of parameters in a similar impact event. Besides, the filtered

data, which takes the average value of 50ms, keeps in agreement with the experimental result and the design code. The failure modes of the finite element analysis are consistent with the failure mode observed in the field study. Therefore, the vehicle model along with the material model used in Chapter 3 can be used for further studying the mechanism of the vehicle-to-pier impact.

Chapter 5 Parametric study of impact load

5.1 Overview

In order to have a comprehensive understanding about which parameter the impact force is sensitive to, parametric studies are to be conducted to investigate the parametric sensitivity. The vehicle and pier model will follow the material model and analysis control setting used in Chapter 3 and Chapter 4. The pier model to be studied is shown in Figure 5-1. The parameters listed in Table 5-1 will be involved in this part.

Among these parameters, mass of the vehicle is changed by the mass of cargo. The impact height is controlled by the distance from the ground to the foot of the pier, which means that a higher impact location with the deeper pier foot. The superstructure is to be simplified into a lateral spring, and a rotational spring to represent the restraint to the pier. The mass of superstructure is lumped at top of the pier. And the vertical force is to simulate the reaction force supporting the superstructure. The pier and footing model are based on the Maryland structural detail manual 02-04, which allows the minimum pier diameter as 0.762m (2'-6"). The column diameter ranges from 0.762m (2'-6") to 1.0668m (3'-6"). Table 5-2 shows the detail of the pier. The detail of the foundation is shown in Figure 5-2. The soil spring is spaced at every 457.2mm (1'-6"). Values of soil spring stiffness are calculated based on Table 4-2 with the undrained cohesion of the clay soil 24.61kPa (514psf), 49.17kPa (1027psf), and 98.35kPa (2054psf) respectively, which is shown in table 5-3. The plastic behaviors of piles are not taken into consideration, which ignores

The aims of the parametric studies are to learn which parameter will contribute more to the impact force, and what kind of failure model will be obtained with specific parameters. The peak dynamic impact force will be compared for each group of parameters.

At the same time, the equivalent static force based on the average value of 50ms will also be compared.

Load cases with different sets of parameters for light-weight truck C2500, medium-weight truck f800, and heavy-weight tractor-trailer truck are respectively listed in Table 5-4, Table 5-5 and Table 5-6.

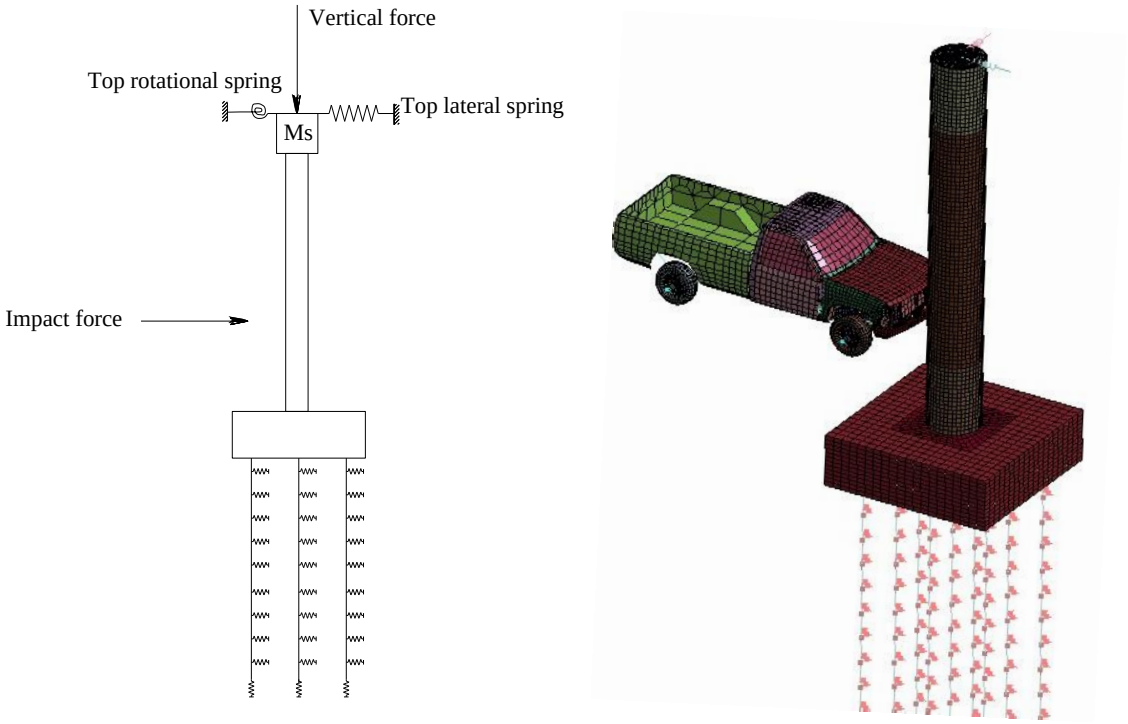

Figure 5-1 the Finite element model to be studied

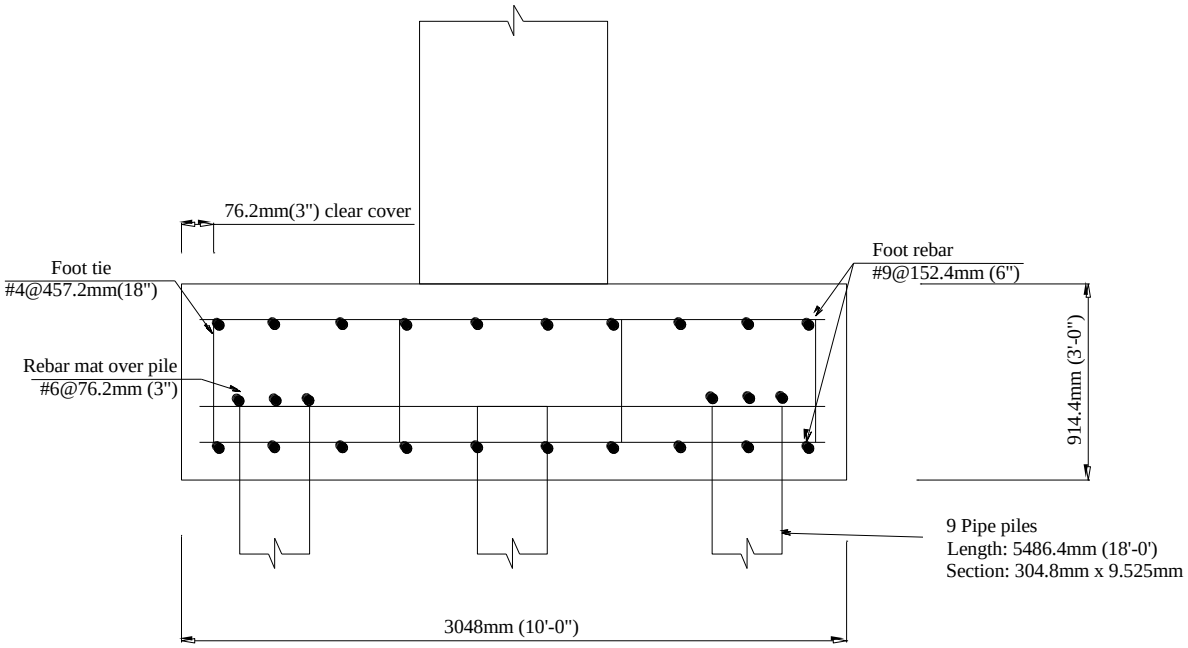

Figure 5-2 Square pile foundation details

Table 5-1 Parameters to be included in the studies

Part	Parameters	Symbol
Pier	Length of the pier	L
	Strength of the longitudinal bar	Fy_s
	Spacing of the hoop	S
	Strength of the concrete	Fy_c
	Diameter of the pier	D
Superstructure	Mass of the superstructure	M_s
	Stiffness of the top lateral spring	K_h
	Stiffness of the top rotational spring	K_r
	Axial Force	P
Foundation	Undrained cohesion of the clay soil	C_u
Vehicle	Impact velocity	V
	Mass of the cargo	M_c
	Height from the ground to the foot	L_I

Table 5-2 Design criteria for typical reinforced concrete pier

Pier Diameter	Longitudinal Rebar	Hoop	Rebar Number
0.762m (2’-6”)	#10	#4	16
0.9144m (3’-0”)			20
1.0668m (3’-6”)			24

Table 5-3 Soil spring properties

Cu	Lateral spring N/mm	Vertical spring N/mm	Point spring N/mm
24.61kPa (514psf)	0.744×10^3	1.659×10^4	2.523×10^4
49.17kPa (1027psf)	1.487×10^3	3.319×10^4	5.050×10^4
98.35kPa (2054psf)	2.974×10^3	6.637×10^4	1.009×10^5

5.2 C2500 Pickup Truck

Table 5-4 Load cases for C2500 pickup truck

Case	V km/h	C_u kPa	Fy_c Mpa	D mm	L mm	Fy_s Mpa	L_I mm	K_r N mm/rad	K_h N/mm	M_c Ton	M_s Ton	P Mpa	S mm
C1	100	98.35	27.58	914.4	5486.4	413.7	1219.2	0	0	0	0	5	304.8
C2	60	-	-	-	-	-	-	-	-	-	-	-	-
C3	80	-	-	-	-	-	-	-	-	-	-	-	-
C4	120	-	-	-	-	-	-	-	-	-	-	-	-
C5	140	-	-	-	-	-	-	-	-	-	-	-	-
C6	-	24.61	-	-	-	-	-	-	-	-	-	-	-
C7	-	49.17	-	-	-	-	-	-	-	-	-	-	-
C8	-	-	41.37	-	-	-	-	-	-	-	-	-	-
C9	-	-	55.16	-	-	-	-	-	-	-	-	-	-
C10	-	-	-	762	-	-	-	-	-	-	-	-	-
C11	-	-	-	1066.8	-	-	-	-	-	-	-	-	-
C12	-	-	-	-	6705.6	-	-	-	-	-	-	-	-
C13	-	-	-	-	7924.8	-	-	-	-	-	-	-	-
C14	-	-	-	-	9144	-	-	-	-	-	-	-	-
C15	-	-	-	-	-	275.8	-	-	-	-	-	-	-
C16	-	-	-	-	-	551.6	-	-	-	-	-	-	-

C17	-	-	-	-	-	-	304.8	-	-	-	-	-	-
C18	-	-	-	-	-	-	2133.6	-	-	-	-	-	-
C19	-	-	-	-	-	-	-	2×10^4	-	-	-	-	-
C20	-	-	-	-	-	-	-	2×10^8	-	-	-	-	-
C21	-	-	-	-	-	-	-	2×10^{12}	-	-	-	-	-
C22	-	-	-	-	-	-	-	-	1×10^3	-	-	-	-
C23	-	-	-	-	-	-	-	-	1×10^5	-	-	-	-
C24	-	-	-	-	-	-	-	-	-	0.43	-	-	-
C25	-	-	-	-	-	-	-	-	-	0.86	-	-	-
C26	-	-	-	-	-	-	-	-	-	1.29	-	-	-
C27	-	-	-	-	-	-	-	-	-	-	335	-	-
C28	-	-	-	-	-	-	-	-	-	-	670	-	-
C29	-	-	-	-	-	-	-	-	-	-	-	0	-
C30	-	-	-	-	-	-	-	-	-	-	-	10	-
C31	-	-	-	-	-	-	-	-	-	-	-	15	-
C32	-	-	-	-	-	-	-	-	-	-	-	-	76.2
C33	-	-	-	-	-	-	-	-	-	-	-	-	152.4
C34	-	-	-	-	-	-	-	-	-	-	-	-	228.6

Note: "-" means that the value in this blank is the same as the value of base case C1

5.2.1 Impact Load

As shown Figure 5-3 and Figure 5-4, for the impact force with respect to the vehicle speeds at 60km/h (37.3Mph), 80km/h (49.7Mph), 100km/h (62.1Mph), 120km/h (74.6 Mph), 140km/h (87.0 Mph), the higher vehicle speeds will yield much higher dynamic and equivalent static impact forces. Compared to the AASHTO design value of 2669kN (600kips) equivalent static force, the finite elemental result shows much smaller result. It

means a much conservative estimation of the impact force based on the latest code for light weight vehicle, like pickup truck, sedan and SUV, etc.

As shown in Figure 5-7 and Figure 5-8, peak dynamic force drops obviously, as the concrete strength of the pier increases. However, the equivalent static impact force shows insensitivity with the variation of the concrete strength.

For the variation of diameter, larger pier diameter will yield higher peak dynamic impact load as shown in Figure 5-9 and Figure 5-10. The equivalent static impact force shows insensitivity to the variation of pier diameter.

With higher impact location from the top of the pier foot, the peak dynamic value of the impact force obtains smaller results. The equivalent static impact force is not sensitive to this change, as shown in Figure 5-15 and Figure 5-16.

There is an obvious increase for the dynamic impact load when the axial force at top of the pier increases. The equivalent static force also is not sensitive to the change of the axial force, which is depicted in Figure 5-25 and Figure 5-26.

According to Figures 5-5, 5-6, 5-11, 5-12, 5-13, 5-14, 5-17, 5-18, 5-19, 5-20, 5-21, 5-22, 5-23, 5-24, 5-27, 5-28, both of the peak dynamic force and equivalent static force of the impact load show insensitivity to the following parameters: the stiffness of the soil, the length of the pier, the yield strength of the steel reinforcement, the impact height of the pier, the stiffness of spring at top of the pier, lumped mass at top of the pier, the loaded cargo mass, and the spacing of the hoop.

It refers that the dynamic characteristics, such as the modal shape and the frequency of the pier, has little influence on the impact load. The material of the structure not directly subjected to the impact, such as the steel, has little effect on the value of the impact load.

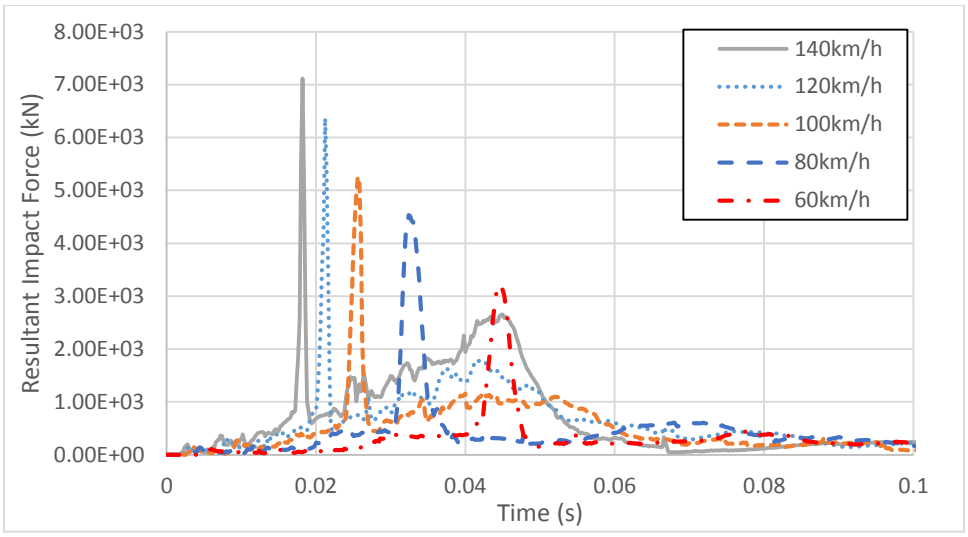

Figure 5-3 Time histories of impact forces with different vehicle speed

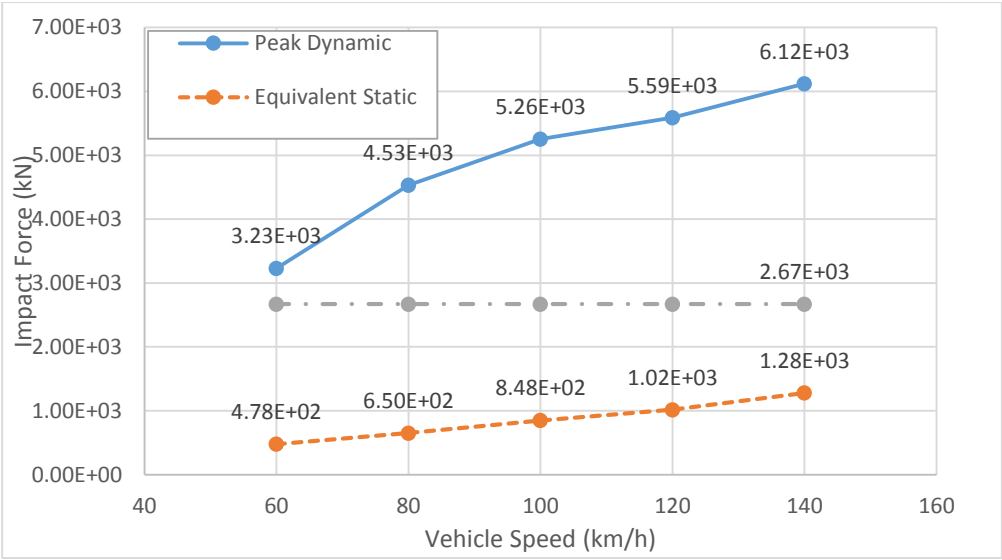

Figure 5-4 Peak dynamic forces and equivalent forces with different vehicle speed

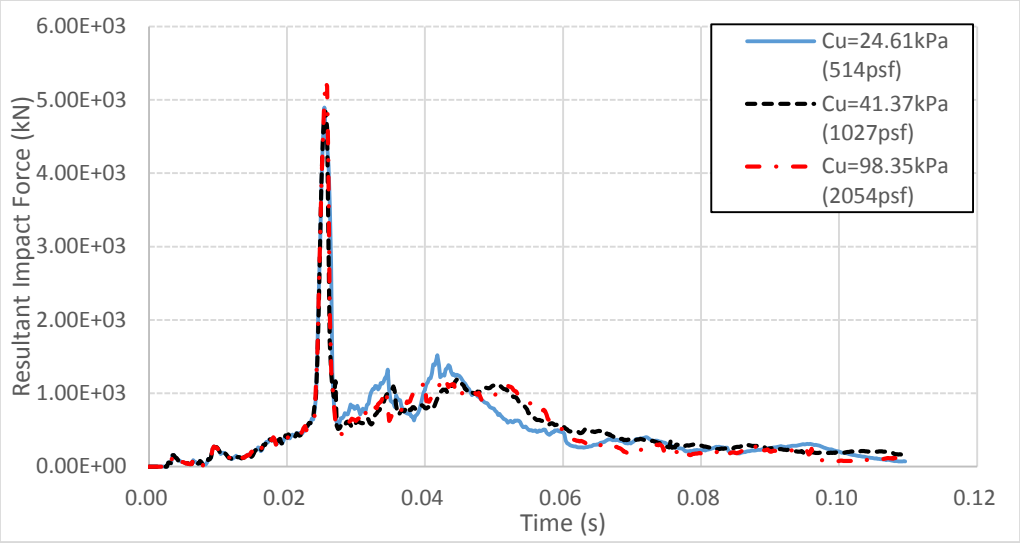

Figure 5-5 Time histories of impact forces with different soil stiffness

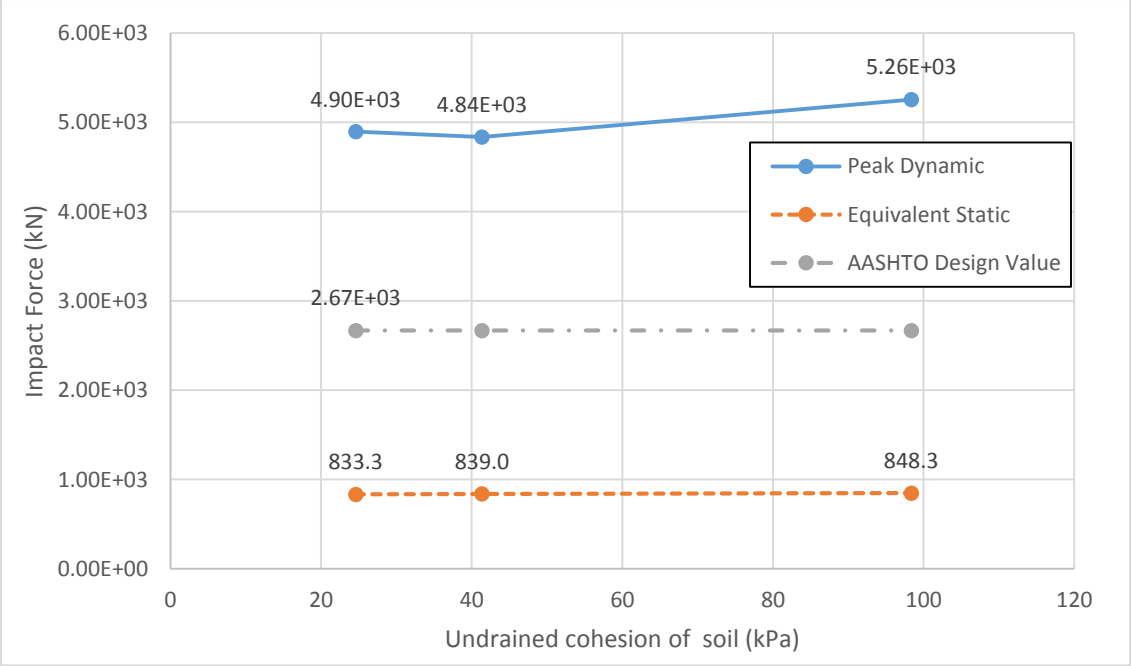

Figure 5-6 Peak dynamic forces and equivalent forces with different soil stiffness

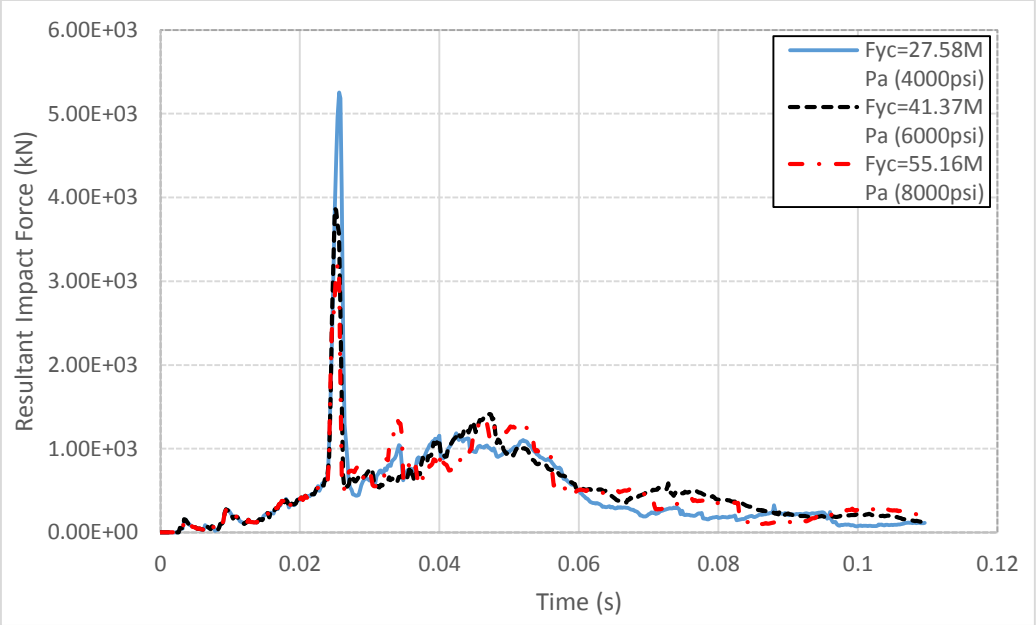

Figure 5-7 Time histories of impact forces with different concrete strength

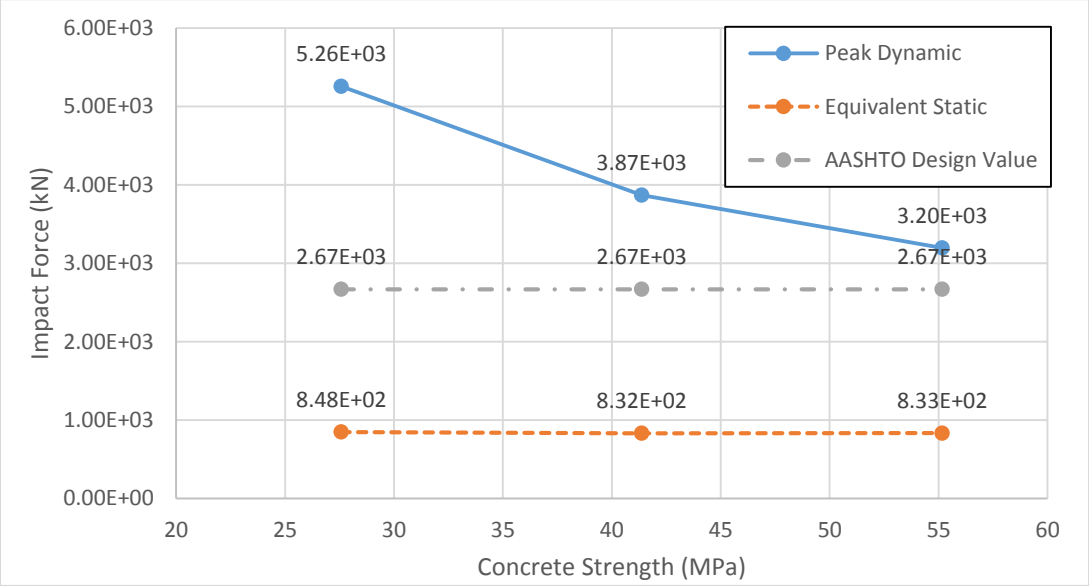

Figure 5-8 Peak dynamic forces and equivalent forces with different concrete strength

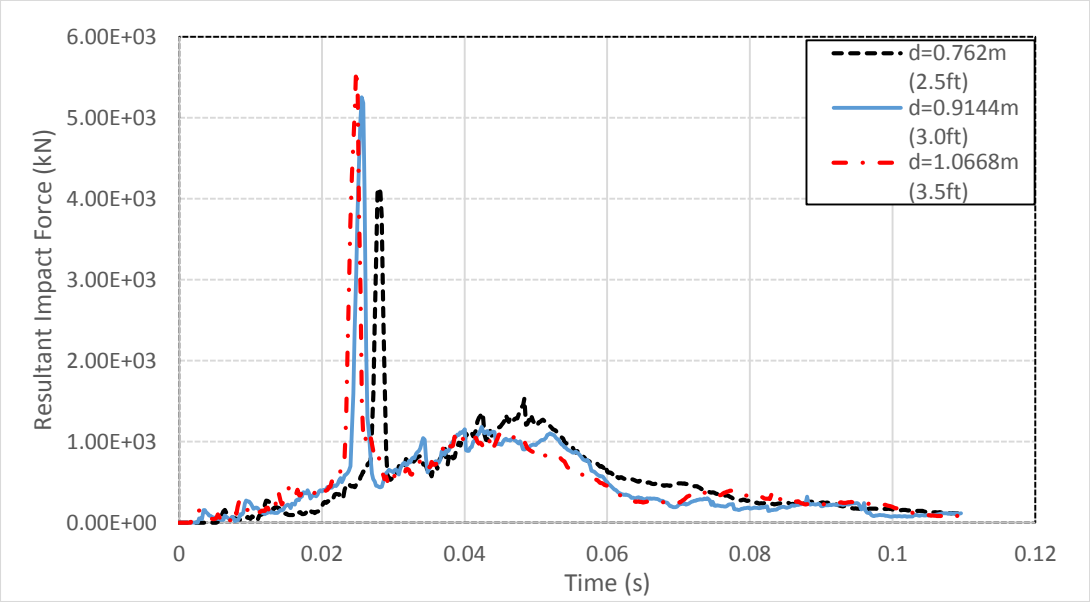

Figure 5-9 Time histories of impact forces with different pier diameter

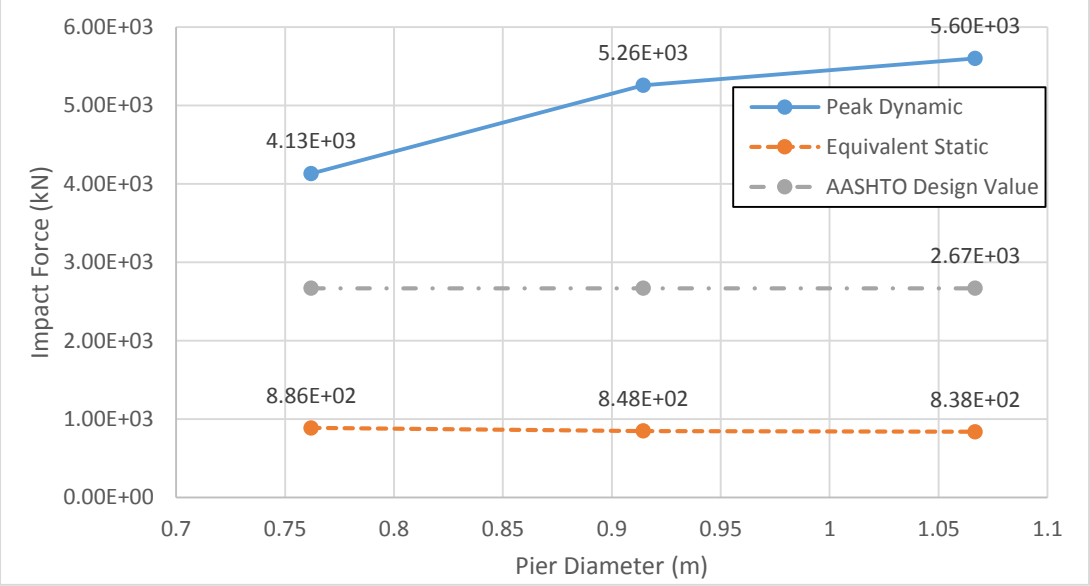

Figure 5-10 Peak dynamic forces and equivalent forces with different pier diameter

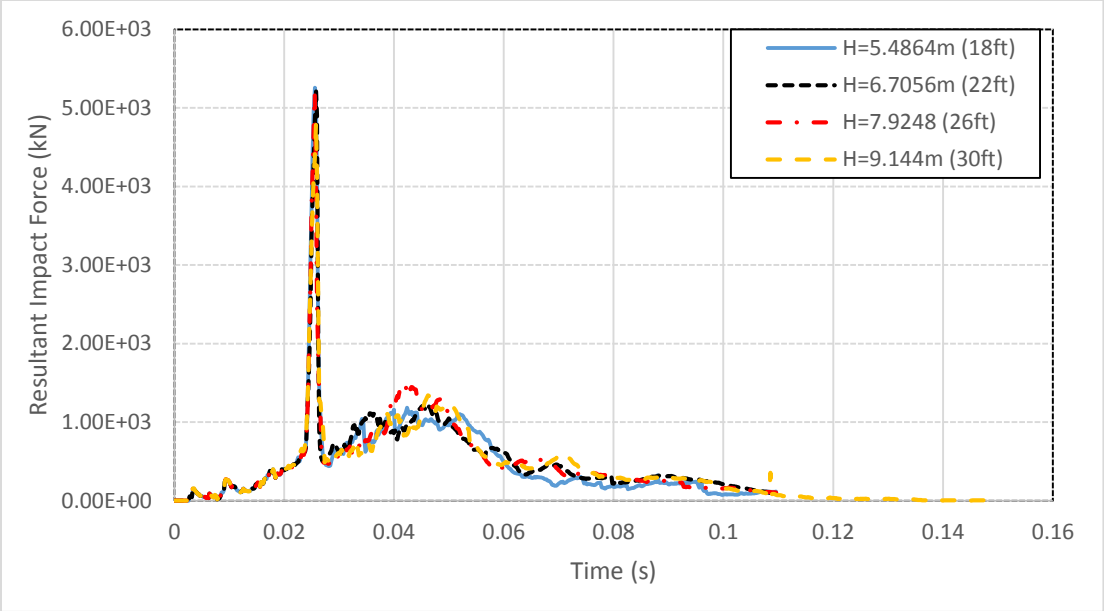

Figure 5-11 Time histories of impact forces with different pier length

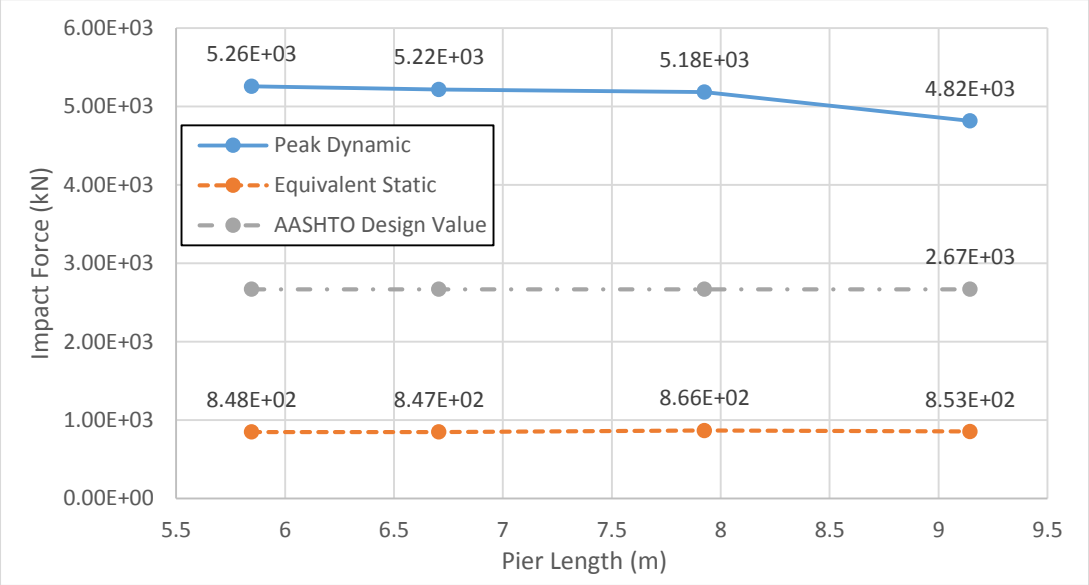

Figure 5-12 Peak dynamic forces and equivalent forces with different pier length

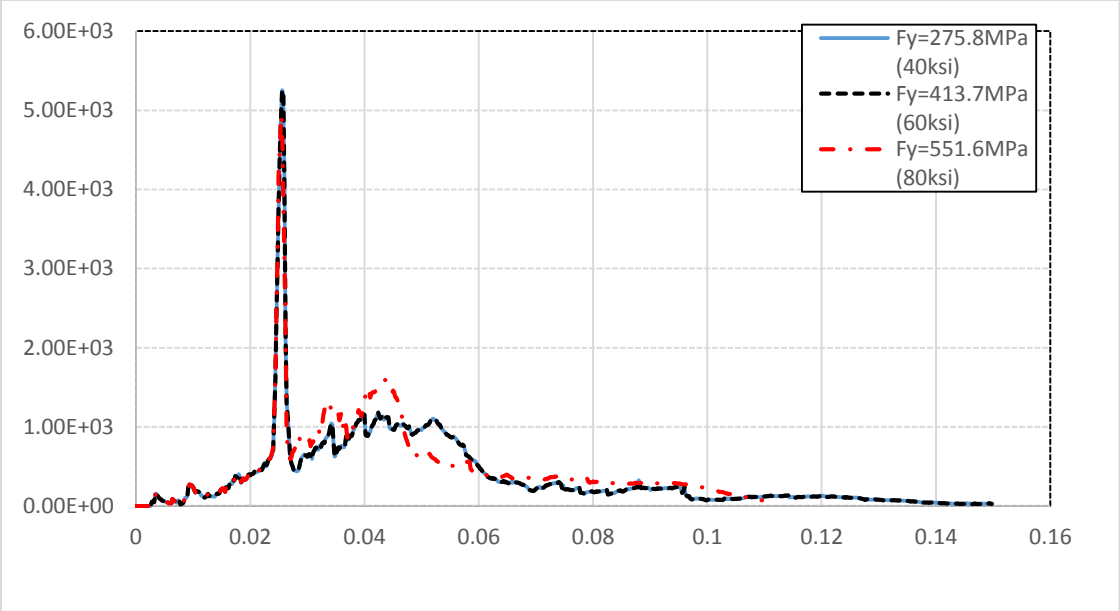

Figure 5-13 Time histories of impact forces with different steel rebar strength

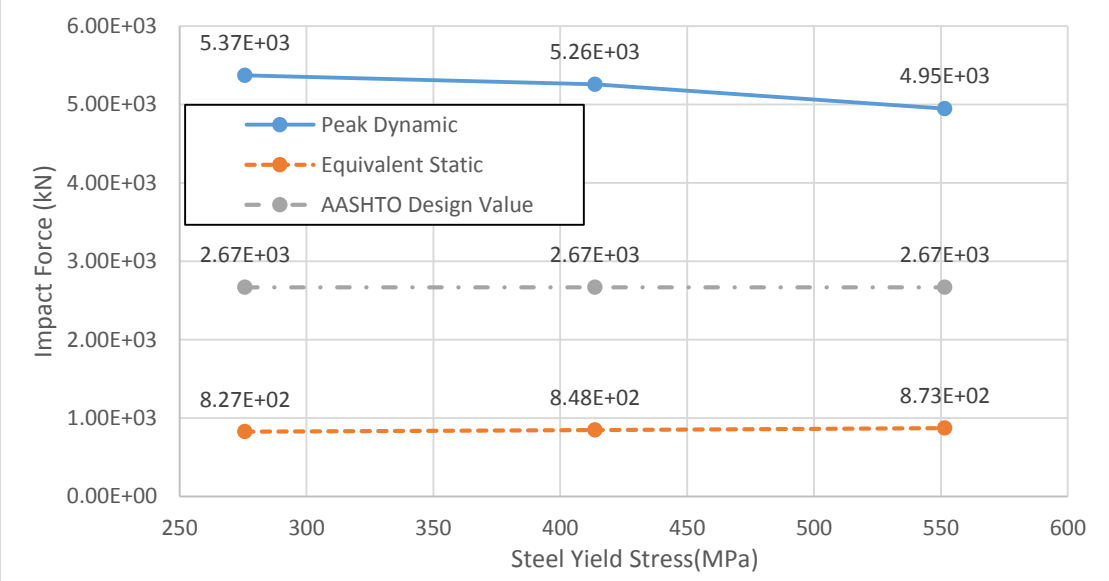

Figure 5-14 Peak dynamic forces and equivalent forces with different steel rebar strength

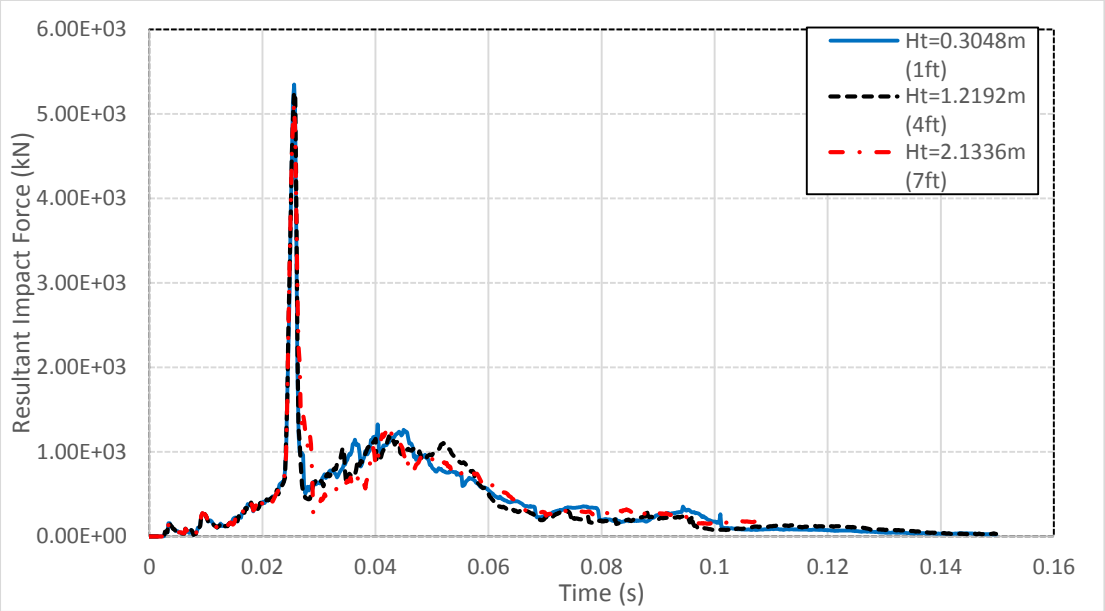

Figure 5-15 Time histories of impact forces with different impact height

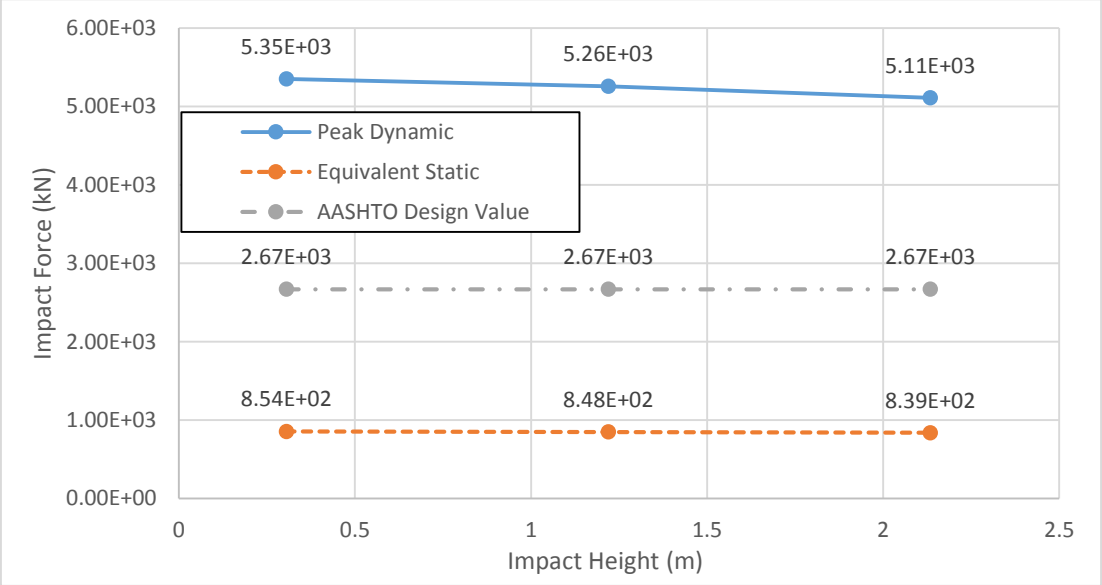

Figure 5-16 Peak dynamic forces and equivalent forces with different impact height

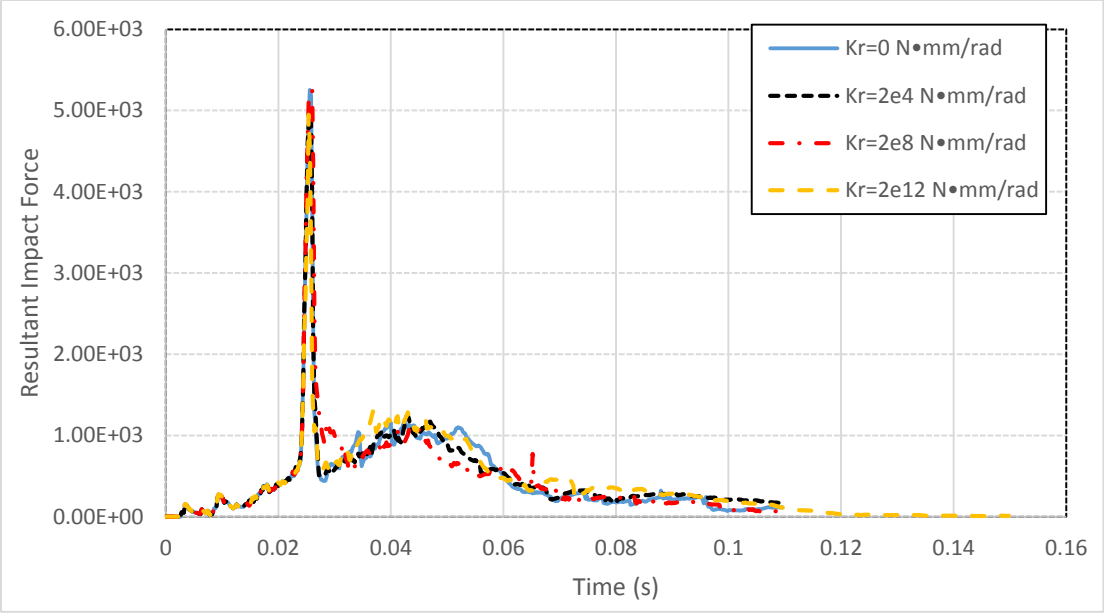

Figure 5-17 Time histories of impact forces with different rotational spring stiffness

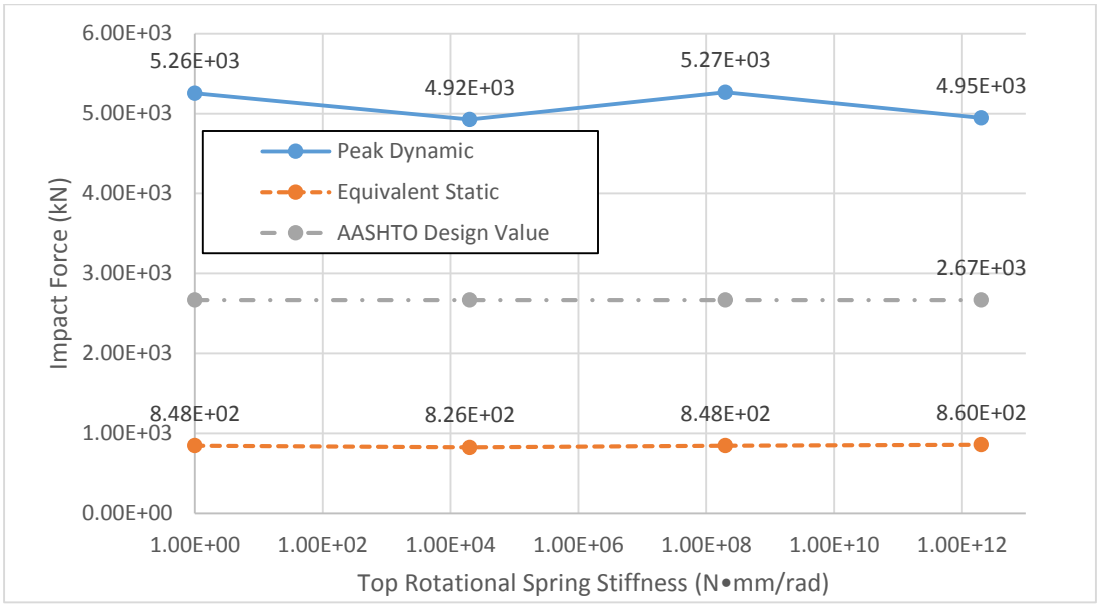

Figure 5-18 Peak dynamic forces and equivalent forces with different rotational spring stiffness

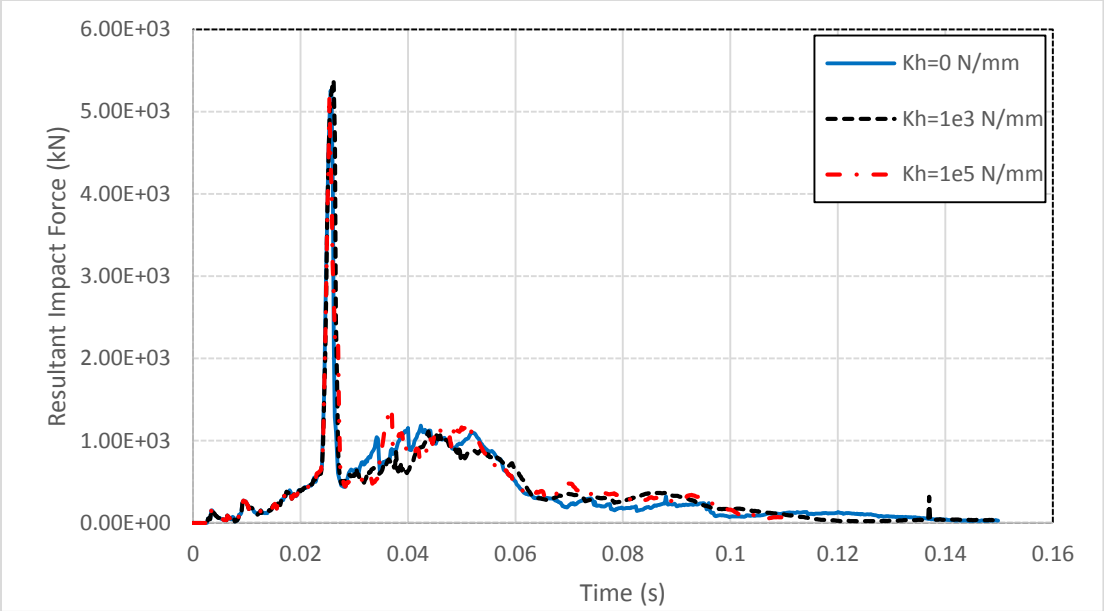

Figure 5-19 Time histories of impact forces with different translational spring stiffness

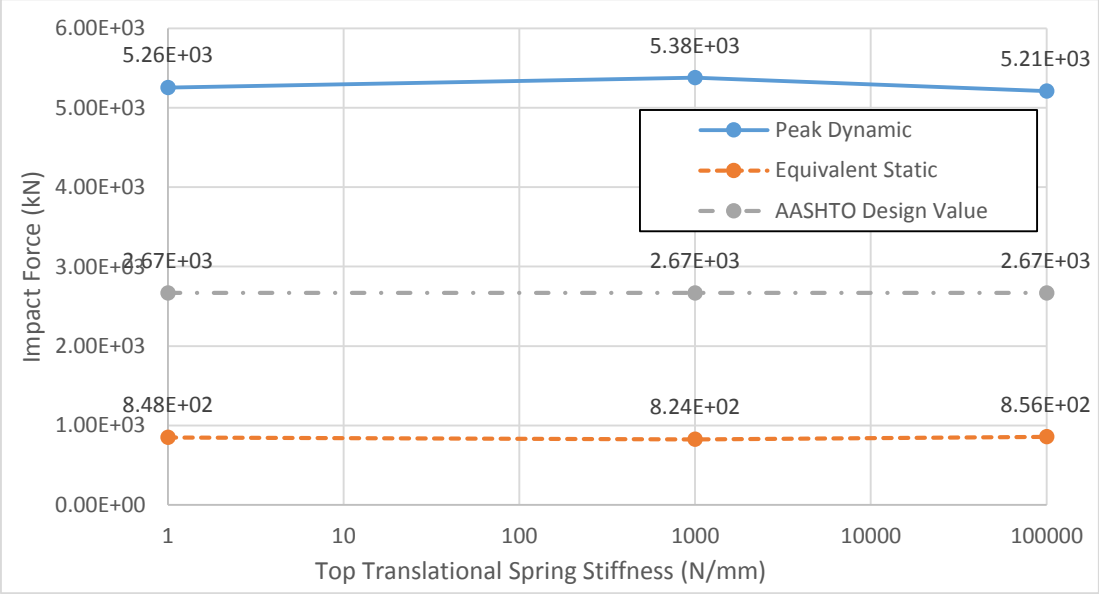

Figure 5-20 Peak dynamic forces and equivalent forces with different translational spring stiffness

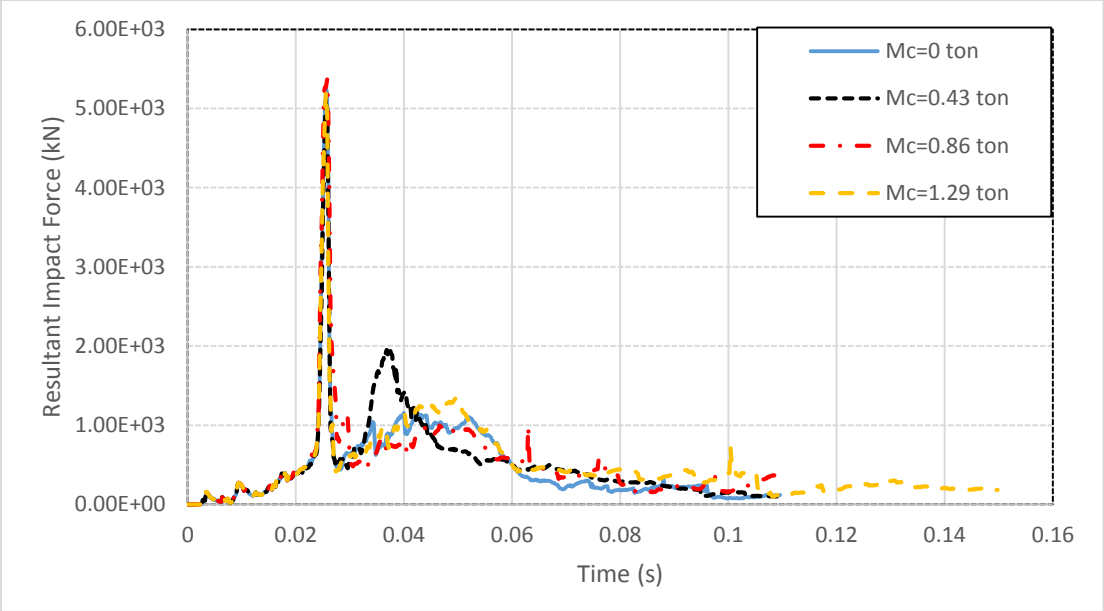

Figure 5-21 Time histories of impact forces with different cargo mass

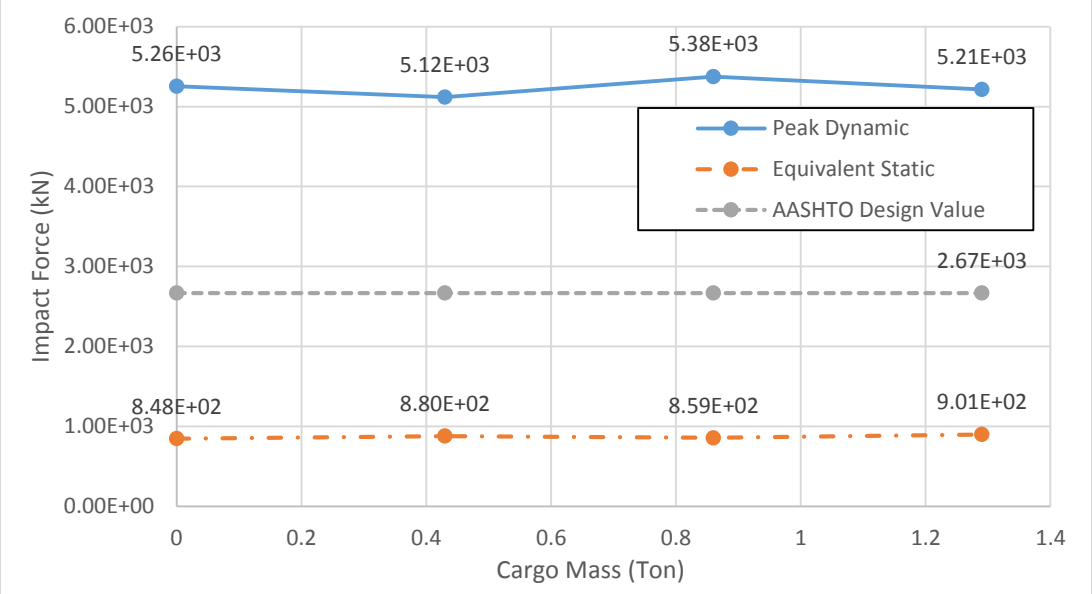

Figure 5-22 Peak dynamic forces and equivalent forces with different cargo mass

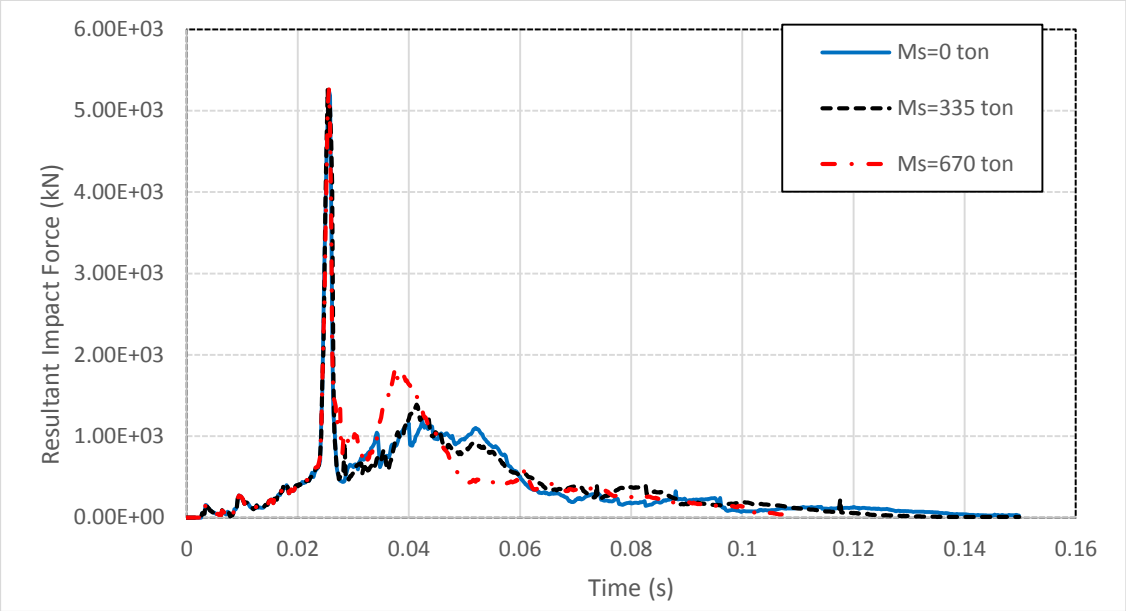

Figure 5-23 Time histories of impact forces with different top mass

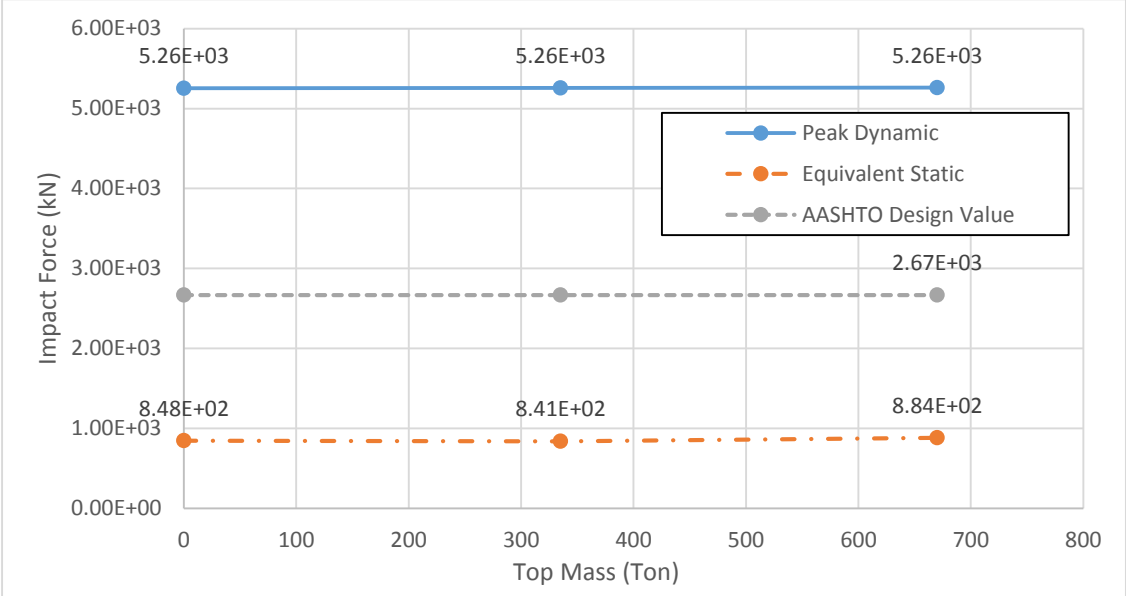

Figure 5-24 Peak dynamic forces and equivalent forces with different top mass

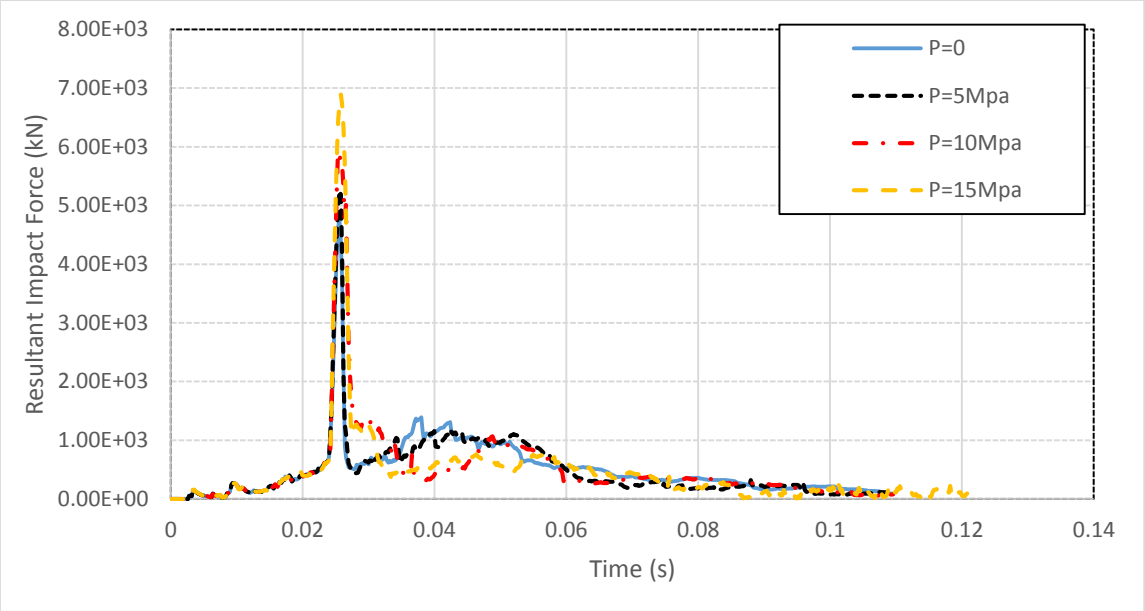

Figure 5-25 Time histories of impact forces with different axial stress

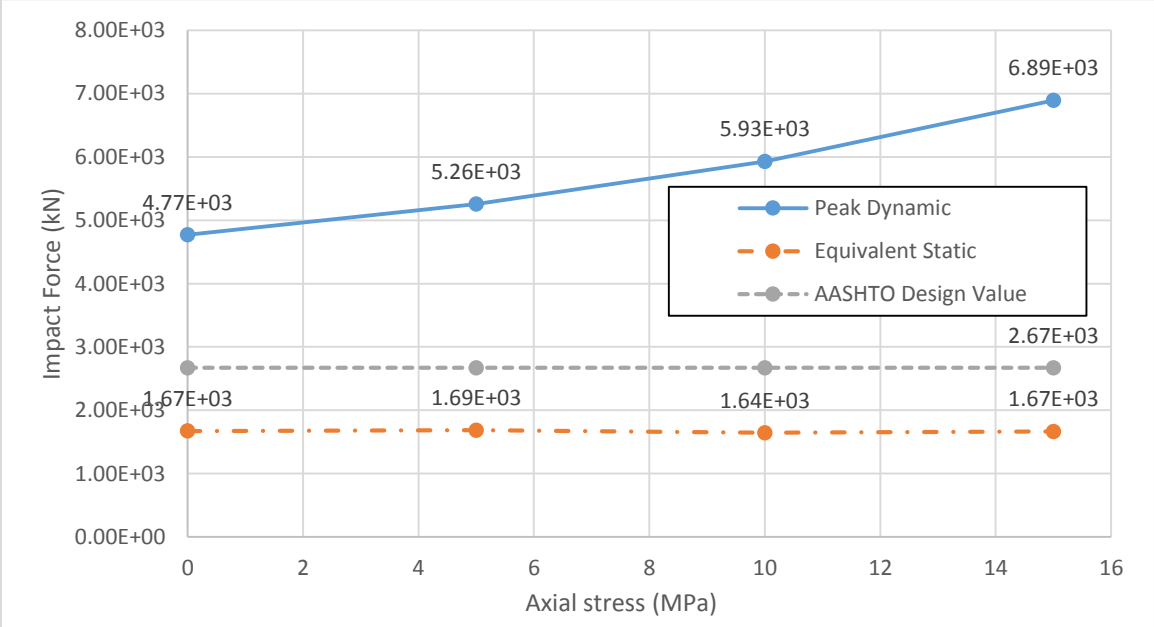

Figure 5-26 Peak dynamic forces and equivalent forces with different axial stress

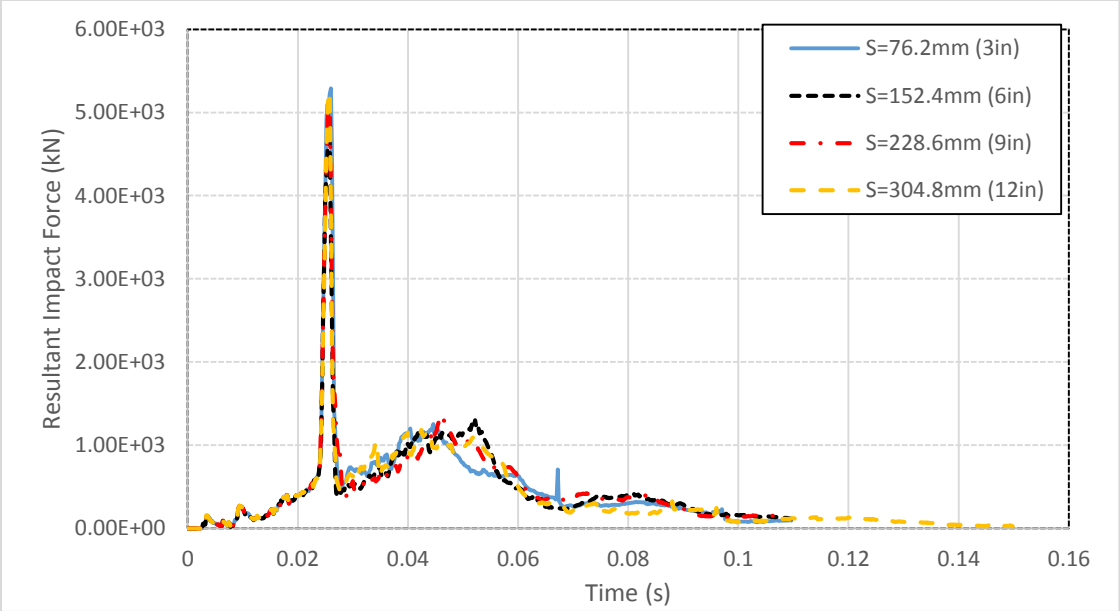

Figure 5-27 Time histories of impact forces with different tie spacing

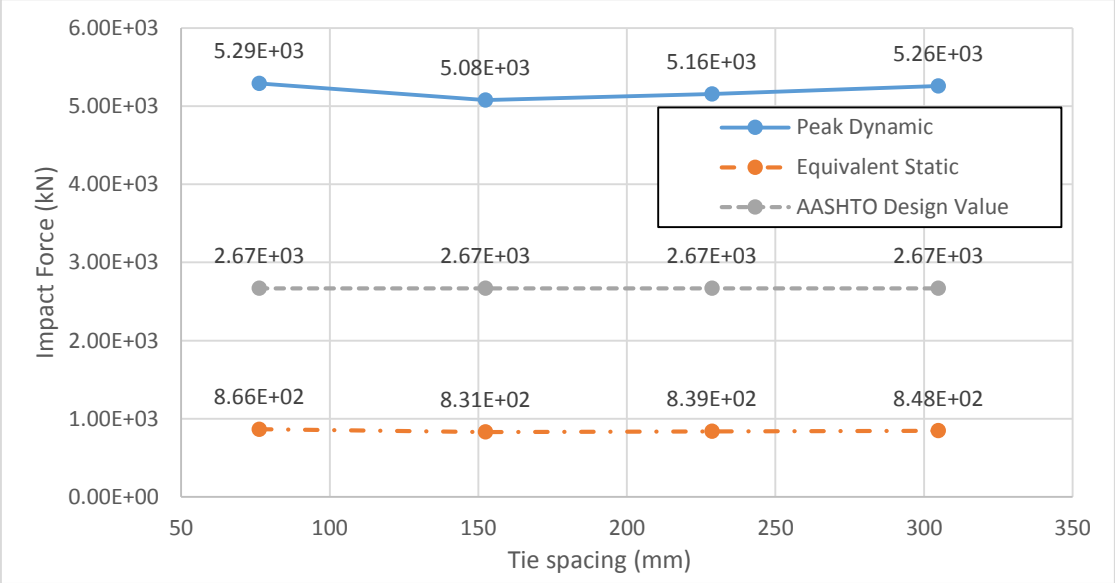

Figure 5-28 Peak dynamic forces and equivalent forces with different tie spacing

5.2.2 Failure mechanism

The failure mechanism is analyzed by the effective plastic strain. By comparing Figures 5-29 (a) (b) and (c), it is found that with increase of impact velocity of the truck, the number of elements in plastic state also increases. Three kinds of failure could be observed.

1. At the impact location, there is local failure due to the impact load.

2. Shear failure at the impact height within 45 ºzone as shown in Figure 4.16.

3. Bending failure happens near the foot of the pier.

Figures 5-29(a) and (d) tell that softer soil could reduce the bending failure near the foot. Figures 5-29 (a) and (e) show the higher grade of concrete can reduce both local and bending failures. Figures 5-29 (f) and (g) infer that larger section of the pier can also reduce the failure. Figures 5-29 (a) and (h) show that the bending failure will be minimized for high pier, but that there will be plastic zone at the location near the top of the pier. When the impact happened near the footing of the pier, the bending failure zone will be replaced by shear failure zone as shown in Figures 5-29 (j) and (k). When restraints are added at the top of the pier as shown in Figure 5-29 (a), (l) and (m), the bending failure is reduced. When there is large lumped mass at the top of the pier, there will also be a bending failure zone, near the top of the pier, which is shown in Figure 5-29 (o). By comparing Figures 5-29 (p) and (q), it refers that increasing the prestressed top axial force, the bending failure would be reduced. Figures 5-29 (n) and (r) show the larger cargo mass and the smaller hoop spacing don’t changes much about the failure mechanism for the impact induced by C2500.

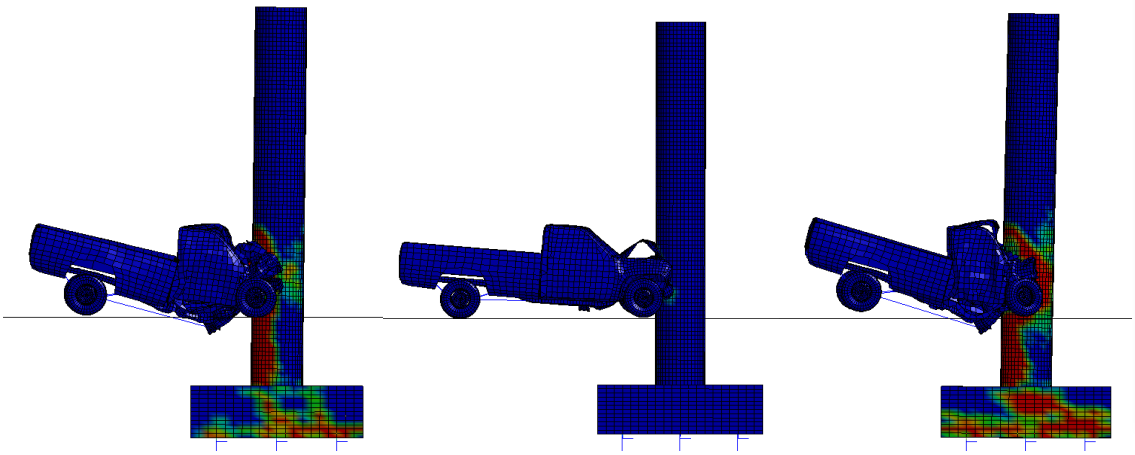

(a) C1 (b) C2 (c) C5

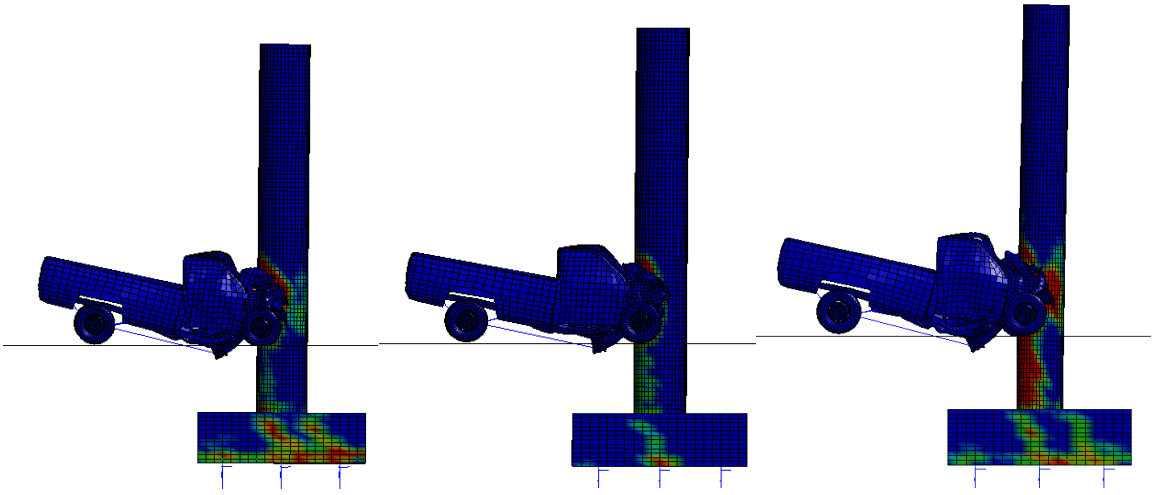

(d) C6 (e) C9 (f) C10

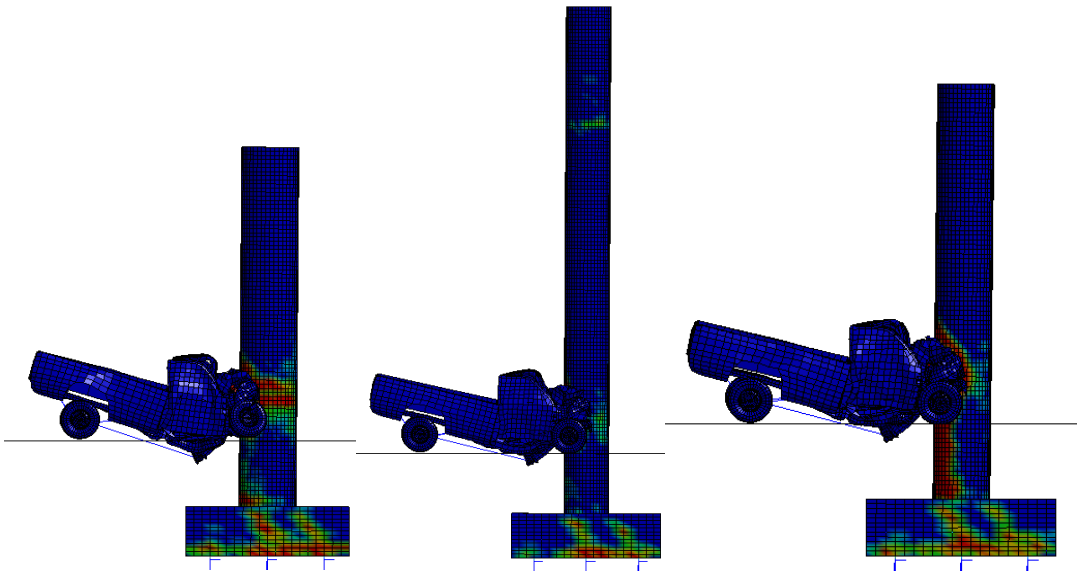

(g) C11 (h) C15 (i) C16

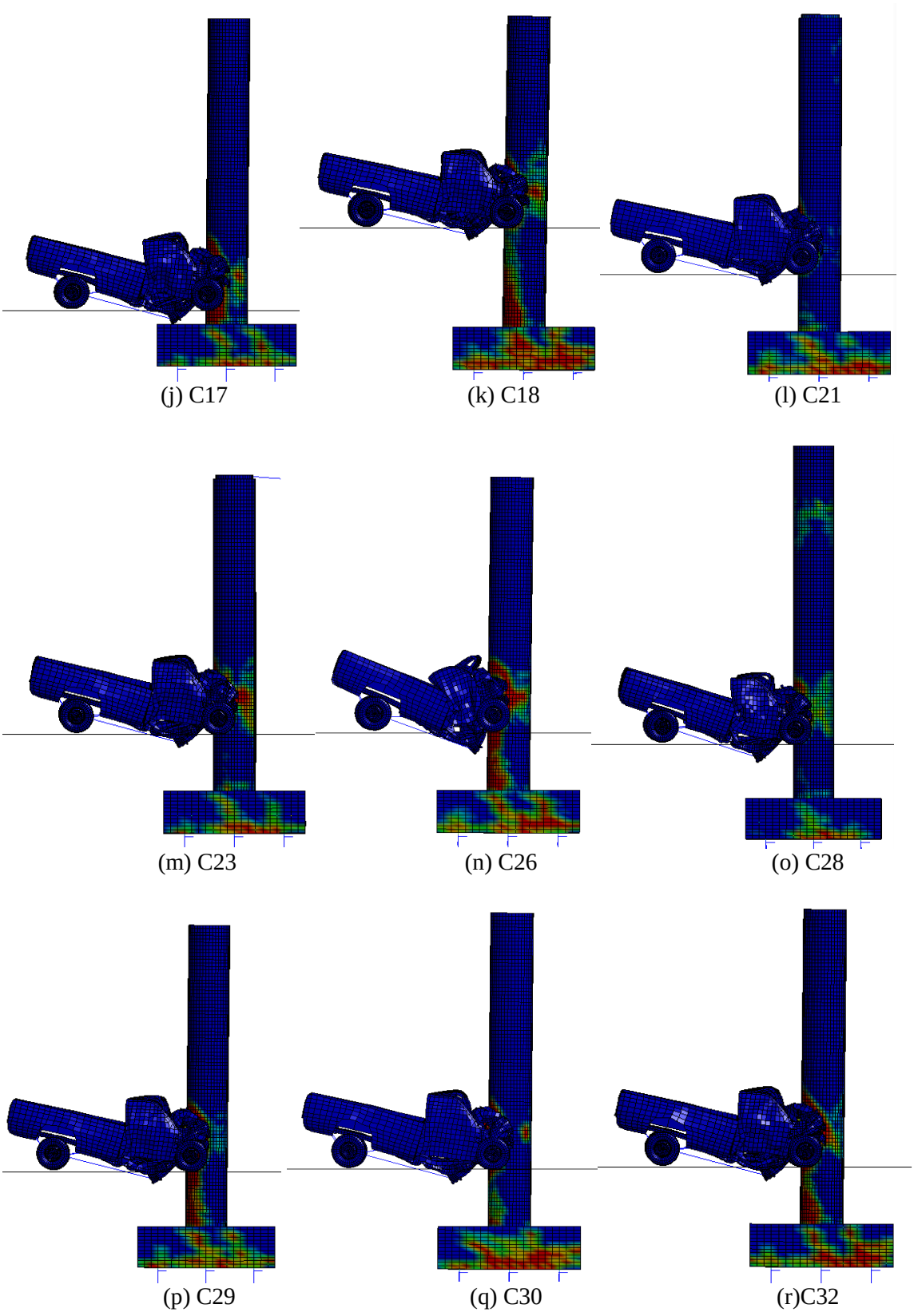

Figure 5-29 Effective plastic strain for the impact induced by C2500 light-weight truck

5.3 F800 Single Unit Truck

Table 5-5 Load cases for F800 single unit truck

Case	V km/h	C_u kPa	Fy_c Mpa	D mm	L mm	Fy_s Mpa	L_I mm	K_r N mm/rad	K_h N/mm	M_c Ton	M_s Ton	P Mpa	S mm
F1	100	98.35	27.58	914.4	5486.4	413.7	1219.2	0	0	2.913	0	5	304.8
F2	60	-	-	-	-	-	-	-	-	-	-	-	-
F3	80	-	-	-	-	-	-	-	-	-	-	-	-
F4	120	-	-	-	-	-	-	-	-	-	-	-	-
F5	140	-	-	-	-	-	-	-	-	-	-	-	-
F6	-	24.61	-	-	-	-	-	-	-	-	-	-	-
F7	-	49.17	-	-	-	-	-	-	-	-	-	-	-
F8	-	-	41.37	-	-	-	-	-	-	-	-	-	-
F9	-	-	55.16	-	-	-	-	-	-	-	-	-	-
F10	-	-	-	762	-	-	-	-	-	-	-	-	-
F11	-	-	-	1066.8	-	-	-	-	-	-	-	-	-
F12	-	-	-	-	7315.2	-	-	-	-	-	-	-	-
F13	-	-	-	-	9144	-	-	-	-	-	-	-	-
F14	-	-	-	-	-	275.8	-	-	-	-	-	-	-
F15	-	-	-	-	-	551.6	-	-	-	-	-	-	-
F16	-	-	-	-	-	-	304.8	-	-	-	-	-	-
F17	-	-	-	-	-	-	2133.6	-	-	-	-	-	-
F18	-	-	-	-	-	-	-	2×10^4	-	-	-	-	-
F19	-	-	-	-	-	-	-	2×10^8	-	-	-	-	-
F20	-	-	-	-	-	-	-	2×10^{12}	-	-	-	-	-
F21	-	-	-	-	-	-	-	-	1×10^3	-	-	-	-
F22	-	-	-	-	-	-	-	-	1×10^5	-	-	-	-
F23	-	-	-	-	-	-	-	-	-	0	-	-	-
F24	-	-	-	-	-	-	-	-	-	1.456	-	-	-
F25	-	-	-	-	-	-	-	-	-	-	335	-	-
F26	-	-	-	-	-	-	-	-	-	-	670	-	-
F27	-	-	-	-	-	-	-	-	-	-	-	0	-
F28	-	-	-	-	-	-	-	-	-	-	-	10	-

F29	-	-	-	-	-	-	-	-	-	-	-	15	-
F30	-	-	-	-	-	-	-	-	-	-	-	-	76.2
F31	-	-	-	-	-	-	-	-	-	-	-	-	152.4
F32	-	-	-	-	-	-	-	-	-	-	-	-	228.6

Note: "-" means that the value in this blank is the same as the value of base case F1

5.3.1 Impact Load

For the impact force with respect to the vehicle speed at 60km/h (37.3Mph), 80km/h (49.7Mph), 100km/h (62.1Mph), 120km/h (74.6 Mph), 140km/h (87.0 Mph). As shown in Figure 5-30 and Figure 5-31, the impact force induced by F800 yields a higher value, compared with the impact force induced by C2500 at the same vehicle speed. The peak impact force ranges from 2.16×10^{3}kN to 1.13×10^{4}kN, while the equivalent static force ranges from 1.34×10^{3}kN to 2.22×10^{3}kN. A higher vehicle speed will lead to higher dynamic and equivalent static impact forces. Moreover, when the vehicle speed exceeds 120km/h, the cargo mass will induce a secondary impact. However, its impact force is smaller than the head-on initial impact. The initial impact is most critical according to the finite elemental analysis result. Compared to the AASHTO design value of 2669kN (600kips) equivalent static force, the finite elemental result shows much smaller result, which means a conservative estimation of the impact force based on the latest code for medium-weight vehicle.

It is shown in Figure 5-34 and Figure 5-35, peak dynamic force drops as the concrete strength of the pier increases. However, the equivalent static impact force shows insensitivity with the variation of the concrete strength.

For the variation of diameter, larger pier diameter will yield higher peak dynamic impact load as shown in Figure 5-36 and Figure 5-37. The equivalent static impact force shows insensitivity to the variation of pier diameter.

With the increase of the pier height, the peak dynamic impact force decreases, while the equivalent static load does not change much, as shown in Figure 5-38 and Figure 5-39.

With higher impact location from the top of the pier footing, the peak dynamic value of the impact force obtains smaller results. The equivalent static impact force is not sensitive to this change, as shown in Figure 5-42 and Figure 5-43.

When the truck is loaded with heavier cargo mass, the peak dynamic load will increase slightly. However, the equivalent static force also changes little, which is plotted in Figure 5-48 and Figure 5-49.

Compared with results of C2500, the increase in the axial force at top of the pier for F800 truck shows little changes in the dynamic impact load. The equivalent static force also is not sensitive to the change of the axial force, which is depicted in Figure 5-52 and Figure 5-53.

It tells in Figures 5-32, 5-33, 5-40, 5-41, 5-44, 5-45, 5-46, 5-47, 5-50, 5-51, 5-54, and 5-55, both peak dynamic force and equivalent static force of the impact load show insensitivity to the following parameters: stiffness of the soil, yield strength of the steel reinforcement, the stiffness of spring at top of the pier, lumped mass at top of the pier, and the spacing of the hoop.

It refers that the boundary condition and top mass which will have large impact on the dynamic characteristics, such as the modal shape and the frequency of the pier, have

little influence on the impact load. The material of the structure not directly subjected to the impact, such as the steel, has little effect on the value of the impact load.

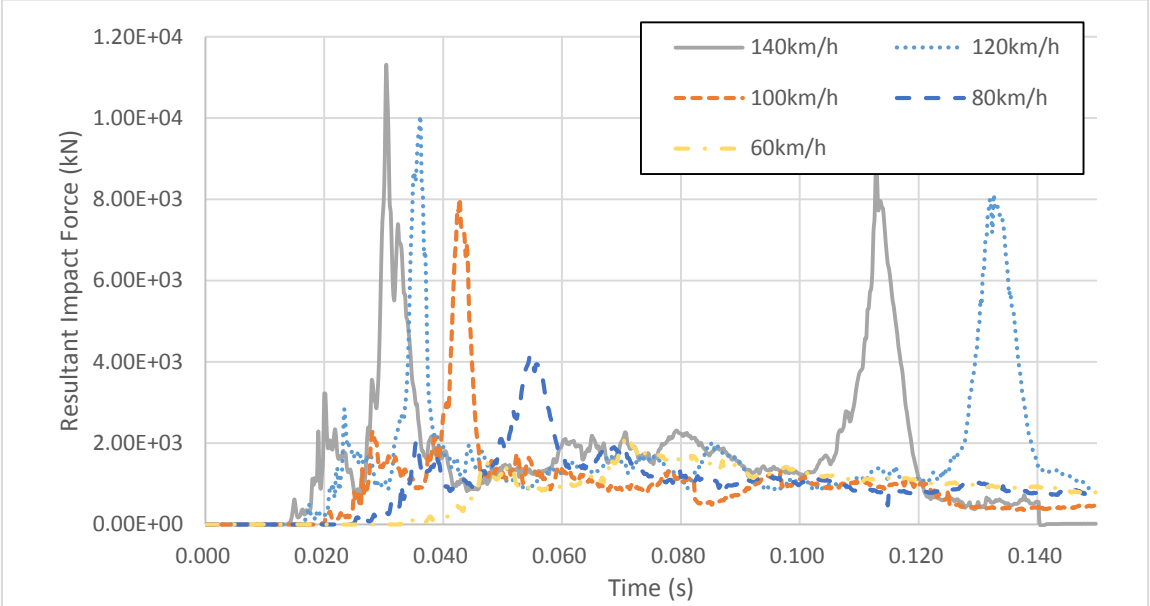

Figure 5-30 Time histories of impact forces with different vehicle speed

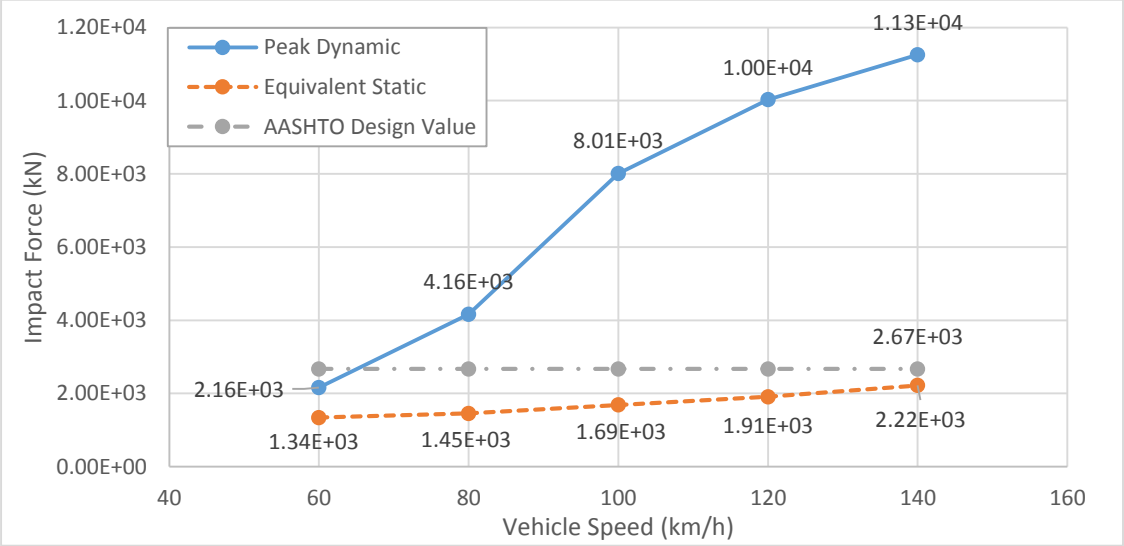

Figure 5-31 Peak dynamic forces and equivalent forces with different vehicle speed

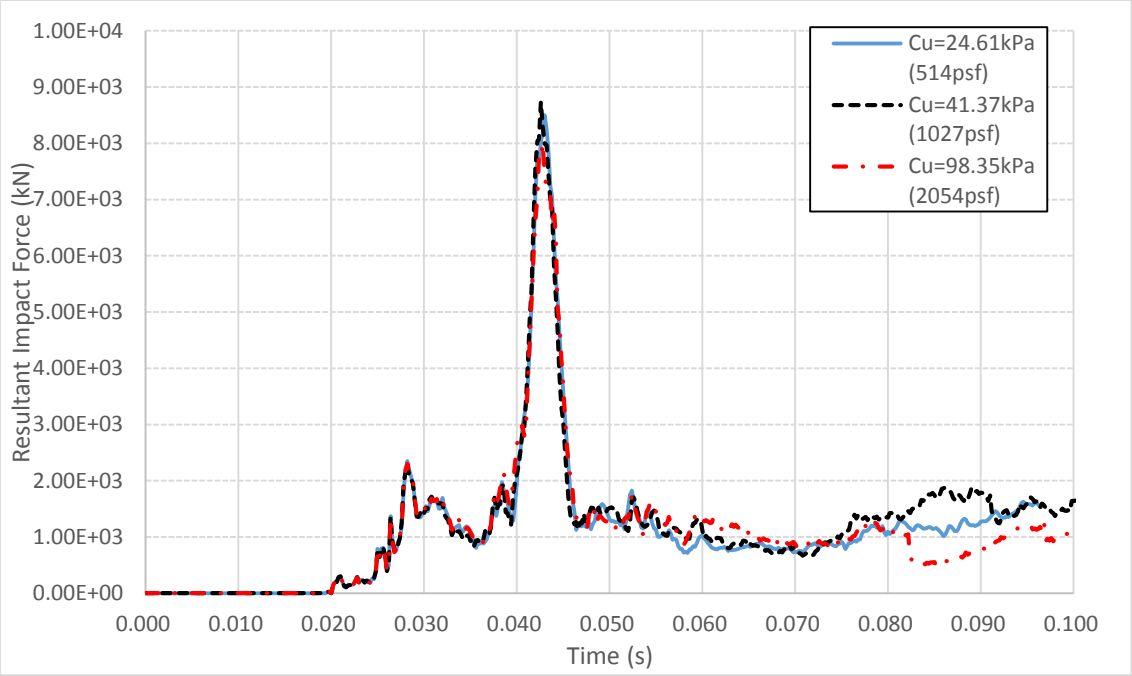

Figure 5-32 Time histories of impact forces with different soil stiffness

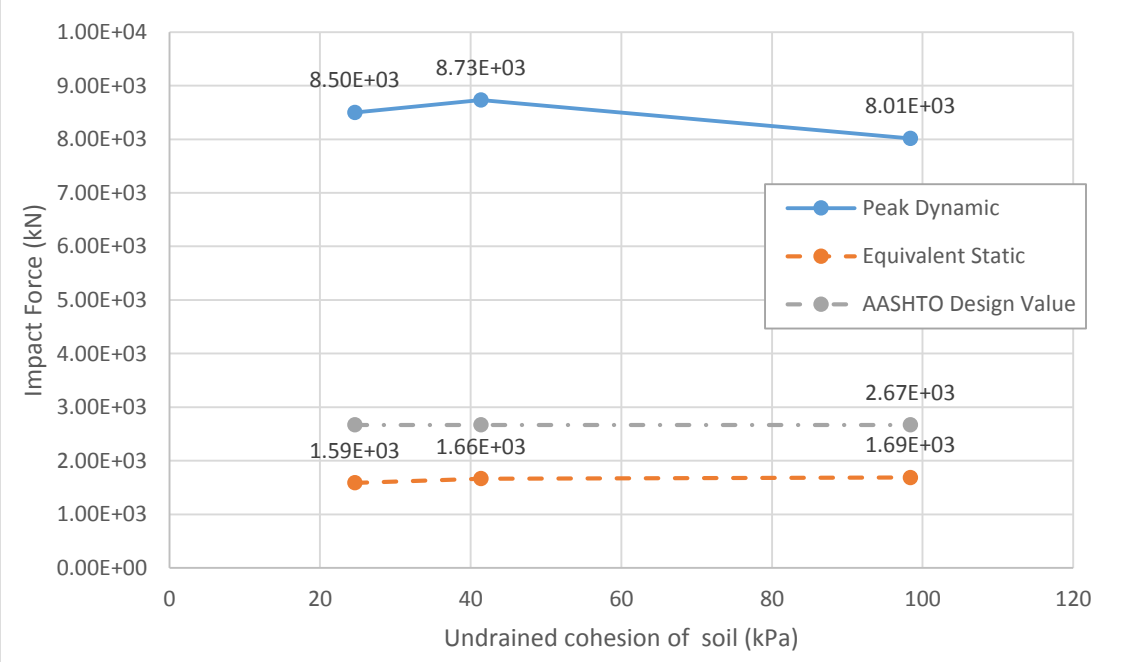

Figure 5-33 Peak dynamic forces and equivalent forces with different soil stiffness

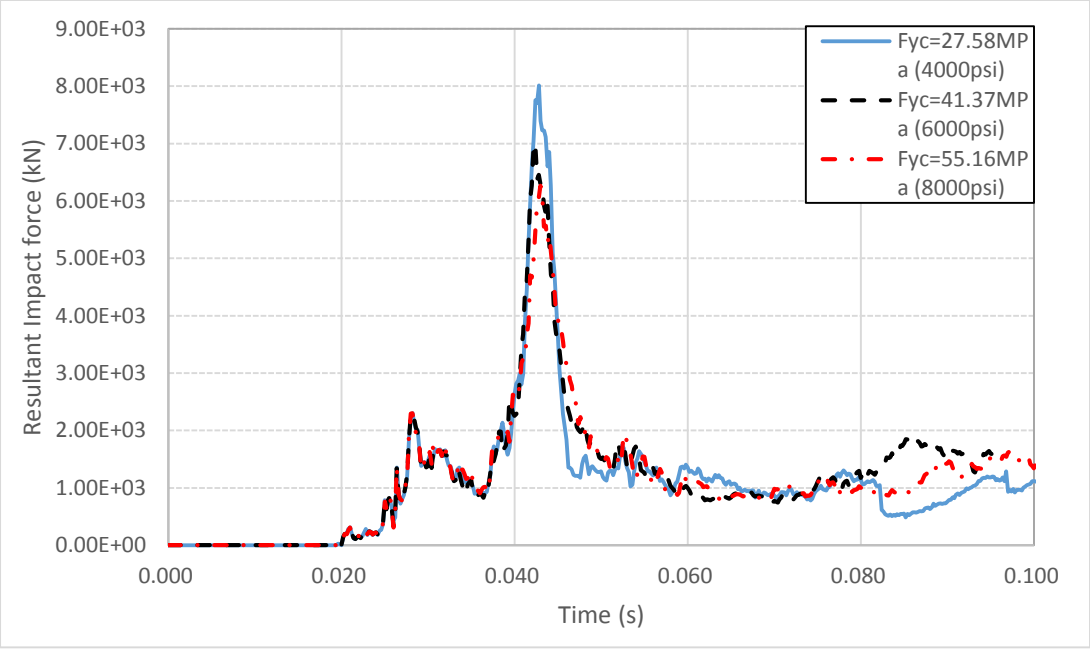

Figure 5-34 Time histories of impact forces with different concrete strength

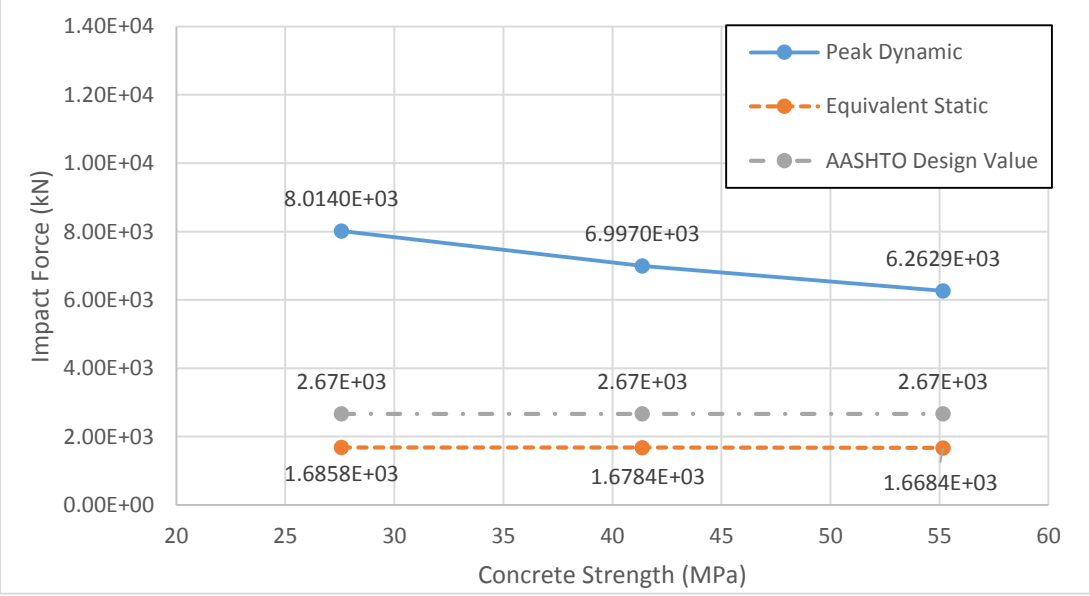

Figure 5-35 Peak dynamic forces and equivalent forces with different concrete strength

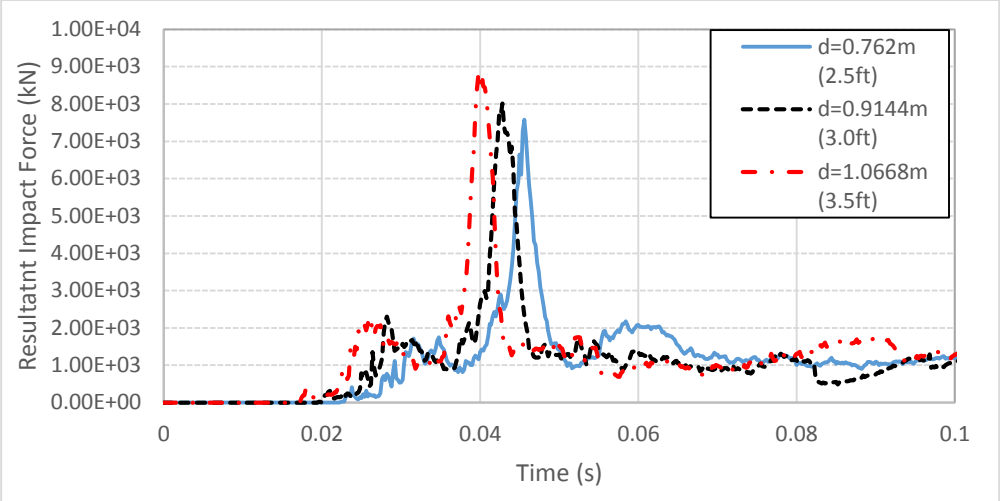

Figure 5-36 Time histories of impact forces with different pier diameter

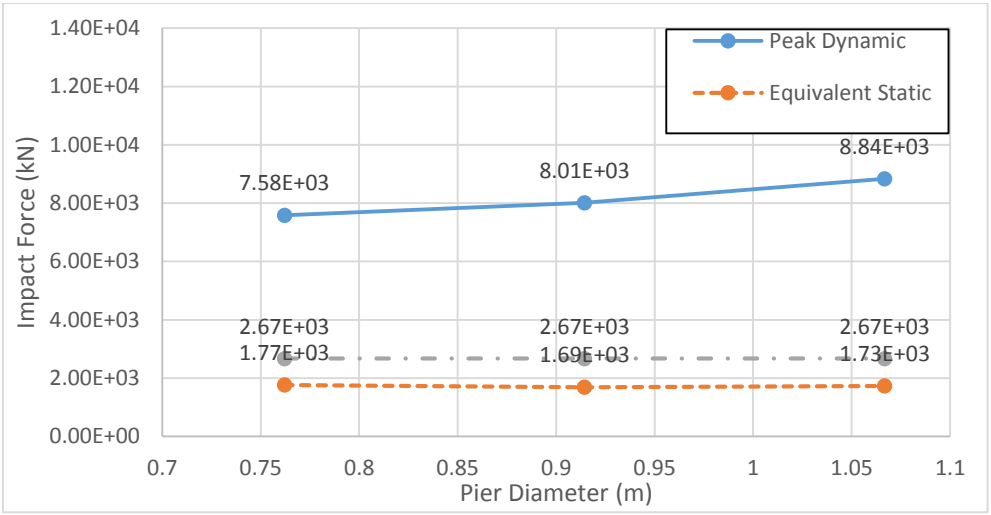

Figure 5-37 Peak dynamic forces and equivalent forces with different pier diameter

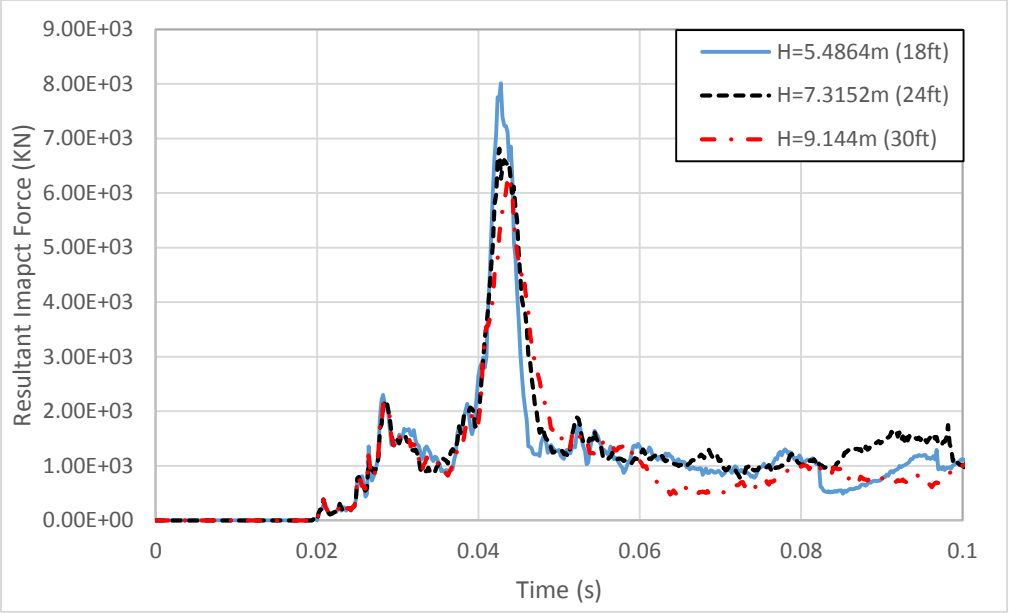

Figure 5-38 Time histories of impact forces with different pier length

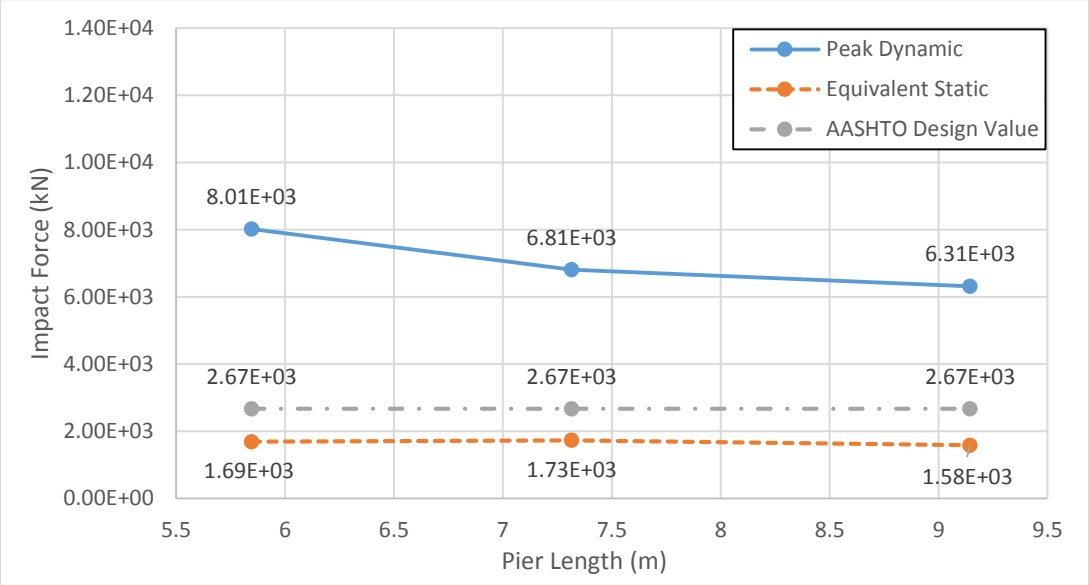

Figure 5-39 Peak dynamic forces and equivalent forces with different pier length

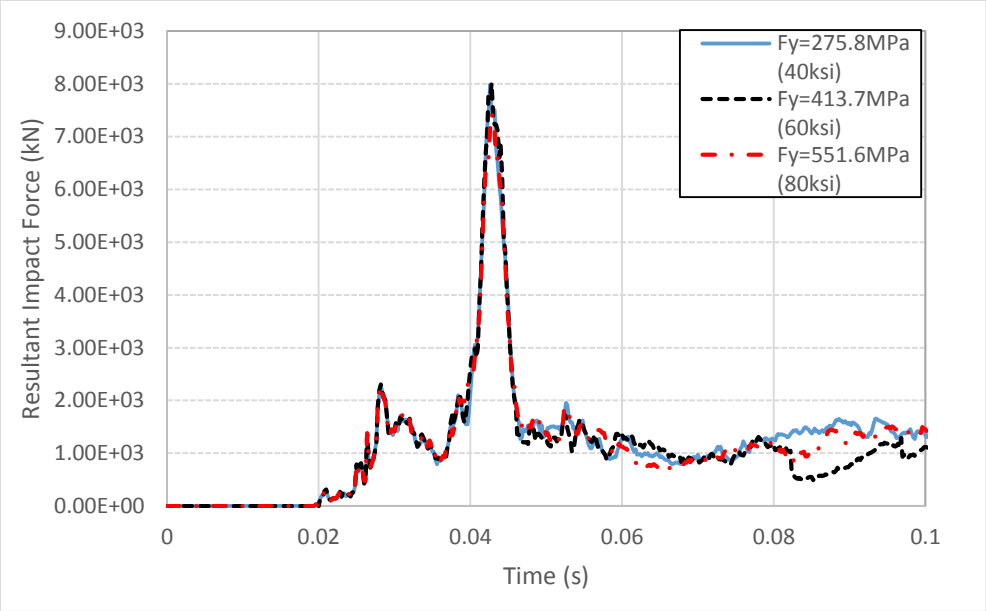

Figure 5-40 Time histories of impact forces with different steel rebar strength

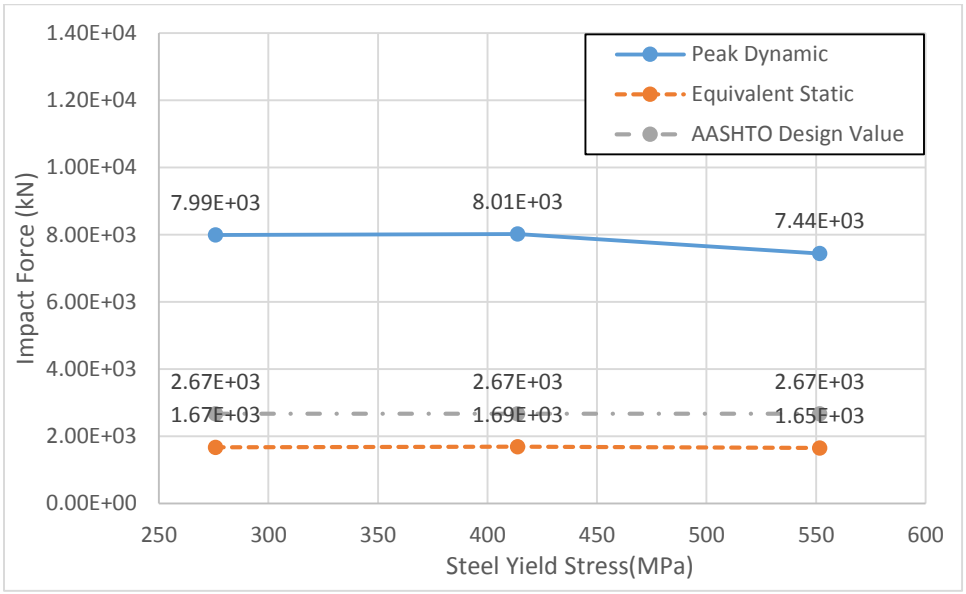

Figure 5-41 Peak dynamic forces and equivalent forces with different steel rebar strength

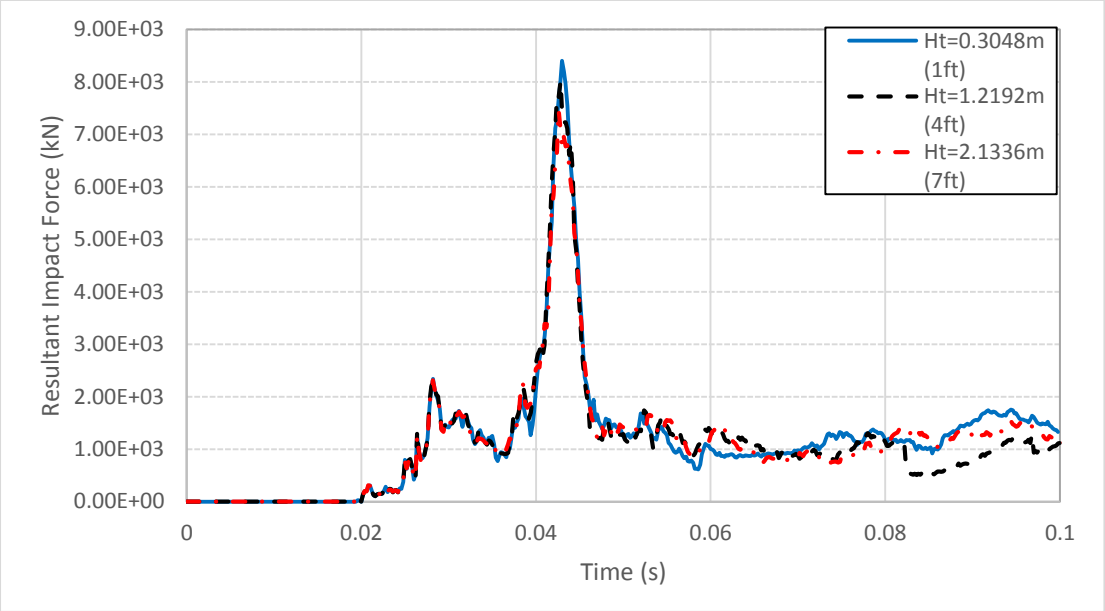

Figure 5-42 Time histories of impact forces with different impact height

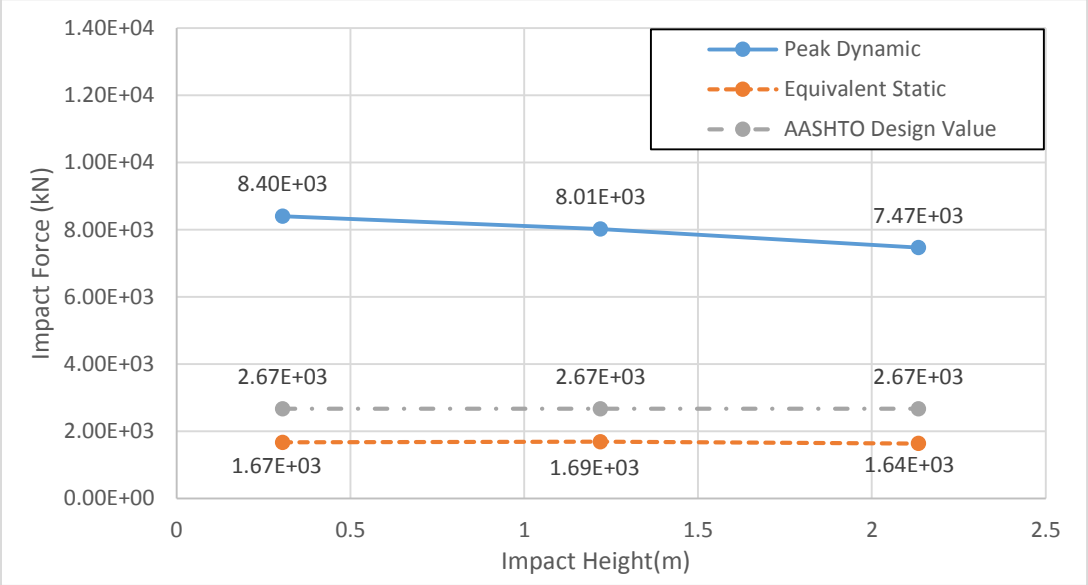

Figure 5-43 Peak dynamic forces and equivalent forces with different impact height

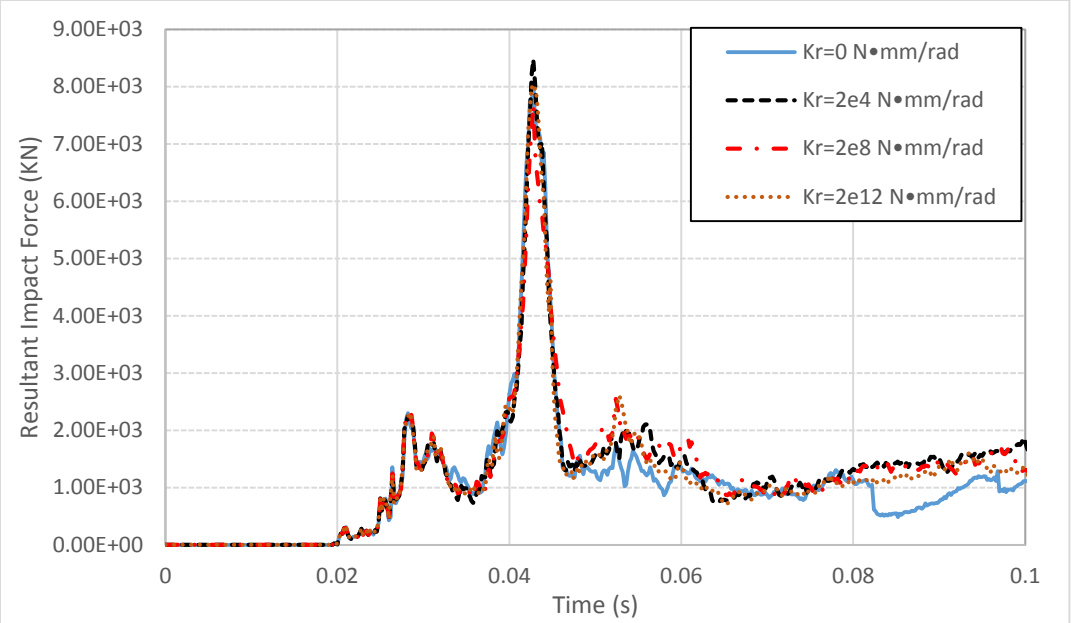

Figure 5-44 Time histories of impact forces with different rotational spring stiffness

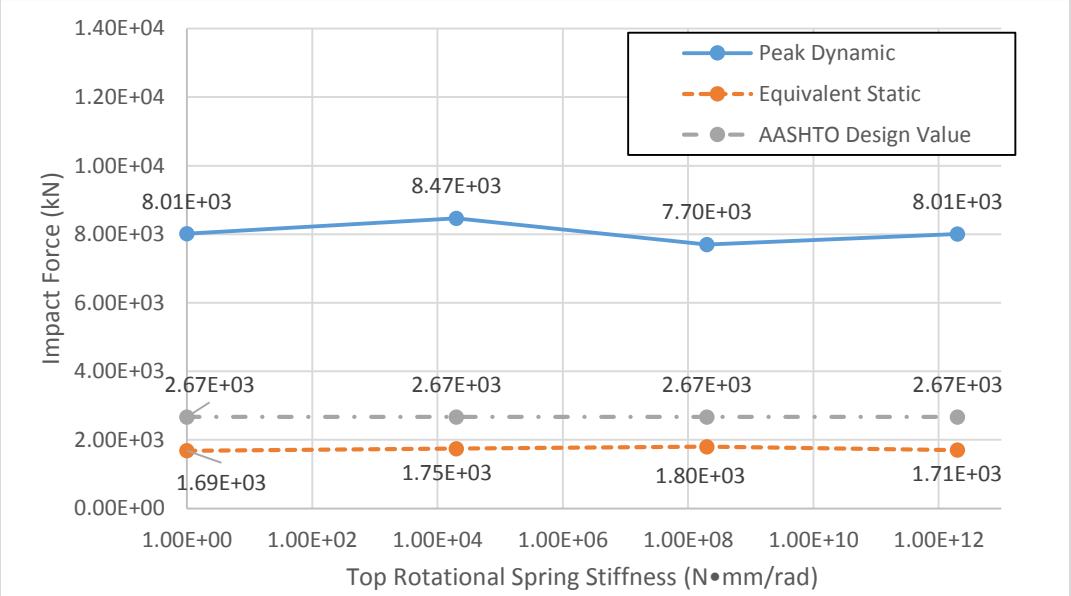

Figure 5-45 Peak dynamic forces and equivalent forces with different rotational spring stiffness

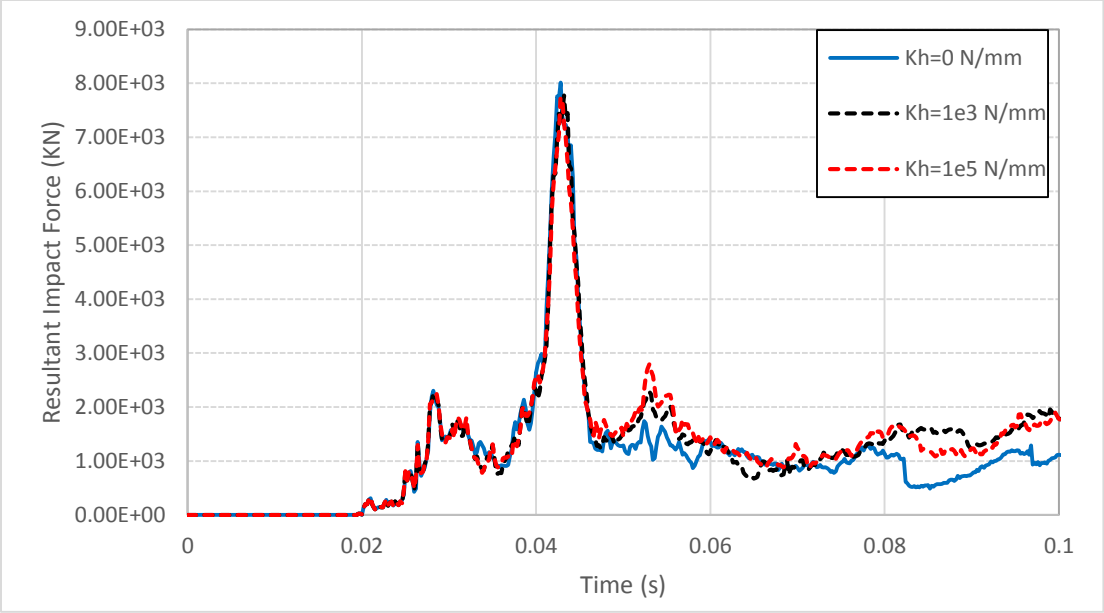

Figure 5-46 Time histories of impact forces with different translational spring stiffness

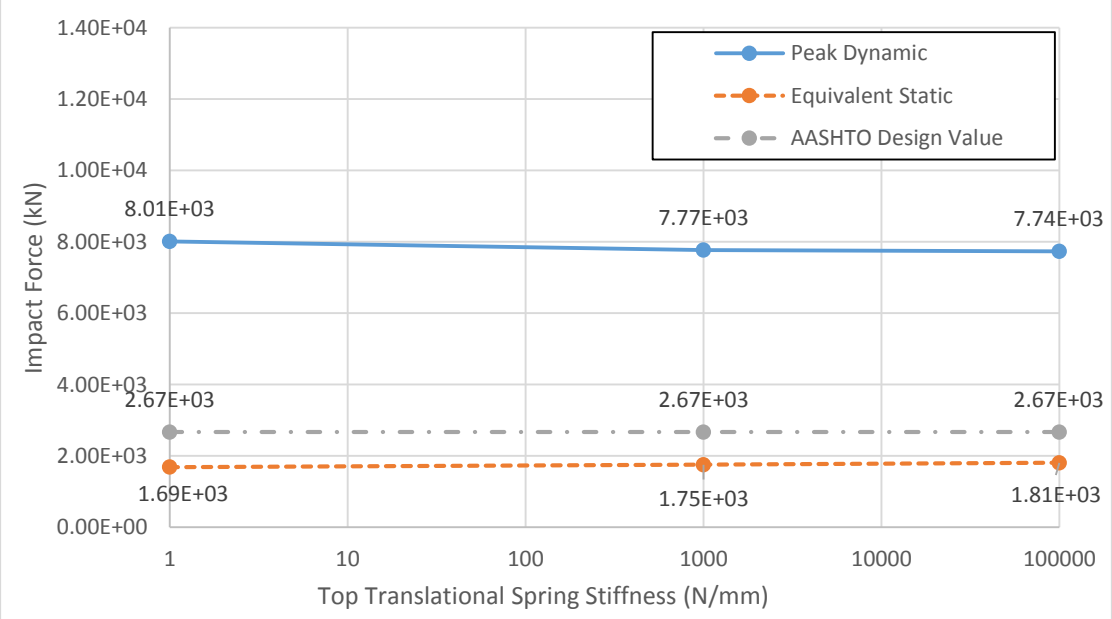

Figure 5-47 Peak dynamic forces and equivalent forces with different translational spring stiffness

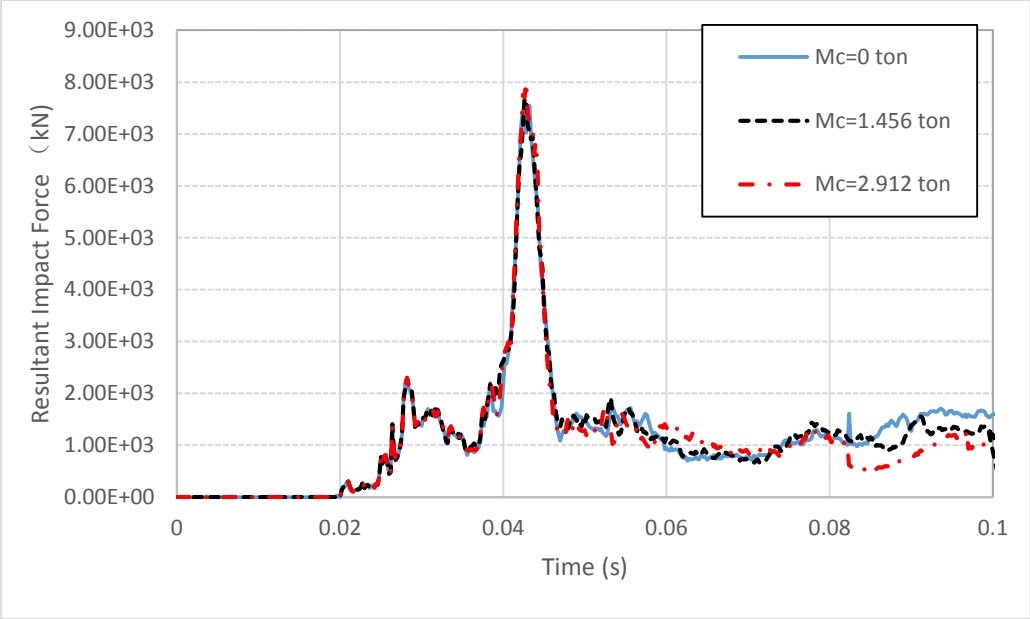

Figure 5-48 Time histories of impact forces with different cargo mass

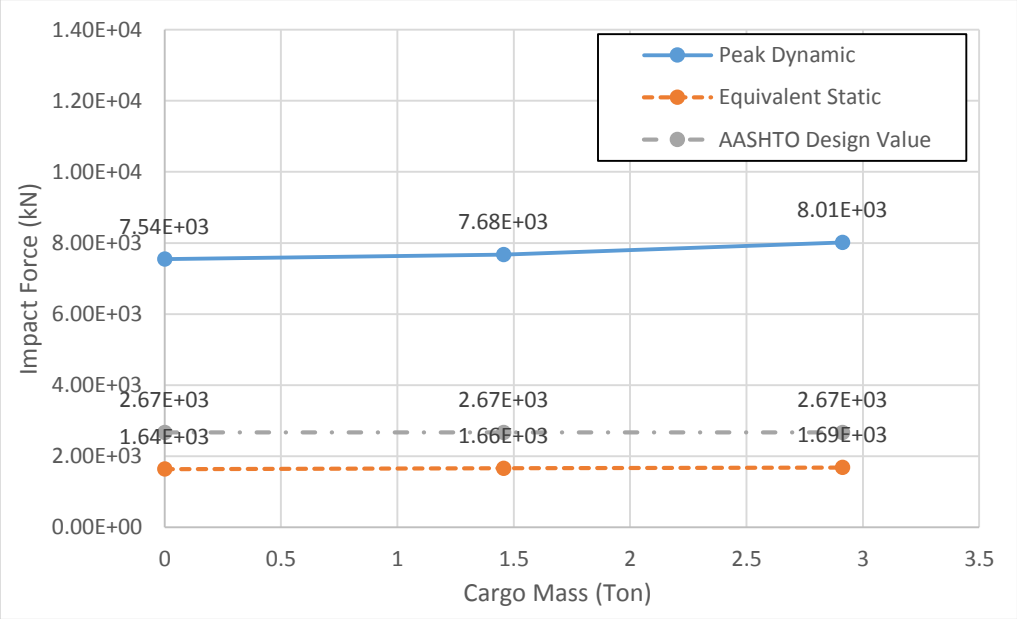

Figure 5-49 Peak dynamic forces and equivalent forces with different cargo mass

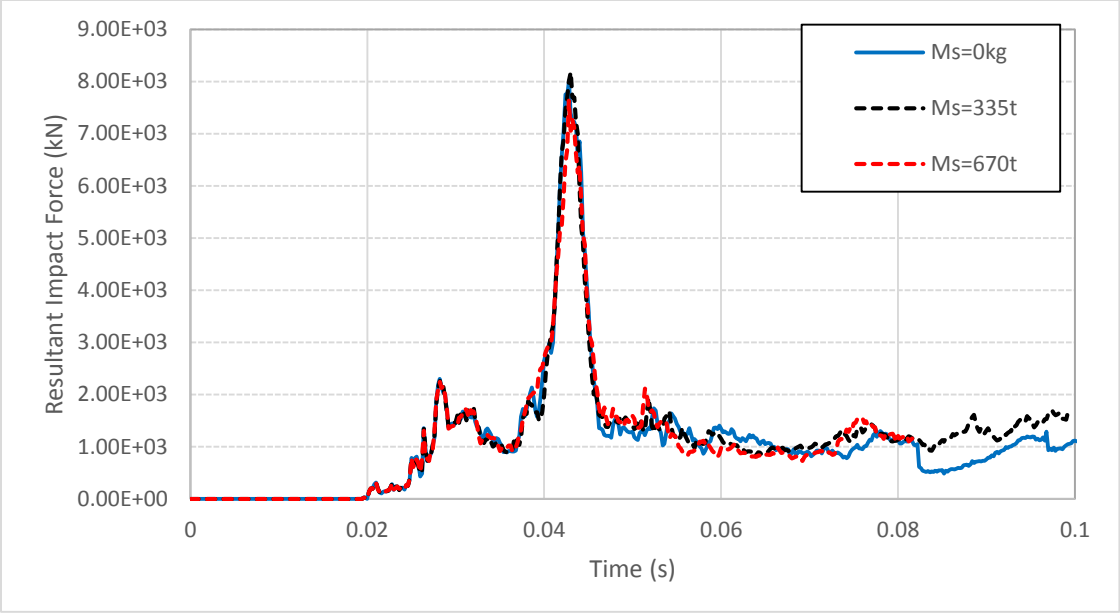

Figure 5-50 Time histories of impact forces with different top mass

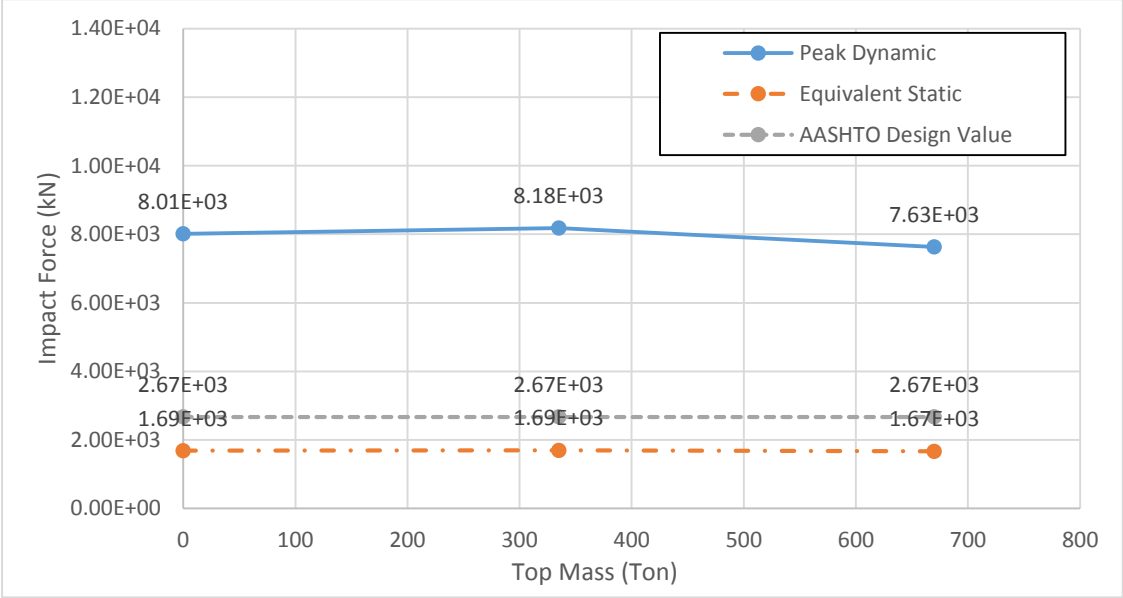

Figure 5-51 Peak dynamic forces and equivalent forces with different top mass

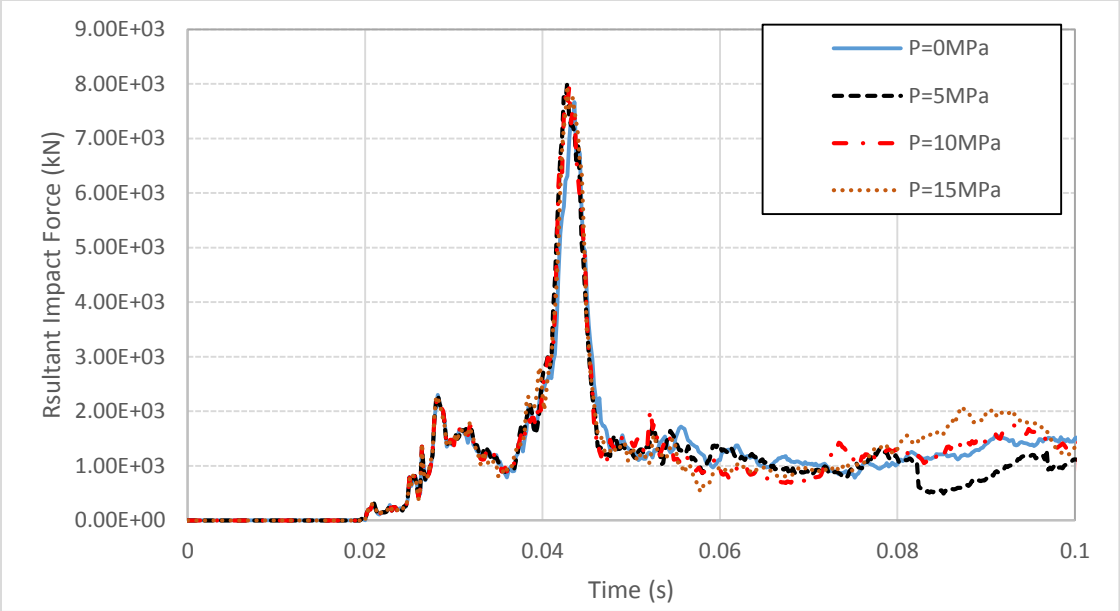

Figure 5-52 Time histories of impact forces with different axial stress

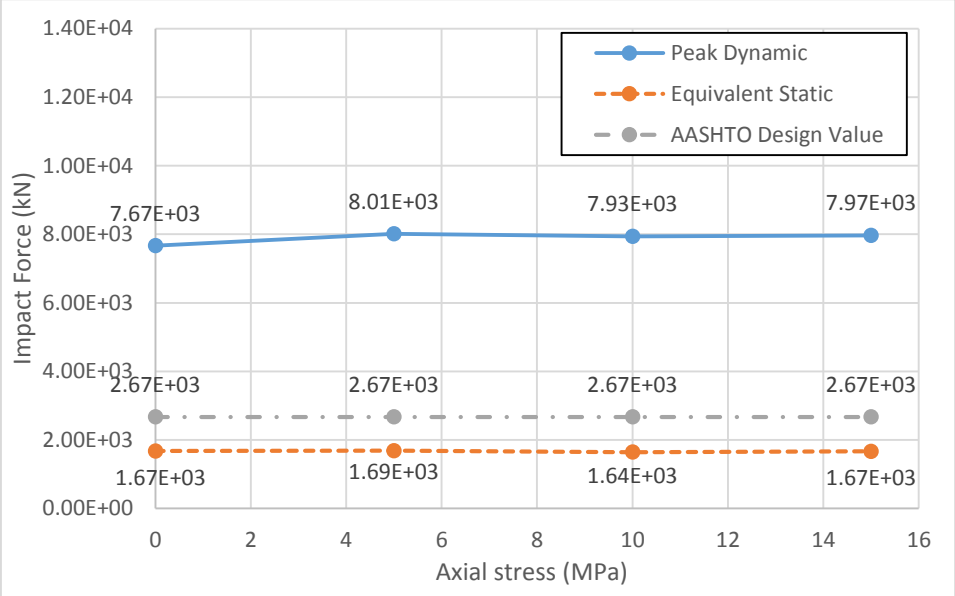

Figure 5-53 Peak dynamic forces and equivalent forces with different axial stress

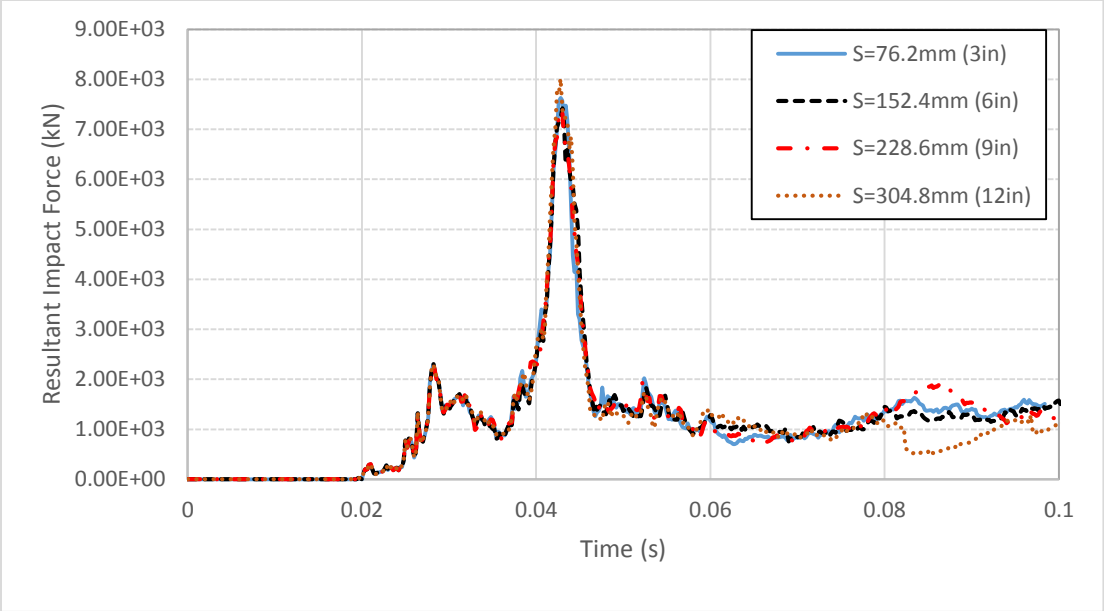

Figure 5-54 Time histories of impact forces with different tie spacing

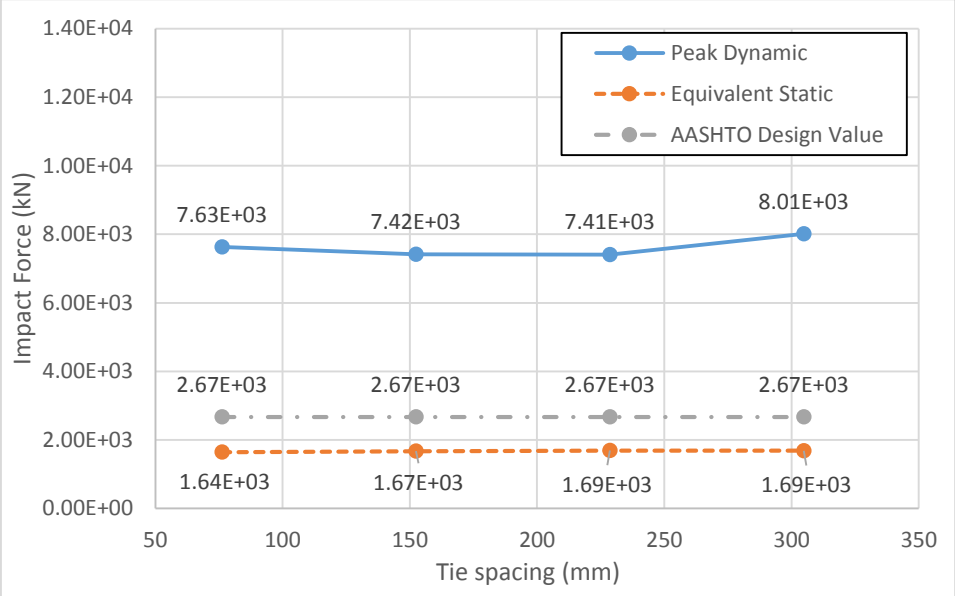

Figure 5-55 Peak dynamic forces and equivalent forces with different tie spacing

5.3.2 Failure mechanism

The failure mechanism is analyzed by the effective plastic strain. Compared with the load case with the same parameters of C2500, the load case of F800 induces more serious damage, as shown in Figure 5-56. Four failures mechanisms could be observed:

1. Local failure at the impact height;

2. Shear failure at the impact height within the 45 °range;

3. Bending failure at the foot of the pier;

4. Bending failure at the middle of the pier on the opposite face of the impact location.

Figure 5-56 (a) shows the spalling of the cover at the impact location compared with 5-29 (a). Figure 5-56 (b) shows with small impact speed at 60km/h, it only yields minor damage. For the speed at 140km/h, the pier near the foot crushes at two bending side, which shows obvious plastic hinge of bending failure. By comparing Figures 5-56 (a) and (d), it is found that with smaller soil stiffness, the plastic deformation could be reduced. Figures 5-56 (a) and (e) show the higher grade of concrete can reduce both local and bending failure near the foot. Figures 5-56 (f) and (g) infer that larger section of the pier can also reduce the failure. Furthermore, Figure 5-56(f) shows the small section pier with diameter 0.762m (2.5ft) could not resist the impact by medium-weight truck at 100km/h, which induces the total failure near the footing of the pier with the combination of bending and shearing. Figures 5-56 (a) and (h) show that taller pier will extend the bending failure zone at the opposite of the impact location of the pier. Figures 5-56 (j) shows that increasing the strength of the steel reinforcement could prevent the spalling at the impact height shown in Figure 5-56(a). When the impact happened near the footing of the pier, the bending failure zone will be replaced by shear failure zone as shown in Figures 5-56 (j) and (k), while higher impact location will distribute the bending failure zone within longer length. When restraints are added at the top of the pier as shown in Figures 5-56 (a), (l) and (m), the bending failure zone will be redistributed. With the bending restraint in Figure 5-56 (l), there will be bending failure near the location of the restraint. Figure 5-56 (m) shows the

wider distribution of the bending failure zone at middle of the pier. Figures 5-56 (n) shows little influence induced by the change of the cargo mass. When there is larger mass from superstructure lumped at the top of the pier, there will also be a bending failure zone near the top of the pier, and the failure at the impact height and the foot could be reduced, as shown in Figure 5-56 (o). By comparing the Figures 5-56 (p) and (q), it refers that increase the prestressed top axial force, the bending failure would be reduced. Figures 5-56 (r) shows the smaller hoop spacing could minimize the shear failure at the impact height.

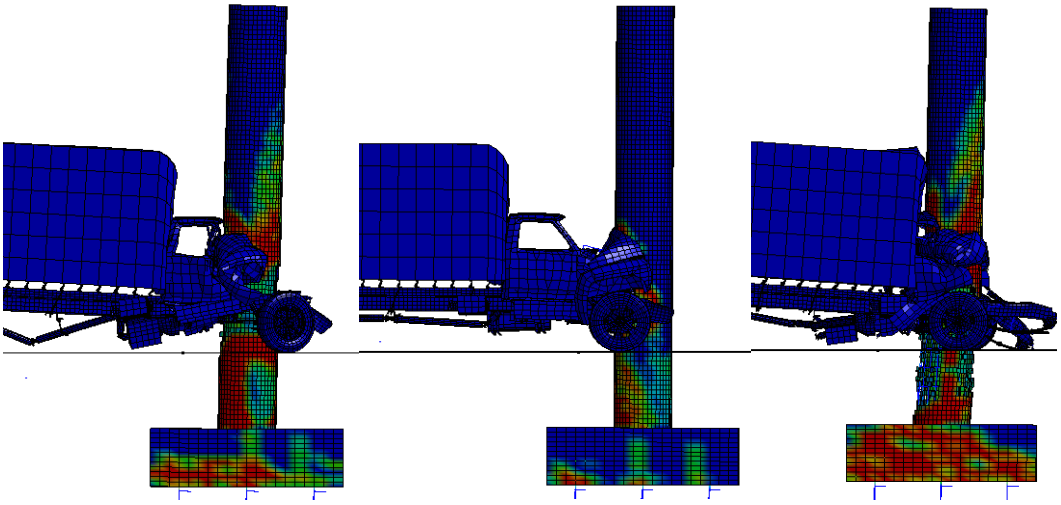

(a) F1 (b) F2 (c) F5

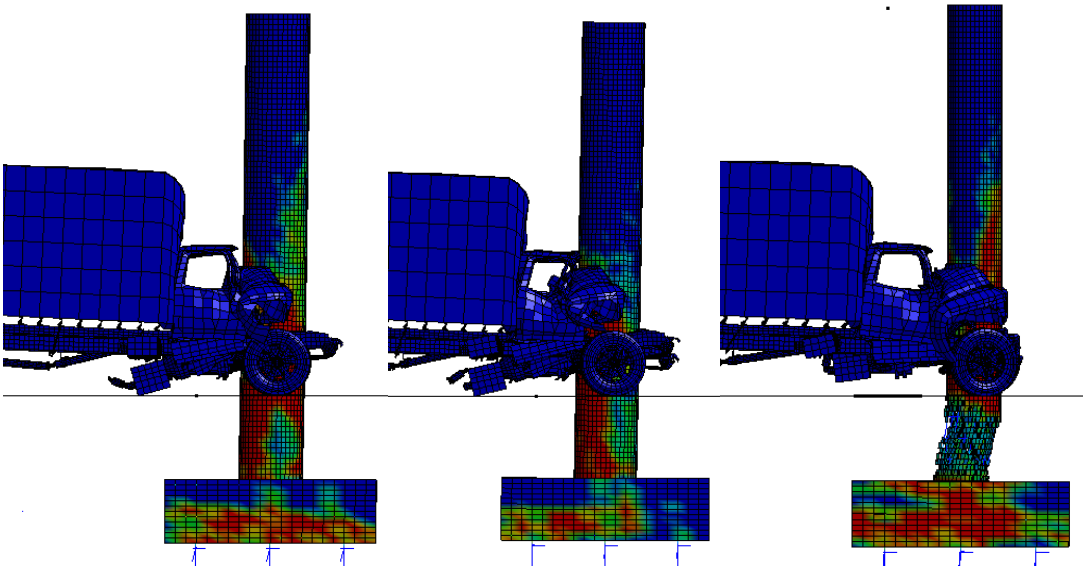

(d) F6 (e) F9 (f) F10

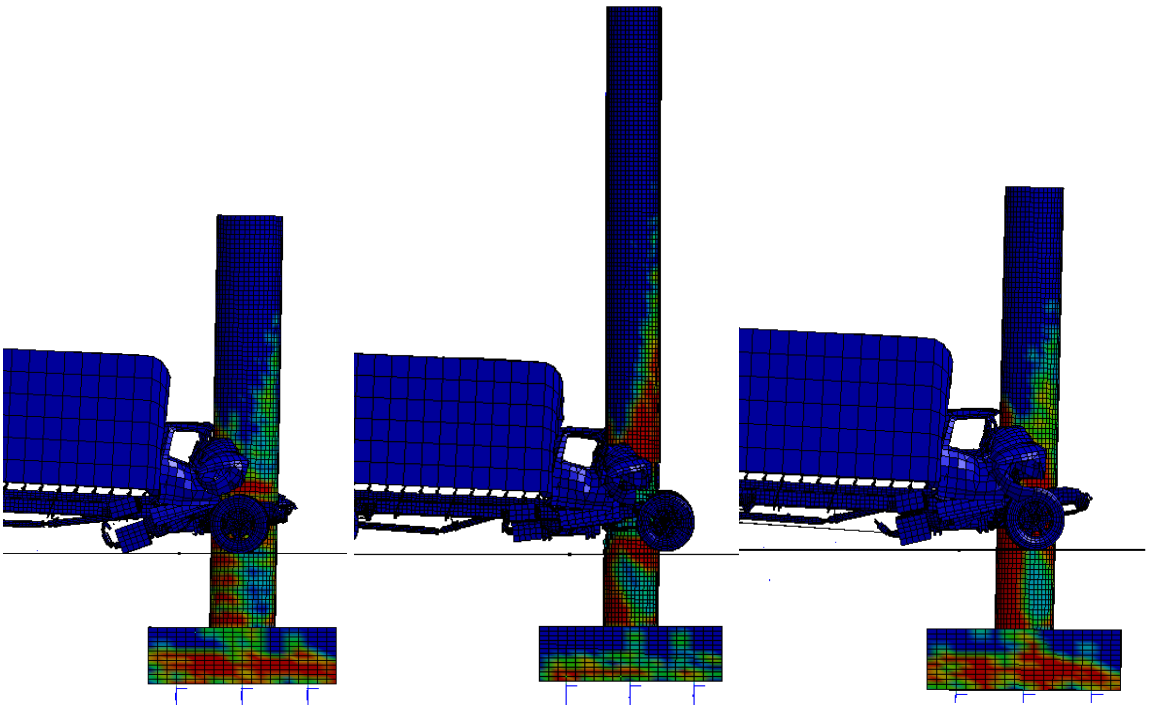

(g) F11 (h) F13 (i) F15

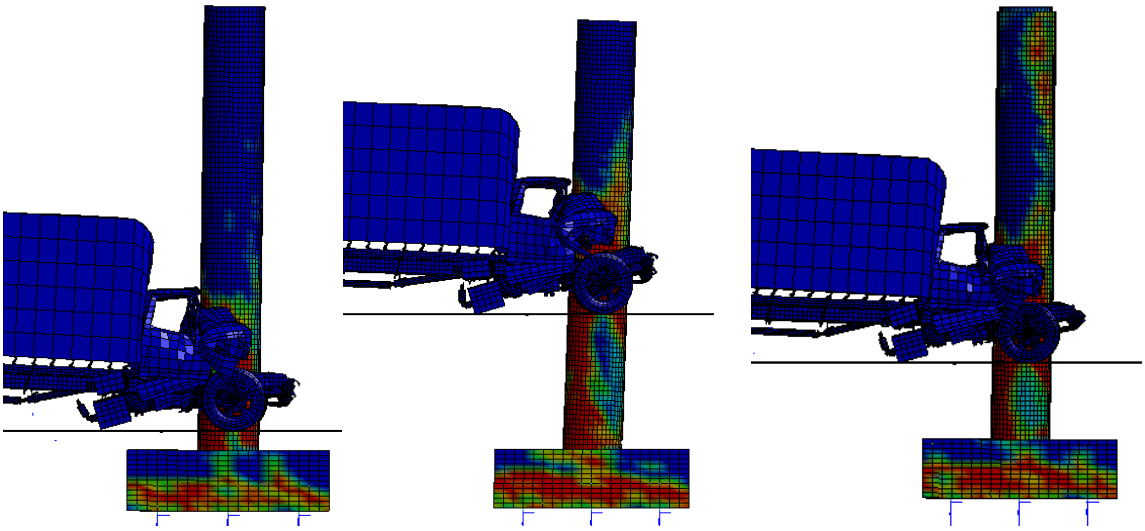

(j) F16 (k) F17 (l) F20

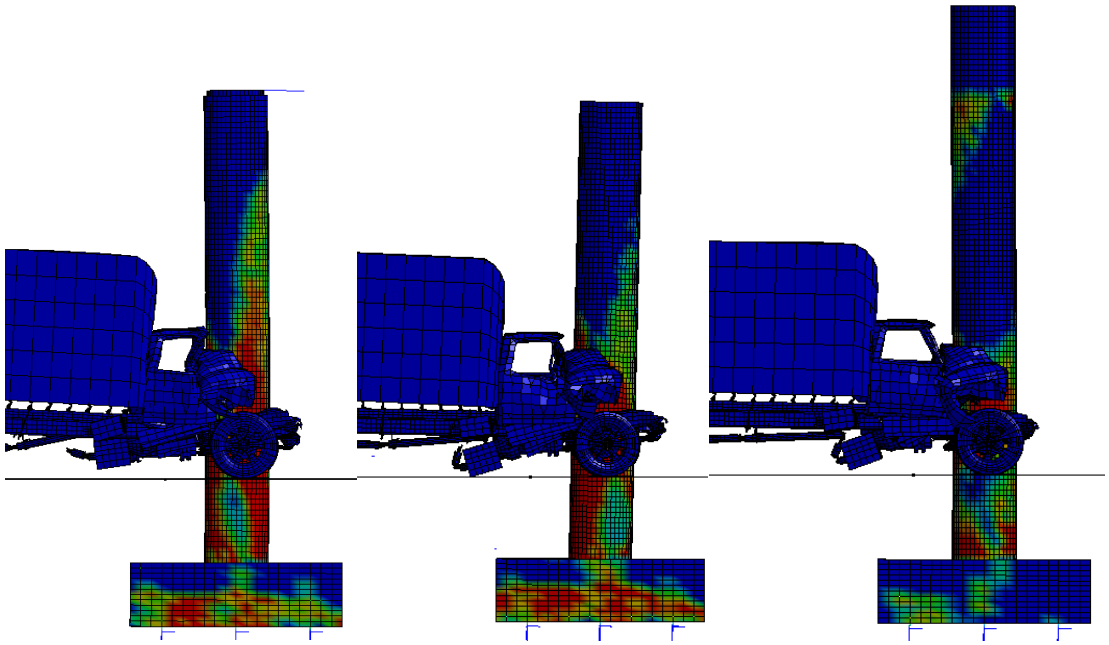

(m) F22 (n) F23 (o) F26

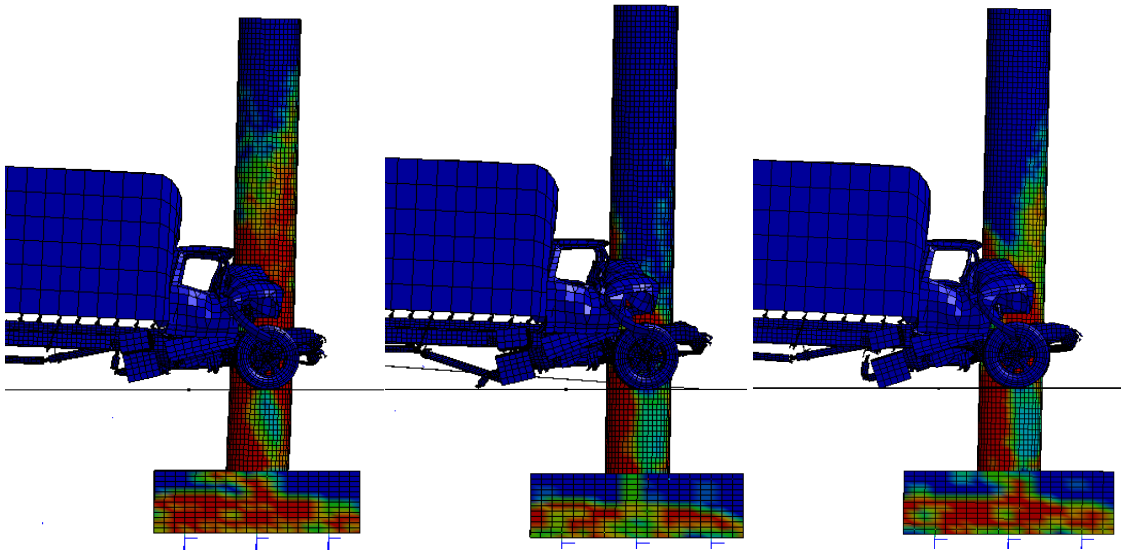

(p) F27 (q) F28 (r) F30

Figure 5-56 Effective plastic strain for the impact induced by F800 medium-weight truck

5.4 Tractor-trailer Truck

Table 5-6 Load cases for tractor-trailer truck

Case	V km/h	C_u kPa	Fy_c Mpa	D mm	L mm	Fy_s Mpa	L_I mm	K_r N mm/rad	K_h N/mm	M_c Ton	M_s Ton	P Mpa	S mm
T1	80	98.35	27.58	914.4	5486.4	413.7	1219.2	0	0	22.179	0	5	76.2

T1	40	-	-	-	-	-	-	-	-	-	-	-	-
T3	60	-	-	-	-	-	-	-	-	-	-	-	-
T4	100	-	-	-	-	-	-	-	-	-	-	-	-
T5	120	-	-	-	-	-	-	-	-	-	-	-	-
T6	-	24.61	-	-	-	-	-	-	-	-	-	-	-
T7	-	49.17	-	-	-	-	-	-	-	-	-	-	-
T8	-	-	41.37	-	-	-	-	-	-	-	-	-	-
T9	-	-	55.16	-	-	-	-	-	-	-	-	-	-
T10	-	-	-	762	-	-	-	-	-	-	-	-	-
T11	-	-	-	1066.8	-	-	-	-	-	-	-	-	-
T12	-	-	-	-	7315.2	-	-	-	-	-	-	-	-
T13	-	-	-	-	9144	-	-	-	-	-	-	-	-
T14	-	-	-	-	-	275.8	-	-	-	-	-	-	-
T15	-	-	-	-	-	551.6	-	-	-	-	-	-	-
T16	-	-	-	-	-	-	304.8	-	-	-	-	-	-
T17	-	-	-	-	-	-	2133.6	-	-	-	-	-	-
T18	-	-	-	-	-	-	-	2×10^{6}	-	-	-	-	-
T19	-	-	-	-	-	-	-	2×10^{12}	-	-	-	-	-
T20	-	-	-	-	-	-	-	-	1×10^{3}	-	-	-	-
T21	-	-	-	-	-	-	-	-	1×10^{5}	-	-	-	-
T22	-	-	-	-	-	-	-	-	-	0	-	-	-
T23	-	-	-	-	-	-	-	-	-	11.089	-	-	-
T25	-	-	-	-	-	-	-	-	-	-	335	-	-
T26	-	-	-	-	-	-	-	-	-	-	670	-	-
T27	-	-	-	-	-	-	-	-	-	-	-	0	-
T28	-	-	-	-	-	-	-	-	-	-	-	10	-
T30	-	-	-	-	-	-	-	-	-	-	-	-	152.4
T31	-	-	-	-	-	-	-	-	-	-	-	-	304.8

Note: "-" means that the value in this blank is the same as the value of base case F1

5.4.1 Impact Load

Compared with C2500 and F800, the tractor-trailer truck has much higher gross weight, which induces larger value of peak dynamic load and equivalent static load with same parameters.

For the impact force with respect to the vehicle speeds at 40km/h (24.9 Mph), 60km/h (37.3Mph), 80km/h (49.7Mph), 100km/h (62.1Mph), and 120km/h (74.6 Mph). As shown in Figure 5-57 and Figure 5-58, the impact force induced by tractor-trailer truck yields a much higher value at the same vehicle speed, compared with the impact force induced by F800 and C2500. The peak impact force ranges from 3.11×10^{3}kN to 1.76×10^{4}kN, while the equivalent static force ranges from 1.92×10^{3}kN to 3.52×10^{3}kN. A higher vehicle speed will lead to higher dynamic and equivalent static impact forces. There is no secondary impact, because the kinetic energy is dissipated before the cargo reach the pier when the speed not exceeding 80km/h. When over 80km/h, this high-speed value will lead to the shear failure of the pier before the secondary impact. Compared to the AASHTO design value of 2669kN (600kips) equivalent static force, the truck at 80km/h will result in the impact load close to the design value. With higher vehicle speed, the equivalent static impact load is much higher. With lower vehicle speed, the equivalent static impact load is smaller than the design value.

It is shown in Figure 5-61 and Figure 5-62 that peak dynamic force drops as the concrete strength of the pier increases. However, the equivalent static impact force shows insensitivity with the variation of the concrete strength.

For the variation of diameter, larger pier diameter will yield higher peak dynamic impact load as shown in Figure 5-63 and Figure 5-64. The equivalent static impact force shows insensitivity to the variation of pier diameter.

With higher impact location from the top of the pier footing, the peak dynamic value of the impact force obtains smaller results. The equivalent static impact force is not sensitive to this change, as shown in Figure 5-69 and Figure 5-70.

When the truck is fully loaded with 22.2ton cargo mass, the peak dynamic load is much larger compared with the case with no cargo mass. The equivalent static force also changes little with the variation of the cargo mass, as shown in Figure 5-75 and Figure 5-76.

The increase in the axial force at top of the pier will induce higher impact load. The equivalent static force also is not sensitive to the change of the axial force, which is depicted in Figure 5-79 and Figure 5-80.

It tells in Figures 5-59, 5-60, 5-65, 5-66, 5-67, 5-68, 5-71, 5-72, 5-73, 5-74, 5-77, 5-78, 5-81, and 5-82, both peak dynamic force and equivalent static force of the impact load show insensitivity to the following parameters: stiffness of the soil, length of the pier, yield strength of the steel reinforcement, the stiffness of spring at top of the pier, lumped mass at top of the pier, and the spacing of the hoop.

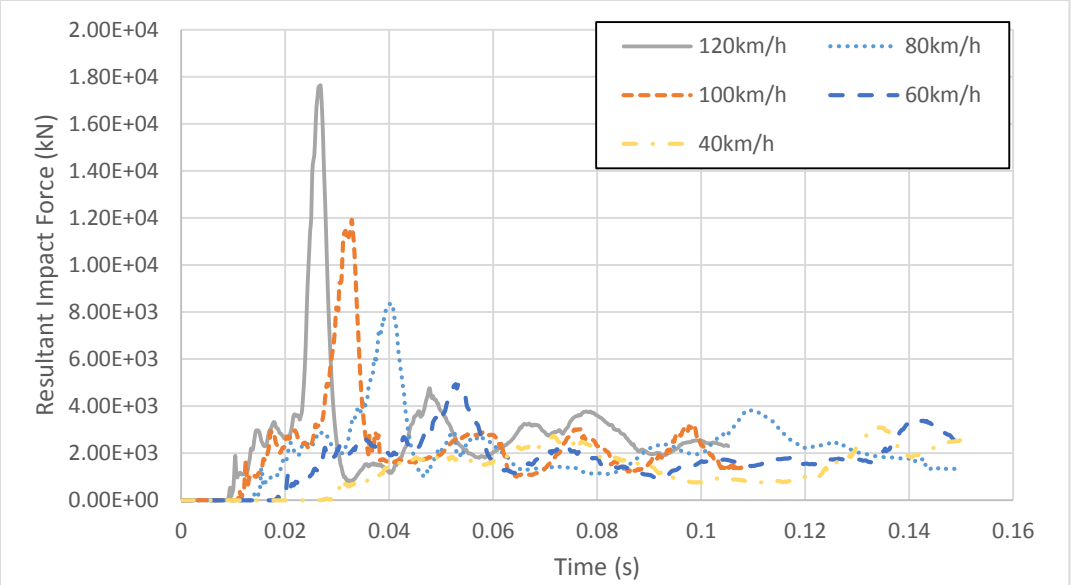

Figure 5-57 Time histories of impact forces with different vehicle speed

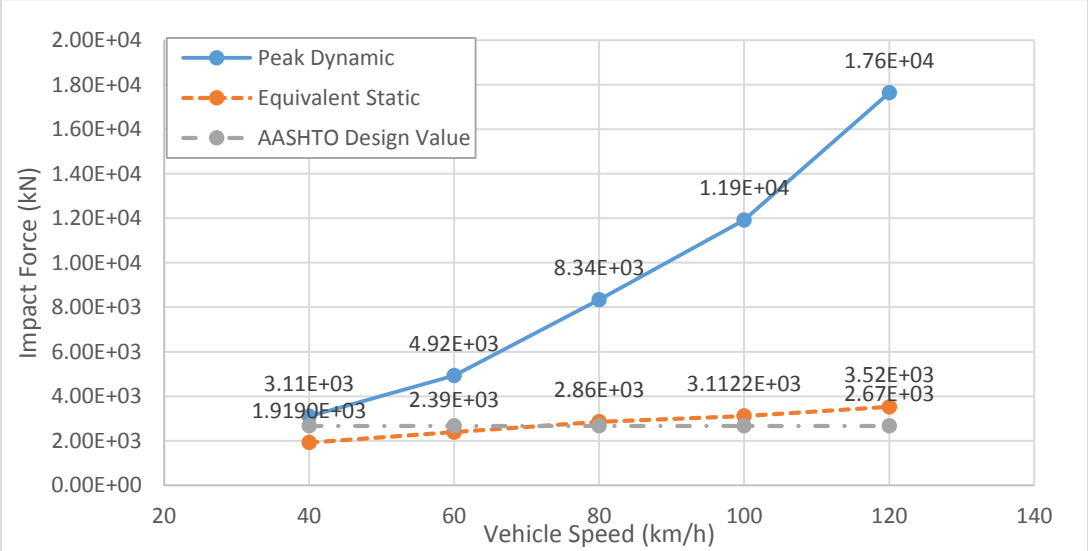

Figure 5-58 Peak dynamic forces and equivalent forces with different vehicle speed

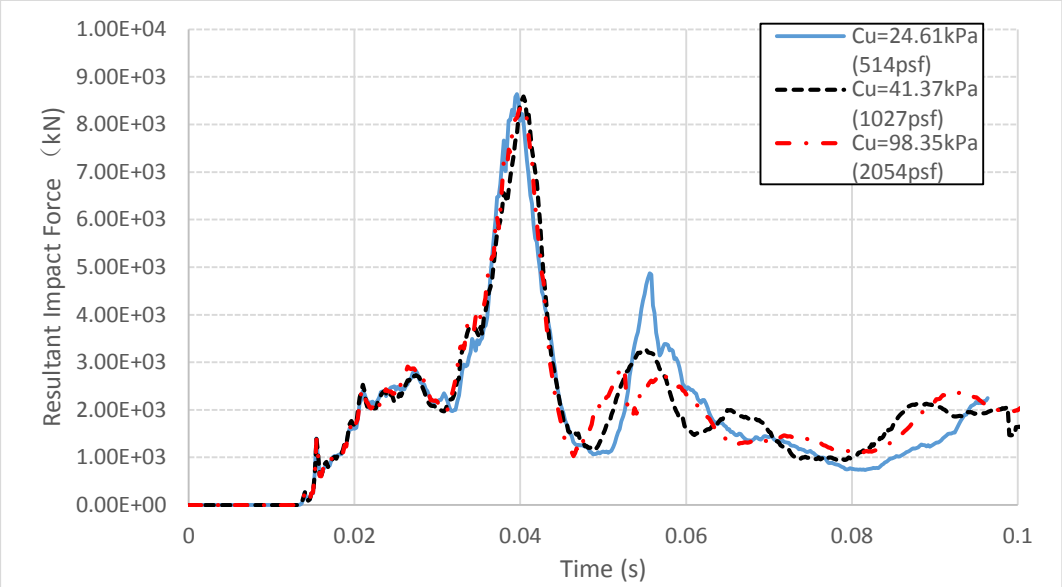

Figure 5-59 Time histories of impact forces with different soil stiffness

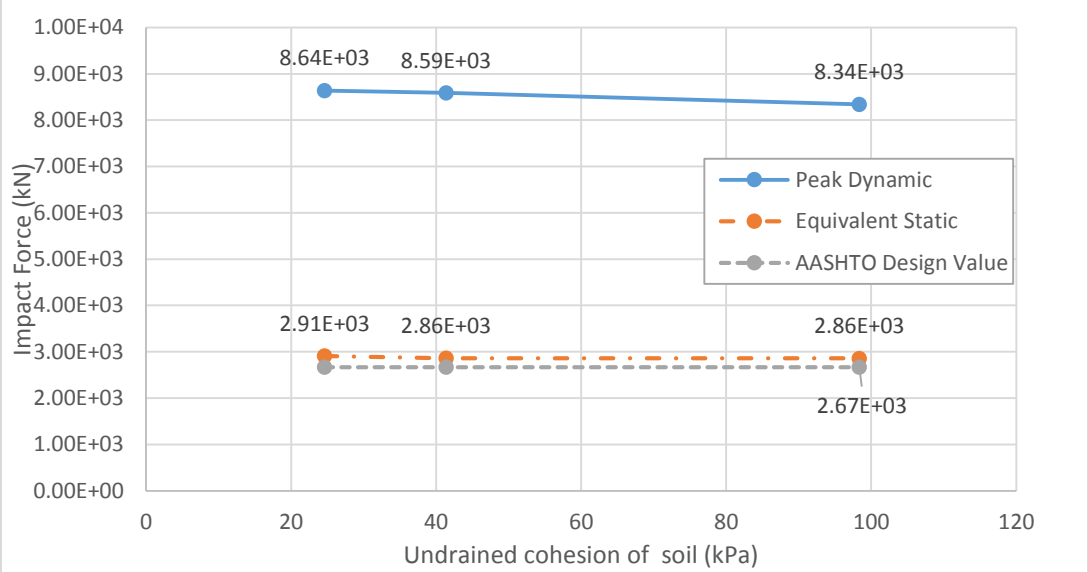

Figure 5-60 Peak dynamic forces and equivalent forces with different soil stiffness

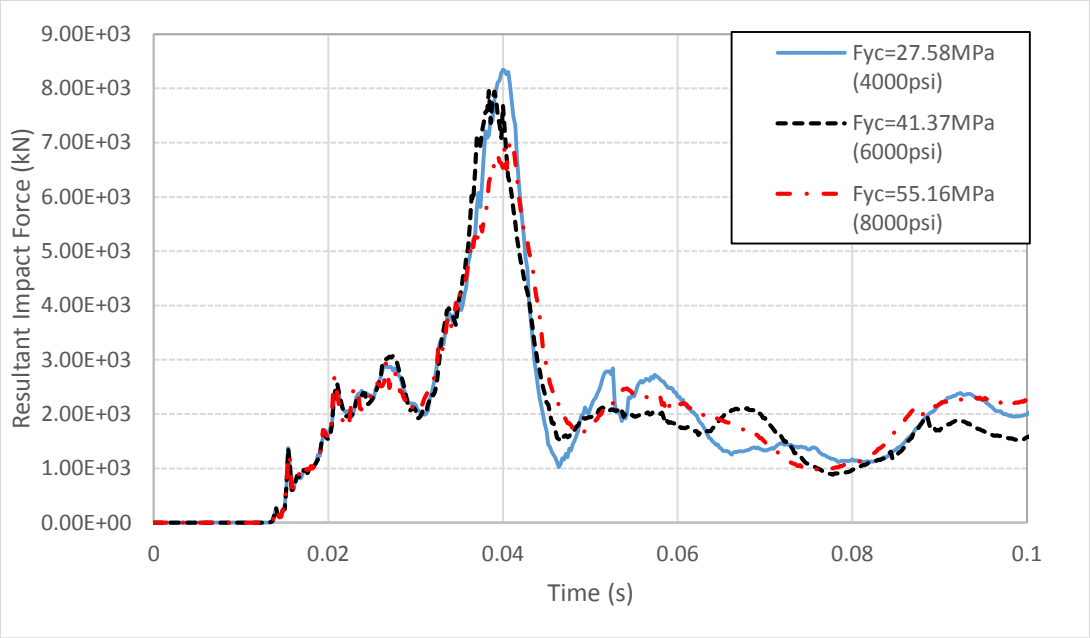

Figure 5-61 Time histories of impact forces with different concrete strength

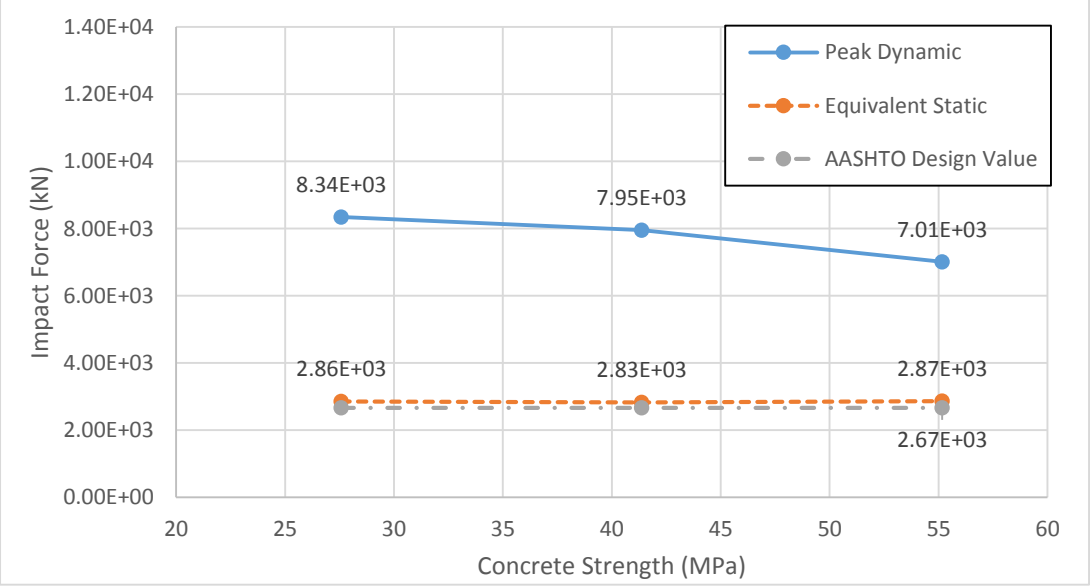

Figure 5-62 Peak dynamic forces and equivalent forces with different concrete strength

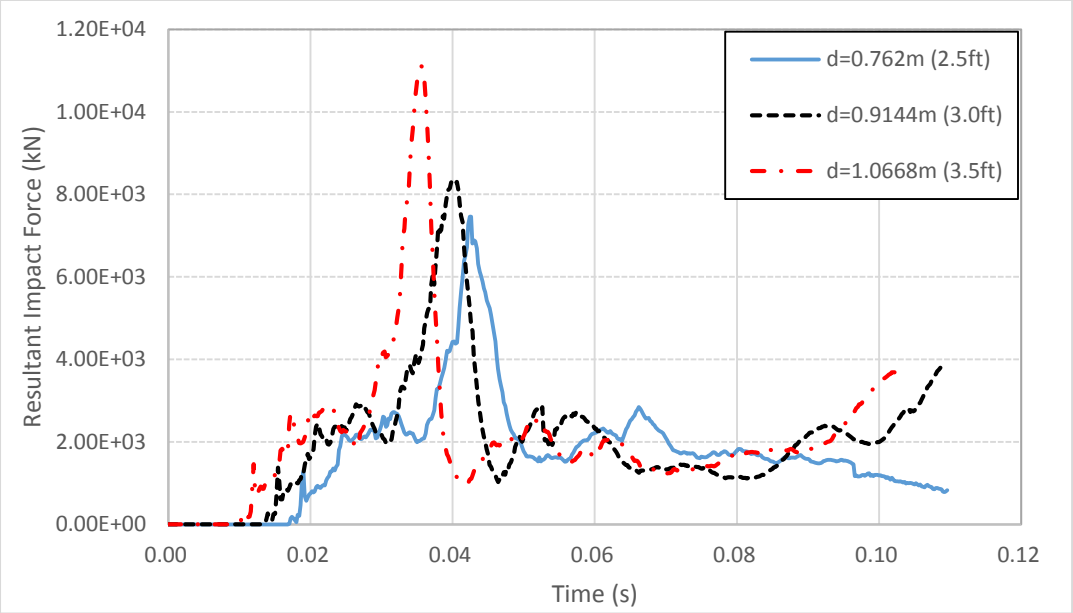

Figure 5-63 Time histories of impact forces with different pier diameter

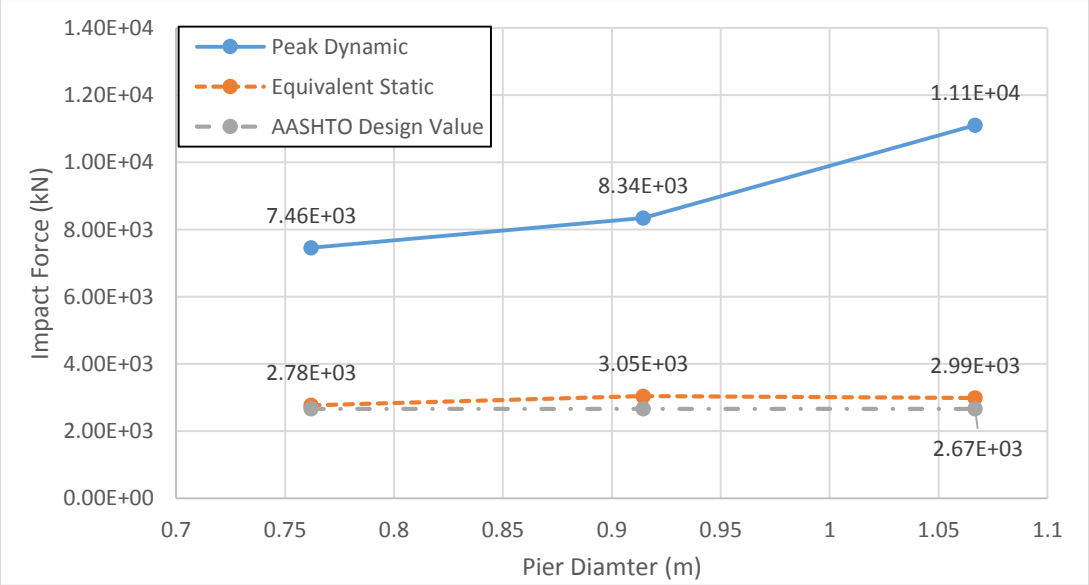

Figure 5-64 Peak dynamic forces and equivalent forces with different pier diameter

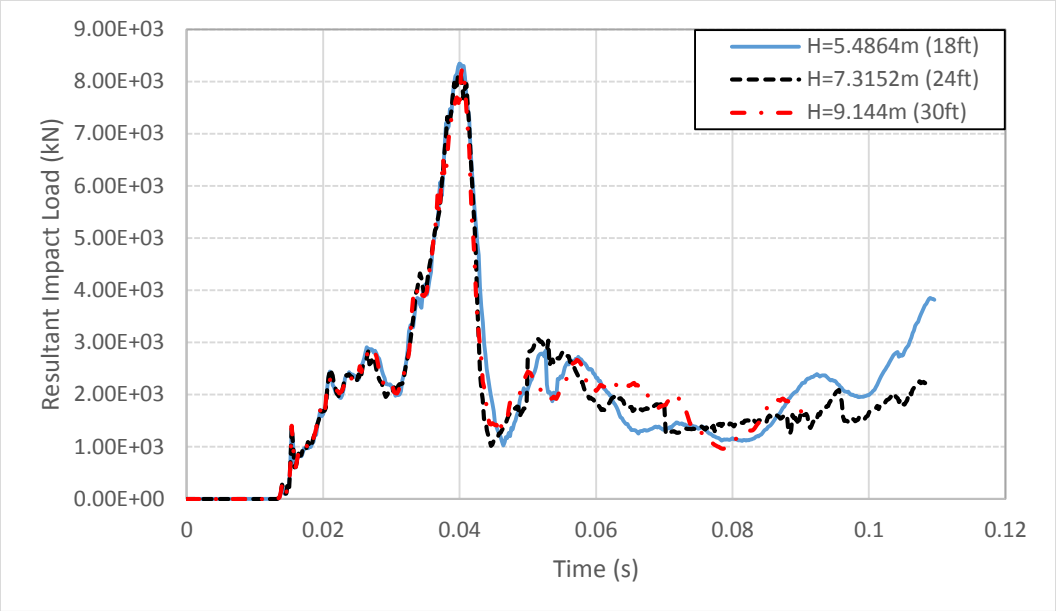

Figure 5-65 Time histories of impact forces with different pier length

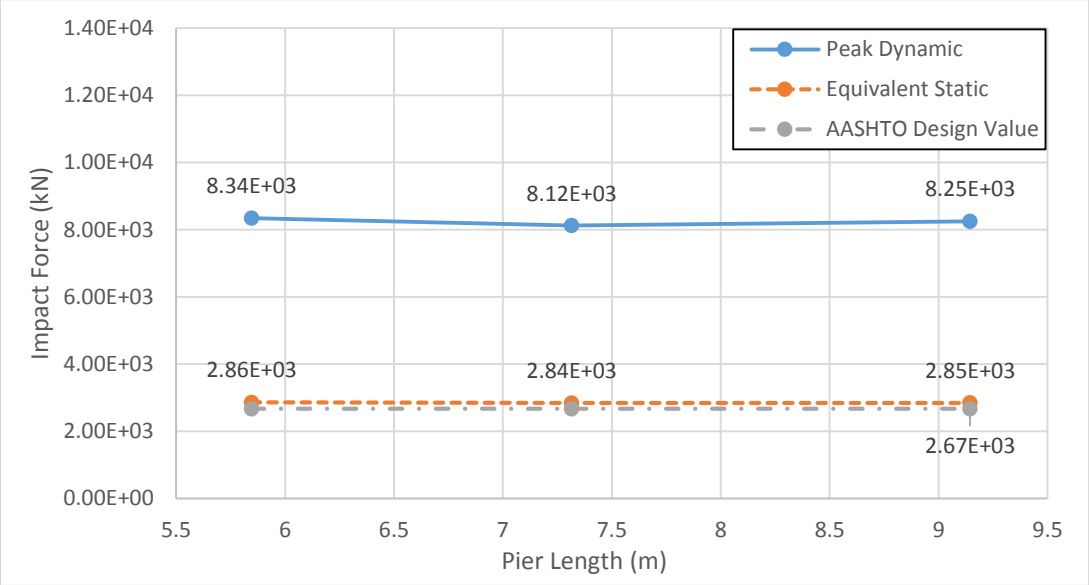

Figure 5-66 Peak dynamic forces and equivalent forces with different pier length

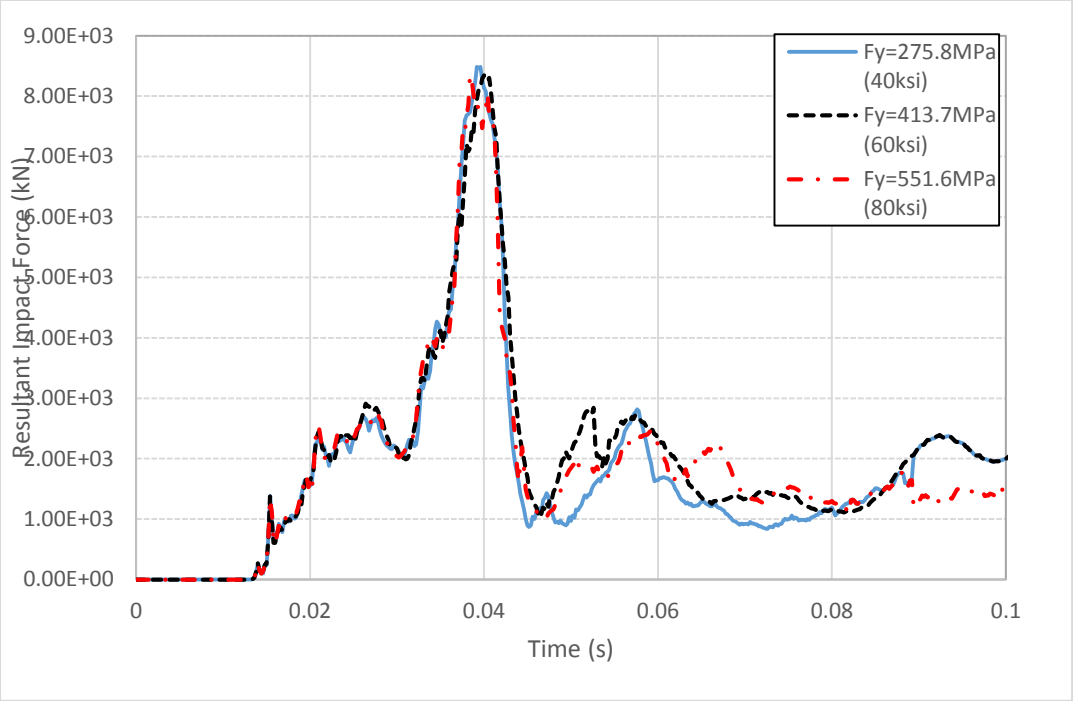

Figure 5-67 Time histories of impact forces with different steel rebar strength

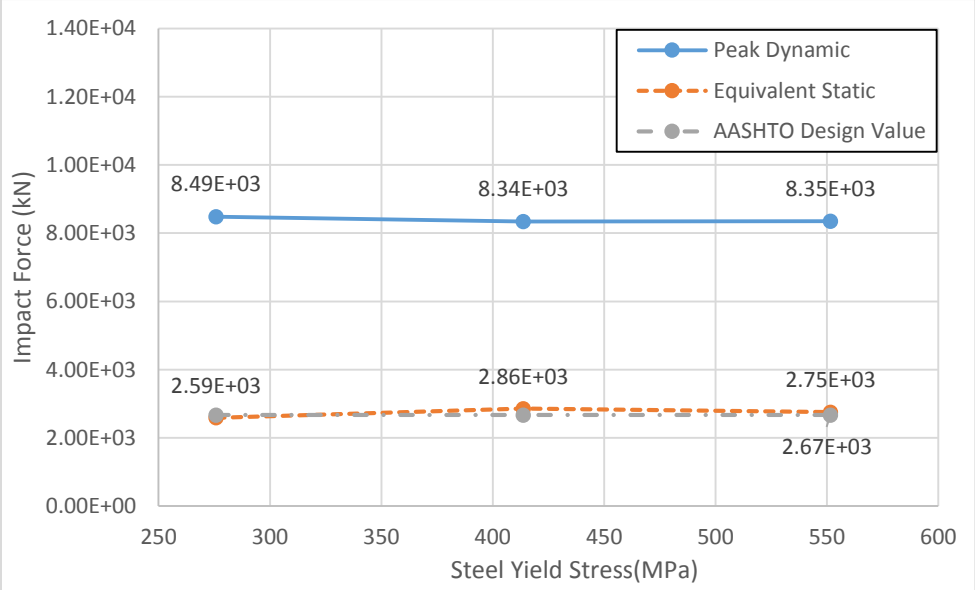

Figure 5-68 Peak dynamic forces and equivalent forces with different steel rebar strength

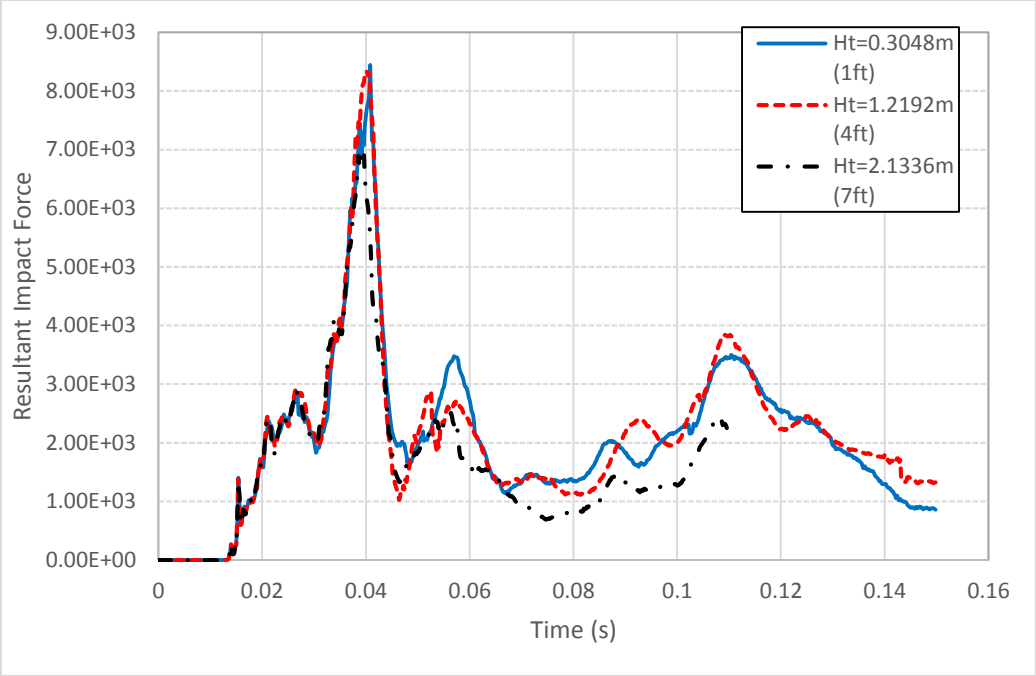

Figure 5-69 Time histories of impact forces with different impact height

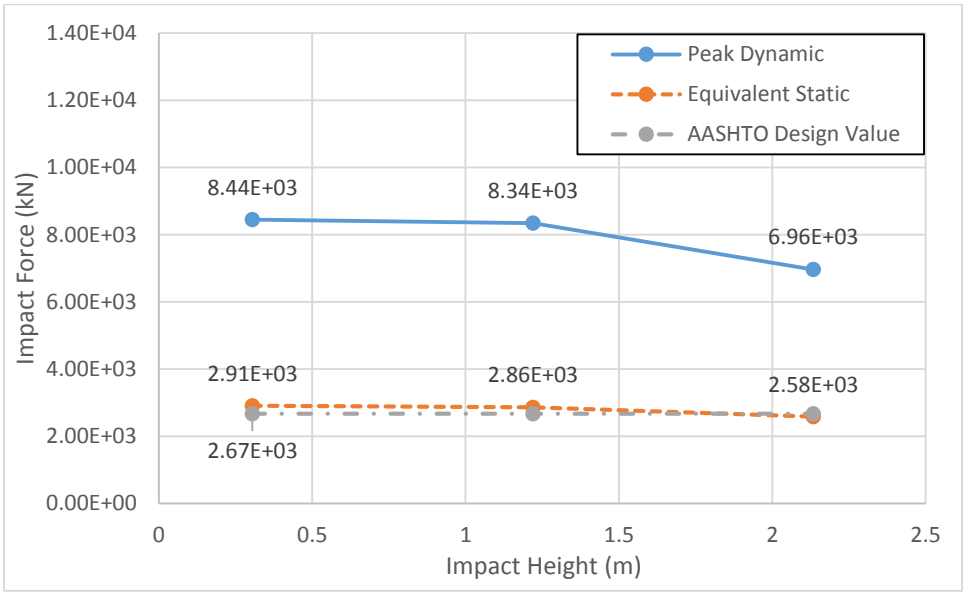

Figure 5-70 Peak dynamic forces and equivalent forces with different impact height

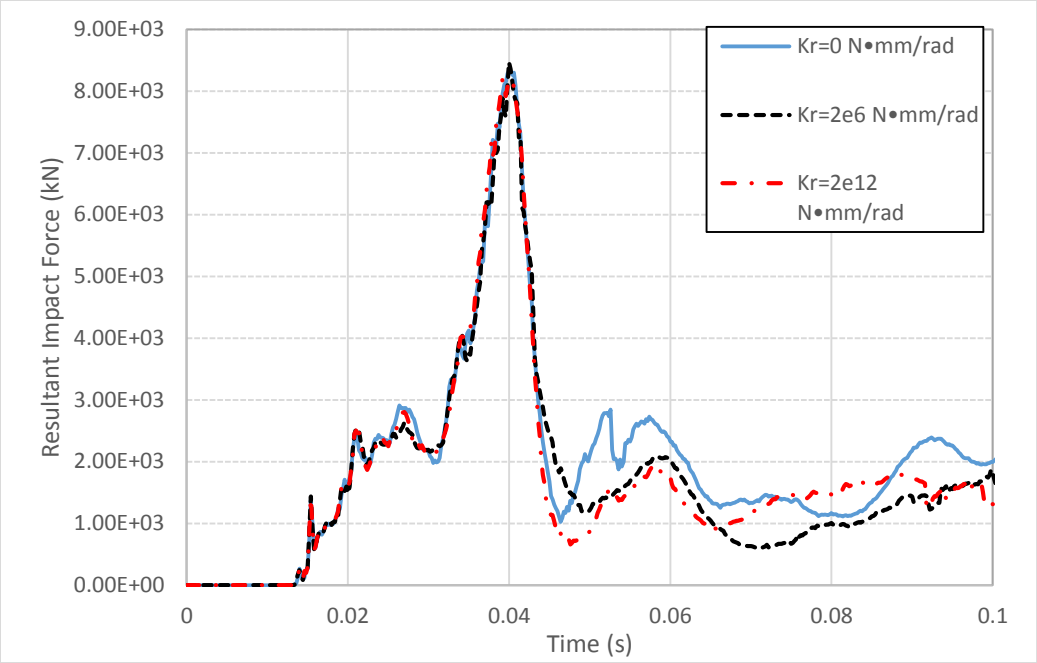

Figure 5-71 Time histories of impact forces with different rotational spring stiffness

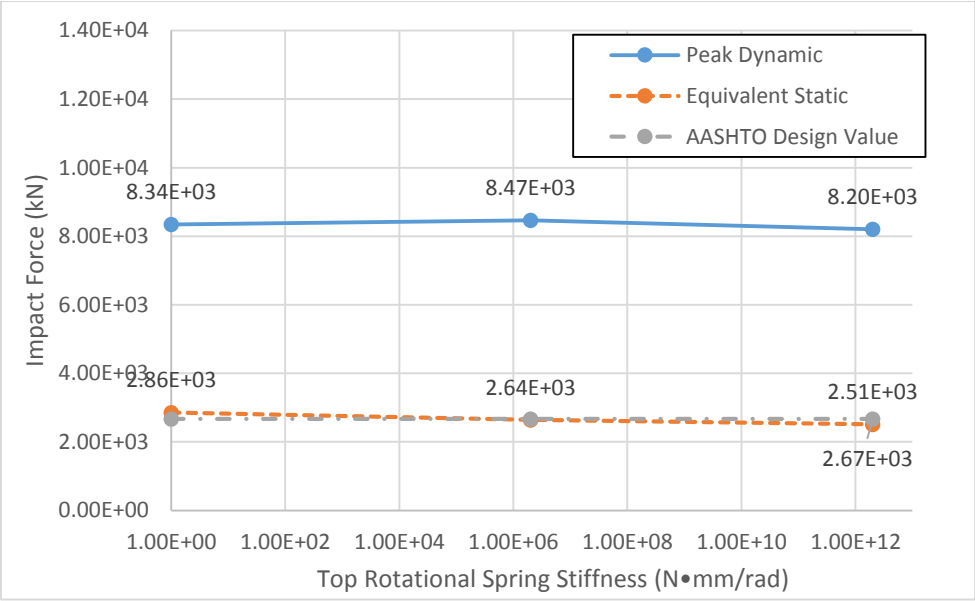

Figure 5-72 Peak dynamic forces and equivalent forces with different rotational spring stiffness

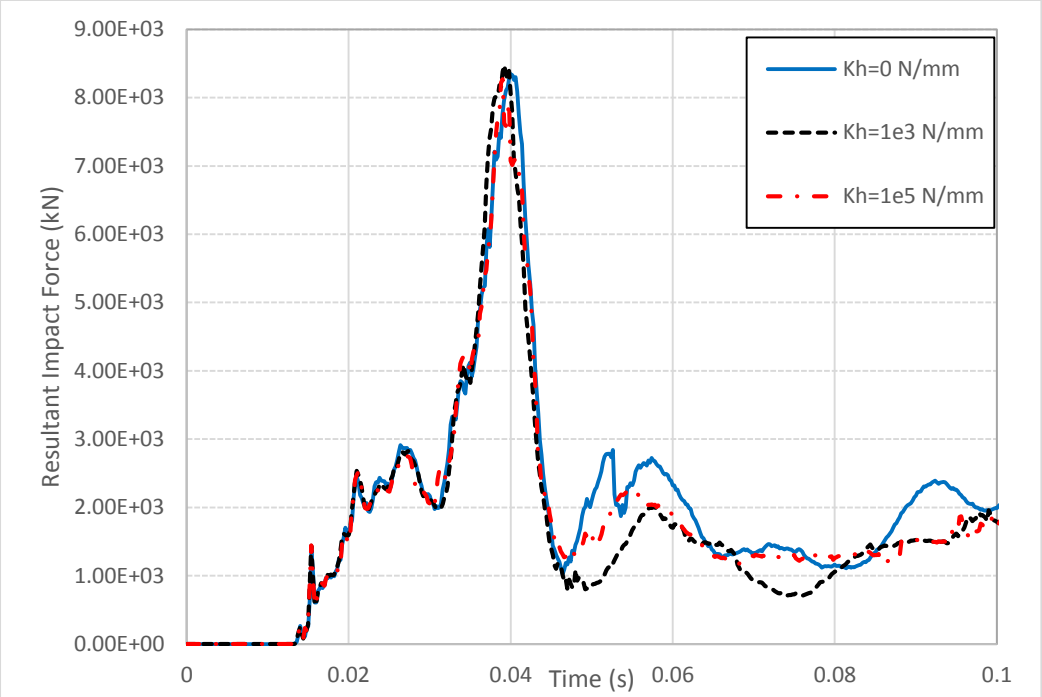

Figure 5-73 Time histories of impact forces with different translational spring stiffness

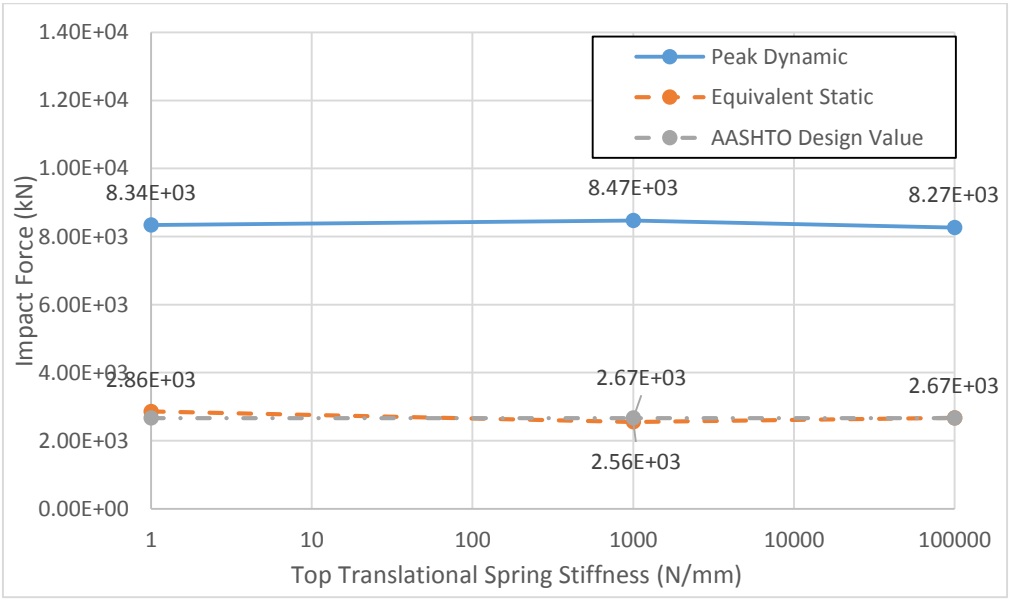

Figure 5-74 Peak dynamic forces and equivalent forces with different translational spring stiffness

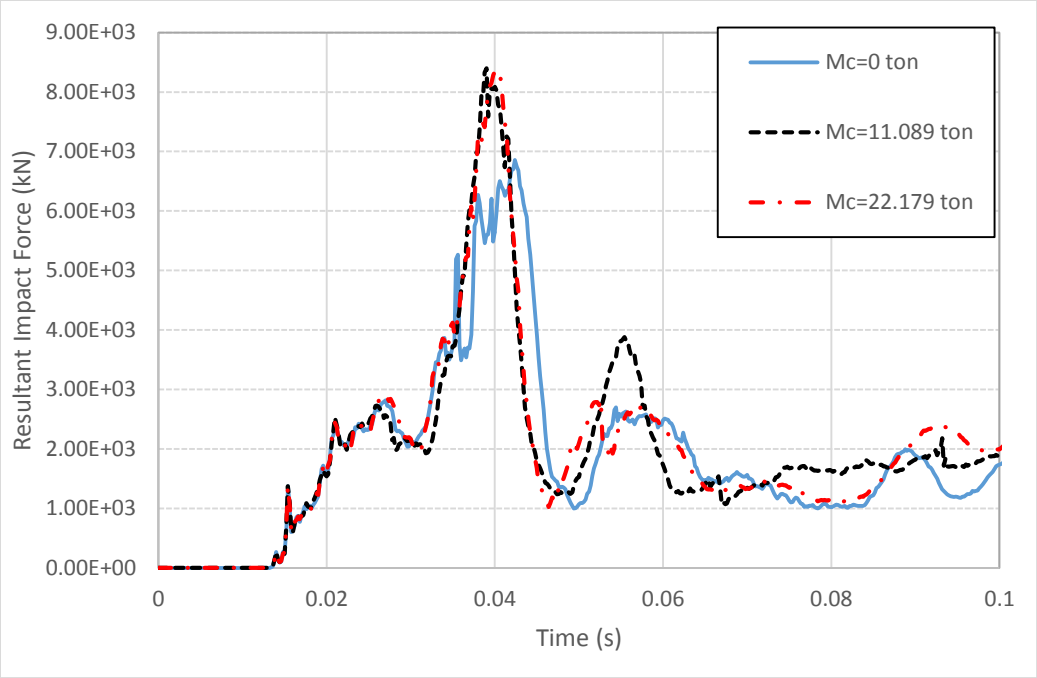

Figure 5-75 Time histories of impact forces with different cargo mass

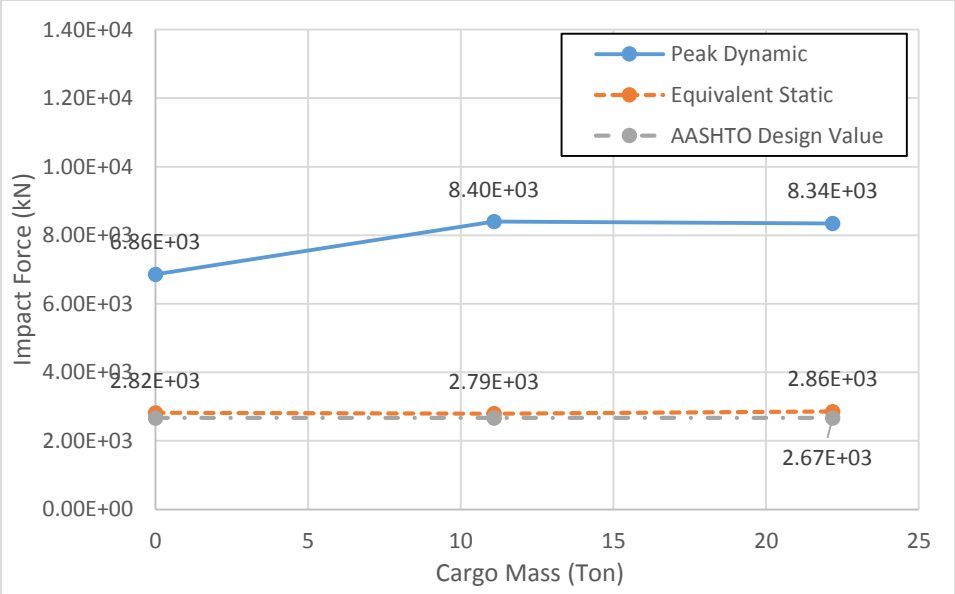

Figure 5-76 Peak dynamic forces and equivalent forces with different cargo mass

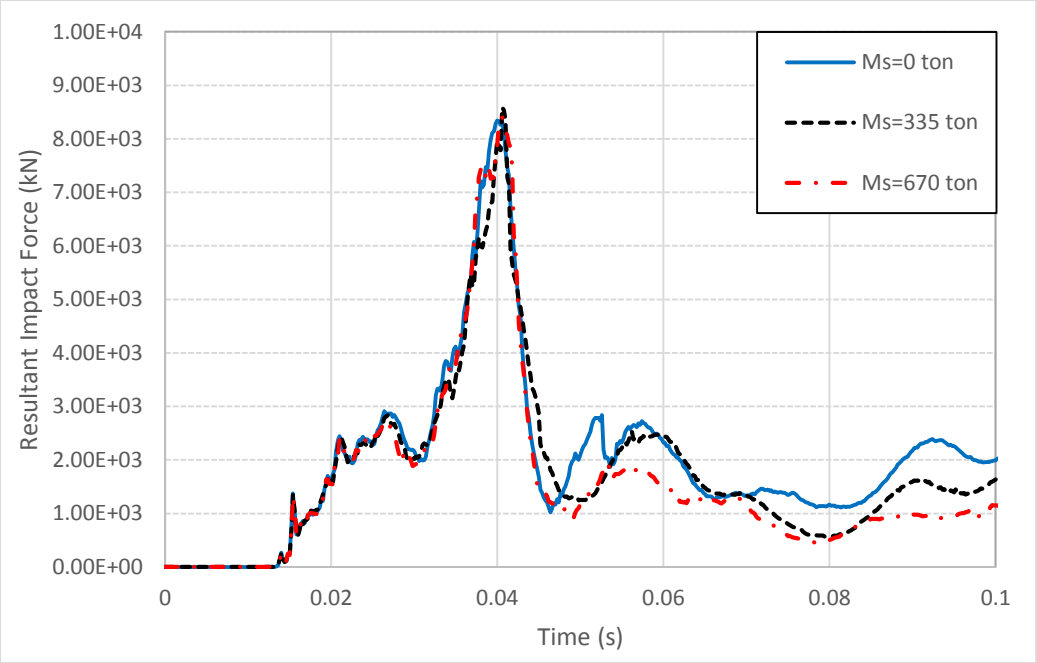

Figure 5-77 Time histories of impact forces with different top mass

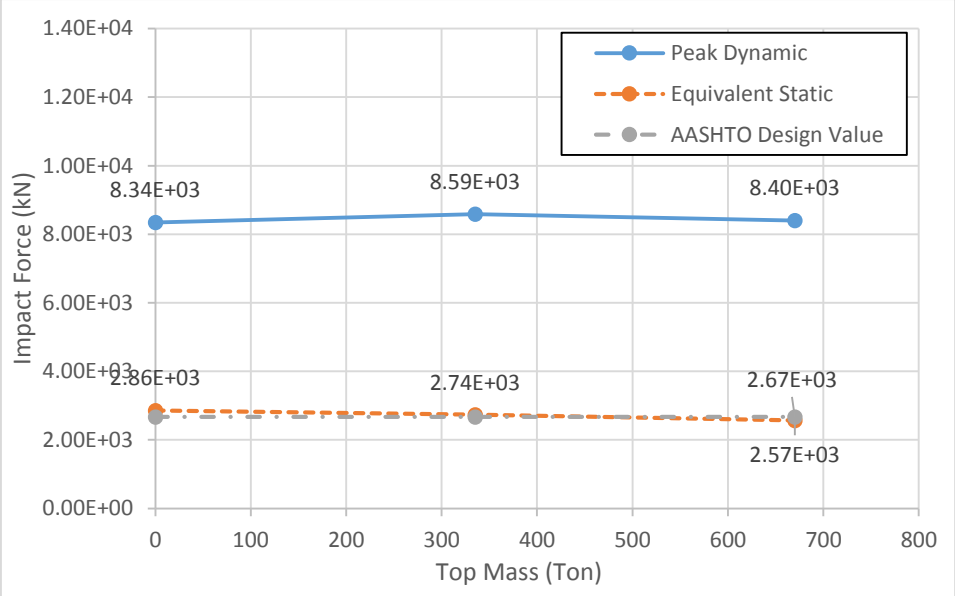

Figure 5-78 Peak dynamic forces and equivalent forces with different top mass

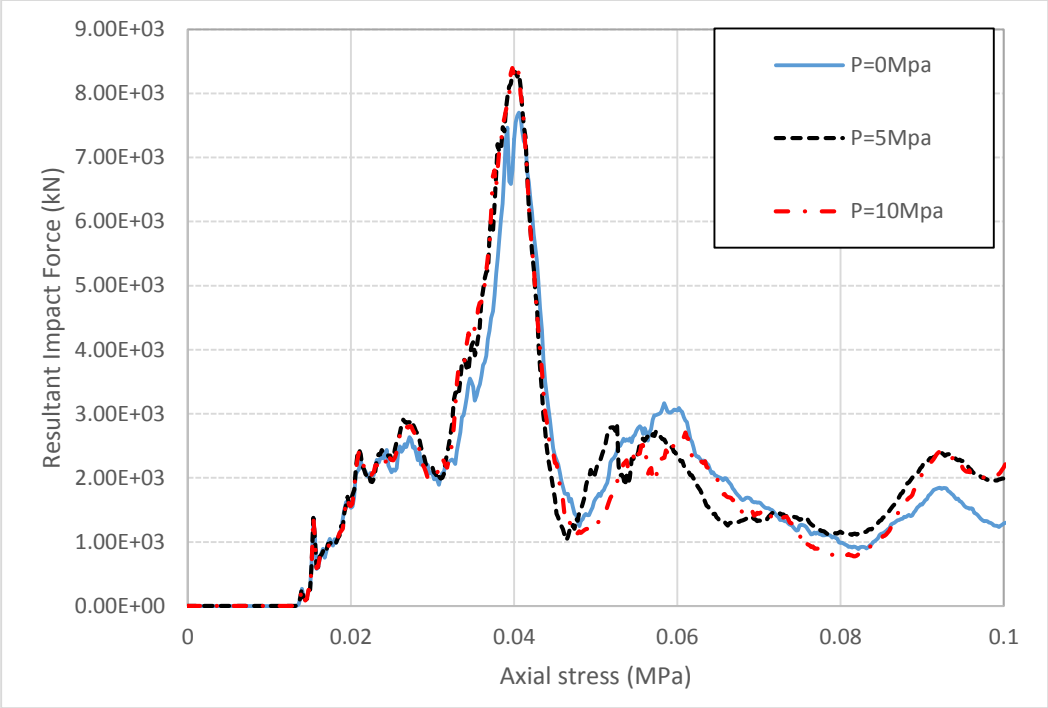

Figure 5-79 Time histories of impact forces with different axial stress

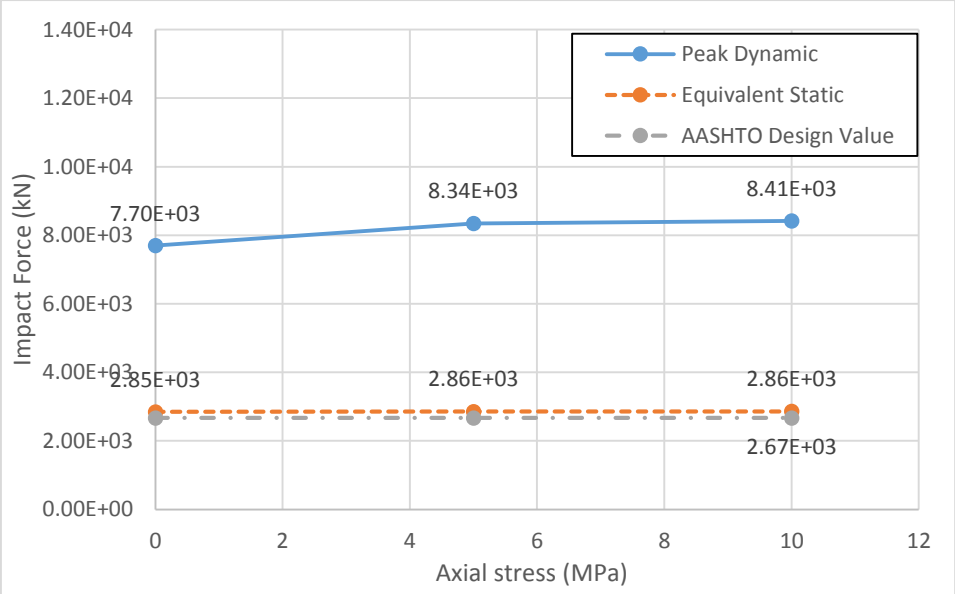

Figure 5-80 Peak dynamic forces and equivalent forces with different axial stress

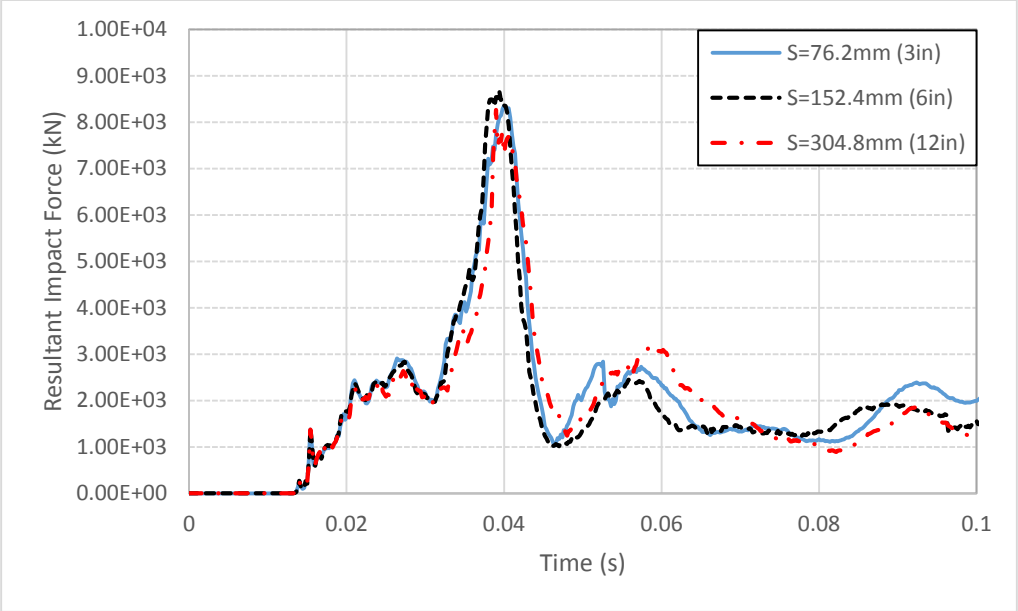

Figure 5-81 Time histories of impact forces with different tie spacing

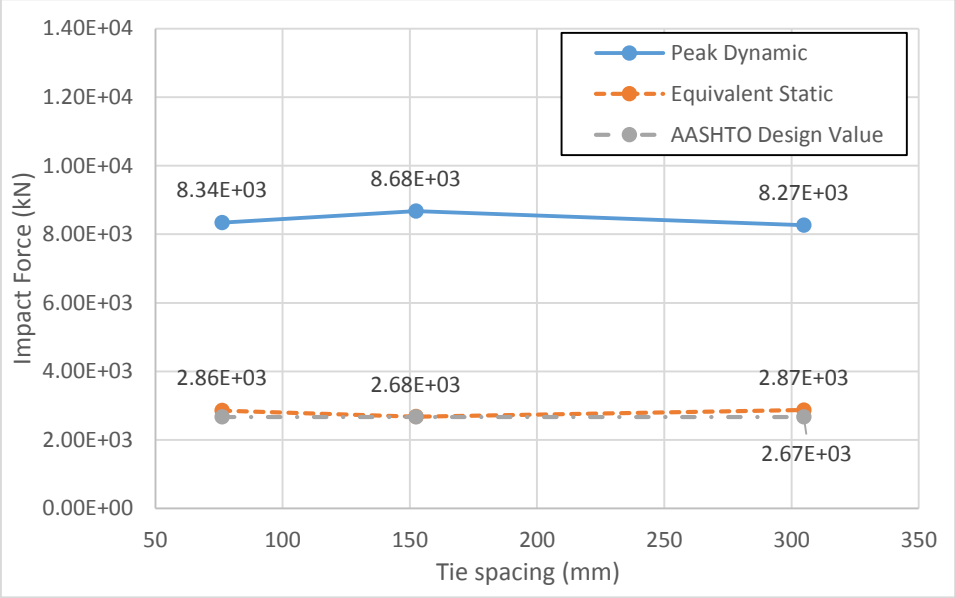

Figure 5-82 Peak dynamic forces and equivalent forces with different tie spacing

5.4.2 Failure mechanism

The failure mechanism is analyzed by the effective plastic strain. Compared with the load cases with the same parameters of C2500 and F800, the load case of tractor-trailer

truck may induce total failure for the pier as shown in Figure 5-83. Four failures mechanisms could be observed:

1. Local failure at the impact height;

2. Shear failure at the impact height within the 45 °range;

3. Bending failure at the foot of the pier;

4. Bending failure at the middle of the pier on the opposite face of the impact location.

Figure 5-83 (a) shows at the impact speed 80km/h, there will be bending failure at the impact height. For the impact speed at 40km/h as shown in Figure 5-83(b) there will be only local damage. However, when the speed increases up to 100km/h, the pier will collapse due to the shear failure, as shown in Figure 5-83 (c). Figures 5-83 (a) and (e) shows the higher grade of concrete can reduce both bending and shear failures at the impact height. Figures 5-83 (f) and (g) infer that larger section of the pier can prevent the shear failure. Furthermore, Figure 5-83(f) shows the small section pier with diameter 0.762m (2.5ft) could not resist the impact by medium-weight truck at 80km/h, which induces the shear failure and leads to the collapse of the pier. Figures 5-83 (a) and (h) show that taller pier will cause the shear failure for large impact load by heavy truck more easily. By comparing Figures 5-83 (a) and (i), it shows that incasing the strength of the steel reinforcement could prevent the shear failure. When the impact happened near the footing of the pier, the bending failure zone will be replaced by shear failure zone as shown in Figures 5-83 (j) and (k), while higher impact location will distribute the bending failure zone within longer length. When restraints are added at the top of the pier as shown in Figures 5-83 (a), (l) and (m), the bending failure zone will be redistributed. With the bending restraint in Figure 5-83 (l), there will be bending failure near the location of the

restraint. Figure 5-83 (m) shows the wider distribution of the bending failure zone at middle of the pier. Furthermore, the restraints at top of the pier will aggravate shear failure at the impact location. Figures 5-83 (n) shows for an empty tractor-truck, its induced damage is smaller. When there is larger mass from superstructure lumped at the top of the pier, near the top of the pier, there will also be bending failure zone. Besides, the failure at the impact height and the foot could be reduced, as shown in Figure 5-83 (o). By comparing Figures 5-83 (p) and (q), it refers that increase the prestressed top axial force, the bending failure would be reduced. Figure 5-83 (r) shows increasing the hoop spacing to 162.4 mm (6in) from 76.2mm (3in) will lead to the shear failure and collapse of the pier at the impact speed of 80km/h.

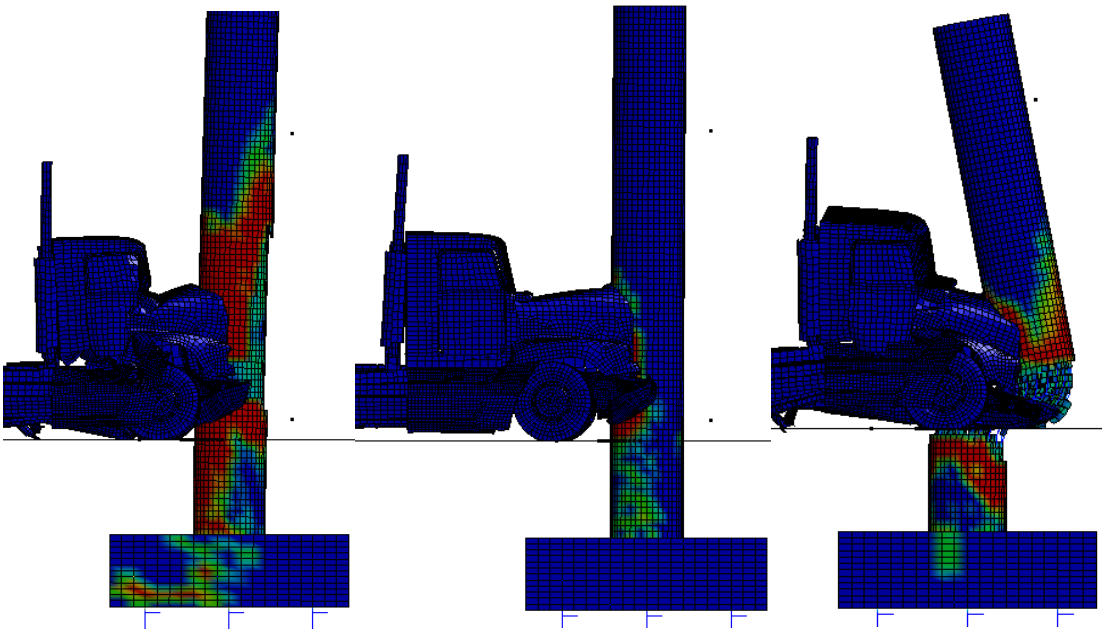

(a) T1 (b) T2 (c) T4

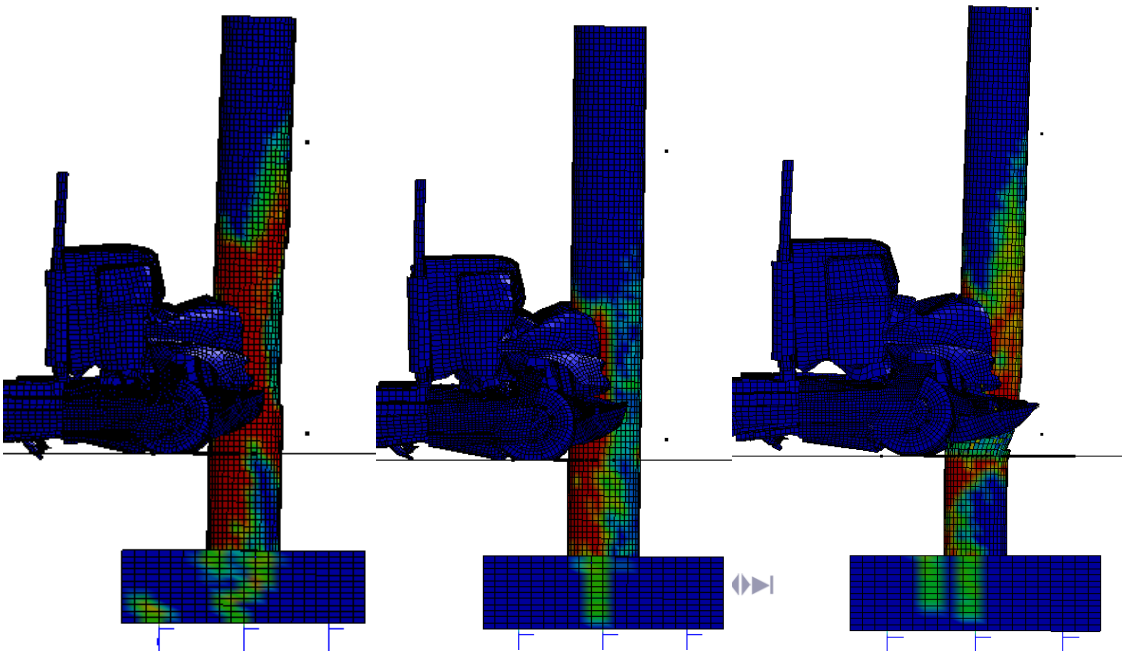

(d) T6 (e) T9 (f) T10

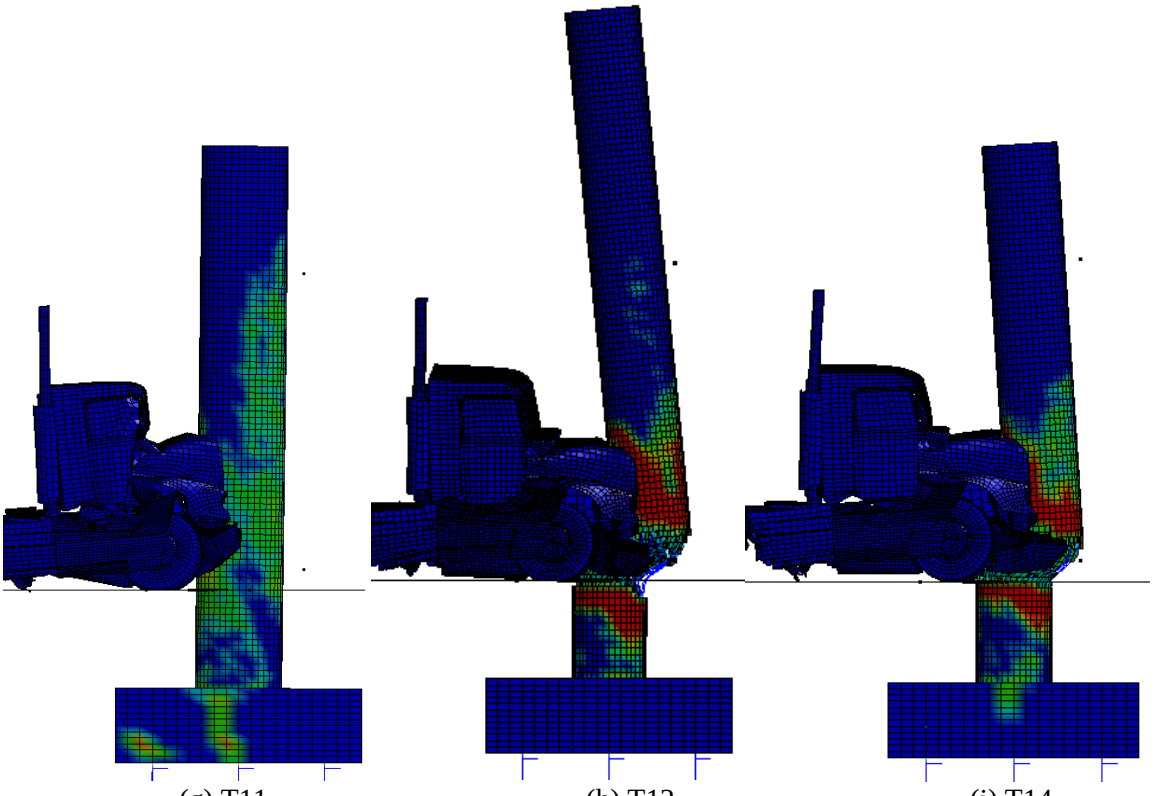

(g) T11 (h) T12 (i) T14

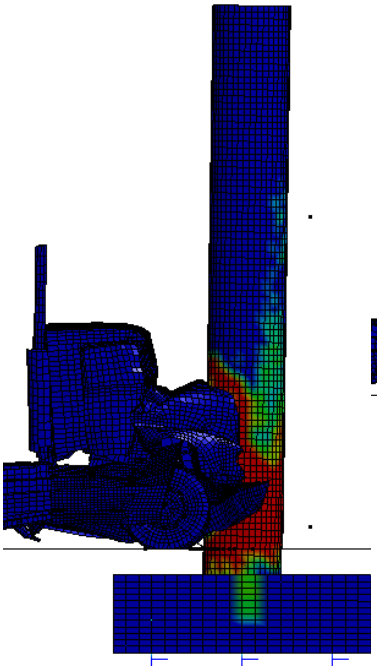

(j) T16

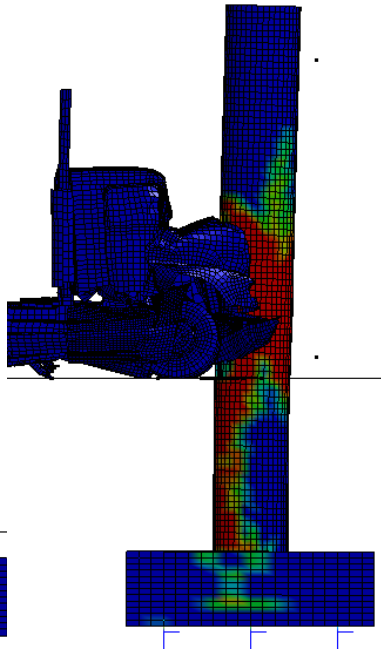

(k) T17

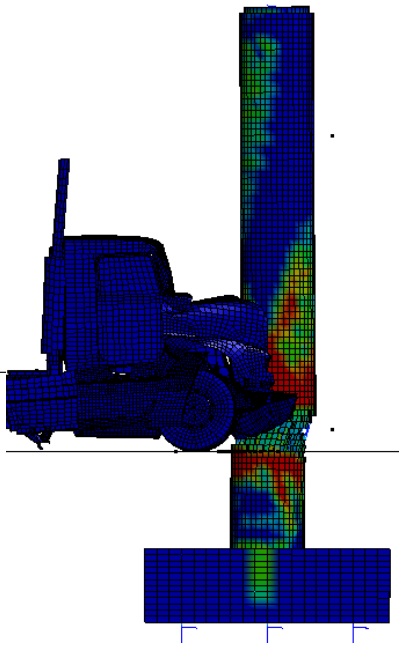

(l) T19

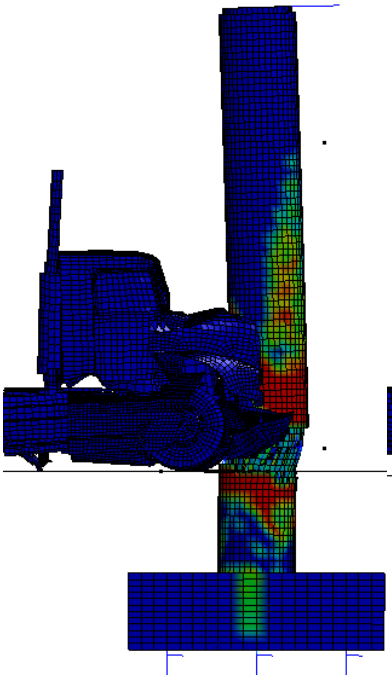

(m) T21

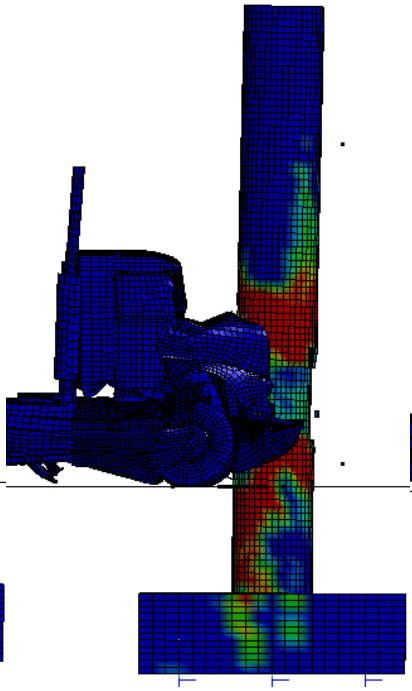

(n) T22

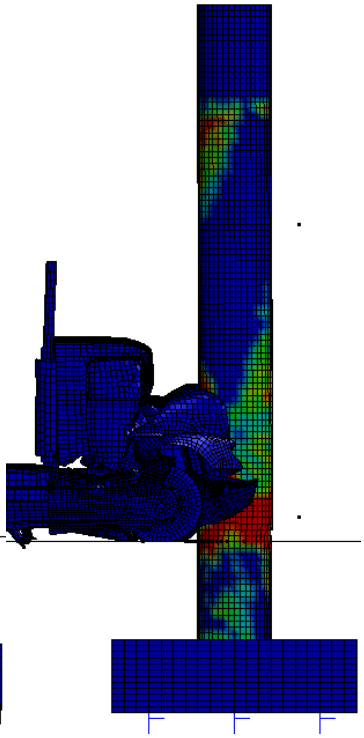

(o) T26

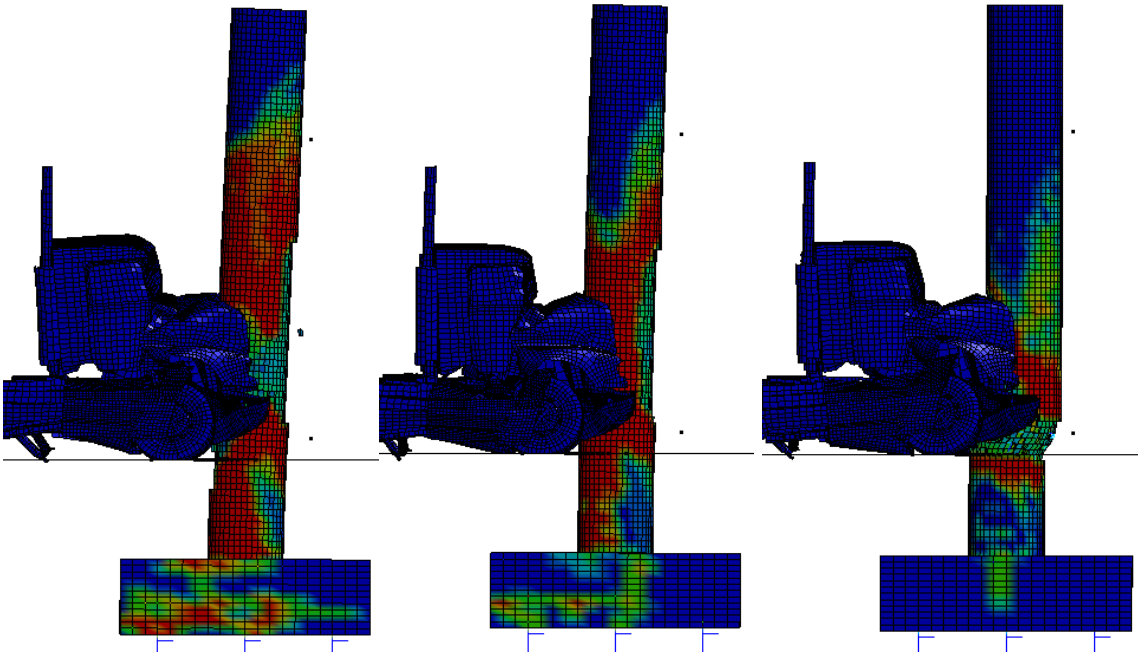

(p)T27 (q)T28 (r)T30

Figure 5-83 Effective plastic strain for the impact induced by tractor-trailer heavy-weight truck

5.5 Summary

This chapter discussed the variation of impact loads with different sets of parameters. Meanwhile, the failure mechanisms of the pier under different trucks' impact are also investigated. It is found that both dynamic peak impact load and equivalent static impact load are most sensitive to the vehicle velocity and type of the truck. The main parameters that the peak dynamic load is sensitive to include concrete strength, pier diameter, pier length, impact height, axial force, and cargo mass. The stiffness of soil springs, restraints and the lumped mass from superstructure have minor influence on the impact load. The steel strength and hoop spacing also affect the impact load little. For light weight truck induced impact, the AASHTO design impact value is conservative even at a high impact speed. For medium-weight truck induced impact, the impact load is close to the AASHTO design value at high impact speed, while smaller at lower speed. For the heavy weight truck,

its impact load exceeds the AASHTO design value when the impact speed is over 80km/h (48 mph). The impact load induced by the truck with the speed as high as 120km/h (72 mph) is much higher than the design value specified in the code, which will result in the insufficient extreme strength design.

For the failure mechanism, mainly four kinds need be taken into consideration: local failure under impact, bending failure at the footing, shear failure at the impact height, and bending failure at the middle of the pier. If the pier is restrained at the top, the bending failure at top of the pier requires attention as well. The most crucial failure is the shear failure at the impact height, which may lead to the collapse of the pier. The impact induced by tractor truck at or over 80km/h has strong possibility leading to the shear failure at the impact height. Increasing the concrete strength, pier diameter, steel strength, or reducing the steel hoop spacing is a way to control the failure. Larger axial force from superstructure can also reduce the failure to some extent. For Maryland standard, the pier section with diameter equal to or over 0.9144m (3ft) is much safer, while the small section with diameter 0.762m could not resist the impact even for medium-weight truck at the impact speed of 100km/h. To consider the pier safety under large impact load, it is necessary to reduce the hoop spacing to 76.2mm (3 in) at least at the impact height.

Chapter 6 Simplified load model for vehicle induced impact

Finite elemental analysis on vehicle-to-pier collision problem is complicated and needs case-by-case analysis for different bridge pier under different vehicle impact model, which raises the need for a simplified impact load calculation method for structural engineer to easily handle the impact load based on their need even without the help of the finite elemental software.

In this chapter, two simplified impact load methods will be discussed to show their feasibility in obtain the required impact loads with respect to different cases.

6.1 Simplified Mass-spring-pier Model

6.1.1 Assumptions of the Simplified Mass-spring-pier Model

Many researchers have already devoted themselves into the impact load model study by simplifying the impact coupling system into mass-spring model to obtain the approximate impact load with different impact objects and structures under impact. Fujikake et al. (2009) used a double-mass spring model to study the rigid impact between a hammer and a concrete beam. Samer et al. (2018) followed the Fujikake's study based on the explicit method, and obtained the response of concrete beam, of which the hysterical properties are also taken into consideration. Chen (2016) used a three-mass-spring model to represent the pier, truck engine, and the rest part of truck, which shows good simulation result.

Based on the study in Chapter 5, it is learned that the impact load shows little sensitivity to the boundary condition of the bridge pier. Therefore, following the previous study, the truck-bridge impact model may be simplified into a mass-spring-pier model as shown in Figure 6-1.

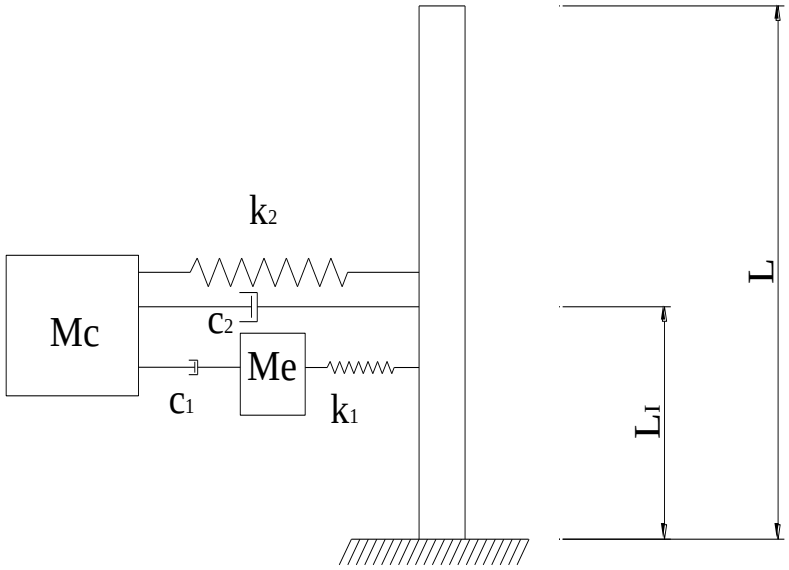

Figure 6-1 Simplified mass-spring-pier impact model

6.1.1.1 Vehicle model

M_e and M_c represent the engine and the rest of the vehicle respectively. The c_1 represent the damping between the engine and vehicle due to deformation and compression during the impact. The k_1 simplifies the impact between the engine and pier into the spring under compression to simulate the contact mechanism. Similarly, c_2 represent the damping between the rest part of the vehicle and pier due to plastic deformation and crush of the soft covering of vehicle during the impact. The k_2 simplifies the impact between the cargo mass and pier into a spring.

Because that engine block is very rigid compared with other parts of the vehicle and the pier, and this contact can be almost treated as rigid body crash into the bridge pier, which means an elastic spring between the engine and pier. And the spring only comes into effect after that the engine surface has crashed into the bridge pier surface. The force-

displacement of k_1 and k_2 could be represented as figure 6-2 (a), where x_e is the distance from the engine to the head of the vehicle, or the distance from the cargo mass to the head of the vehicle. According to the study in Chapter 5, it is known that only F800 with speed over 100MPh would yield secondary impact by cargo mass. Besides, the secondary impact load is lower than the primary impact load led by engine. Therefore, this study will focus on the primary rigid impact between the engine and the pier. The secondary impact by cargo mass with the spring stiffness k_2 will be ignored here.

Based on the parametric study in Chapter 5, the damping force induced by c_1 and c_2 will be simplified into the constant damping force as a friction damper if only there is relative movement and compression between two parts as shown in Figure 6-2 (b)

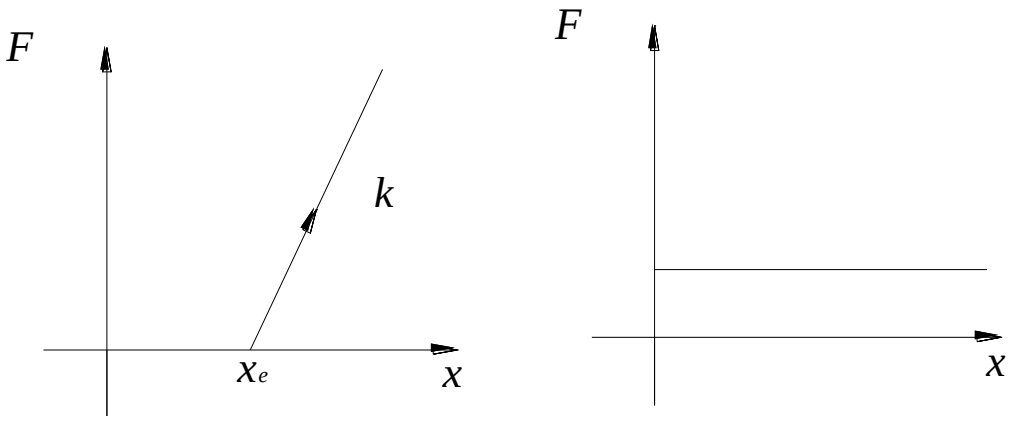

(a) Spring model (b) Damping model

Figure 6-2 Assumption of the spring and damping between the vehicle and the pier

1) C2500

According to the case study of C1 to C5 in Chapter 5, it is assumed that the constant damping force is equal to the equivalent static load of case C2

$$D_2 = 4.7820 \times 10^4 \text{ N} \qquad \text{Eq. 6-1}$$

The k_1 value can be obtained based on the linear regression of the impact-displacement diagram of the engine, as shown in Figure 6-3

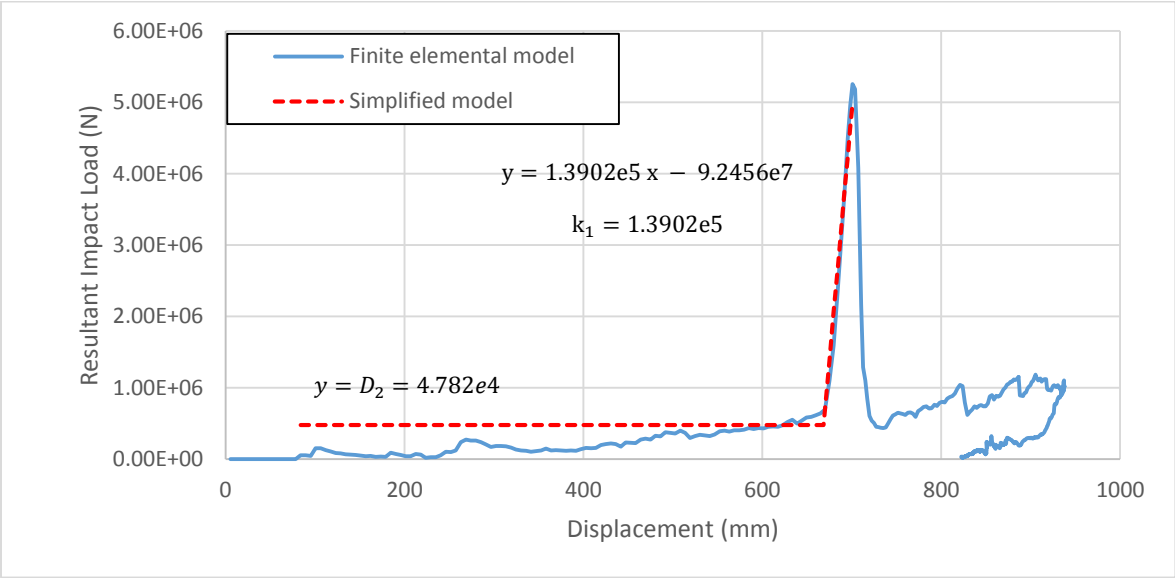

Figure 6-3 Resultant impact force respect to different engine displacement of F800

Based on the linear regression function of the impact -displacement diagram:

$$x_e = \frac{D_2 + 9.2456e7}{k_1} - 84 = 585mm \qquad \text{Eq. 6-2}$$

The constant damping force due to c_1 is obtained based on the theorem of momentum:

$$D_1 = \frac{M_e \Delta v}{\Delta t} = 4.26 \times 10^4 \ N \qquad \text{Eq. 6-3}$$

Where the M_e is the dry mass of the engine with 0.307 ton; $\Delta v = 0.29 \times 10^4 mm$; $\Delta t = 0.0212s$.

2) F800

According to the case study of F1 to F5 in Chapter 5, it is known that there is no obvious rigid impact load for the case F2 with the initial velocity 60km/h. Therefore, it is

assumed that the constant damping force resulted from c_2 is equal to the equivalent static load of case F2.

$$D_2 = 1.3423 \times 10^{6}\ \text{N} \qquad \text{Eq. 6.4}$$

The k_1 value can be obtained based on the linear regression of the impact-displacement diagram of the engine, as shown in Figure 6-4.

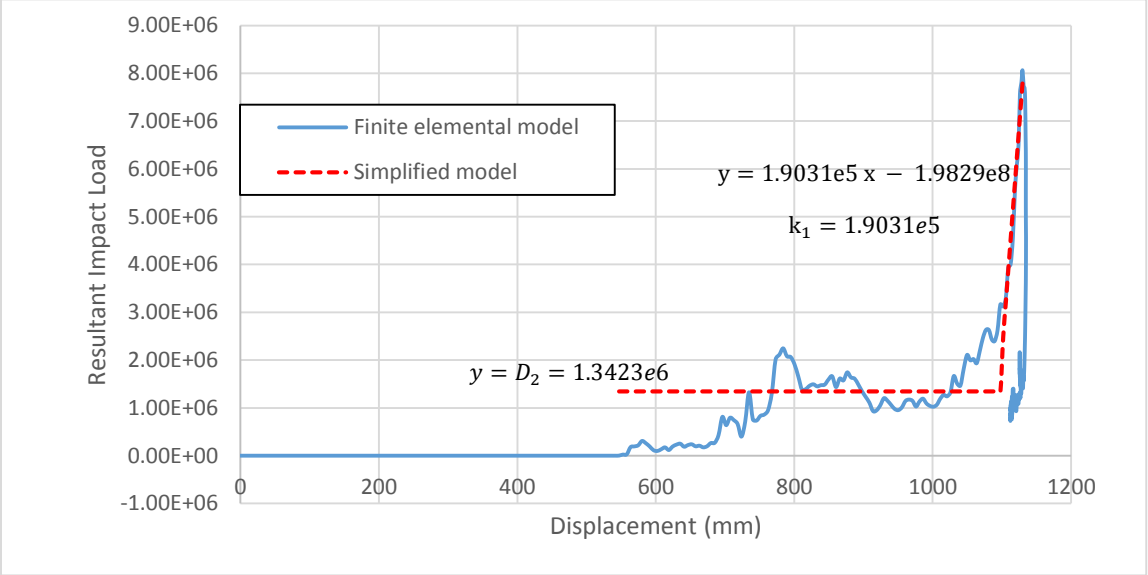

Figure 6-4 Resultant impact force respect to different engine displacement of F800

Based on the linear regression function of the impact -displacement diagram:

$$x_e = \frac{D_2 + 1.9851\text{e}8}{\text{k}_1} - 556 = 493\text{mm} \qquad \text{Eq. 6.5}$$

The constant damping force due to c_1 is obtained based on the theorem of momentum:

$$D_1 = \frac{M_e \Delta v}{\Delta t} = 2.43 \times 10^{5}\ \text{N} \qquad \text{Eq. 6.6}$$

Where the M_e is the dry mass of the engine with 0.59 ton; $\Delta v = 0.72 \times 10^{4} mm$; $\Delta t = 0.0174 s$.

3) Tractor-trailer

According to the case study of T1 to T5 in Chapter 5, it is known that there is no obvious rigid impact load for the case T2 with the initial velocity 40km/h. Therefore, it is assumed that the constant damping force resulted from c_2 is equal to the equivalent static load of case F2

$$D_2 = 1.9190 \times 10^{6}\ \text{N} \qquad \text{Eq. 6.7}$$

The k_1 value can be obtained based on the linear regression of the impact-displacement diagram of the engine, as shown in Figure 6-5.

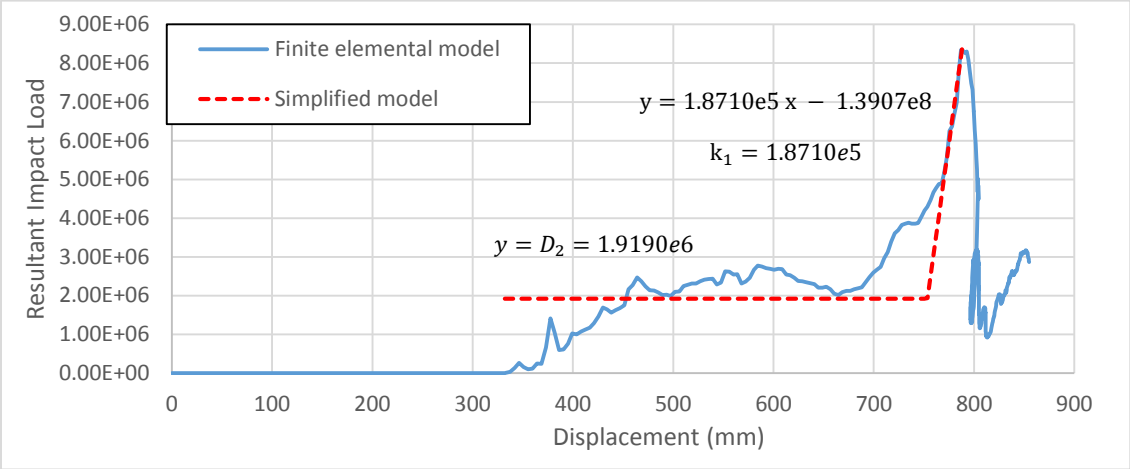

Figure 6-5 Resultant impact force respect to different engine displacement of Tractor-trailer truck

Based on the linear regression function of the impact -displacement diagram:

$$x_e = \frac{D_2 + 1.3907\text{e}8}{\text{k}_1} - 332 = 422\text{mm} \qquad \text{Eq. 6.8}$$

The constant damping force due to c_1 is obtained based on the theorem of momentum:

$$D_1 = \frac{M_e \Delta v}{\Delta t} = 3.53 \times 10^{5}\ \text{N} \qquad \text{Eq. 6.9}$$

Where the M_e is the dry mass of the engine with 1.287 ton; $\Delta v = 0.625 \times 10^{4} mm$; $\Delta t = 0.0228 s$.

6.1.1.2 Pier model

To perform the analysis of the pier, the pier is also transformed into a linear SDOF mass-spring system based on Rayleigh-Ritz method according to the Chopra (2000):

$$M_P = \bar{m} \int \varphi(y)^2 \, dx \qquad \text{Eq. 6.10}$$

Where M_P is the equivalent mass of the pier; $\bar{m}$ is the mass per unit length of the pier; $\varphi(y)$ is assumed as the static deflection shape divided by the deflection at the nominal impact height under unit load.

For the pier fixed on one end, based on the linear elastic theory, the relation between the deflection and curvature at the impact height can be given as:

$$EI\phi_I = M_I \qquad \text{Eq. 6.11}$$

$$\delta_I = \frac{P_I {L_I}^3}{3EI} = \frac{M_I {L_I}^2}{3EI} \qquad \text{Eq. 6.12}$$

$$\phi_I = \frac{3}{{L_I}^2}\delta_I \qquad \text{Eq. 6.13}$$

Where the ϕ_I is the curvature of the beam at the impact height; δ_I is the deflection at the impact height; M_I is the moment at the impact height; L_I is the impact height.

(1) Concrete model

Mander model (Mander, 1988) is assumed here to describe the constitutive model of the concrete. The tensile stress of concrete is ignore. The stress f_c of confined concrete respected to strain ε_c can be calculated as:

$$f_c = \frac{{f_{cc}}' xr}{r - 1 + x^r} \qquad \text{Eq. 6.14}$$

$$x = \frac{\varepsilon_c}{\varepsilon_{cc}} \qquad \text{Eq. 6.15}$$

$$\varepsilon_{cc} = \varepsilon_{co}\left[1 + 5\left(\frac{f_{cc}{}'}{f_{co}{}'} - 1\right)\right] \quad \text{Eq. 6.16}$$

$$r = \frac{E_c}{E_c - E_{sec}} \quad \text{Eq. 6.17}$$

$$E_c = 5000\sqrt{f_{co}{}'}\text{MPa} \quad \text{Eq. 6.18}$$

$$E_{sec} = \frac{f_{cc}{}'}{\varepsilon_{cc}} \quad \text{Eq. 6.19}$$

$$f_{cc}{}' = f_{co}{}'\left(-1.254 + 2.254\sqrt{1 + \frac{7.94f_l{}'}{f_{co}{}'}} - 2\frac{f_l{}'}{f_{co}{}'}\right) \quad \text{Eq. 6.20}$$

$$f_l{}' = \frac{1}{2}k_e\rho_s f_{yh} \quad \text{Eq. 6.21}$$

$$k_e = \frac{\left(1 - \frac{s'}{2d_s}\right)^2}{1 - \rho_{cc}} \quad \text{Eq. 6.22}$$

$$\rho_s = \frac{4A_{sp}}{d_s s} \quad \text{Eq. 6.23}$$

Where $f_{cc}{}'$ and $f_{co}{}'$ are the strength of confined concrete and unconfined concrete respectively; s' is the clear spacing of circular hoop; s is the spacing of the circular hoop; A_{sp} is the area of hoop section; d_s is the diameter of the hoop enclosed area (core section); ρ_{cc} is the ratio of area of longitudinal reinforcement to the area of core section.

Due to dynamic analysis, the unloading branches for the Mander model is also required:

$$f_c = f_{un} - \frac{f_{un}xr}{r - 1 + x^r} \quad \text{Eq. 6.24}$$

$$r = \frac{E_u}{E_u - E_{sec}} \quad \text{Eq. 6.25}$$

$$E_{sec} = \frac{f_{un}}{\varepsilon_{un} - \varepsilon_{pl}} \quad \text{Eq. 6.26}$$

$$x = \frac{\varepsilon_c - \varepsilon_{un}}{\varepsilon_{pl} - \varepsilon_{un}} \quad \text{Eq. 6.27}$$

$$\varepsilon_{pl} = \varepsilon_{un} - \frac{(\varepsilon_{un} + \varepsilon_a) f_{un}}{(f_{un} + E_c \varepsilon_a)} \quad \text{Eq. 6.28}$$

$$\varepsilon_a = a\sqrt{\varepsilon_{un}\varepsilon_{cc}} \quad \text{Eq. 6.29}$$

$$a = \max\left(\frac{\varepsilon_{cc}}{\varepsilon_{cc} + \varepsilon_{un}}, \frac{0.09\varepsilon_{un}}{\varepsilon_{cc}}\right) \quad \text{Eq. 6.30}$$

$$E_u = bcE_c \quad \text{Eq. 6.31}$$

$$b = \frac{f_{un}}{f_{co}'} \geq 1 \quad \text{Eq. 6.32}$$

$$c = \left(\frac{\varepsilon_{cc}}{\varepsilon_{un}}\right)^{0.5} \leq 1 \quad \text{Eq. 6.33}$$

Where ε_{un} and f_{un} are the strain and stress of the unloading point.

Based on the Mander model the stress-strain relationship of the concrete could be calculated for the concrete with the strength 27.58MPa (4000psi), as shown in Figure 6-6.

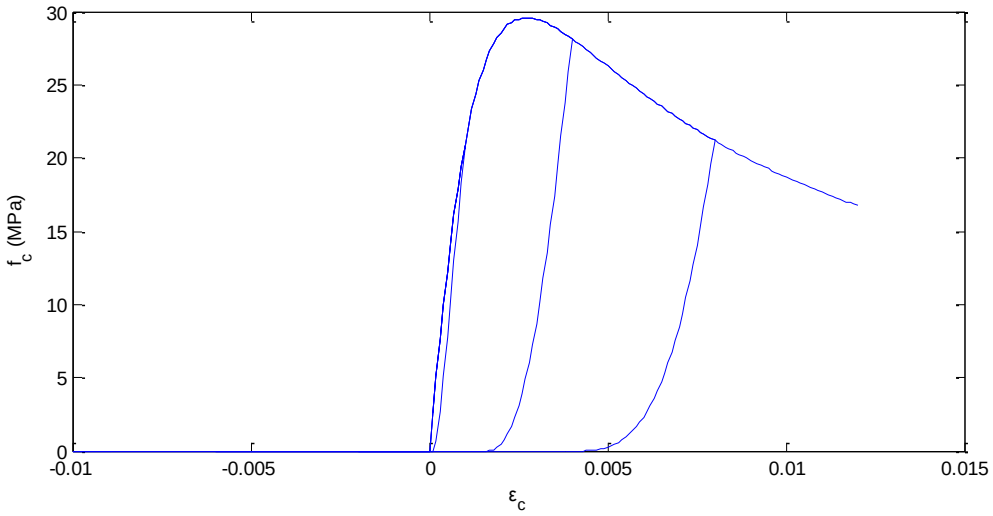

Figure 6-6 stress-strain relationship for confined concrete

(2) Steel model

Steel uses bilinear model following Section 3.2.2.2. The unloading stiffness is equal to the steel stiffness.

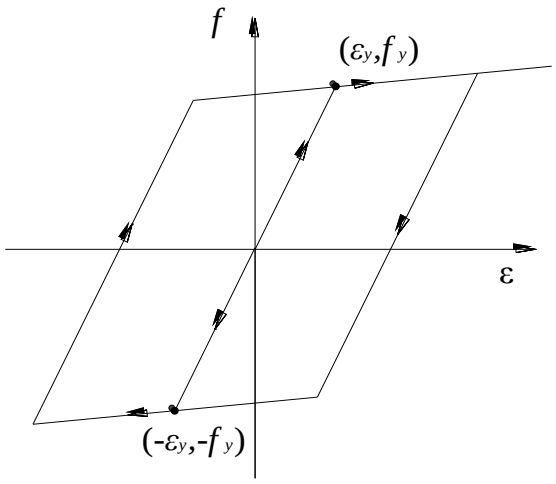

Figure 6-7 stress-strain relationship for steel reinforcement

(3) Fiber model of pier section for Analytical Moment-Curvature Relationship

The section of the concrete pier is divided into n-fiber concrete elements and m-fiber reinforcement elements, as shown in Figure 6-8. The axial load and bending moment acting on the section at any curvature ϕ can be obtained as:

$$N = \int_A f dA = \sum_{i=1}^{n} f_{ci} A_{ci} + \sum_{J=1}^{M} f_{sj} A_{sj} \qquad \text{Eq. 6.34}$$

$$M = \int_A f y dA = \sum_{i=1}^{n} f_{ci} y_{ci} A_{ci} + \sum_{J=1}^{M} f_{si} y_{sj} A_{sj} \qquad \text{Eq. 6.35}$$

Where y is the distance from the element to the neutral axis.

Due to the nonlinear variation of the stress in concrete element, the neutral axis will shift up and down during the dynamic variation. In each steps of analysis, Eq. 6.34 will be

first calculated based on the initial axial load to find the location of the neutral axis with several trials. Then, based on the Eq.6.35, the moment corresponding to specific curvature could be found. Take the strain rate of 104 s^{-1}, which is a common value for impact loading based on Sierakowsi, S.K. Chaturved (1997). The dynamic increase factor of steel reinforcement takes 1.3, while dynamic increase factor of concrete takes 1.5. The moment-curvature relationship of the pier of base cases C1, F1 and T1 under cyclic load is plotted in Figure 6-9. Finally based on the Eq. 6.35, the relationship between the moment and the deflection at the nominal impact height could be obtained.

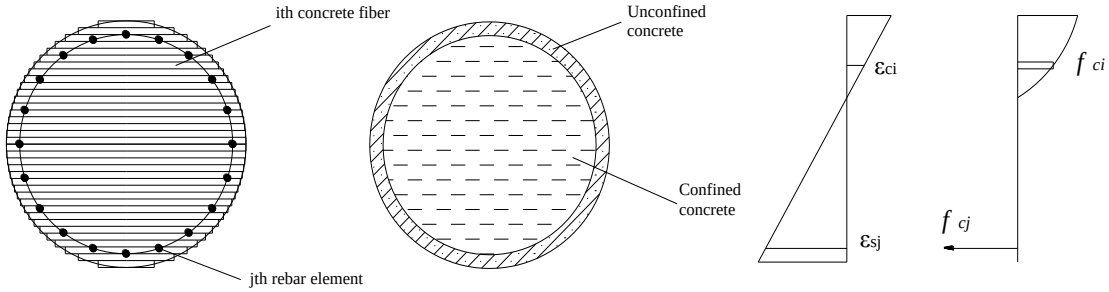

Figure 6-8 Fiber element model for concrete section

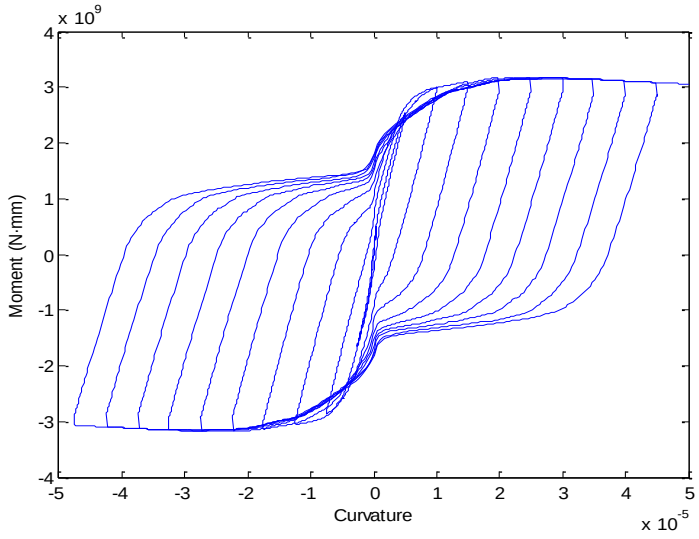

Figure 6-9 Moment-curvature relationship of concrete section

6.1.2 Explicit dynamic analysis for the coupling system

Explicit dynamic analysis is conducted based on central difference method following Section 2.3.2. The impact load in the 0.1 second after initial contact between the truck and the pier will be considered. The time step takes Δt=10^{-5} second and total 10000 steps.

At the n^{th} time step,

$$\underline{u}^n = \begin{bmatrix} {u_e}^n \\ {u_P}^n \end{bmatrix} \quad \text{Eq. 6.36}$$

$$\dot{\underline{u}}^n = \frac{\underline{u}^{n-1} + \underline{u}^{n+1}}{2\Delta t} \qquad \ddot{\underline{u}}^n = \frac{\underline{u}^{n-1} - 2\underline{u}^n + \underline{u}^{n+1}}{\Delta t^2} \quad \text{Eq. 6.37}$$

Given the initial condition at $t = 0$, and $t = -\Delta t$

$$\underline{u}^0 = \begin{bmatrix} 0 \\ 0 \end{bmatrix}; \underline{u}^{-1} = \begin{bmatrix} -v\Delta t \\ 0 \end{bmatrix} \quad \text{Eq. 6.38}$$

The mass matrix could be written as:

$$\boldsymbol{M} = \begin{bmatrix} \boldsymbol{M_e} & \\ & \boldsymbol{M_P} \end{bmatrix} \quad \text{Eq. 6.39}$$

Assume that the constant damping force is equal to D_1 and D_2 for the assumed damper c_1 and c_2, the equation of motion can be changed to:

$$\boldsymbol{M}\frac{\underline{u}^{n-1} - 2\underline{u}^n + \underline{u}^{n+1}}{\Delta t^2} + \boldsymbol{D} + \boldsymbol{f}s^n = 0 \quad \text{Eq. 6.40}$$

$$\boldsymbol{D} = \begin{bmatrix} D_1 \\ -D_2 \end{bmatrix} \quad \text{Eq. 6.41}$$

$$\boldsymbol{f}s^n = \begin{bmatrix} f_e \\ f_P \end{bmatrix} \quad \text{Eq. 6.42}$$

The force in assumed spring k_1:

$$f_e = \begin{cases} k_1({u_e}^n - {u_P}^n - x_e) & ({u_e}^n - {u_P}^n - x_e) > 0 \\ 0 & ({u_e}^n - {u_P}^n - x_e) < 0 \end{cases} \quad \text{Eq. 6.43}$$

The force acting on the pier due to the spring k_1 and its own resistance based on moment-curvature relationship:

$$f_P = -fe + M({u_P}^n)/L_I \quad \text{Eq. 6.44}$$

Where $M({u_P}^n)$ is the moment when the deflection is equal to ${u_P}^n$ at the impact height; L_I is the nominal impact height.

Transferring the known quantities to the right side, there is:

$$\boldsymbol{K_t}^* \underline{u}^{n+1} = \underline{P}^{n*} \quad \text{Eq. 6.45}$$

$$\boldsymbol{K_t}^* = \frac{\boldsymbol{M}}{\Delta t^2} \quad \text{Eq. 6.46}$$

$$\underline{P}^{n*} = -\boldsymbol{D} - \frac{\boldsymbol{M}}{\Delta t^2}\underline{u}^{n-1} - fs^n + \frac{2\boldsymbol{M}}{\Delta t^2}\underline{u}^n \quad \text{Eq. 6.47}$$

$$\underline{u}^{n+1} = {\boldsymbol{K_t}^*}^{-\mathbf{1}} \underline{P}^{n*} \quad \text{Eq. 6.48}$$

6.1.3 Analyzed result

To verify the feasibility of the simplified model, the cases C1 to C5, F1 toF5 and T1 to T5 with three classes of truck crashing into the pier with initial speeds 60km/h, 80km/h, 100km/h, 120km/h and 140km/h are analyzed following the previous assumption. An example MATLAB code for the truck F800 at 100km/h initial velocity can be referred in the **Appendix A**.

6.1.3.1 C2500

As shown in Figure 6.10 and Table 6.1, the result obtained based on explicit dynamic analysis of the simplified model shows good fits with the finite elemental result with the velocities at 80km/h, 100km/h, and 120km/h. For the truck at speed 60km/h, the peak dynamic load of analytical result is smaller than the peak value of the finite elemental result, while the equivalent value of the analytical result is larger than the value of the finite

elemental result. For truck moving at velocity 140km/h, the peak dynamic value of the simplified model is larger than the peak dynamic value of the finite elemental model.

Table 6-1 Comparison of peak dynamic load and equivalent static load (C2500)

Initial velocity	Peak dynamic load (kN)			Equivalent static load (kN)		
	Finite element	Simplified model	error	Finite element	Simplified model	error
60km/h	3227.2	2643.342	18.09%	478.2	606.6411	26.86%
80km/h	4531.8	4172.598	7.93%	644.7	697.2915	8.15%
100km/h	5255.7	5507.335	4.79%	848.3	776.41	8.47%
120km/h	6366.5	6767.559	6.30%	1019.5	851.1317	16.51%
140km/h	7118.3	7993.685	12.30%	1288.1	923.8179	28.28%

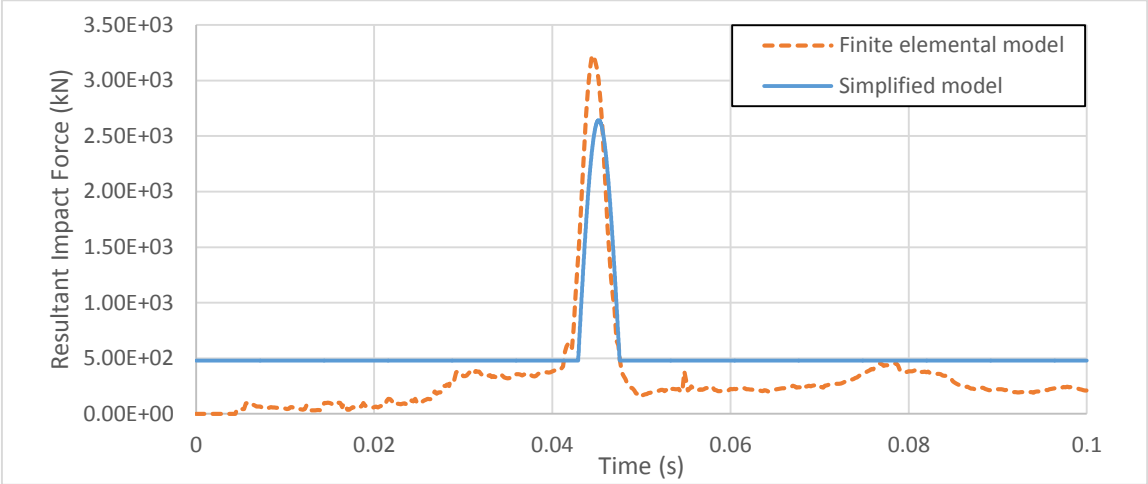

(a) Initial truck velocity at 60km/h

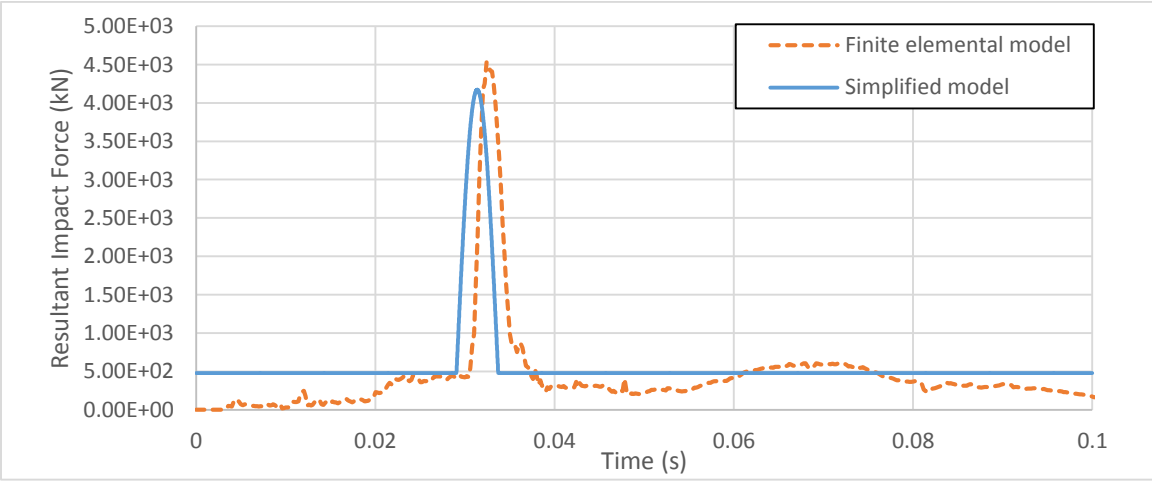

(b) Initial truck velocity at 80km/h

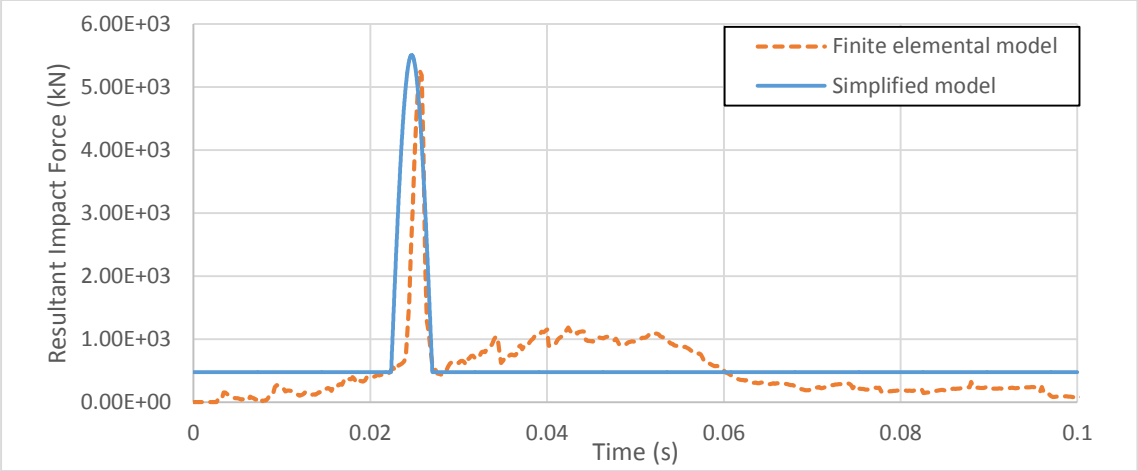

(c) Initial truck velocity at 100km/h

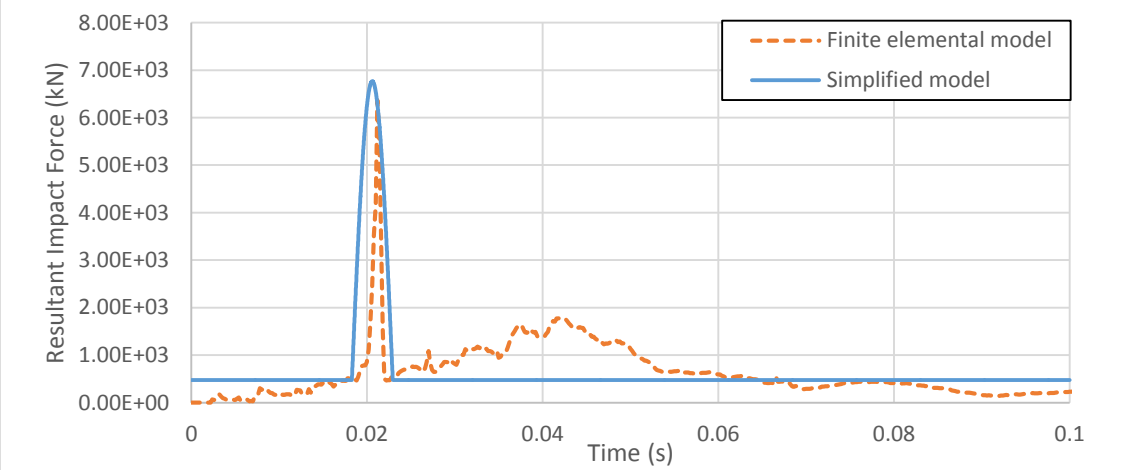

(d) Initial truck velocity at 120km/h

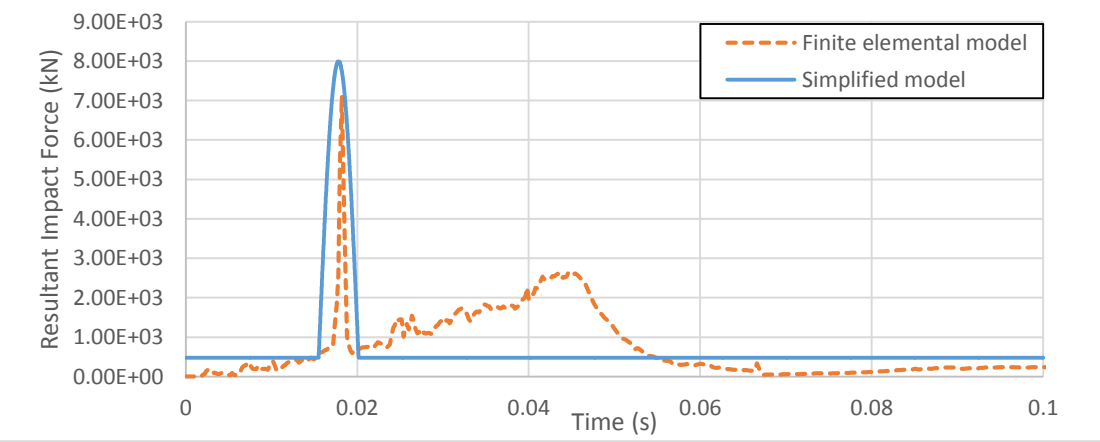

(d) Initial truck velocity at 140km/h

Figure 6-10 Comparison of the finite elemental result in Chapter 5 with the analytical result based on simplified impact model for C2500

6.1.3.2 F800

As shown in Figure 6-11, the result obtained based on explicit dynamic analysis of the simplified model shows good fits with the finite elemental result. For the truck at speed 60km/h, the analytical result has no rigid impact load induced between the engine and the pier. The curve shows a constant damping force induced by the crushing of soft parts of truck. For the truck at the initial velocity over 60km/h, the analytical result shows obvious peak dynamic impact load above the constant damping force. For the truck speed at 80km/h, the peak impact load of simplified model happens later than the finite elemental model. However, the value of the peak impact load matches well with the finite elemental model. For the truck at the impact speed over the 80km/h, both the corresponding time and the value of the peak impact load matches well with the finite elemental result. Based on Table 6-2, the equivalent static force of the simplified model also shows good consistence with the finite elemental result.

Table 6-2 Comparison of peak dynamic load and equivalent static load (F800)

Initial velocity	Peak dynamic load (kN)			Equivalent static load (kN)		
	Finite element	Simplified model	error	Finite element	Simplified model	error
60km/h	2160.1	1342.3	37.86%	1342.3	1342.3	0.00%
80km/h	4162.1	4298.2	3.27%	1654.3	1552.2	6.17%
100km/h	8014.0	7557.8	5.69%	1685.8	1783.5	5.80%
120km/h	10029.2	10062.5	0.33%	1908.4	1961.4	2.78%
140km/h	11251.5	12331.8	9.60%	2219.2	2122.7	4.35%

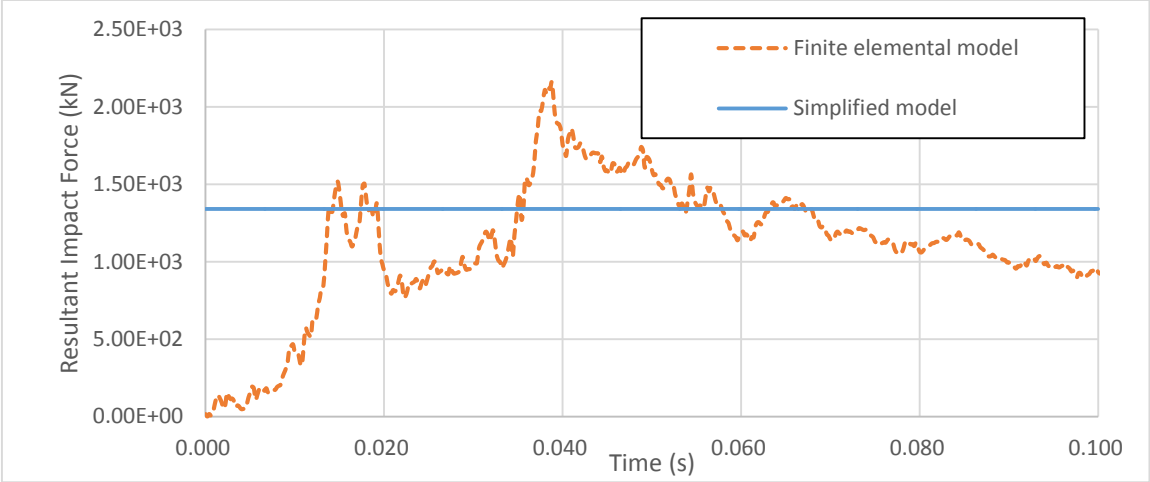

(a) Initial truck velocity at 60km/h

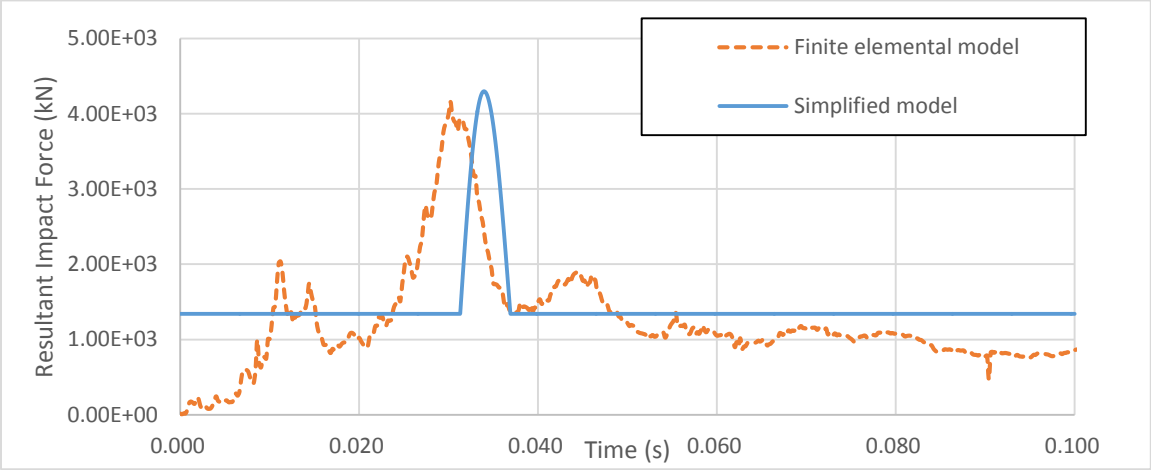

(b) Initial truck velocity at 80km/h

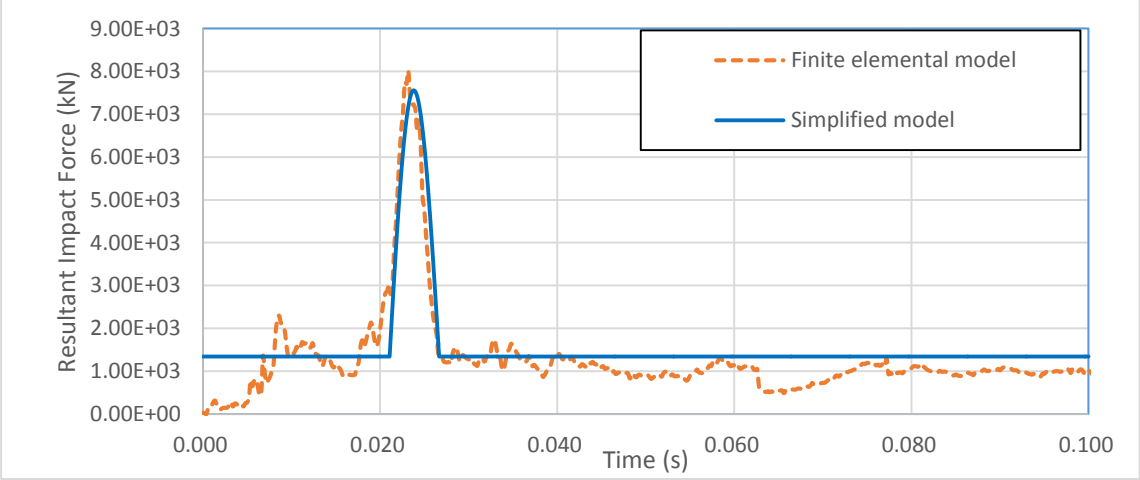

(c) Initial truck velocity at 100km/h

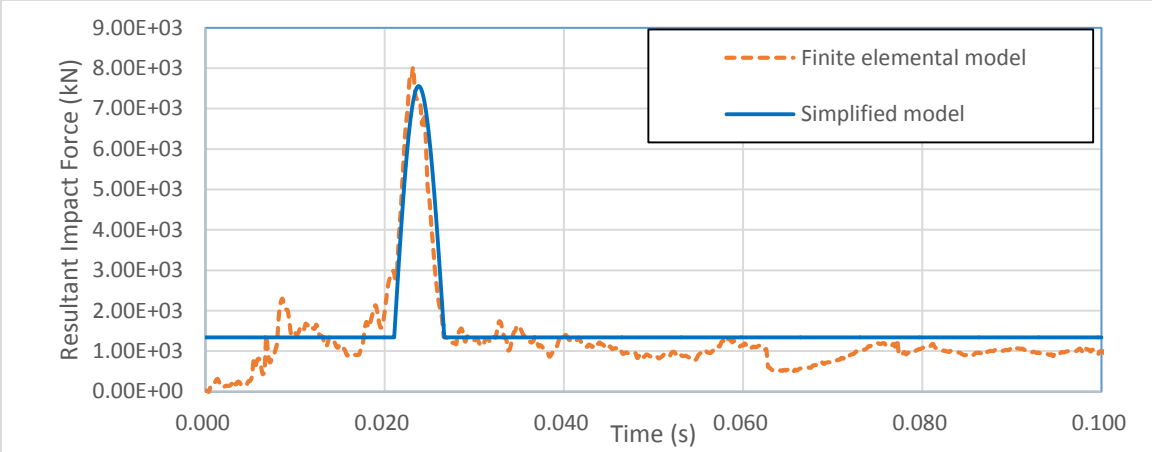

(d) Initial truck velocity at 120km/h

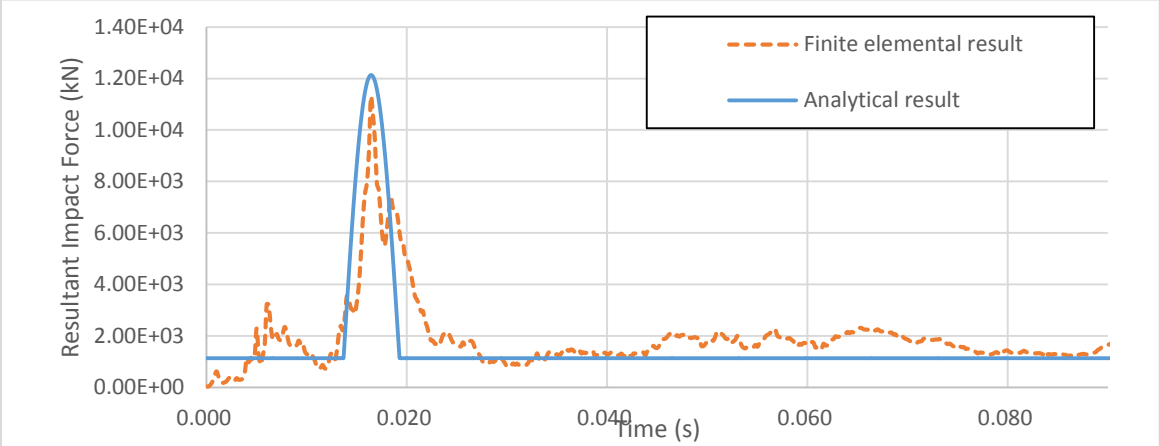

(d) Initial truck velocity at 140km/h

Figure 6-11 Comparison of the finite elemental result in Chapter 5 with the analytical result based on simplified impact model for F800

6.1.3.3 Tractor-trailer truck

As shown in Figure 6-12, the result obtained based on explicit dynamic analysis of the simplified model shows good fits with the finite elemental result. For the truck at speed 40km/h, the analytical result has no rigid impact load induced between the engine and the pier. The curve shows a constant damping force induced by the crushing of soft parts of truck. For the truck at the initial velocity over 40km/h, the analytical result shows obvious peak dynamic impact load above the constant damping force. For the truck speed

at 60km/h, the peak impact load of simplified model happens later than the finite elemental model. However, the value of the peak impact load matches well with the finite elemental model. For the truck at the impact speed over 60km/h, the corresponding time of the peak impact load matches well with the finite elemental result. The peak dynamic values of the simplified model at 80km/h and 100km/h are slightly larger than the peak dynamic value of the finite elemental model. The peak dynamic value of the simplified model at 140km/h is slightly smaller than the finite elemental model. Based on Table 6-3, the equivalent static force of the simplified model also shows good consistence with the finite elemental result.

Table 6-3 Comparison of peak dynamic load and equivalent static load (tractor-trailer)

Initial velocity	Peak dynamic load (kN)			Equivalent static load (kN)		
	Finite element	Simplified model	error	Finite element	Simplified model	error
40km/h	2742.4	1919.0	30.02%	1919.0	1919.0	0.00%
60km/h	4924.9	4427.3	10.10%	2386.3	2182.0	8.56%
80km/h	9457.1	9198.9	2.73%	2858.2	2675.9	6.38%
100km/h	11923.7	12670.4	6.26%	3112.2	3036.1	2.45%
120km/h	17634.7	15814.4	10.32%	3521.8	3362.4	4.53%

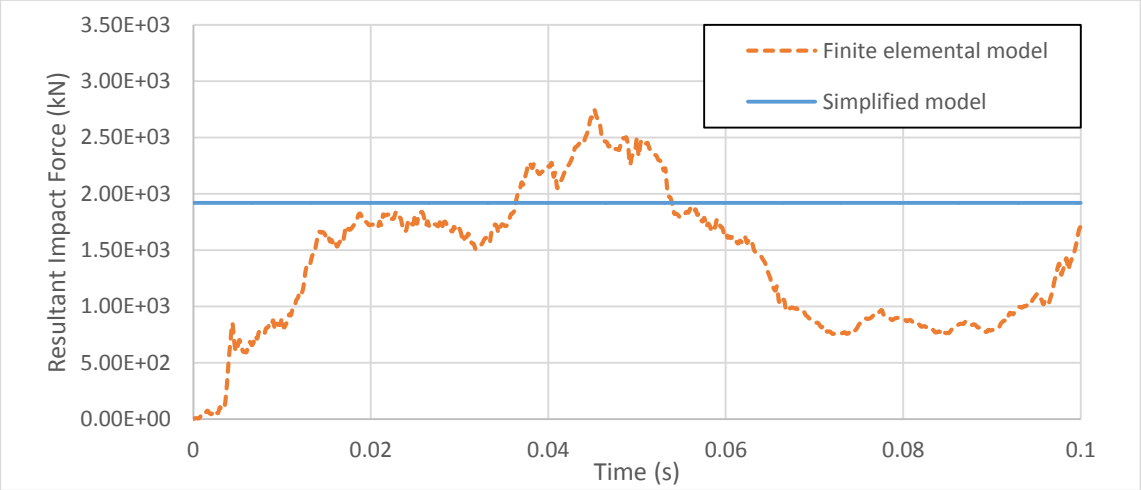

(a) Initial truck velocity at 40km/h

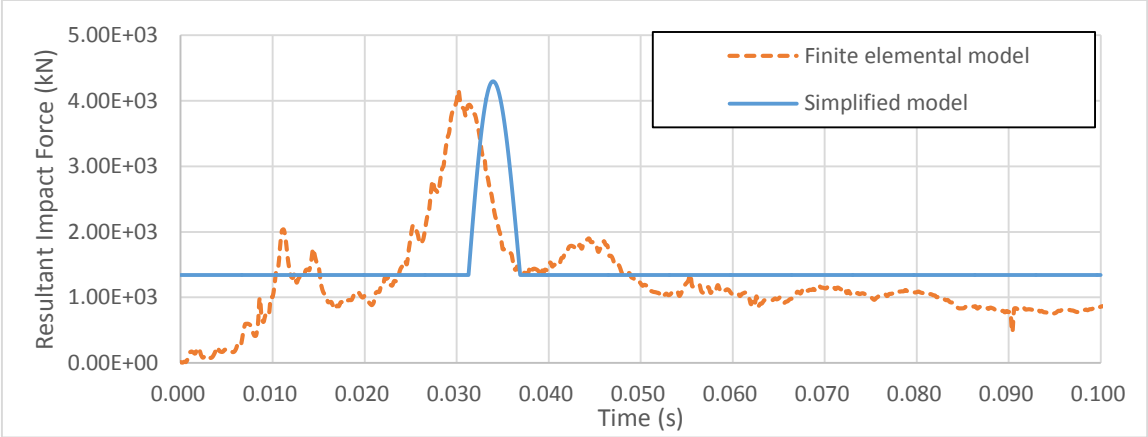

(b) Initial truck velocity at 60km/h

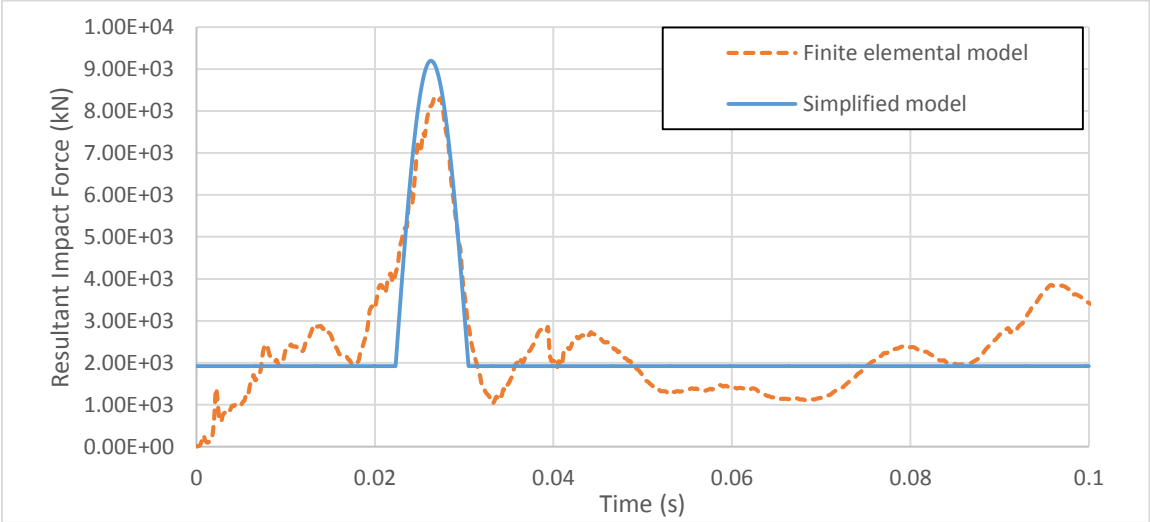

(c) Initial truck velocity at 80km/h

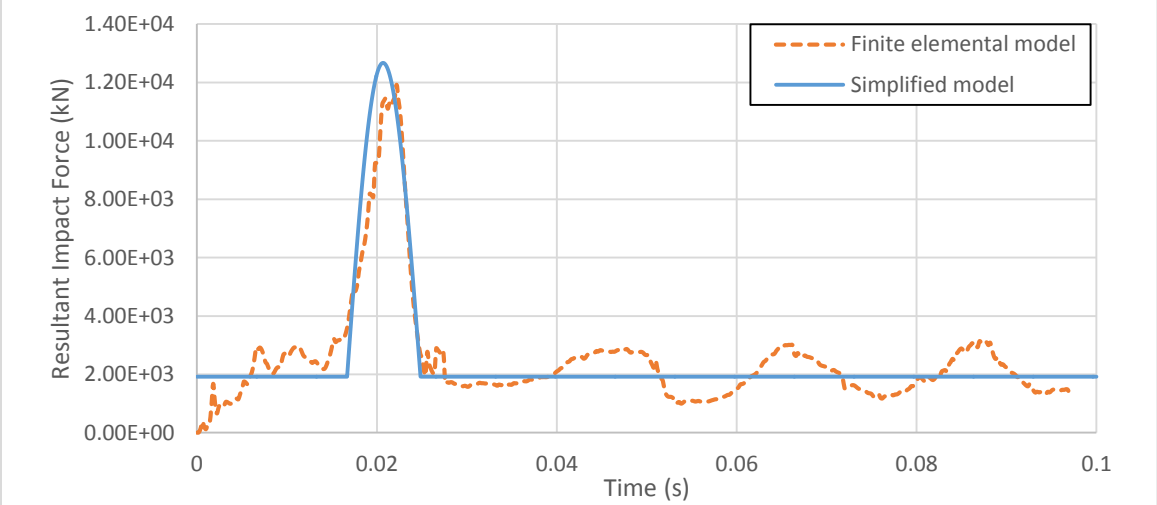

(d) Initial truck velocity at 100km/h

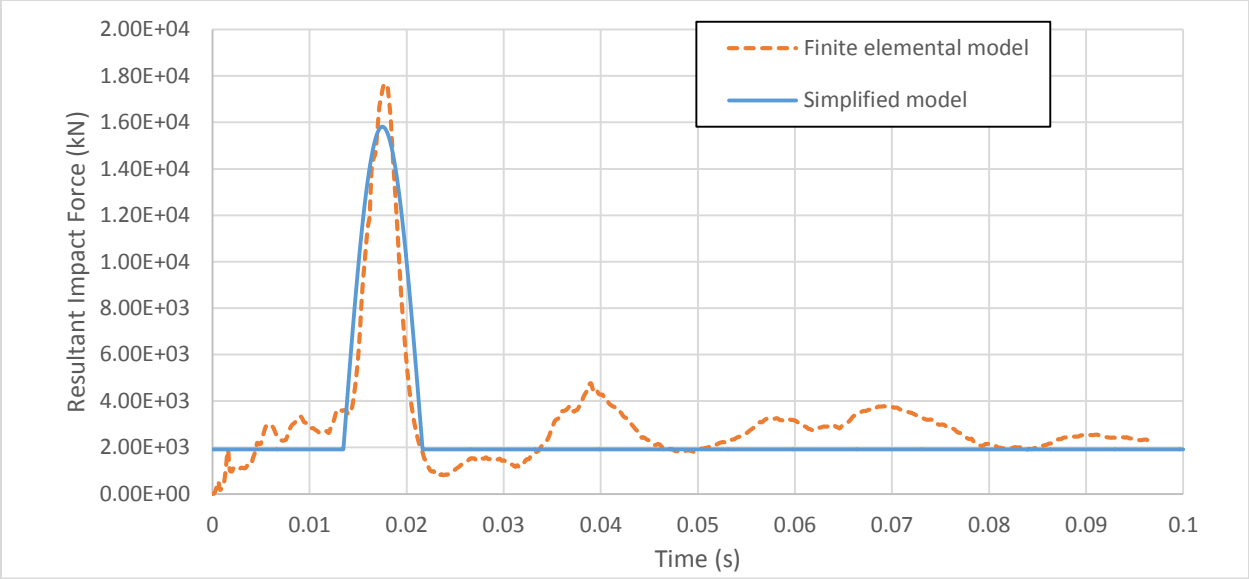

(d) Initial truck velocity at 120km/h

Figure 6-12 Comparison of the finite elemental result in Chapter 5 with the analytical result based on simplified impact model for tractor-trailer truck

6.2 Impact Load Model Based on Response Surface Method

6.2.1 Overview

As we can see in the previous section, the simplified model based on the dynamic method can reflect the impact load to some extent, but where there is limitation in accuracy based on the assumed dynamic system. Besides, it is still required for the case-by-case analysis based on explicit dynamic method to obtain the impact load. For the requirement of the small-time steps in analysis, computer aided computation is inevitable during the analysis. To move forward a step to obtain the impact load without the help of computer, response surface method becomes a good tool.

The response surface method was first introduced by Box and Wilson in 1951. It is a method based on empirical models, which based on existing data to predict the unknown but desirable target. The response surface model is based on the Taylor approximation of

a function with multiple variables. Taking the second-order Taylor expansion as an example, for an arbitrary function with n variables, $x_1 \; to \; x_n$, we can approximate the accurate value of the function by the second order polynomial:

$$f(x_1, \dots, x_n) \approx f(\tilde{x}_1, \dots, \tilde{x}_n) + \sum_{p=1}^{n} f_{x_p}(\tilde{x}_1, \dots, \tilde{x}_n)\left(x_p - \tilde{x}_p\right) +$$

$$\frac{1}{2!}\sum_{p=1}^{n}\sum_{q=1}^{n} f_{x_p x_q}(\tilde{x}_1, \dots, \tilde{x}_n)\left(x_p - \tilde{x}_p\right)\left(x_q - \tilde{x}_q\right) + \epsilon \qquad \text{Eq. 6.49}$$

Where $(\tilde{x}_1, \dots, \tilde{x}_n)$ is a fixed point and ϵ is the higher order smaller quantities of $(\tilde{x}_1, \dots, \tilde{x}_n)$. The ϵ can be ignored, if the distances$|x_p - \tilde{x}_p|$, are all sufficiently small. This equation can be expressed approximately after ignoring the higher order smaller quantities ϵ as:

$$f_{RS}(x_1, \dots, x_n) = C_0 + C_1 x_1 + \cdots + C_n x_n + C_{11} {x_1}^2 + C_{12} x_1 x_2 + \cdots + C_{n-1,n} x_{n-1} x_n + C_{n,n} {x_n}^2$$

Eq. 6.50

$$\epsilon = f(x_1, \dots, x_n) - f_{RS}(x_1, \dots, x_n) \qquad \text{Eq. 6.51}$$

For a load model of which the close form is difficult to obtained, with at least $(n^2 + 3n + 2)/2$ known groups of $(f(x_1, \dots, x_n), x_1, \dots, x_n)$, the factors $C_0, \dots, C_{n,n}$ could be get. And in this way, the approximate formulation for $f(x_1, \dots, x_n)$ with second order of variables could be obtained. In matrix equation, the Eq. 6.49 could be expressed as:

$$\underbrace{\begin{pmatrix} f(x_1, \dots, x_n)^1 \\ \vdots \\ f(x_1, \dots, x_n)^i \\ \vdots \\ f(x_1, \dots, x_n)^N \end{pmatrix} = \begin{bmatrix} 1 & {x_1}^1 & \dots & {x_n}^1 & {x_1}^{2\,1} & x_1 {x_2}^1 & \cdots & {x_n}^{2\,1} \\ & \vdots & & & & \vdots & & \\ 1 & {x_1}^i & \dots & {x_n}^i & {x_1}^{2\,i} & x_1 {x_2}^i & \cdots & {x_n}^{2\,i} \\ & \vdots & & & & \vdots & & \\ 1 & {x_1}^N & \dots & {x_n}^N & {x_1}^{2\,N} & x_1 {x_2}^N & \cdots & {x_n}^{2\,N} \end{bmatrix} \begin{pmatrix} C_0 \\ C_1 \\ \vdots \\ C_n \\ C_{11} \\ C_{12} \\ \vdots \\ C_{n,n} \end{pmatrix} + \begin{pmatrix} \epsilon_1 \\ \vdots \\ \epsilon_i \\ \vdots \\ \epsilon_N \end{pmatrix}}$$

$$\boldsymbol{Y} = \boldsymbol{X}\boldsymbol{C} + \boldsymbol{\epsilon} \qquad \text{Eq. 6.52}$$

Where $(1,\ {x_1}^i, \dots,\ {x_n}^i, {x_1}^{2^i}, x_1{x_2}^i, \dots, {x_n}^{2^i})$ is the i[th] group of variables, and N $>$ $(n^2 + 3n + 2)/2$; $\boldsymbol{Y}$ is the response vector, or called as the vector of observed values; $\boldsymbol{X}$ is the matrix of variables; $\boldsymbol{C}$ is the vector of parameters; $\boldsymbol{\epsilon}$ is the error vector.

Based on linear regression, with N groups of variables, the parameter vector with least-squares estimation method. The approximation response function Eq. 6.50 could be obtained.

To design the N groups of variables, statistical criteria are used to minimize the variance of estimators. The D-optimal design method will be used in the design in this section. D-optimal design can be used for a limited number of designs and can save more computational effort compared with the standard method. In the multiple regression setting, the matrix $\boldsymbol{X}$ is often used to represent the data matrix of independent variables. The D-optimality minimizes the overall variance of the estimated regression coefficients by maximizing the determinant of matrix $\boldsymbol{X'X}$, or equivalently minimizing the value of determinant of matrix $\left|(\boldsymbol{X'X})^{-1}\right|$.

In accordance to the study of Chapter 5, the response impact loads are not sensitive to all of parameters. Due to the high computation resource consumption required during the analysis for each case, following sensitive parameters are included here: the impact velocity of truck, the concrete strength, the diameter of the pier, the length of the pier, the height of the impact location, axial stress on the pier, and the mass of the cargo. The number of parameters is seven, which requires at least 36 groups of parameters for the design. Five groups of Lack-of-fit points and five groups of replicate randomly generated points are added to the model to increase the robustness of the estimation. Besides, the parameter

groups in Chapter 5 are also added to the design as the Lack-of-fit points to increase robustness.

The process of the response surface method is shown in the following flow chart (Figure 6-13).

To check the accuracy, R-square and root-mean-square error (RMSE) are used:

$$R^2 = 1 - \frac{\sum_{i=1}^{N}\left[{f_{RS}}^i - f^i\right]}{\sum_{i=1}^{N}\left[f^i - \bar{f}\right]} \quad \text{Eq. 6.53}$$

$$RMSE = \frac{1}{N\bar{f}}\sqrt{\sum_{i=1}^{N}\left[{f_{RS}}^i - f^i\right]^2} \quad \text{Eq. 6.54}$$

Where $f_{RS}(i)$ is the impact load obtained based on the response surface model corresponding to the i[th] group of variables; $f(i)$ is the impact load from FEM corresponding to the i[th] group of variables; N is the total N groups of variables, that is, N design points.

Cook's Distance is also included to measure the influence of each set of parameters on the response surface model (Cook, 1977). Cook's Distance for the estimation of the ith group of parameters is calculated as (Chatterjee and Hadi, 2012):

$$D_i = \frac{r_i^2}{p+1}\left(\frac{Leverage_i}{1 - Leverage_i}\right) \quad \text{Eq. 6.55}$$

$$\boldsymbol{H} = \boldsymbol{X}(\boldsymbol{X}'\boldsymbol{X})^{-1}\boldsymbol{X}' \quad \text{Eq. 6.56}$$

$$Leverage_i = i^{th}\ diagonal\ element\ of\ \boldsymbol{H} \quad \text{Eq. 6.57}$$

$$r_i = \frac{\epsilon_i}{\hat{\sigma}\sqrt{1 - Leverage_i}} \quad \text{Eq. 6.58}$$

$$\hat{\sigma}^2 = \frac{\sum_{i=1}^{N}{\epsilon_i}^2}{n - p - 1} \quad \text{Eq. 6.59}$$

$$\epsilon_i = f^i - {f_{RS}}^i \quad \text{Eq. 6.60}$$

where p is the number of terms in the model.

Cook's distance can be thought of as the average squared difference between the predictions that result from the full data set and those that result from a reduced data set (deleting the i^{th} observation) compared to the error mean squared of the fitted model. An equivalent interpretation of D_i is as a standardized weighted distance between the vector of regression coefficients obtained from the full model and the vector obtained after deleting the i^{th} case. If the value of D_i is substantially less than 1, deleting the i^{th} case will not change the estimates of the regression coefficients very much. If the value of D_i is larger than 1, it means that by deleting this i^{th} case, the regression function of the response surface model will change obviously. It means that the data of the i^{th} case is abnormal, which need to be considered excluded during the regression analysis.

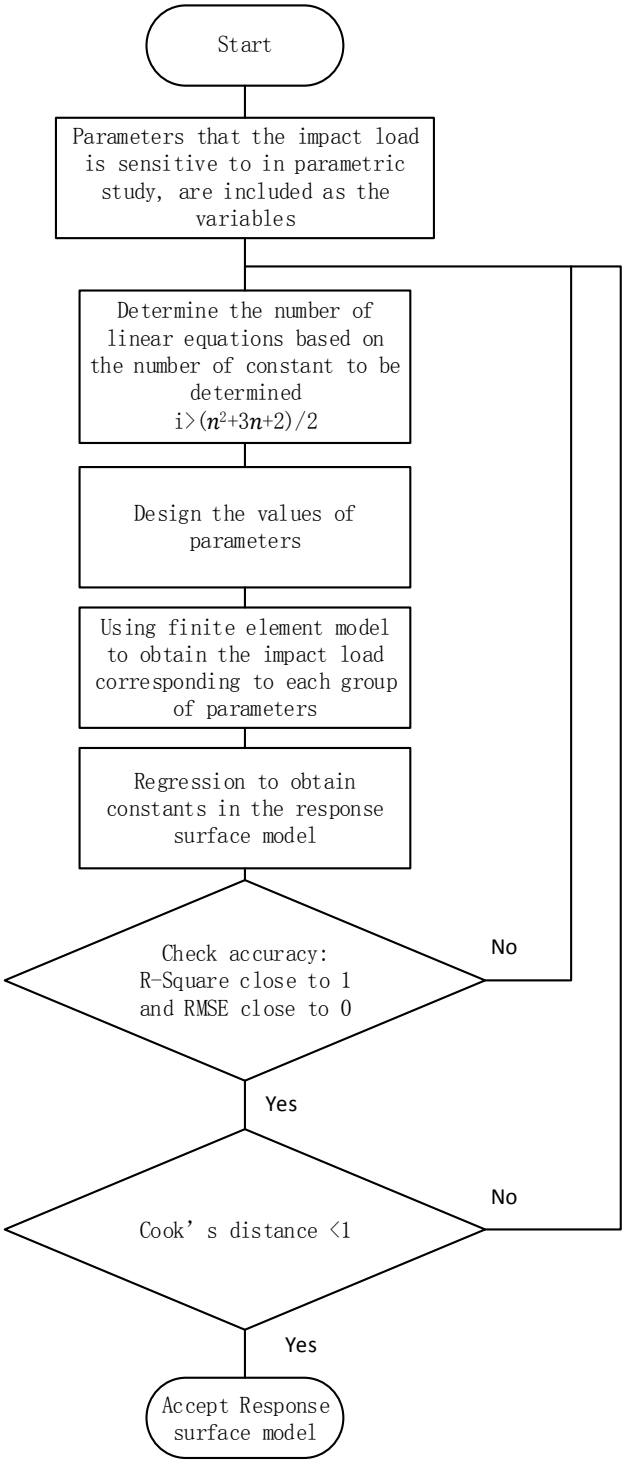

Figure 6-13 Flow chart of response surface method to determine the impact load model

6.2.2 Response surface model

6.2.2.1 C2500

Table 6-4 Factors for the regression analysis of C2500

Variables	Name	Units	Minimum	Maximum	Level	L[1]	L[2]	L[3]	L[4]	L[5]
A	Velocity	km/h	60.00	140.00	5	60	80	100	120	140
B	Concrete Strength	MPa	27.58	55.16	3	27.58	41.37	55.16		
C	Diameter	m	0.7620	1.07	3	0.762	0.9144	1.0668		
D	Length	m	5.49	9.14	3	5.4864	7.3152	9.144		
E	Impact height	m	0.3048	2.13	3	0.3048	1.2192	2.1336		
F	Axial stress	MPa	0.0000	10.00	3	0	5	10		
G	Cargo	Ton	0.0000	1.28	3	0	0.64	1.28		

$$f_{RS}(A,B,C,D,E,F,G) = \alpha_0 + \alpha_1 A + \alpha_2 B + \alpha_3 C + \alpha_4 D + \alpha_5 E + \alpha_6 F + \alpha_7 G + \alpha_8 AB$$
$$+\alpha_9 AC + \alpha_{10} AD + \alpha_{11} AE + \alpha_{12} AF + \alpha_{13} AG + \alpha_{14} BC + \alpha_{15} BD + \alpha_{16} BE + \alpha_{17} BF$$
$$+\alpha_{18} BG + \alpha_{19} CD + \alpha_{20} CE + \alpha_{21} CF + \alpha_{22} CG + \alpha_{23} DE + \alpha_{24} DF + \alpha_{25} DG + \alpha_{26} EF$$
$$+\alpha_{27} EG + \alpha_{28} FG + \alpha_{29} A^2 + \alpha_{30} B^2 + \alpha_{31} C^2 + \alpha_{32} D^2 + \alpha_{33} E^2 + \alpha_{34} F^2 + \alpha_{35} G^2$$

Eq. 6.61

Design-Expert 11 is used in this study for the response surface model analysis. Table 6-4 shows the seven variables and their range for the regression analysis. Eq. 6.61 is the quadratic response surface model for C2500. Total 36 factors $\alpha_0, \alpha_1, \ldots, \alpha_{35}$ are included in Eq. 6.61. To determine the value for the 36 factors, 36 cases with different parameters sets, 5 groups of Lack-of-fit points and 5 groups of replicates are generated based on D-optimal method. Besides, 15 cases in Section 2, Chapter 5 are added in to increase the sample size and robustness. Therefore, totally 61 cases are included in the analysis for C2500, as shown in Table 6-5.

The responses to be determined are two most important indexes: peak dynamic load and equivalent static load. The peak dynamic Impact load shows the dynamic characteristics during the impact, which is also key index to determine if there is possible local damage. The equivalent static load is the significant index for structural design. For the bridge design code like AASHTO, the equivalent static impact load is the key index for the extreme strength design. Table 6-5 shows the responses corresponding to 61 cases.

As shown in Table 6-5, responses of case 23 and 38 are ignored due to their large cook's distance, which is over 1. The factors based on linear regression are shown in Table 6-6. The coded value of coefficient is to normalize the range of variables from -1 to 1, where the minimum value is corresponding to -1, the medium value is corresponding to 0, and the maximum value is corresponding to 1. For the coded equation, the α_1 is much larger than other factors, which means the responses are most sensitive to the change of velocity.

The diagnostics based on cook's distance and analysis of variance (ANOVA) is shown in Table 6-7 and Table 6-8 for peak dynamic impact load and equivalent static impact load. The cook's distances for all cases are smaller than 1 after ignorance of cases 23 and 38. Values of R^2 are all close to 1.0, and values of RMSE are close to 0. It means the response surface model shows good fitting.

The 3D plot of response surface model is shown in Figures 6-14 and 6-15 based on the basic group of parameters A=100km/h, B=27.58MPa, C=0.9144m, D=5.4864m, E=1.2192m, F=5MPa, and G=0 ton. All the design points are close to the response surface, which means the response surface model fits the designs points well. Also, the 3D plot shows the response is sensitive to the velocity compared with other parameters.

Table 6-5 Design layout for response surface model of C2500

Case	Variables							Responses	
	A	B	C	D	E	F	G	Peak Dynamic Load (N)	Equivalent Static Load (N)
1	60	41.37	1.0668	9.144	2.1336	0	0	2.5406E+06	4.5531E+05
2	60	55.16	0.762	5.4864	2.1336	10	0.64	2.9765E+06	4.5344E+05
3	60	27.58	0.762	5.4864	0.3048	5	1.28	3.9418E+06	4.9960E+05
4	60	55.16	1.0668	7.3152	0.3048	5	0.64	2.9670E+06	4.6702E+05
5	60	27.58	0.9144	5.4864	1.2192	0	0.64	3.5450E+06	4.8564E+05
6	60	41.37	1.0668	9.144	2.1336	0	0	2.5406E+06	4.5531E+05
7	140	55.16	0.762	5.4864	0.3048	5	0.64	4.9929E+06	1.0116E+06
8	140	27.58	0.762	9.144	0.3048	10	0.64	5.4446E+06	1.0684E+06
9	140	55.16	0.762	5.4864	2.1336	0	1.28	4.5446E+06	9.8622E+05
10	140	27.58	0.9144	7.3152	0.3048	0	1.28	5.8186E+06	1.2377E+06
11	100	27.58	0.762	9.144	2.1336	0	1.28	4.0089E+06	8.7885E+05
12	60	41.37	0.762	7.3152	1.2192	5	0	2.7805E+06	4.7776E+05
13	140	41.37	0.762	9.144	2.1336	0	0	4.3205E+06	1.2129E+06
14	60	27.58	1.0668	7.3152	2.1336	0	1.28	3.6251E+06	4.5807E+05
15	120	27.58	1.0668	9.144	2.1336	10	0.64	5.8362E+06	9.7941E+05
16	140	27.58	1.0668	5.4864	0.3048	10	0	5.9141E+06	1.1487E+06
17	60	55.16	1.0668	5.4864	1.2192	10	0	3.4309E+06	4.6275E+05
18	140	27.58	0.762	5.4864	2.1336	10	0	6.2403E+06	1.2054E+06
19	140	55.16	1.0668	9.144	0.3048	0	0	5.4411E+06	1.2685E+06
20	80	41.37	0.9144	5.4864	2.1336	5	1.28	4.0702E+06	6.9699E+05
21	60	55.16	1.0668	9.144	2.1336	10	1.28	4.6475E+06	4.8546E+05
22	60	27.58	0.762	9.144	2.1336	10	0	3.4482E+06	5.0660E+05
23	60	55.16	0.762	9.144	0.3048	10	0	~~4.4955E+06~~	~~5.7585E+05~~
24	100	55.16	0.762	7.3152	2.1336	0	0	2.8632E+06	8.5788E+05
25	80	55.16	0.9144	5.4864	0.3048	10	1.28	4.1079E+06	5.2893E+05
26	140	27.58	1.0668	5.4864	1.2192	10	1.28	6.1227E+06	1.1499E+06
27	140	55.16	0.762	5.4864	2.1336	10	0	5.1340E+06	1.1339E+06
28	140	27.58	1.0668	5.4864	0.3048	10	0	5.9141E+06	1.1487E+06
29	140	55.16	0.762	5.4864	2.1336	0	1.28	4.5446E+06	9.8622E+05
30	100	41.37	1.0668	5.4864	0.3048	0	1.28	4.6215E+06	8.2160E+05
31	140	27.58	1.0668	5.4864	1.2192	10	1.28	6.1227E+06	1.1499E+06
32	100	55.16	0.9144	9.144	1.2192	0	0.64	5.0968E+06	8.5123E+05
33	140	55.16	1.0668	9.144	0.3048	10	1.28	5.6012E+06	9.0370E+05
34	140	27.58	1.0668	9.144	1.2192	5	0	5.9080E+06	1.1713E+06
35	60	27.58	0.762	9.144	2.1336	10	0	3.4482E+06	5.0660E+05
36	140	55.16	1.0668	5.4864	2.1336	10	0	6.6542E+06	1.1993E+06
37	60	55.16	0.762	5.4864	0.3048	0	0	2.1127E+06	4.7385E+05
38	60	27.58	1.0668	9.144	0.3048	10	1.28	~~4.4074E+06~~	~~4.9274E+05~~
39	140	55.16	1.0668	9.144	2.1336	0	1.28	5.5729E+06	1.1277E+06
40	140	55.16	0.762	9.144	2.1336	10	1.28	9.9274E+06	1.0223E+06
41	140	41.37	0.9144	7.3152	2.1336	5	0.64	5.4066E+06	1.2435E+06

42	60	55.16	0.762	9.144	0.3048	0	1.28	4.9061E+06	4.3231E+05
43	60	41.37	0.762	7.3152	1.2192	10	1.28	3.5032E+06	4.6423E+05
44	60	27.58	1.0668	5.4864	2.1336	10	0	4.4604E+06	4.8120E+05
45	60	27.58	0.762	9.144	0.3048	0	0	2.7271E+06	4.7763E+05
46	140	27.58	1.0668	5.4864	2.1336	0	0	5.8858E+06	1.2069E+06
47	60	27.58	0.9144	5.4864	1.2192	5	0	3.2272E+06	4.7820E+05
48	80	27.58	0.9144	5.4864	1.2192	5	0	4.5318E+06	6.5030E+05
49	100	27.58	0.9144	5.4864	1.2192	5	0	5.2557E+06	8.4826E+05
50	120	27.58	0.9144	5.4864	1.2192	5	0	5.5884E+06	1.0155E+06
51	140	27.58	0.9144	5.4864	1.2192	5	0	6.1183E+06	1.2802E+06
52	100	41.37	0.9144	5.4864	1.2192	5	0	3.8706E+06	8.3221E+05
53	100	55.16	0.9144	5.4864	1.2192	5	0	3.1973E+06	8.3301E+05
54	100	27.58	0.762	5.4864	1.2192	5	0	4.1321E+06	8.8644E+05
55	100	27.58	1.0668	5.4864	1.2192	5	0	5.6001E+06	8.3807E+05
56	100	27.58	0.9144	9.144	1.2192	5	0	4.8160E+06	8.5341E+05
57	100	27.58	0.9144	5.4864	0.3048	5	0	5.2557E+06	8.4826E+05
58	100	27.58	0.9144	5.4864	2.1336	5	0	5.1105E+06	8.3862E+05
59	100	27.58	0.9144	5.4864	1.2192	0	0	4.7710E+06	8.4786E+05
60	100	27.58	0.9144	5.4864	1.2192	10	0	5.9300E+06	8.7957E+05
61	100	27.58	0.9144	5.4864	1.2192	5	1.28	5.2125E+06	9.0055E+05

Note: the values with line through are ignored because their cook's distances are over 1

Table 6-6 Factors for the response surface model of C2500

	Peak Dynamic Load		Equivalent static Load	
Factors	Coded ($\times 10^6\ N$)	Actual ($\times 10^6\ N$)	Coded ($\times 10^5\ N$)	Actual ($\times 10^5\ N$)
α_0	4.502677	-2.327607	8.563567	-10.953706
α_1	1.391181	0.082008	3.423841	0.104349
α_2	0.308009	-0.406598	-0.214314	-0.112126
α_3	-0.192623	13.628777	0.015799	16.733182
α_4	0.184267	1.203739	-0.027582	1.284919
α_5	0.192022	-3.797480	0.280059	-0.930559
α_6	0.544130	-0.383476	-0.236693	0.123752
α_7	-0.026893	4.380744	-0.250447	1.978817
α_8	-0.149730	-0.000271	-0.205542	-0.000373
α_9	-0.048693	-0.007988	0.109956	0.018037
α_{10}	0.198916	0.002719	0.008360	0.000114
α_{11}	0.103004	0.002816	0.000948	0.000026
α_{12}	0.313478	0.001567	-0.143073	-0.000715
α_{13}	0.065119	0.002544	-0.232052	-0.009065
α_{14}	-0.103793	-0.049388	0.229758	0.109325
α_{15}	0.821459	0.032573	0.154104	0.006111
α_{16}	-0.154244	-0.012232	0.034799	0.002760
α_{17}	0.436584	0.006332	-0.071033	-0.001030
α_{18}	0.247196	0.028009	-0.259128	-0.029361

α_{19}	-0.289705	-1.039454	-0.104010	-0.373185
α_{20}	0.419155	3.007834	0.015102	0.108373
α_{21}	-0.141898	-0.186217	-0.012175	-0.015978
α_{22}	-0.382768	-3.924381	0.005437	0.055747
α_{23}	0.205324	0.122783	0.115205	0.068892
α_{24}	0.159484	0.017441	-0.124492	-0.013615
α_{25}	-0.499989	-0.427183	-0.080302	-0.068609
α_{26}	0.472584	0.103365	0.342370	0.074884
α_{27}	0.205296	0.350804	0.091661	0.156628
α_{28}	-0.409222	-0.127882	-0.015872	-0.004960
α_{29}	-0.491877	-0.000307	-0.090559	-0.000057
α_{30}	0.524686	0.002759	0.022426	0.000118
α_{31}	-0.059327	-2.554358	-0.257988	-11.107849
α_{32}	-0.396729	-0.118621	-0.273176	-0.081679
α_{33}	-0.054168	-0.064785	0.014524	0.017370
α_{34}	0.180311	0.007212	-0.077136	-0.003085
α_{35}	0.348551	0.850955	0.011433	0.027913

Table 6-7 Diagnostics and ANOVA for response surface model of peak dynamic load of C2500

Case	Observed value f (N)	Predicted value f_{RS} (N)	Residual ϵ	Leverage	Cook's distance
1	2.541E+06	2.543E+06	-2305.34	0.490	0.000
2	2.977E+06	2.856E+06	1.207E+05	0.855	0.378
3	3.942E+06	3.831E+06	1.108E+05	0.803	0.162
4	2.967E+06	2.887E+06	80134.46	0.782	0.068
5	3.545E+06	3.672E+06	-1.266E+05	0.646	0.053
6	2.541E+06	2.543E+06	-2305.34	0.490	0.000
7	4.993E+06	4.909E+06	83687.71	0.851	0.171
8	5.445E+06	5.442E+06	2799.65	0.945	0.002
9	4.545E+06	4.504E+06	40441.84	0.481	0.002
10	5.819E+06	5.840E+06	-21679.15	0.874	0.017
11	4.009E+06	3.953E+06	55452.82	0.877	0.113
12	2.780E+06	2.762E+06	18461.33	0.592	0.001
13	4.320E+06	4.249E+06	71541.03	0.831	0.095
14	3.625E+06	3.492E+06	1.331E+05	0.840	0.370
15	5.836E+06	5.873E+06	-36771.45	0.728	0.008
16	5.914E+06	6.068E+06	-1.536E+05	0.436	0.021
17	3.431E+06	3.413E+06	18201.92	0.700	0.002
18	6.240E+06	6.304E+06	-63780.07	0.702	0.020
19	5.441E+06	5.462E+06	-21234.26	0.895	0.023
20	4.070E+06	4.078E+06	-7832.33	0.594	0.000
21	4.648E+06	4.675E+06	-27705.46	0.884	0.032

22	3.448E+06	3.457E+06	-8517.58	0.471	0.000
24	2.863E+06	2.853E+06	10227.04	0.785	0.001
25	4.108E+06	4.248E+06	-1.396E+05	0.810	0.277
26	6.123E+06	6.050E+06	72356.25	0.450	0.005
27	5.134E+06	5.256E+06	-1.216E+05	0.777	0.148
28	5.914E+06	6.068E+06	-1.536E+05	0.436	0.021
29	4.545E+06	4.504E+06	40441.84	0.481	0.002
30	4.622E+06	4.552E+06	69160.24	0.836	0.094
31	6.123E+06	6.050E+06	72356.25	0.450	0.005
32	5.097E+06	4.984E+06	1.124E+05	0.518	0.018
33	5.601E+06	5.535E+06	65716.63	0.907	0.286
34	5.908E+06	5.887E+06	20914.19	0.682	0.002
35	3.448E+06	3.457E+06	-8517.58	0.471	0.000
36	6.654E+06	6.465E+06	1.894E+05	0.807	0.495
37	2.113E+06	2.043E+06	70056.07	0.807	0.068
39	5.573E+06	5.671E+06	-98594.92	0.885	0.415
40	9.927E+06	9.902E+06	24954.32	0.941	0.108
41	5.407E+06	5.643E+06	-2.362E+05	0.535	0.088
42	4.906E+06	4.990E+06	-83700.91	0.845	0.157
43	3.503E+06	3.487E+06	16028.35	0.812	0.004
44	4.460E+06	4.639E+06	-1.787E+05	0.724	0.193
45	2.727E+06	2.799E+06	-72050.73	0.842	0.111
46	5.886E+06	5.926E+06	-39785.65	0.857	0.042
47	3.227E+06	3.314E+06	-86551.56	0.388	0.005
48	4.532E+06	4.321E+06	2.108E+05	0.128	0.005
49	5.256E+06	5.082E+06	1.732E+05	0.096	0.002
50	5.588E+06	5.598E+06	-9525.93	0.116	0.000
51	6.118E+06	5.867E+06	2.508E+05	0.315	0.027
52	3.871E+06	3.797E+06	73500.28	0.306	0.002
53	3.197E+06	3.561E+06	-3.638E+05	0.369	0.078
54	4.132E+06	4.439E+06	-3.074E+05	0.449	0.089
55	5.600E+06	5.607E+06	-6690.81	0.349	0.000
56	4.816E+06	4.808E+06	7966.60	0.324	0.000
57	5.256E+06	5.093E+06	1.630E+05	0.363	0.015
58	5.110E+06	4.964E+06	1.465E+05	0.303	0.009
59	4.771E+06	4.905E+06	-1.345E+05	0.336	0.009
60	5.930E+06	5.620E+06	3.099E+05	0.378	0.060
61	5.213E+06	5.534E+06	-3.217E+05	0.356	0.057
Standard deviation		2.089E+05			
Mean value (N)		4.684E+06			
R^2		0.9904			
RMSE		0.003625			

Table 6-8 Diagnostics and ANOVA for response surface model of equivalent static load of C2500

Case	Observed value f (N)	Predicted value f_{RS} (N)	Residual ϵ	Leverage	Cook's distance
1	4.553E+05	4.516E+05	3735.30	0.490	0.001
2	4.534E+05	4.609E+05	-7487.81	0.855	0.118
3	4.996E+05	5.095E+05	-9908.03	0.803	0.105
4	4.670E+05	4.626E+05	4426.61	0.782	0.017
5	4.856E+05	4.818E+05	3816.60	0.646	0.004
6	4.553E+05	4.516E+05	3735.30	0.490	0.001
7	1.012E+06	1.020E+06	-8736.00	0.851	0.151
8	1.068E+06	1.067E+06	1365.75	0.945	0.030
9	9.862E+05	9.921E+05	-5854.15	0.481	0.003
10	1.238E+06	1.239E+06	-1696.84	0.874	0.008
11	8.788E+05	8.666E+05	12279.80	0.877	0.451
12	4.778E+05	4.921E+05	-14298.04	0.592	0.038
13	1.213E+06	1.227E+06	-13626.76	0.831	0.280
14	4.581E+05	4.753E+05	-17209.32	0.840	0.504
15	9.794E+05	9.903E+05	-10853.49	0.728	0.060
16	1.149E+06	1.149E+06	-357.49	0.436	0.000
17	4.627E+05	4.743E+05	-11524.27	0.700	0.054
18	1.205E+06	1.229E+06	-23540.82	0.702	0.227
19	1.268E+06	1.268E+06	545.62	0.895	0.001
20	6.970E+05	6.815E+05	15446.76	0.594	0.045
21	4.855E+05	4.839E+05	1573.25	0.884	0.008
22	5.066E+05	5.057E+05	899.94	0.471	0.000
24	8.579E+05	8.477E+05	10141.83	0.785	0.090
25	5.289E+05	5.219E+05	7016.47	0.810	0.057
26	1.150E+06	1.157E+06	-6645.82	0.450	0.003
27	1.134E+06	1.113E+06	21161.90	0.777	0.363
28	1.149E+06	1.149E+06	-357.49	0.436	0.000
29	9.862E+05	9.921E+05	-5854.15	0.481	0.003
30	8.216E+05	8.175E+05	4113.09	0.836	0.027
31	1.150E+06	1.157E+06	-6645.82	0.450	0.003
32	8.512E+05	8.580E+05	-6783.62	0.518	0.005
33	9.037E+05	9.003E+05	3351.48	0.907	0.060
34	1.171E+06	1.174E+06	-2379.86	0.682	0.002
35	5.066E+05	5.057E+05	901.94	0.471	0.000
36	1.199E+06	1.204E+06	-4799.71	0.807	0.026
37	4.738E+05	4.588E+05	15058.54	0.807	0.255
39	1.128E+06	1.129E+06	-841.25	0.885	0.002
40	1.022E+06	1.024E+06	-2113.99	0.941	0.063
41	1.243E+06	1.219E+06	24251.96	0.535	0.076
42	4.323E+05	4.333E+05	-1022.07	0.845	0.002
43	4.642E+05	4.698E+05	-5616.20	0.812	0.038
44	4.812E+05	4.642E+05	16981.91	0.724	0.142

45	4.776E+05	4.790E+05	-1323.38	0.842	0.003
46	1.207E+06	1.196E+06	10872.75	0.857	0.255
47	4.782E+05	4.688E+05	9440.02	0.388	0.005
48	6.503E+05	6.682E+05	-17906.15	0.128	0.003
49	8.483E+05	8.631E+05	-14863.29	0.096	0.001
50	1.015E+06	1.054E+06	-38032.75	0.116	0.011
51	1.280E+06	1.239E+06	40802.64	0.315	0.058
52	8.322E+05	8.500E+05	-17741.41	0.306	0.010
53	8.330E+05	8.413E+05	-8258.69	0.369	0.003
54	8.864E+05	8.489E+05	37571.70	0.449	0.108
55	8.381E+05	8.258E+05	12279.18	0.349	0.006
56	8.534E+05	8.429E+05	10556.02	0.324	0.004
57	8.483E+05	8.607E+05	-12476.28	0.363	0.007
58	8.386E+05	8.684E+05	-29801.20	0.303	0.029
59	8.479E+05	8.579E+05	-10087.30	0.336	0.004
60	8.796E+05	8.529E+05	26690.26	0.378	0.036
61	9.006E+05	8.809E+05	19626.79	0.356	0.017
Standard deviation		2.3168E+04			
Mean value (N)		8.3171E+05			
R^2		0.9974			
RMSE		0.002264			

6.2.2.2 F800

Table 6-9 Factors for the regression analysis of F800

Variables	Name	Units	Minimum	Maximum	Level	L[1]	L[2]	L[3]	L[4]	L[5]
A	Velocity	km/h	60.00	140.00	5	60	80	100	120	140
B	Concrete Strength	MPa	27.58	55.16	3	27.58	41.37	55.16		
C	Diameter	m	0.7620	1.07	3	0.762	0.9144	1.0668		
D	Length	m	5.49	9.14	3	5.4864	7.3152	9.144		
E	Impact height	m	0.3048	2.13	3	0.3048	1.2192	2.1336		
F	Axial stress	MPa	0.0000	10.00	3	0	5	10		
G	Cargo	Ton	0.0000	2.913	3	0	0.64	1.28		

$$f_{RS}(A,B,C,D,E,F,G) = \beta_0 + \beta_1 A + \beta_2 B + \beta_3 C + \beta_4 D + \beta_5 E + \beta_6 F + \beta_7 G + \beta_8 AB$$

$$+\beta_9 AC + \beta_{10} AD + \beta_{11} AE + \beta_{12} AF + \beta_{13} AG + \beta_{14} BC + \beta_{15} BD + \beta_{16} BE + \beta_{17} BF$$

$$+\beta_{18}BG + \beta_{19}CD + \beta_{20}CE + \beta_{21}CF + \beta_{22}CG + \beta_{23}DE + \beta_{24}DF + \beta_{25}DG + \beta_{26}EF$$
$$+\beta_{27}EG + \beta_{28}FG + \beta_{29}A^2 + \beta_{30}B^2 + \beta_{31}C^2 + \beta_{32}D^2 + \beta_{33}E^2 + \beta_{34}F^2 + \beta_{35}G^2$$

Eq. 6.62

Table 6-9 shows the seven variables and their ranges for the regression analysis. Eq. 6.62 is the quadratic response surface model for F800. Total 36 factors $\beta_0, \beta_1, \ldots, \beta_{35}$ are included in Eq. 6.62. To determine the value for the 36 factors, 36 cases with different parameters sets, 5 Lack-of-fit points and 5 replicated design points are generated based on D-optimal method. Besides, 17 cases in Section 3, Chapter 5 are added in to increase the sample size and robustness. Therefore, totally 63 cases are included in the analysis for F800, as shown in Table 6-10. The 63 sets of responses of peak dynamic load and equivalent static load are also listed in Table 6-10.

As shown in Table 6-10, the response of peak dynamic load if case 20 is ignored due to their large cook's distance, which is over 1. The factors based on linear regression are shown in Table 6-11. The coded value of coefficient is to normalize the range of variables from -1 to 1, where the minimum value is corresponding to -1, the medium value is corresponding to 0, and the maximum value is corresponding to 1. For the coded equation, the β_1 is much larger than other factors, which means the response is most sensitive to the change of velocity.

The diagnostics based on cook's distance and analysis of variance (ANOVA) is shown in Table 6.12 and Table 6.13 for peak dynamic impact load and equivalent static impact load. The cook's distances for all cases are smaller than 1. Values of R^2 are all close to 1.0, and values of RMSE are close to 0, which indicates that the response surface model shows good fitting.

The 3D plot of response surface model is shown in Figures 6-16 and 6-17 based on the basic group of parameters A=100km/h, B=27.58MPa, C=0.9144m, D=5.4864m, E=1.2192m, F=5MPa, and G=2.913 ton. All the design points are close to the response surface, which means the response surface model fits the designs points well. Also, the 3D plot shows the response is sensitive to the velocity compared with other parameters.

Table 6-10 Design layout for response surface model of F800

Case	Variables							Responses	
	A	B	C	D	E	F	G	Peak Dynamic Load (N)	Equivalent Static Load (N)
1	60	27.58	1.0668	9.144	2.1336	10	2.913	2.2767E+06	1.4286E+06
2	60	55.16	1.0668	5.4864	0.3048	10	2.913	2.4121E+06	1.4620E+06
3	140	41.37	1.0668	5.4864	0.3048	10	0	1.2026E+07	2.2709E+06
4	60	55.16	0.762	9.144	0.3048	10	2.913	2.2824E+06	1.3675E+06
5	140	27.58	0.9144	5.4864	0.3048	0	2.913	1.1105E+07	2.0510E+06
6	60	55.16	0.762	5.4864	0.3048	0	2.913	2.1429E+06	1.3992E+06
7	140	55.16	1.0668	7.3152	2.1336	10	0	9.5864E+06	2.2710E+06
8	140	27.58	0.9144	9.144	2.1336	5	0	1.0567E+07	1.6297E+06
9	60	27.58	0.762	9.144	2.1336	0	2.913	1.7822E+06	1.2830E+06
10	140	27.58	0.762	5.4864	2.1336	10	2.913	1.0475E+07	2.0589E+06
11	100	41.37	0.9144	9.144	1.2192	10	2.913	8.5415E+06	1.7313E+06
12	60	55.16	1.0668	9.144	2.1336	0	2.913	2.2535E+06	1.4204E+06
13	60	27.58	0.762	9.144	1.2192	10	0	2.0470E+06	1.2918E+06
14	140	55.16	1.0668	9.144	0.3048	10	2.913	1.0337E+07	2.2905E+06
15	60	55.16	1.0668	9.144	2.1336	0	2.913	2.2535E+06	1.4204E+06
16	60	27.58	1.0668	5.4864	0.3048	0	0	2.2783E+06	1.4456E+06
17	60	27.58	0.9144	5.4864	0.3048	10	1.4565	2.3108E+06	1.3823E+06
18	140	41.37	0.9144	7.3152	0.3048	5	1.4565	8.9287E+06	2.0221E+06
19	140	27.58	0.762	5.4864	2.1336	0	0	1.0518E+07	1.7159E+06
20	100	27.58	0.762	9.144	0.3048	0	0	~~6.5417E+06~~	1.7212E+06
21	80	41.37	0.762	7.3152	1.2192	0	1.4565	3.2086E+06	1.7777E+06
22	80	27.58	1.0668	5.4864	2.1336	0	2.913	5.1743E+06	1.6133E+06
23	120	55.16	1.0668	7.3152	0.3048	0	0	9.1222E+06	1.9528E+06
24	120	55.16	1.0668	7.3152	0.3048	0	0	9.1222E+06	1.9528E+06
25	100	55.16	0.762	5.4864	1.2192	5	1.4565	7.9965E+06	1.7341E+06
26	100	27.58	0.762	5.4864	0.3048	5	2.913	8.0127E+06	1.7377E+06
27	140	41.37	1.0668	9.144	2.1336	0	1.4565	1.0218E+07	2.3737E+06
28	60	27.58	1.0668	9.144	0.3048	0	2.913	2.4407E+06	1.4160E+06
29	60	27.58	1.0668	5.4864	2.1336	10	0	2.2645E+06	1.4250E+06
30	140	55.16	0.762	9.144	1.2192	5	0	9.7036E+06	2.1168E+06
31	100	55.16	0.762	9.144	2.1336	10	1.4565	8.2846E+06	1.7759E+06
32	140	27.58	0.762	9.144	0.3048	10	2.913	1.1940E+07	1.7988E+06

33	60	27.58	1.0668	5.4864	2.1336	10	0	2.2645E+06	1.4250E+06
34	60	55.16	0.762	5.4864	2.1336	10	2.913	1.8156E+06	1.3354E+06
35	60	41.37	0.9144	7.3152	0.3048	5	2.913	2.1253E+06	1.3003E+06
36	140	27.58	0.762	9.144	0.3048	10	2.913	1.1940E+07	1.7988E+06
37	140	27.58	1.0668	7.3152	1.2192	10	1.4565	1.2900E+07	2.2644E+06
38	140	55.16	1.0668	5.4864	2.1336	5	1.4565	8.9115E+06	2.2644E+06
39	60	27.58	1.0668	5.4864	0.3048	0	0	2.2783E+06	1.4456E+06
40	60	41.37	0.9144	7.3152	2.1336	5	1.4565	2.2583E+06	1.3300E+06
41	60	55.16	1.0668	9.144	0.3048	10	0	2.3283E+06	1.5134E+06
42	140	55.16	0.762	7.3152	2.1336	0	2.913	1.1038E+07	2.0162E+06
43	80	41.37	0.9144	7.3152	0.3048	10	0	4.8373E+06	1.6815E+06
44	60	55.16	0.762	9.144	2.1336	0	0	5.7966E+06	1.2541E+06
45	140	55.16	0.762	5.4864	0.3048	10	2.913	8.8577E+06	2.3986E+06
46	60	55.16	0.762	5.4864	0.3048	10	0	2.0123E+06	2.1765E+06
47	60	27.58	0.9144	5.4864	1.2192	5	2.913	2.1601E+06	1.3423E+06
48	80	27.58	0.9144	5.4864	1.2192	5	2.913	4.1621E+06	1.4543E+06
49	100	27.58	0.9144	5.4864	1.2192	5	2.913	8.0140E+06	1.6858E+06
50	120	27.58	0.9144	5.4864	1.2192	5	2.913	1.0029E+07	1.9084E+06
51	140	27.58	0.9144	5.4864	1.2192	5	2.913	1.1251E+07	2.2192E+06
52	100	41.37	0.9144	5.4864	1.2192	5	2.913	6.9970E+06	1.6784E+06
53	100	55.16	0.9144	5.4864	1.2192	5	2.913	6.2629E+06	1.6684E+06
54	100	27.58	0.762	5.4864	1.2192	5	2.913	7.5799E+06	1.6858E+06
55	100	27.58	1.0668	5.4864	1.2192	5	2.913	8.8395E+06	1.7298E+06
56	100	27.58	0.9144	7.3152	1.2192	5	2.913	6.8112E+06	1.7283E+06
57	100	27.58	0.9144	9.144	1.2192	5	2.913	6.3149E+06	1.5827E+06
58	100	27.58	0.9144	5.4864	0.3048	5	2.913	8.4011E+06	1.6677E+06
59	100	27.58	0.9144	5.4864	2.1336	5	2.913	7.4651E+06	1.6355E+06
60	100	27.58	0.9144	5.4864	1.2192	0	2.913	7.6681E+06	1.6731E+06
61	100	27.58	0.9144	5.4864	1.2192	10	2.913	7.9346E+06	1.6442E+06
62	100	27.58	0.9144	5.4864	1.2192	5	0	7.5449E+06	1.6378E+06
63	100	27.58	0.9144	5.4864	1.2192	5	1.4565	7.6769E+06	1.6622E+06

Note: the values with line through are ignored because their cook's distances are over 1

Table 6-11 Factors for the response surface model of F800

	Peak Dynamic Load		Equivalent static Load	
Factors	Coded $(\times 10^6\ N)$	Actual $(\times 10^6\ N)$	Coded $(\times 10^5\ N)$	Actual $(\times 10^5\ N)$
β_0	6.630253	-10.6895	17.65085	65.0855
β_1	4.00908	0.257036	3.570033	-0.10082
β_2	-0.08952	0.39686	0.651179	0.194781
β_3	0.443173	-21.2902	0.25238	-103.355
β_4	-0.31375	-1.75522	-0.33106	0.70082
β_5	0.418352	6.167244	-0.44925	-6.81419
β_6	0.328059	0.645745	0.32963	-0.10586
β_7	-0.03843	1.422529	0.254732	-3.90037
β_8	-0.48541	-0.00088	0.191868	0.000348

β_9	0.217676	0.035708	0.491692	0.080658
β_{10}	-0.04056	-0.00055	0.05292	0.000723
β_{11}	-0.11295	-0.00309	0.322041	0.008805
β_{12}	0.050582	0.000253	0.025825	0.000129
β_{13}	0.008978	0.000154	0.900735	0.015461
β_{14}	-0.54332	-0.25853	-0.09906	-0.04713
β_{15}	0.083563	0.003313	0.299538	0.011877
β_{16}	0.211007	0.016734	-0.35209	-0.02792
β_{17}	-0.73247	-0.01062	0.744356	0.010796
β_{18}	-0.47821	-0.02381	-0.40017	-0.01992
β_{19}	0.073783	0.264732	0.204979	0.735458
β_{20}	-0.94432	-6.77639	0.829373	5.95153
β_{21}	-0.33629	-0.44132	0.031161	0.040893
β_{22}	-0.17588	-0.79238	0.537572	2.42181
β_{23}	0.350669	0.209698	0.457639	0.273666
β_{24}	0.57665	0.063063	-0.66294	-0.0725
β_{25}	0.196664	0.073833	0.368141	0.138209
β_{26}	-0.66818	-0.14615	0.402538	0.088044
β_{27}	-0.71592	-0.53755	0.617172	0.463404
β_{28}	-0.16395	-0.02251	-0.18216	-0.02501
β_{29}	-1.17378	-0.00073	0.501911	0.000314
β_{30}	0.524686	-0.00043	-0.49885	-0.00262
β_{31}	-0.059327	22.42371	1.048095	45.1264
β_{32}	-0.396729	0.039742	-0.52361	-0.15656
β_{33}	-0.054168	0.033961	-0.67263	-0.80446
β_{34}	0.180311	-0.00127	0.335763	0.013431
β_{35}	0.348551	0.162395	-0.22722	-0.10711

Table 6-12 Diagnostics and ANOVA for response surface model of peak dynamic load of F800

Case	Observed value f (N)	Predicted value f_{RS} (N)	Residual ϵ	Leverage	Cook's distance
1	2.28E+06	2.33E+06	-53616.43	0.896	0.025
2	2.41E+06	2.06E+06	3.52E+05	0.864	0.603
3	1.20E+07	1.24E+07	-3.49E+05	0.83	0.367
4	2.28E+06	2.30E+06	-15528.1	0.879	0.002
5	1.11E+07	1.11E+07	49701.754	0.701	0.002
6	2.14E+06	2.36E+06	-2.19E+05	0.829	0.142
7	9.59E+06	9.56E+06	21472.664	0.81	0.001
8	1.06E+07	1.05E+07	24935.959	0.708	0.001
9	1.78E+06	1.38E+06	4.06E+05	0.809	*0.384*
10	1.05E+07	1.07E+07	-2.24E+05	0.781	0.086

11	8.54E+06	7.66E+06	8.80E+05	0.462	0.129
12	2.25E+06	2.30E+06	-43276.91	0.485	0.000
13	2.05E+06	2.02E+06	27245.033	0.918	0.011
14	1.03E+07	1.04E+07	-83993.84	0.949	0.267
15	2.25E+06	2.30E+06	-43276.91	0.485	0.000
16	2.28E+06	2.29E+06	-8826.201	0.48	0.000
17	2.31E+06	2.59E+06	-2.76E+05	0.645	0.041
18	8.93E+06	9.19E+06	-2.60E+05	0.437	*0.010*
19	1.05E+07	1.09E+07	-3.52E+05	0.852	0.506
21	3.21E+06	3.85E+06	-6.39E+05	0.606	0.167
22	5.17E+06	5.30E+06	-1.24E+05	0.693	0.012
23	9.12E+06	9.02E+06	97962.607	0.482	0.002
24	9.12E+06	9.02E+06	97962.607	0.482	0.002
25	8.00E+06	7.52E+06	4.80E+05	0.454	0.037
26	8.01E+06	7.48E+06	5.30E+05	0.55	0.080
27	1.02E+07	1.03E+07	-38959.03	0.825	0.004
28	2.44E+06	2.14E+06	3.05E+05	0.898	0.840
29	2.26E+06	2.29E+06	-27046.6	0.482	0.000
30	9.70E+06	9.48E+06	2.24E+05	0.845	0.184
31	8.28E+06	8.67E+06	-3.85E+05	0.803	0.320
32	1.19E+07	1.19E+07	26932.599	0.473	0.000
33	2.26E+06	2.29E+06	-27046.6	0.482	0.000
34	1.82E+06	1.88E+06	-67581.14	0.938	0.118
35	2.13E+06	1.96E+06	1.68E+05	0.434	0.004
36	1.19E+07	1.19E+07	26932.599	0.473	0.000
37	1.29E+07	1.24E+07	4.74E+05	0.678	0.154
38	8.91E+06	9.03E+06	-1.15E+05	0.757	0.018
39	2.28E+06	2.29E+06	-8826.201	0.48	0.000
40	2.26E+06	2.01E+06	2.51E+05	0.517	0.015
41	2.33E+06	2.58E+06	-2.52E+05	0.907	0.699
42	1.10E+07	1.08E+07	2.23E+05	0.896	*0.427*
43	4.84E+06	4.66E+06	1.77E+05	0.479	0.006
44	5.80E+06	5.76E+06	33782.313	0.91	*0.013*
45	8.86E+06	9.02E+06	-1.60E+05	0.895	0.216
46	2.01E+06	1.97E+06	44013.243	0.887	0.014
47	2.16E+06	2.04E+06	1.23E+05	0.424	0.002
48	4.16E+06	5.19E+06	-1.03E+06	0.134	0.020
49	8.01E+06	7.76E+06	2.59E+05	0.083	0.001
50	1.00E+07	9.73E+06	2.95E+05	0.114	0.001
51	1.13E+07	1.11E+07	1.26E+05	0.319	0.001
52	7.00E+06	7.19E+06	-1.89E+05	0.275	0.002
53	6.26E+06	6.45E+06	-1.90E+05	0.298	0.002
54	7.58E+06	7.54E+06	40538.398	0.336	0.000
55	8.84E+06	9.01E+06	-1.74E+05	0.385	0.003
56	6.81E+06	7.42E+06	-6.11E+05	0.283	0.022
57	6.31E+06	7.35E+06	-1.04E+06	0.311	0.074
58	8.40E+06	8.64E+06	-2.42E+05	0.279	0.003
59	7.47E+06	6.92E+06	5.41E+05	0.389	0.032

60	7.67E+06	7.40E+06	2.65E+05	0.327	0.005
61	7.93E+06	8.04E+06	-1.09E+05	0.35	0.001
62	7.54E+06	7.27E+06	2.76E+05	0.306	0.005
63	7.677E+06	7.168E+06	5.091E+05	0.241	0.011
Standard deviation		5.148E+05			
Mean value (N)		6.550E+06			
R^2		0.9909			
RMSE		0.00646			

Table 6-13 Diagnostics and ANOVA for response surface model of equivalent static load of F800

Case	Observed value f (N)	Predicted value f_{RS} (N)	Residual ϵ	Leverage	Cook's distance
1	1.429E+06	1.426E+06	2678.29	0.893	0.005
2	1.462E+06	1.446E+06	16045.77	0.858	0.093
3	2.271E+06	2.238E+06	33171.14	0.799	0.184
4	1.368E+06	1.398E+06	-30897.77	0.878	0.477
5	2.051E+06	2.098E+06	-47491.69	0.694	0.141
6	1.399E+06	1.388E+06	11483.37	0.828	0.031
7	2.271E+06	2.335E+06	-64180.28	0.810	0.779
8	1.630E+06	1.652E+06	-22442.47	0.704	0.034
9	*1.283E+06*	*1.316E+06*	*-33219.48*	*0.799*	*0.185*
10	2.059E+06	2.095E+06	-36023.31	0.781	0.178
11	1.731E+06	1.701E+06	30090.68	0.459	0.012
12	1.420E+06	1.429E+06	-8489.12	0.485	0.001
13	1.292E+06	1.297E+06	-5393.30	0.918	0.033
14	2.290E+06	2.302E+06	-11331.98	0.949	0.392
15	1.420E+06	1.429E+06	-8489.12	0.485	0.001
16	1.446E+06	1.463E+06	-17476.97	0.475	0.004
17	1.382E+06	1.414E+06	-32156.56	0.645	0.045
18	*2.022E+06*	*2.118E+06*	*-95606.82*	*0.393*	*0.083*
19	1.716E+06	1.712E+06	3459.99	0.848	0.004
20	1.721E+06	1.720E+06	832.38	0.906	0.001
21	1.778E+06	1.708E+06	69345.01	0.461	0.065
22	1.613E+06	1.607E+06	5973.32	0.691	0.002
23	1.953E+06	1.938E+06	14766.34	0.478	0.003
24	1.953E+06	1.938E+06	14766.34	0.478	0.003
25	1.734E+06	1.841E+06	-1.070E+05	0.415	0.117
26	1.738E+06	1.713E+06	25119.93	0.512	0.011
27	2.374E+06	2.361E+06	12202.61	0.821	0.032
28	1.416E+06	1.380E+06	36155.59	0.896	0.918
29	1.425E+06	1.417E+06	7637.34	0.482	0.001
30	2.117E+06	2.095E+06	21839.22	0.782	0.066
31	1.776E+06	1.721E+06	54900.54	0.762	0.341

32	1.799E+06	1.796E+06	2431.61	0.473	0.000
33	1.425E+06	1.417E+06	7637.34	0.482	0.001
34	1.335E+06	1.329E+06	6782.38	0.902	0.036
35	1.300E+06	1.319E+06	-18803.00	0.403	0.003
36	1.799E+06	1.796E+06	2431.61	0.473	0.000
37	2.264E+06	2.225E+06	39365.09	0.677	0.085
38	2.264E+06	2.223E+06	41387.69	0.730	0.145
39	1.446E+06	1.463E+06	-17476.97	0.475	0.004
40	1.330E+06	1.314E+06	16122.81	0.436	0.003
41	1.513E+06	1.508E+06	5842.27	0.907	0.030
42	*2.016E+06*	*2.014E+06*	*1919.36*	*0.881*	*0.002*
43	1.681E+06	1.695E+06	-13165.35	0.434	0.002
44	*1.254E+06*	*1.272E+06*	*-17629.71*	*0.909*	*0.291*
45	2.399E+06	2.371E+06	27480.58	0.893	0.494
46	2.176E+06	2.157E+06	19411.52	0.882	0.201
47	1.342E+06	1.294E+06	47976.46	0.350	0.016
48	1.454E+06	1.468E+06	-13693.86	0.121	0.000
49	1.686E+06	1.667E+06	19089.89	0.083	0.000
50	1.908E+06	1.891E+06	17773.67	0.114	0.000
51	2.219E+06	2.140E+06	79705.16	0.312	0.035
52	1.678E+06	1.712E+06	-33357.09	0.272	0.005
53	1.668E+06	1.657E+06	11349.83	0.294	0.001
54	1.686E+06	1.703E+06	-17316.70	0.329	0.002
55	1.730E+06	1.840E+06	-1.102E+05	0.384	0.104
56	1.728E+06	1.693E+06	35470.49	0.281	0.006
57	1.583E+06	1.614E+06	-31511.83	0.306	0.005
58	1.668E+06	1.593E+06	74468.64	0.279	0.025
59	1.635E+06	1.606E+06	29771.85	0.336	0.006
60	1.673E+06	1.694E+06	-20631.24	0.324	0.003
61	1.644E+06	1.707E+06	-62757.60	0.334	0.025
62	1.638E+06	1.609E+06	28401.17	0.298	0.004
63	1.662E+06	1.661E+06	1396.85	0.239	0.000
Standard deviation		5.7349E+04			
Mean value (N)		1.717E+06			
R^2		0.9854			
RMSE		0.00276			

6.2.2.3 Tractor-trailer truck

Table 6-14 Factors for the regression analysis of tractor-trailer truck

Variables	Name	Units	Minimum	Maximum	Level	L[1]	L[2]	L[3]	L[4]	L[5]
A	Velocity	km/h	40.00	120.00	5	40	60	80	100	120
B	Concrete Strength	MPa	27.58	55.16	3	27.58	41.37	55.16		

C	Diameter	m	0.7620	1.07	3	0.762	0.9144	1.0668		
D	Length	m	5.49	9.14	3	5.4864	7.3152	9.144		
E	Impact height	m	0.3048	2.13	3	0.3048	1.2192	2.1336		
F	Axial stress	MPa	0.0000	10.00	3	0	5	10		
G	Cargo	Ton	0.0000	22.179	3	0	11.09	22.179		

$$f_{RS}(A,B,C,D,E,F,G) = \gamma_0 + \gamma_1 A + \gamma_2 B + \gamma_3 C + \gamma_4 D + \gamma_5 E + \gamma_6 F + \gamma_7 G + \gamma_8 AB$$
$$+\gamma_9 AC + \gamma_{10} AD + \gamma_{11} AE + \gamma_{12} AF + \gamma_{13} AG + \gamma_{14} BC + \gamma_{15} BD + \gamma_{16} BE + \gamma_{17} BF$$
$$+\gamma_{18} BG + \gamma_{19} CD + \gamma_{20} CE + \gamma_{21} CF + \gamma_{22} CG + \gamma_{23} DE + \gamma_{24} DF + \gamma_{25} DG + \gamma_{26} EF$$
$$+\gamma_{27} EG + \gamma_{28} FG + \gamma_{29} A^2 + \gamma_{30} B^2 + \gamma_{31} C^2 + \gamma_{32} D^2 + \gamma_{33} E^2 + \gamma_{34} F^2 + \gamma_{35} G^2$$

Eq. 6.63

Table 6-14 shows the seven variables and their ranges for the regression analysis. The designs points are discretely distributed at their design levels. Eq. 6.63 is the quadratic response surface model for tractor-trailer truck. Total 36 factors $\gamma_0, \gamma_1, \ldots, \gamma_{35}$ are included in Eq. 6.63. To determine the value for the 36 factors, 36 cases with different parameters sets, 5 Lack-of-fit points and 5 replicated design points are generated based on D-optimal method. Besides, 17 cases in Section 3, Chapter 5 are added in to increase the sample size and robustness. Therefore, totally 63 cases with different groups of parameters and responses are included in the analysis for tractor-trailer truck, as shown in Table 6-15.

The factors based on linear regression are shown in Table 6-16. The coded value of coefficient is to normalize the range of variables from -1 to 1, where the minimum value is corresponding to -1, the medium value is corresponding to 0, and the maximum value is corresponding to 1. For the coded equation, the γ_1 is much larger than other factors, which means the responses is most sensitive to the change of velocity.

The diagnostics based on cook's distance and analysis of variance (ANOVA) is shown in Table 6-17 and Table 6-18 for peak dynamic impact load and equivalent static impact load. The cook's distances for all cases are smaller than 1. Values of R^2 are all close to 1.0, and values of RMSE are close to 0, which indicates that the response surface model shows good fitting.

The 3D plot of response surface model is shown in Figures 6-8 and 6-9 based on the basic group of parameters A=100km/h, B=27.58MPa, C=0.9144m, D=5.4864m, E=1.2192m, F=5MPa, and G=22.179 ton. All the design points are close to the response surface, which means the response surface model fits the designs points well. Also, the 3D plot shows the response is sensitive to the velocity compared with other parameters.

Table 6-15 Design layout for response surface model of tractor-trailer truck

Case	Variables							Responses	
	A	B	C	D	E	F	G	Peak Dynamic Load (N)	Equivalent Static Load (N)
1	40	55.16	0.762	9.144	0.3048	10	0	3.4619E+06	1.2285E+06
2	80	41.37	0.762	5.4864	1.2192	10	11.0895	1.0121E+07	2.5005E+06
3	40	55.16	0.762	9.144	2.1336	0	22.179	1.7149E+06	2.2995E+06
4	40	27.58	1.0668	5.4864	0.3048	10	0	2.7548E+06	1.7274E+06
5	40	27.58	0.762	9.144	0.3048	0	22.179	1.9289E+06	1.3252E+06
6	80	27.58	0.9144	5.4864	2.1336	10	0	9.5244E+06	2.8214E+06
7	60	27.58	1.0668	9.144	1.2192	10	0	6.8068E+06	2.3703E+06
8	40	27.58	0.762	5.4864	0.3048	5	22.179	2.1252E+06	2.0344E+06
9	40	55.16	1.0668	9.144	2.1336	10	11.0895	2.8614E+06	1.6051E+06
10	40	55.16	0.762	5.4864	0.3048	0	11.0895	2.1145E+06	2.0041E+06
11	120	27.58	0.9144	7.3152	0.3048	5	11.0895	1.7659E+07	3.5847E+06
12	100	55.16	1.0668	5.4864	0.3048	10	0	1.0190E+07	3.0335E+06
13	80	41.37	0.762	9.144	1.2192	5	0	8.6926E+06	2.5215E+06
14	120	27.58	1.0668	9.144	0.3048	0	0	2.0769E+07	3.6278E+06
15	40	27.58	0.762	5.4864	2.1336	0	22.179	1.9126E+06	1.9536E+06
16	40	55.16	1.0668	5.4864	1.2192	5	22.179	2.4520E+06	1.7415E+06
17	40	27.58	1.0668	5.4864	2.1336	5	22.179	2.6966E+06	1.8981E+06
18	80	27.58	1.0668	5.4864	0.3048	0	22.179	1.0220E+07	2.8853E+06
19	100	41.37	1.0668	9.144	2.1336	5	22.179	1.1900E+07	3.4272E+06
20	80	27.58	1.0668	5.4864	0.3048	0	22.179	1.0220E+07	2.8853E+06
21	40	41.37	1.0668	9.144	0.3048	10	22.179	2.4932E+06	1.9003E+06
22	120	41.37	1.0668	7.3152	2.1336	10	0	1.7971E+07	3.5437E+06

23	40	27.58	1.0668	9.144	2.1336	0	22.179	2.3190E+06	1.5052E+06
24	120	27.58	0.762	9.144	0.3048	10	0	1.4901E+07	2.4729E+06
25	120	55.16	0.762	9.144	2.1336	10	22.179	1.6006E+07	2.5510E+06
26	40	27.58	0.762	9.144	2.1336	0	0	2.7663E+06	1.3999E+06
27	120	27.58	0.762	5.4864	2.1336	5	22.179	1.4304E+07	3.5092E+06
28	120	27.58	0.762	9.144	2.1336	0	22.179	1.4778E+07	2.7548E+06
29	80	27.58	0.762	7.3152	0.3048	0	0	8.3097E+06	2.6637E+06
30	100	41.37	0.762	9.144	0.3048	10	22.179	1.0769E+07	3.2134E+06
31	120	55.16	1.0668	9.144	1.2192	0	22.179	1.9481E+07	3.4803E+06
32	40	27.58	0.762	7.3152	2.1336	10	22.179	3.5317E+06	2.2011E+06
33	40	55.16	1.0668	5.4864	2.1336	0	0	2.1534E+06	1.8325E+06
34	80	27.58	0.762	7.3152	0.3048	0	0	8.3097E+06	2.6637E+06
35	120	55.16	0.762	9.144	0.3048	0	11.0895	1.6099E+07	3.2187E+06
36	120	27.58	1.0668	5.4864	2.1336	0	0	1.5672E+07	3.5898E+06
37	120	55.16	1.0668	5.4864	2.1336	0	22.179	1.7877E+07	3.2495E+06
38	40	55.16	1.0668	9.144	0.3048	0	0	2.9305E+06	1.9843E+06
39	120	55.16	0.762	5.4864	2.1336	5	0	1.6073E+07	3.2817E+06
40	120	27.58	0.9144	7.3152	0.3048	5	11.0895	1.7659E+07	3.5847E+06
41	120	41.37	1.0668	7.3152	2.1336	10	0	1.7971E+07	3.5437E+06
42	120	55.16	0.762	5.4864	0.3048	10	22.179	1.6815E+07	3.3439E+06
43	120	55.16	0.9144	9.144	2.1336	0	0	1.5576E+07	3.5722E+06
44	120	41.37	0.9144	5.4864	0.3048	0	0	1.6636E+07	3.5934E+06
45	120	27.58	1.0668	5.4864	1.2192	10	22.179	1.8760E+07	3.4939E+06
46	120	41.37	0.9144	5.4864	0.3048	0	0	1.6636E+07	3.5934E+06
47	40	27.58	0.9144	5.4864	1.2192	5	22.179	2.1601E+06	1.3423E+06
48	60	27.58	0.9144	5.4864	1.2192	5	22.179	4.9249E+06	2.3863E+06
49	80	27.58	0.9144	5.4864	1.2192	5	22.179	8.3425E+06	2.8580E+06
50	100	27.58	0.9144	5.4864	1.2192	5	22.179	1.1924E+07	3.1123E+06
51	120	27.58	0.9144	5.4864	1.2192	5	22.179	1.7635E+07	3.5218E+06
52	80	41.37	0.9144	5.4864	1.2192	5	22.179	7.9537E+06	2.8298E+06
53	80	55.16	0.9144	5.4864	1.2192	5	22.179	7.0132E+06	2.8663E+06
54	80	27.58	0.762	5.4864	1.2192	5	22.179	7.4634E+06	2.7753E+06
55	80	27.58	1.0668	5.4864	1.2192	5	22.179	1.1108E+07	2.9915E+06
56	80	27.58	0.9144	7.3152	1.2192	5	22.179	8.1201E+06	2.8389E+06
57	80	27.58	0.9144	9.144	1.2192	5	22.179	8.2502E+06	2.8461E+06
58	80	27.58	0.9144	5.4864	0.3048	5	22.179	8.4439E+06	2.9086E+06
59	80	27.58	0.9144	5.4864	2.1336	5	22.179	6.9615E+06	2.5847E+06
60	80	27.58	0.9144	5.4864	1.2192	0	22.179	7.6976E+06	2.8485E+06
61	80	27.58	0.9144	5.4864	1.2192	10	22.179	8.4141E+06	2.8627E+06
62	80	27.58	0.9144	5.4864	1.2192	5	0	6.8596E+06	2.8173E+06
63	80	27.58	0.9144	5.4864	1.2192	5	11.0895	8.3987E+06	2.8025E+06

Table 6-16 Factors for the response surface model of tractor-trailer truck

	Peak Dynamic Load		Equivalent static Load	
Factors	Coded ($\times 10^6\ N$)	Actual ($\times 10^6\ N$)	Coded ($\times 10^5\ N$)	Actual ($\times 10^5\ N$)
γ_0	8.889389	4.174923	29.18179	6.002955
γ_1	6.865914	-0.11118	7.883143	0.509356
γ_2	-0.18992	0.422433	0.46696	0.660195
γ_3	0.417361	-38.587	0.975437	-103.369
γ_4	-0.04677	2.084407	-0.53181	5.842994
γ_5	0.00549	3.298193	-0.27507	2.227506
γ_6	0.134067	0.533173	-1.04737	0.820623
γ_7	-0.06459	-0.12258	0.569889	0.289221
γ_8	0.003224	5.85E-06	-0.63602	-0.00115
γ_9	0.632972	0.103834	1.073208	0.176051
γ_{10}	0.099999	0.001367	-0.3731	-0.0051
γ_{11}	-0.43816	-0.01198	-1.01407	-0.02772
γ_{12}	-0.35636	-0.00178	-0.59336	-0.00297
γ_{13}	0.574775	0.001296	-0.28269	-0.00064
γ_{14}	-0.47741	-0.22717	-0.7044	-0.33517
γ_{15}	-0.11736	-0.00465	0.552715	0.021916
γ_{16}	0.396327	0.031431	-0.26954	-0.02138
γ_{17}	0.073125	0.001061	-1.54085	-0.02235
γ_{18}	-0.04174	-0.00027	0.023875	0.000156
γ_{19}	0.251363	0.901884	1.048898	3.763416
γ_{20}	-0.23306	-1.6724	-0.4007	-2.87539
γ_{21}	-0.3373	-0.44266	0.470922	0.618008
γ_{22}	0.300136	0.177591	-0.82898	-0.49051
γ_{23}	-0.22258	-0.1331	0.194711	0.116436
γ_{24}	-0.34645	-0.03789	0.085623	0.009364
γ_{25}	-0.21603	-0.01065	0.161948	0.007985
γ_{26}	0.554441	0.121269	-0.31117	-0.06806
γ_{27}	-0.23899	-0.02357	-0.68908	-0.06796
γ_{28}	-0.16175	-0.00292	0.543671	0.009805
γ_{29}	1.867885	0.001167	-3.32544	-0.00208
γ_{30}	-0.54128	-0.00285	-0.57887	-0.00304
γ_{31}	0.483897	20.83451	1.116026	48.05121
γ_{32}	-0.54445	-0.16279	-2.36625	-0.7075
γ_{33}	-0.50619	-0.6054	1.181414	1.41296
γ_{34}	0.396827	0.015873	-1.31902	-0.05276
γ_{35}	-0.09293	-0.00076	1.278742	0.010398

Table 6-17 Diagnostics and ANOVA for response surface model of peak dynamic load of tractor-trailer truck

Case	Observed value f (N)	Predicted value f_{RS} (N)	Residual ϵ	Leverage	Cook's distance
1	3.4619E+06	3.3412E+06	1.2073E+05	0.90345	0.100016
2	1.0121E+07	9.9243E+06	1.9677E+05	0.705627	0.022322
3	1.7149E+06	1.5387E+06	1.7618E+05	0.927336	0.385964
4	2.7548E+06	3.1596E+06	-4.0482E+05	0.777987	0.183144
5	1.9289E+06	2.1132E+06	-1.8429E+05	0.795262	0.045624
6	9.5244E+06	8.7218E+06	8.0262E+05	0.714548	0.399979
7	6.8068E+06	6.6105E+06	1.9633E+05	0.74298	0.030695
8	2.1252E+06	1.9568E+06	1.6841E+05	0.549038	0.005421
9	2.8614E+06	3.0998E+06	-2.3845E+05	0.853199	0.159388
10	2.1145E+06	2.2071E+06	-9.2535E+04	0.853714	0.024186
11	1.7659E+07	1.7591E+07	6.7688E+04	0.389184	0.000338
12	1.0190E+07	1.0453E+07	-2.6273E+05	0.871802	0.259264
13	8.6926E+06	8.6012E+06	9.1466E+04	0.451569	0.000889
14	2.0769E+07	2.0737E+07	3.1844E+04	0.9002	0.006489
15	1.9126E+06	1.3879E+06	5.2474E+05	0.704756	0.157626
16	2.4520E+06	2.1583E+06	2.9370E+05	0.642504	0.030704
17	2.6966E+06	2.6398E+06	5.6788E+04	0.493112	0.000438
18	1.0220E+07	1.0628E+07	-4.0771E+05	0.425863	0.015205
19	1.1900E+07	1.2517E+07	-6.1725E+05	0.57892	0.088078
20	1.0220E+07	1.0628E+07	-4.0771E+05	0.425863	0.015205
21	2.4932E+06	2.3037E+06	1.8946E+05	0.813376	0.059351
22	1.7971E+07	1.7875E+07	9.5867E+04	0.436102	0.000892
23	2.3190E+06	2.4771E+06	-1.5806E+05	0.743352	0.019962
24	1.4901E+07	1.5244E+07	-3.4323E+05	0.851168	0.320527
25	1.6006E+07	1.5666E+07	3.4070E+05	0.882071	0.521279
26	2.7663E+06	3.0240E+06	-2.5775E+05	0.844778	0.16493
27	1.4304E+07	1.5017E+07	-7.1326E+05	0.480109	0.063983
28	1.4778E+07	1.4287E+07	4.9073E+05	0.777169	0.266875
29	8.3097E+06	8.1611E+06	1.4865E+05	0.455562	0.002405
30	1.0769E+07	1.0924E+07	-1.5457E+05	0.527702	0.004002
31	1.9481E+07	1.9446E+07	3.5289E+04	0.790146	0.001582
32	3.5317E+06	3.8540E+06	-3.2231E+05	0.822773	0.192672
33	2.1534E+06	2.1584E+06	-4.9955E+03	0.867853	8.78E-05
34	8.3097E+06	8.1611E+06	1.4865E+05	0.455562	0.002405
35	1.6099E+07	1.6576E+07	-4.7681E+05	0.759339	0.211043
36	1.5672E+07	1.6013E+07	-3.4076E+05	0.825421	0.222663
37	1.7877E+07	1.7464E+07	4.1261E+05	0.821222	0.309711
38	2.9305E+06	2.6749E+06	2.5562E+05	0.851694	0.179143
39	1.6073E+07	1.6252E+07	-1.7924E+05	0.83058	0.065821
40	1.7659E+07	1.7591E+07	6.7688E+04	0.389184	0.000338

41	1.7971E+07	1.7875E+07	9.5867E+04	0.436102	0.000892
42	1.6815E+07	1.6397E+07	4.1714E+05	0.753894	0.153352
43	1.5576E+07	1.5591E+07	-1.5731E+04	0.758516	0.000228
44	1.6636E+07	1.6337E+07	2.9946E+05	0.4475	0.009308
45	1.8760E+07	1.9238E+07	-4.7774E+05	0.686977	0.113298
46	1.6636E+07	1.6337E+07	2.9946E+05	0.4475	0.009308
47	2.1601E+06	2.5537E+06	-3.9353E+05	0.270847	0.005586
48	4.9249E+06	4.8215E+06	1.0339E+05	0.102633	9.65E-05
49	8.3425E+06	8.0233E+06	3.1923E+05	0.082175	0.000704
50	1.1924E+07	1.2159E+07	-2.3525E+05	0.105811	0.000519
51	1.7635E+07	1.7229E+07	4.0607E+05	0.281627	0.006371
52	7.9537E+06	8.4502E+06	-4.9652E+05	0.269809	0.008833
53	7.0132E+06	7.7946E+06	-7.8146E+05	0.328829	0.031563
54	7.4634E+06	7.5636E+06	-1.0018E+05	0.311421	0.000467
55	1.1108E+07	9.4507E+06	1.6569E+06	0.238555	0.079973
56	8.1201E+06	8.4223E+06	-3.0211E+05	0.307047	0.004132
57	8.2502E+06	7.7324E+06	5.1782E+05	0.328641	0.013843
58	8.4439E+06	7.9243E+06	5.1962E+05	0.281207	0.010405
59	6.9615E+06	7.1098E+06	-1.4829E+05	0.317321	0.00106
60	7.6976E+06	8.1744E+06	-4.7688E+05	0.325609	0.011528
61	8.4141E+06	8.6657E+06	-2.5162E+05	0.347093	0.00365
62	6.8596E+06	7.6369E+06	-7.7730E+05	0.295466	0.025465
63	8.3987E+06	7.9230E+06	4.7565E+05	0.343343	0.012755
Standard deviation		6.264E+05			
Mean value (N)		9.660E+06			
R^2		0.9949			
RMSE		0.00535			

Table 6-18 Diagnostics and ANOVA for response surface model of equivalent static load of tractor-trailer truck

Case	Observed value f (N)	Predicted value f_{RS} (N)	Residual ϵ	Leverage	Cook's distance
1	1.2285E+06	1.2302E+06	-1.6527E+03	0.90345	0.180
2	2.5005E+06	2.5614E+06	-6.0891E+04	0.705627	0.008
3	2.2995E+06	2.2926E+06	6.8861E+03	0.927336	0.000
4	1.7274E+06	1.6751E+06	5.2292E+04	0.777987	0.035
5	1.3252E+06	1.3164E+06	8.7883E+03	0.795262	0.010
6	2.8214E+06	2.7653E+06	5.6084E+04	0.714548	0.050
7	2.3703E+06	2.3831E+06	-1.2838E+04	0.74298	0.002
8	2.0344E+06	1.9625E+06	7.1872E+04	0.549038	0.032
9	1.6051E+06	1.6264E+06	-2.1322E+04	0.853199	0.002
10	2.0041E+06	2.0131E+06	-9.0353E+03	0.853714	0.016

11	3.5847E+06	3.5531E+06	3.1630E+04	0.389184	0.021
12	3.0335E+06	3.0442E+06	-1.0676E+04	0.871802	0.004
13	2.5215E+06	2.5093E+06	1.2165E+04	0.451569	0.001
14	3.6278E+06	3.6281E+06	-2.9709E+02	0.9002	0.007
15	1.9536E+06	1.8594E+06	9.4174E+04	0.704756	0.000
16	1.7415E+06	1.6166E+06	1.2487E+05	0.642504	0.000
17	1.8981E+06	1.7332E+06	1.6487E+05	0.493112	0.083
18	2.8853E+06	2.8854E+06	-8.4218E+01	0.425863	0.091
19	3.4272E+06	3.3429E+06	8.4314E+04	0.57892	0.060
20	2.8853E+06	2.8854E+06	-8.4218E+01	0.425863	0.000
21	1.9003E+06	1.9956E+06	-9.5254E+04	0.813376	0.027
22	3.5437E+06	3.5562E+06	-1.2468E+04	0.436102	0.000
23	1.5052E+06	1.5526E+06	-4.7364E+04	0.743352	0.246
24	2.4729E+06	2.5724E+06	-9.9522E+04	0.851168	0.000
25	2.5510E+06	2.6452E+06	-9.4243E+04	0.882071	0.029
26	1.3999E+06	1.4442E+06	-4.4304E+04	0.844778	0.441
27	3.5092E+06	3.3721E+06	1.3712E+05	0.480109	0.653
28	2.7548E+06	2.8355E+06	-8.0670E+04	0.777169	0.080
29	2.6637E+06	2.6464E+06	1.7299E+04	0.455562	0.039
30	3.2134E+06	3.0324E+06	1.8096E+05	0.527702	0.118
31	3.4803E+06	3.5467E+06	-6.6474E+04	0.790146	0.001
32	2.2011E+06	2.1168E+06	8.4286E+04	0.822773	0.090
33	1.8325E+06	1.9285E+06	-9.6018E+04	0.867853	0.092
34	2.6637E+06	2.6464E+06	1.7299E+04	0.455562	0.216
35	3.2187E+06	3.3077E+06	-8.9038E+04	0.759339	0.531
36	3.5898E+06	3.6753E+06	-8.5547E+04	0.825421	0.001
37	3.2495E+06	3.2571E+06	-7.5802E+03	0.821222	0.121
38	1.9843E+06	1.9538E+06	3.0518E+04	0.851694	0.230
39	3.2817E+06	3.2617E+06	2.0036E+04	0.83058	0.002
40	3.5847E+06	3.5531E+06	3.1630E+04	0.389184	0.042
41	3.5437E+06	3.5562E+06	-1.2468E+04	0.436102	0.013
42	3.3439E+06	3.3076E+06	3.6308E+04	0.753894	0.001
43	3.5722E+06	3.4217E+06	1.5046E+05	0.758516	0.000
44	3.5934E+06	3.6048E+06	-1.1367E+04	0.4475	0.019
45	3.4939E+06	3.5302E+06	-3.6345E+04	0.686977	0.341
46	3.5934E+06	3.6048E+06	-1.1367E+04	0.4475	0.000
47	1.3423E+06	1.6582E+06	-3.1590E+05	0.270847	0.011
48	2.3863E+06	2.3381E+06	4.8207E+04	0.102633	0.000
49	2.8580E+06	2.8517E+06	6.2771E+03	0.082175	0.059
50	3.1123E+06	3.1990E+06	-8.6798E+04	0.105811	0.000
51	3.5218E+06	3.3801E+06	1.4169E+05	0.281627	0.000
52	2.8298E+06	2.9034E+06	-7.3630E+04	0.269809	0.001
53	2.8663E+06	2.8393E+06	2.6956E+04	0.328829	0.013
54	2.7753E+06	2.9831E+06	-2.0785E+05	0.311421	0.003
55	2.9915E+06	2.9435E+06	4.7951E+04	0.238555	0.001
56	2.8389E+06	2.9961E+06	-1.5721E+05	0.307047	0.033
57	2.8461E+06	2.6672E+06	1.7888E+05	0.328641	0.001
58	2.9086E+06	3.0588E+06	-1.5022E+05	0.281207	0.018

59	2.5847E+06	2.8809E+06	-2.9626E+05	0.317321	0.027
60	2.8485E+06	2.6247E+06	2.2380E+05	0.325609	0.014
61	2.8627E+06	2.8150E+06	4.7744E+04	0.347093	0.069
62	2.8173E+06	2.7749E+06	4.2366E+04	0.295466	0.042
63	2.8025E+06	2.6854E+06	1.1703E+05	0.343343	0.002
Standard deviation		1.548E+05			
Mean value (N)		2.705E+06			
R^2		0.9779			
RMSE		0.00472			

6.3 Summary

Based on the study in this chapter, it shows that both the simplified model of mass-spring system, and the response surface model could be applied to the approximate impact force. The simplified mass-spring model is suitable to obtain the time history of the impact force. However, appropriate assumption must be made for the spring stiffness and damper. Besides, it is very hard to include the shear failure into the simulation while it is the common failure mechanism during truck-to-pier impact. To finish the calculation of the explicit analysis, computer-aided computation is required. Also, for each different truck and pier, the individual case-by-case analysis is needed.

Relatively, the response surface model can provide an approximation equation for impact load, which is convenient and easy to be applied to different impact scenario by varying the value of parameters, if only the parameters have been included into the model in advance. However, the response surface mode cannot be applied to the time history, while it is good at getting the response of key index. Another drawback is that prerequisite database is needed for the regression analysis. Sometimes, a large number of design points are required in order to increase the precision of the fitting function. If the response has large discreteness, the regression model may be trapped in finding better fitting.

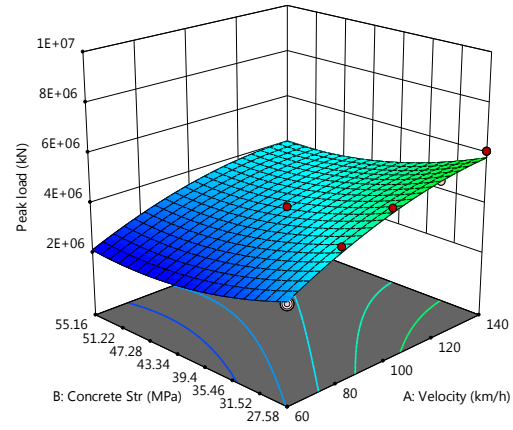

(a) A:B

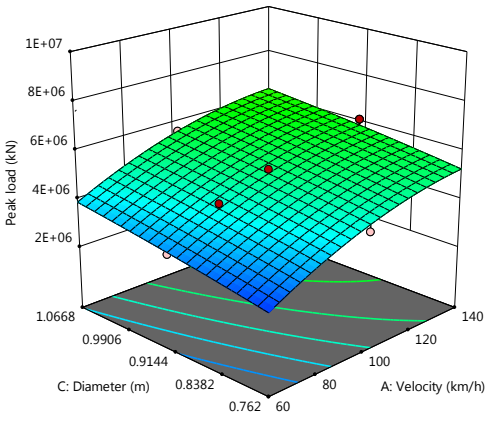

(b) A:C

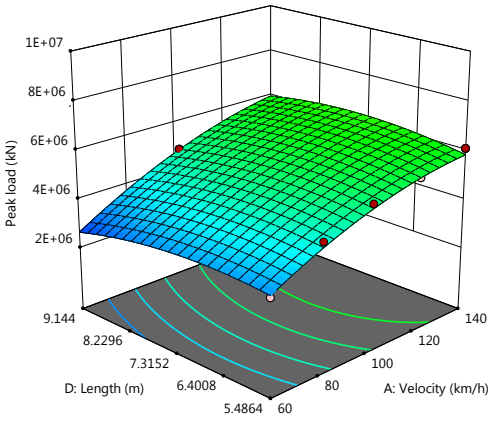

(c) A:D

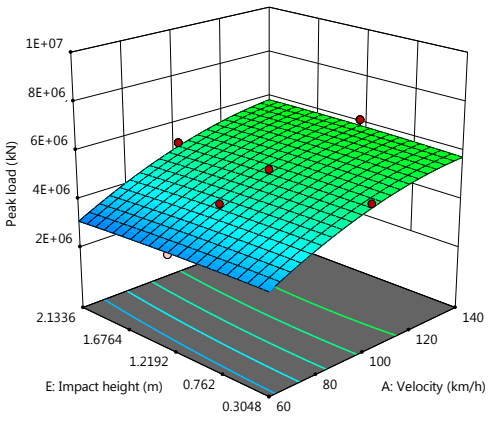

(d) A:E

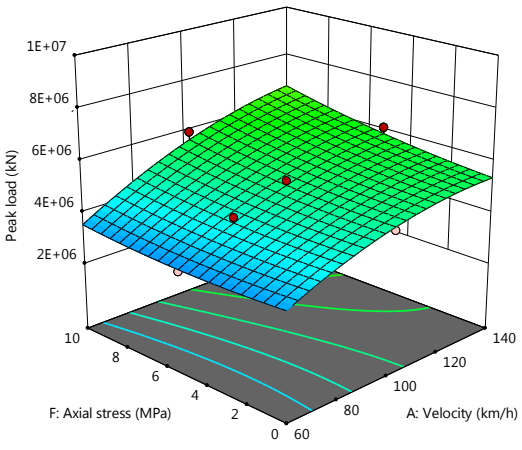

(e) A:F

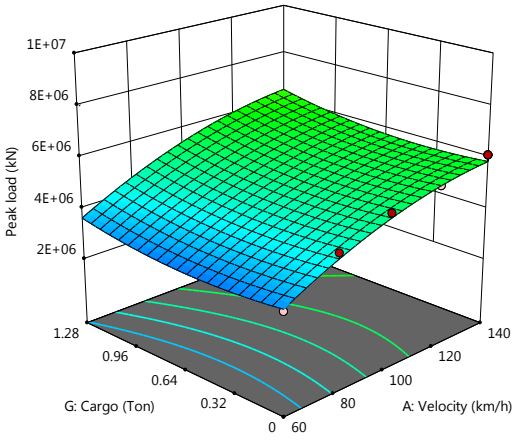

(f) A:G

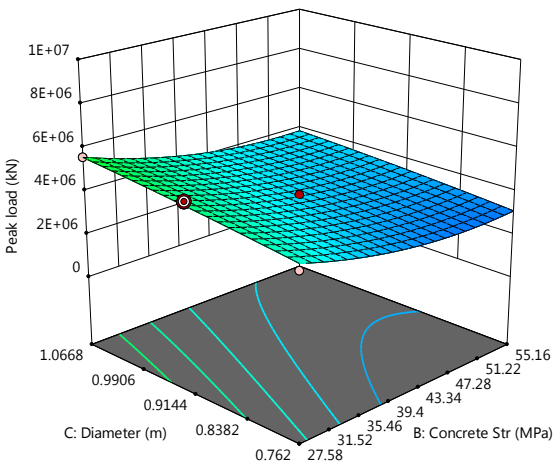

(g) B:C

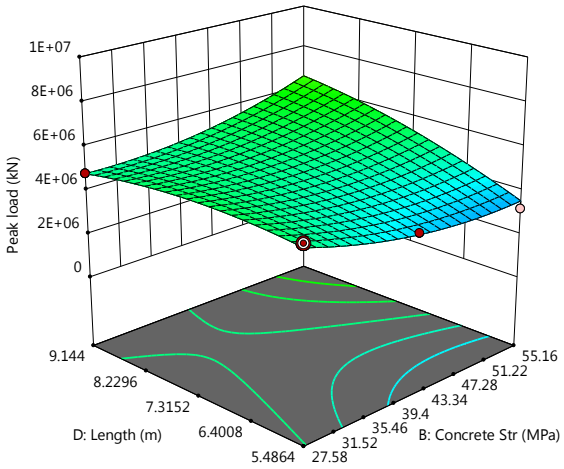

(h) B:D

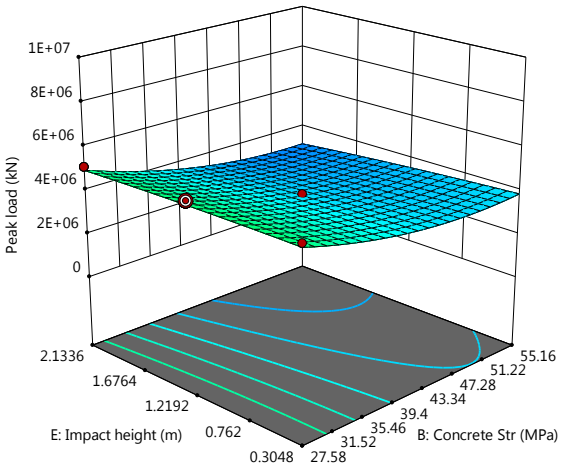

(i) B:E

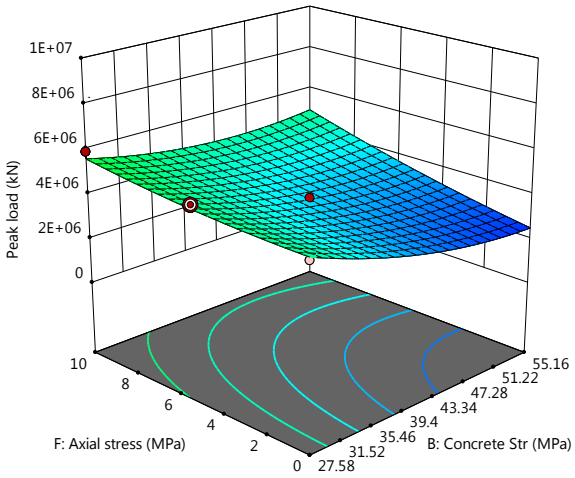

(j) B:F

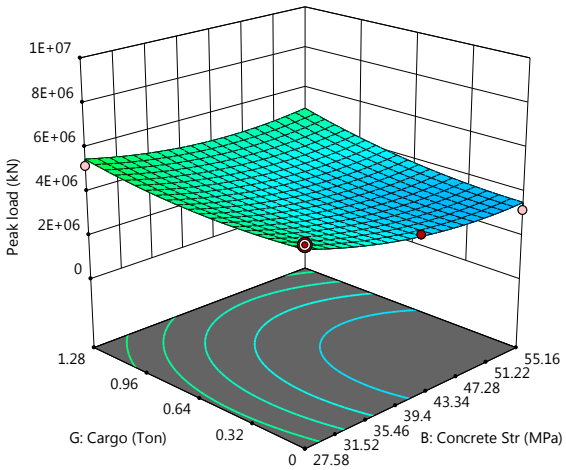

(k) B:G

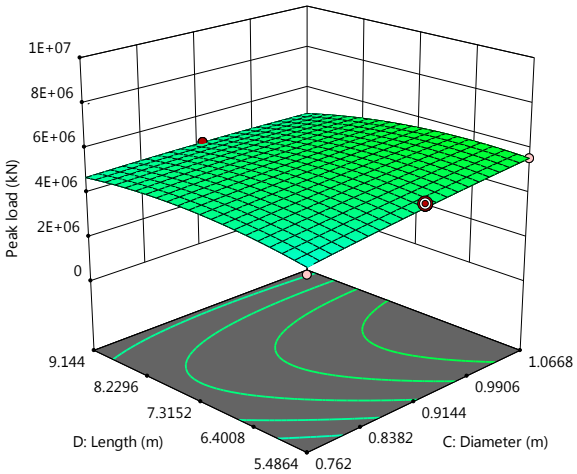

(l) C:D

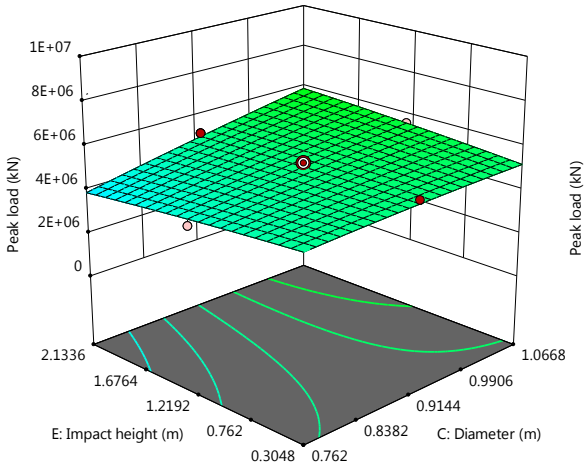

(m) C:E

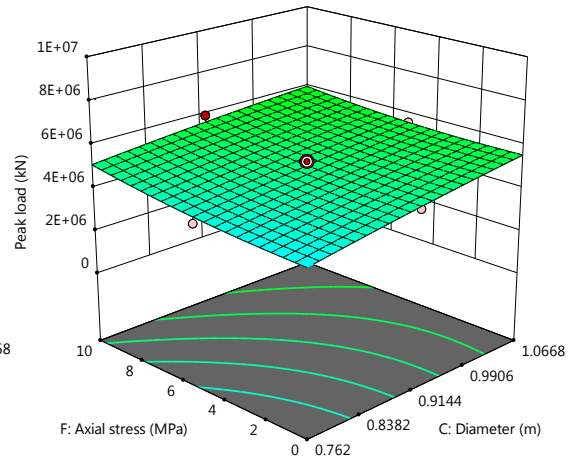

(n) C:F

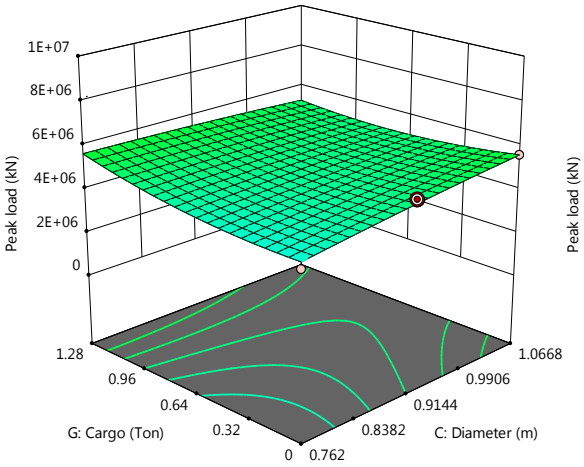

(o) C:G

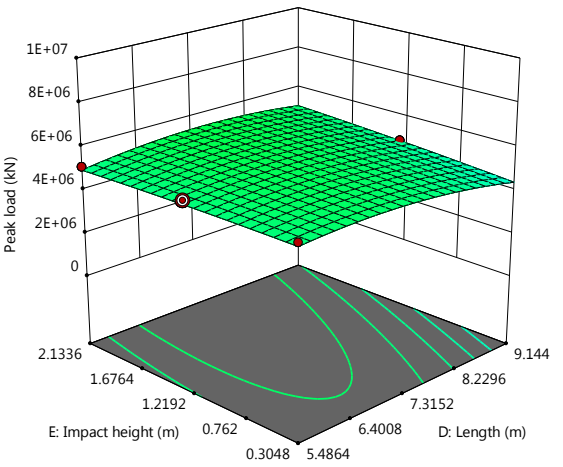

(p) D:E

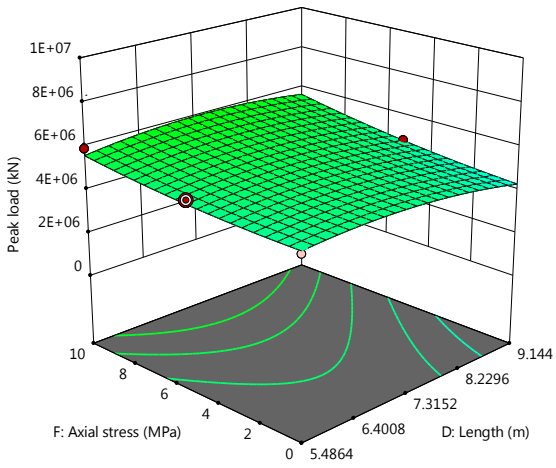

(q) D:F

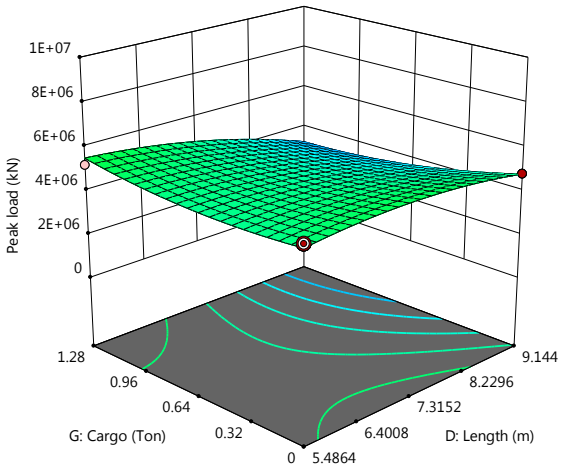

(r) D:G

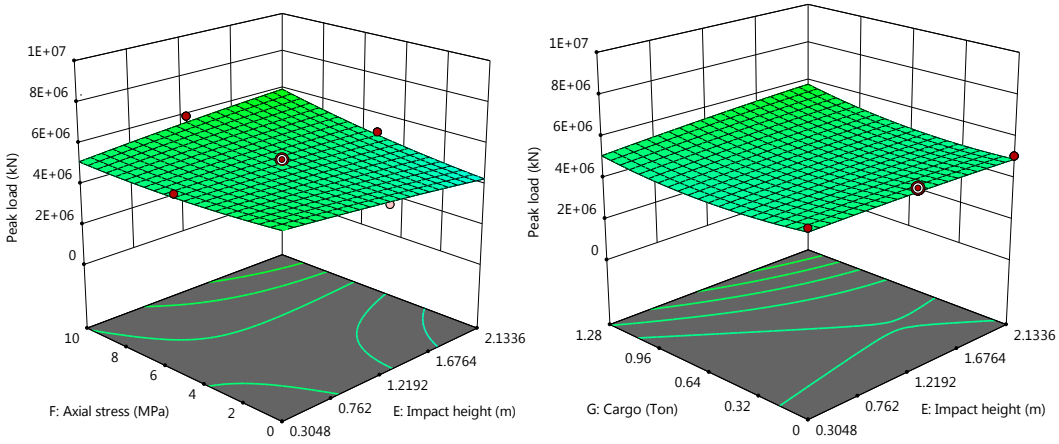

(s) E:F (t) E:G

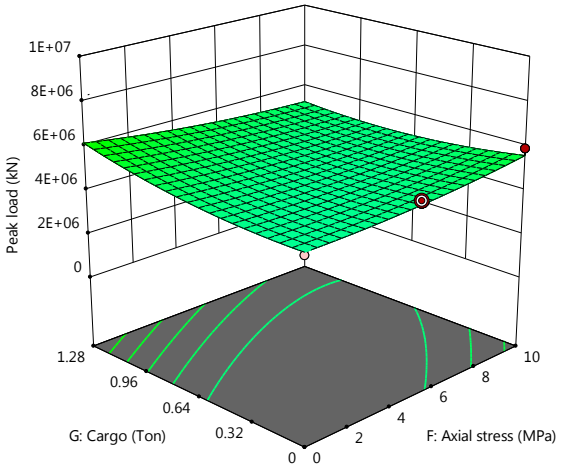

(u) F:G

Figure 6-14 3D response surface plot of peak dynamic load of C2500

(Basic parameters: A=100km/h, B=27.58MPa, C=0.9144m, D=5.4864m, E=1.2192m, F=5MPa, G=0 ton)

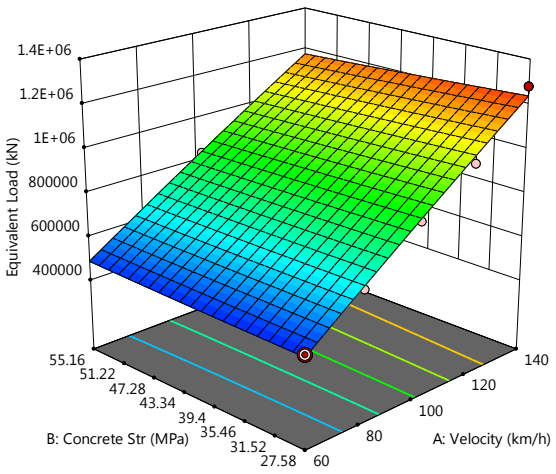

(a) A:B

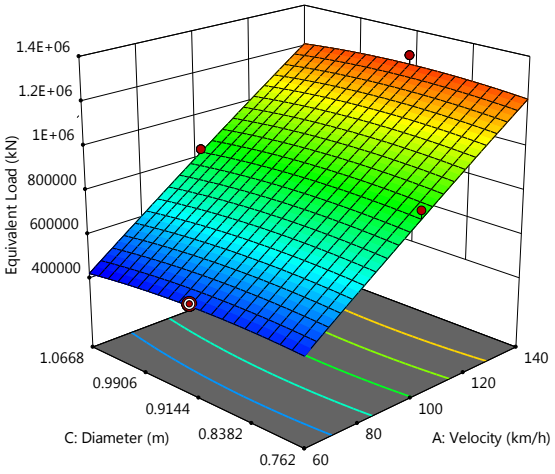

(b) A:C

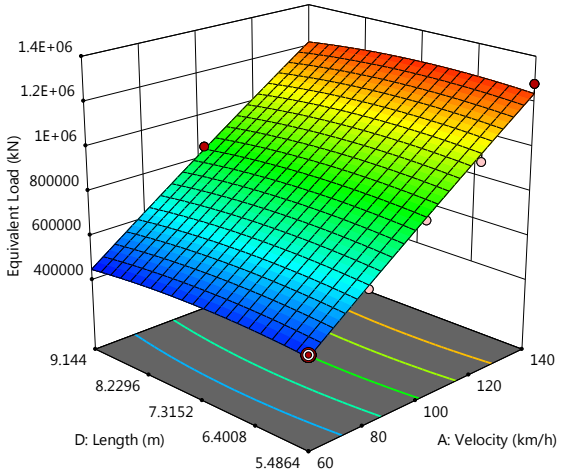

(c) A:D

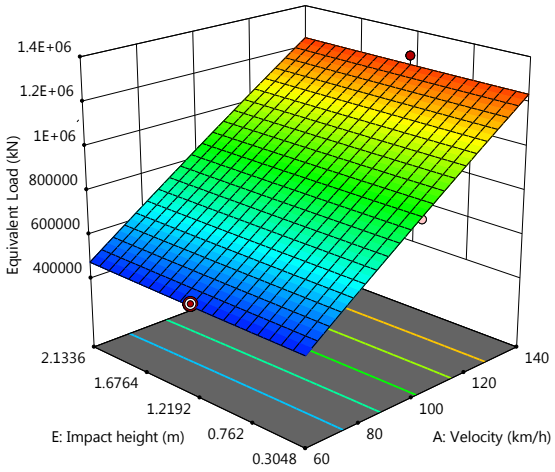

(d) A:E

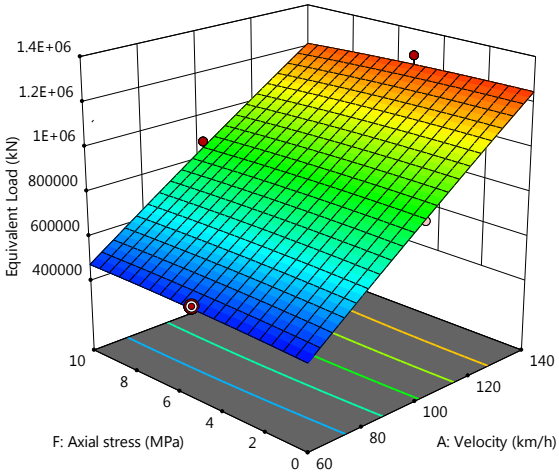

(e) A:F

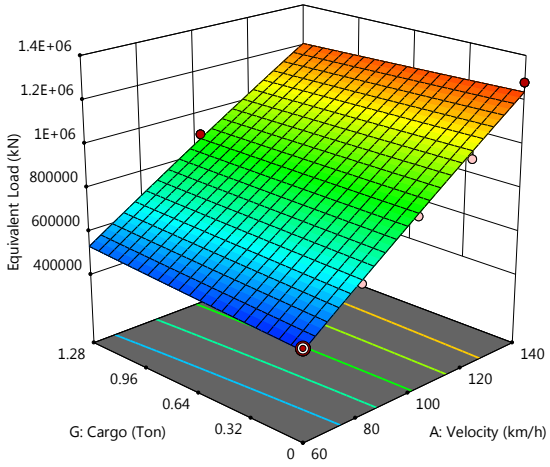

(f) A:G

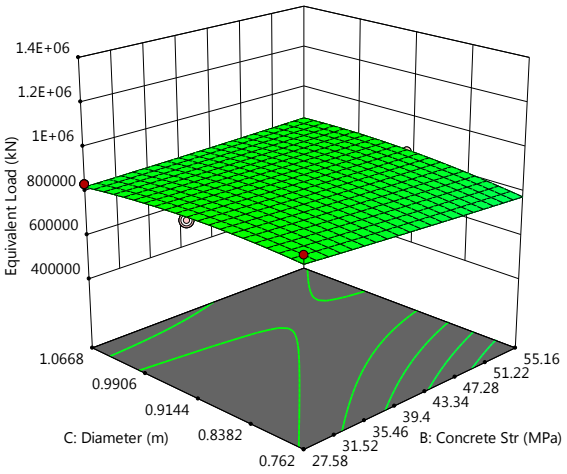

(g) B:C

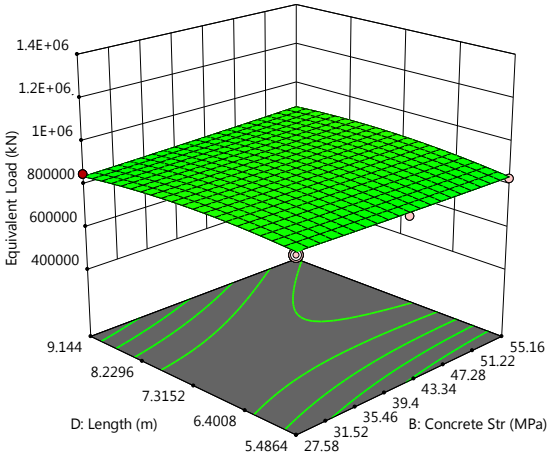

(h) B:D

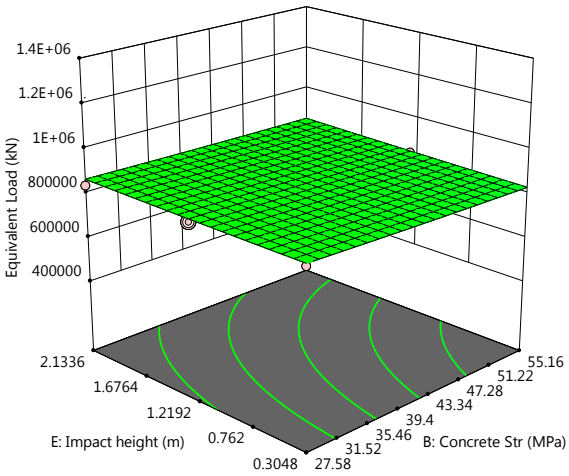

(i) B:E

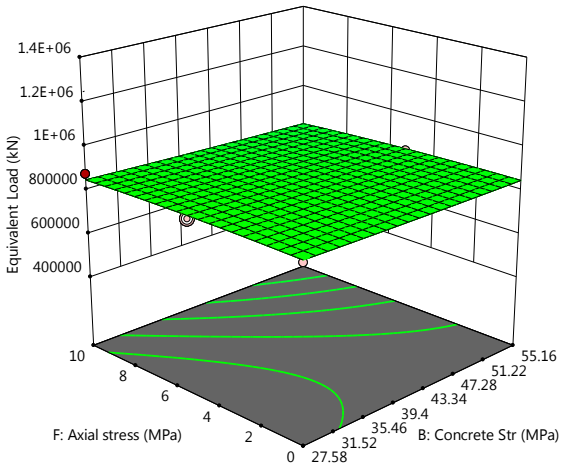

(j) B:F

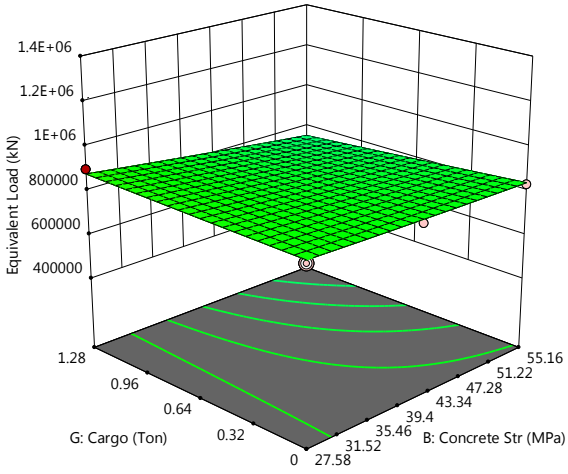

(k) B:G

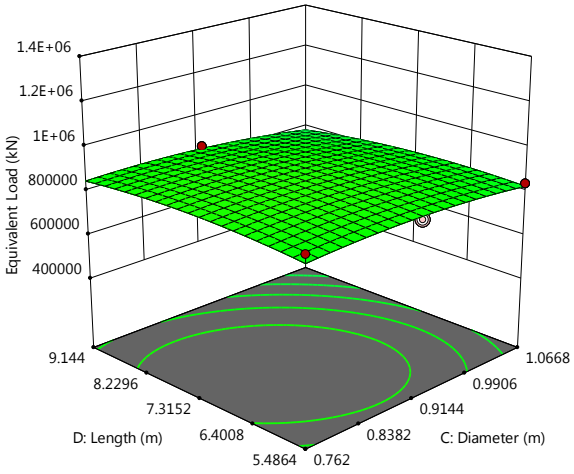

(l) C:D

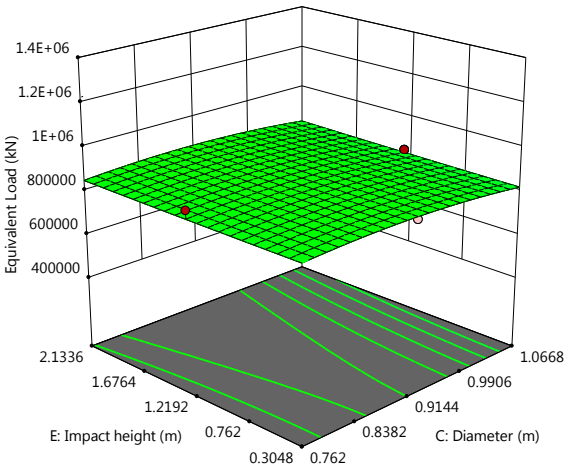

(m) C:E

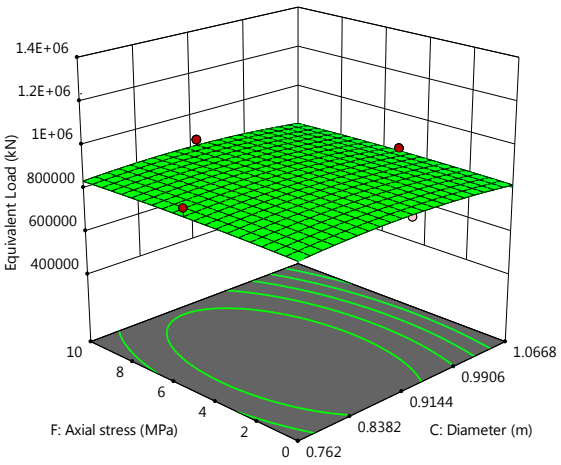

(n) C:F

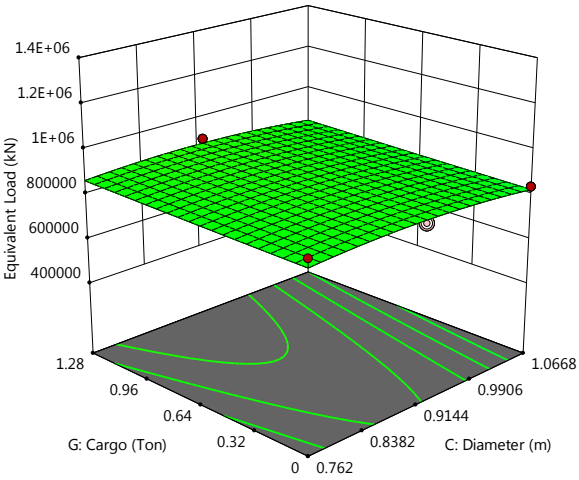

(o) C:G

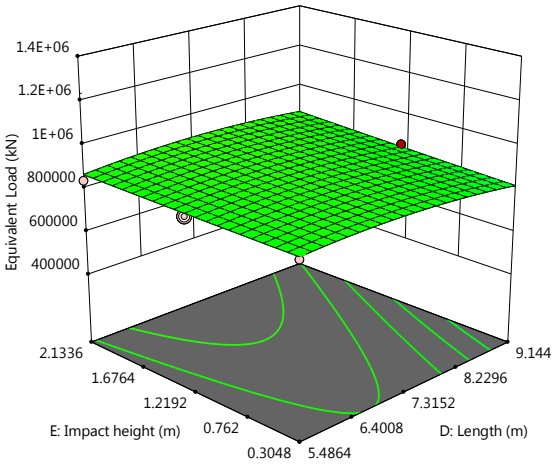

(p) D:E

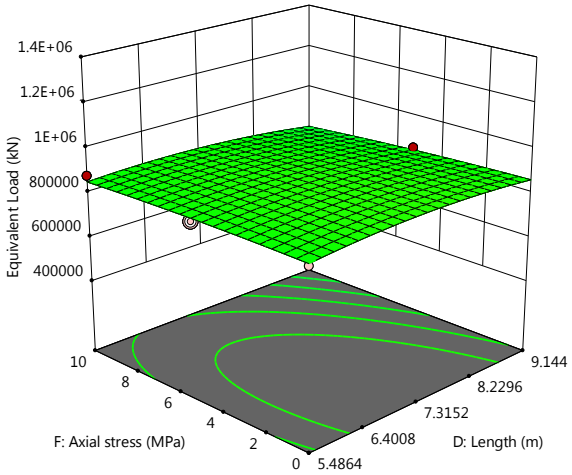

(q) D:F

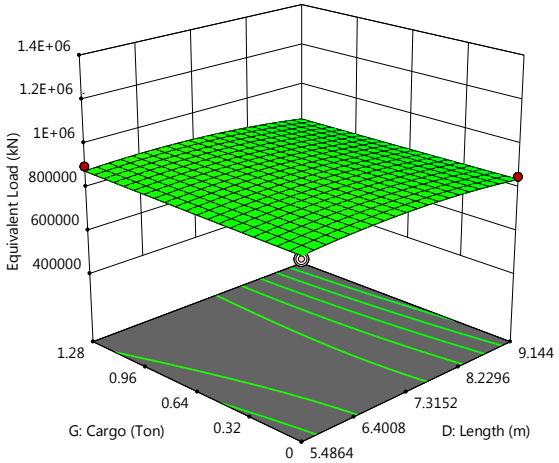

(r) D:G

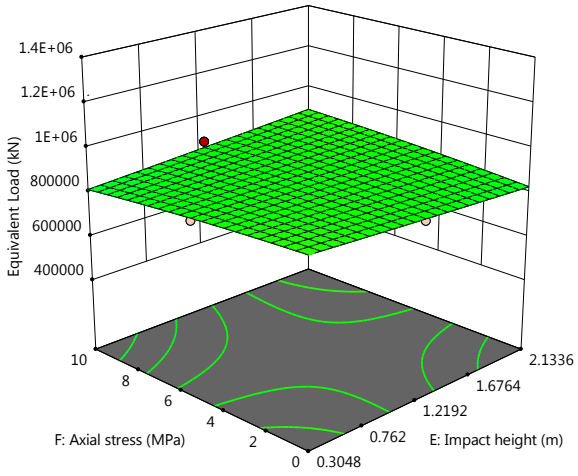

(s) E:F

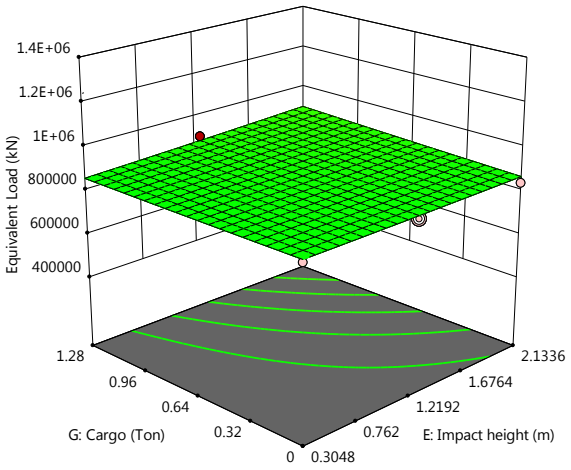

(t) E:G

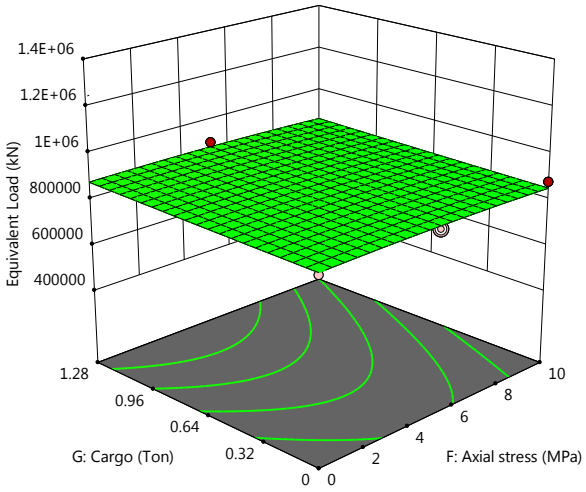

(u) F:G

Figure 6-15 3D response surface plot of equivalent static load of C2500

(Basic parameters: A=100km/h, B=27.58MPa, C=0.9144m, D=5.4864m, E=1.2192m, F=5MPa, G=0 ton)

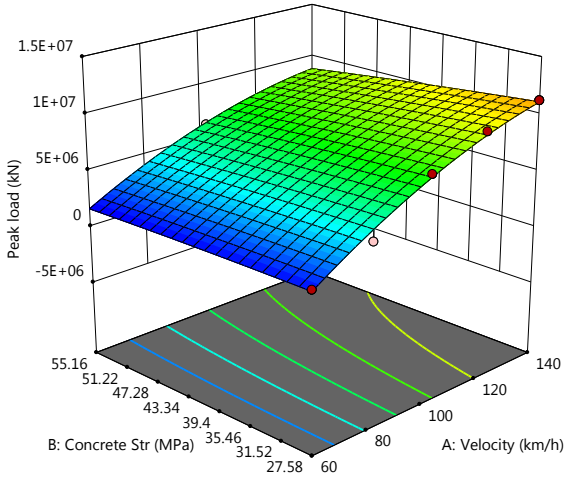

(a) A:B

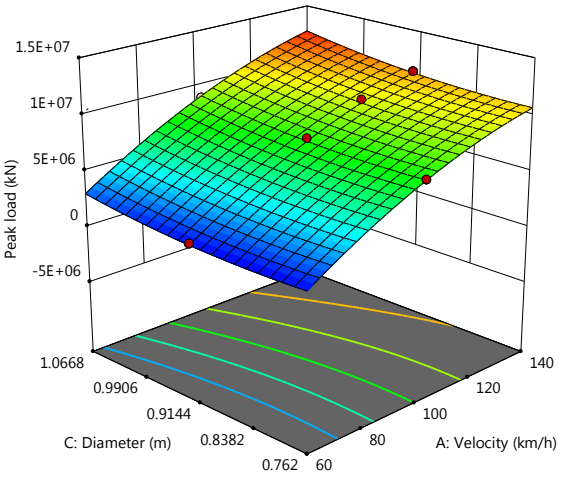

(b) A:C

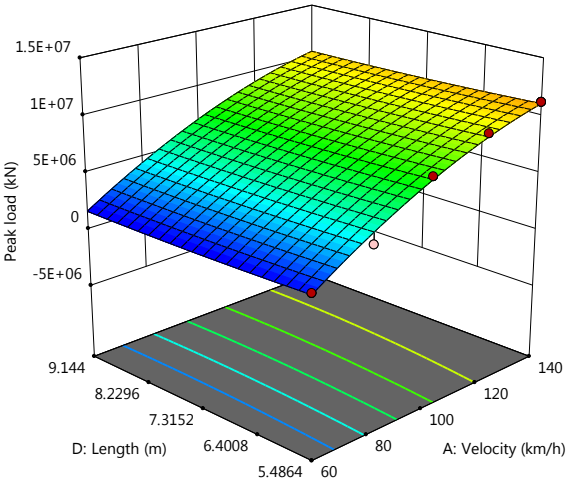

(c) A:D

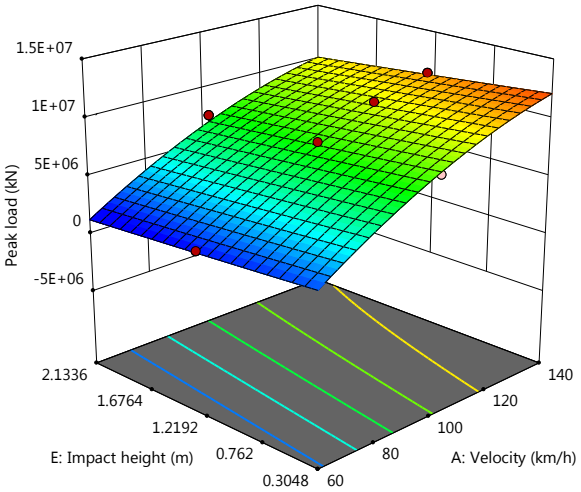

(d) A:E

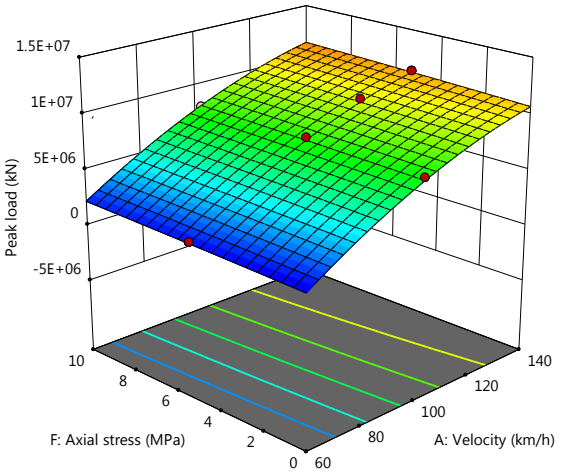

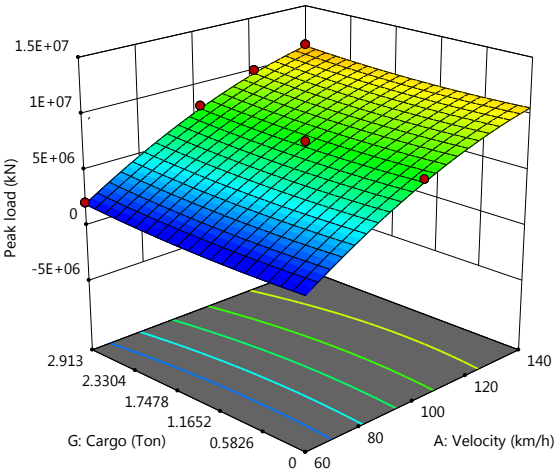

(e) A:F

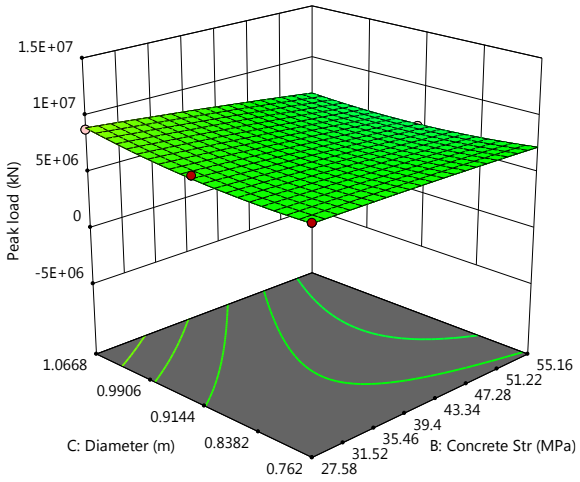

(f) A:G

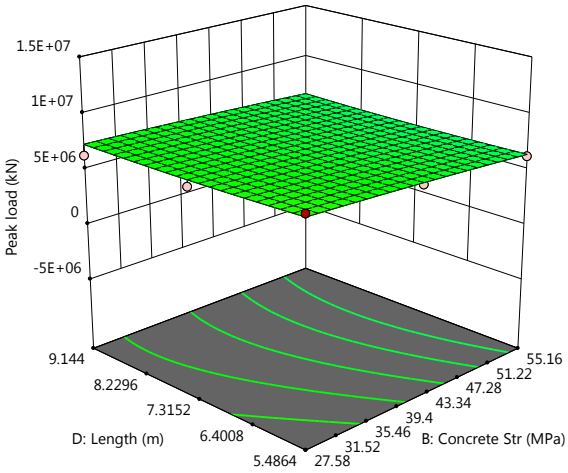

(g) B:C

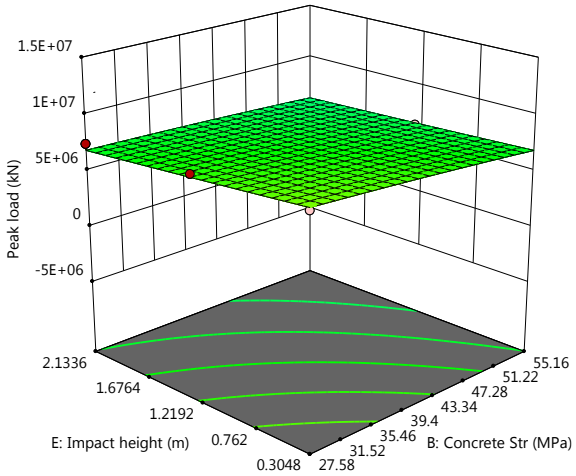

(h) B:D

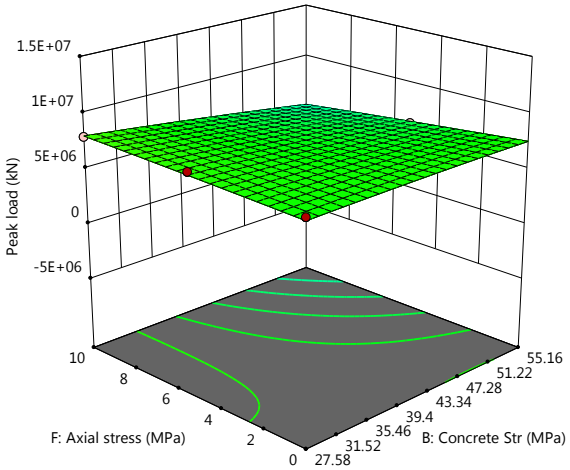

(i) B:E

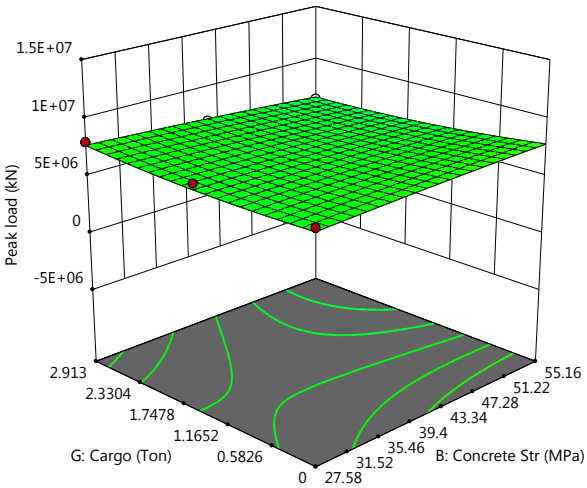

(j) B:F

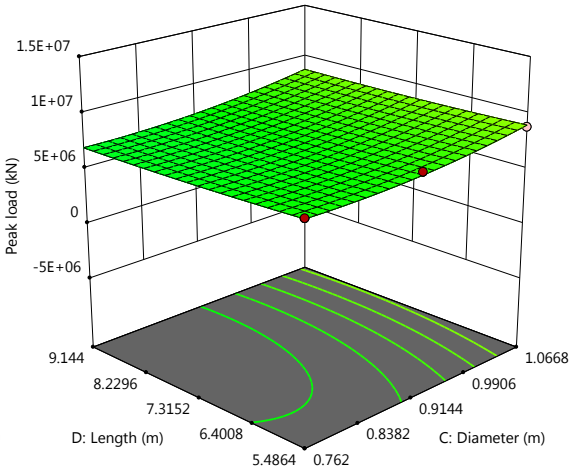

(k) B:G

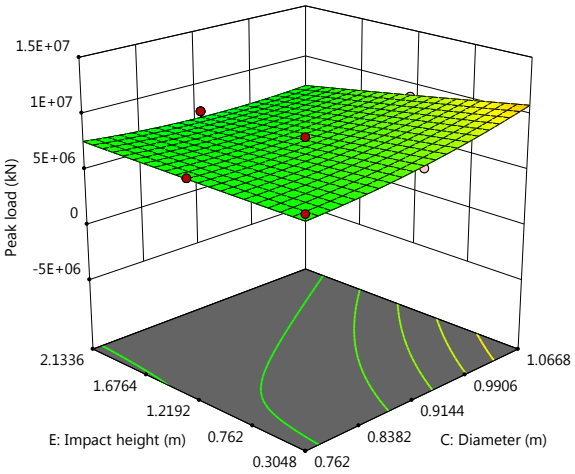

(l) C:D

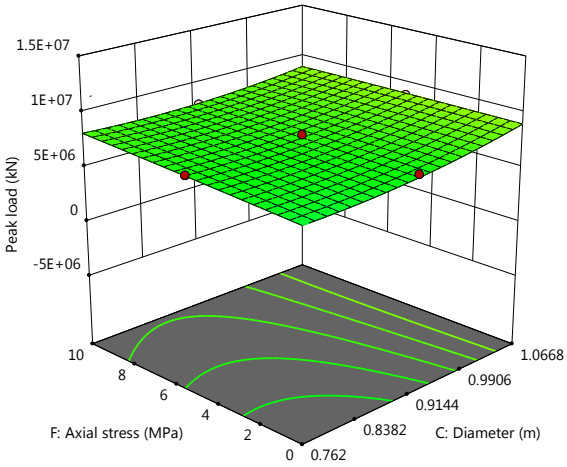

(m) C:E

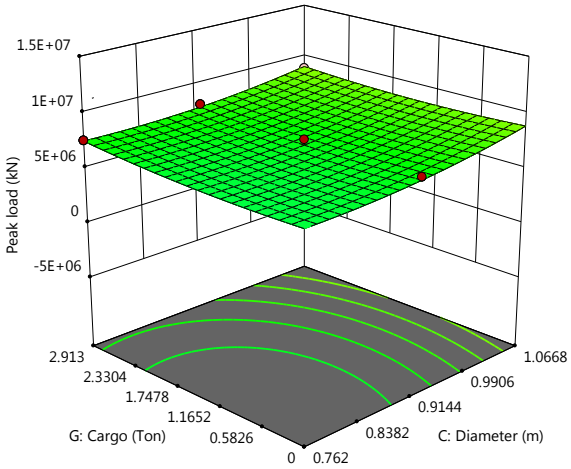

(n) C:F

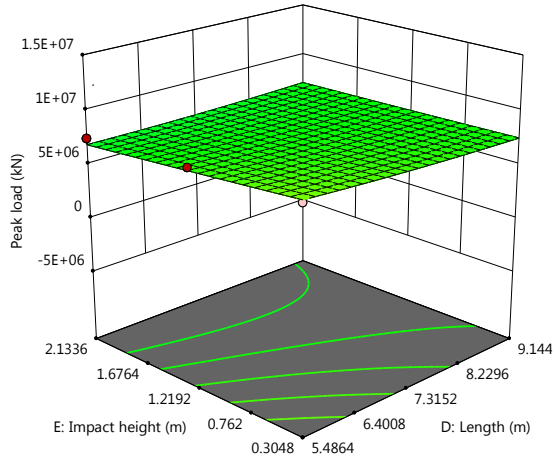

(o) C:G

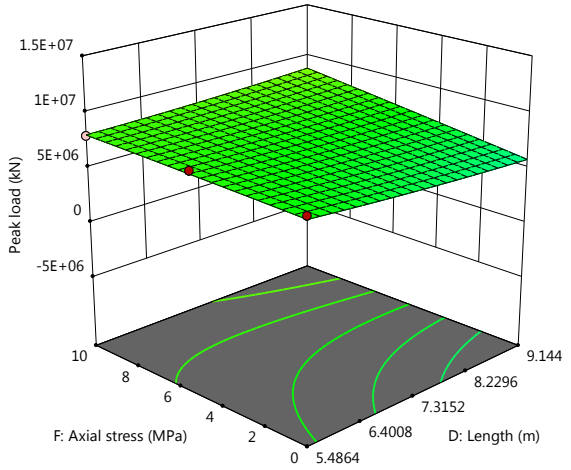

(p) D:E

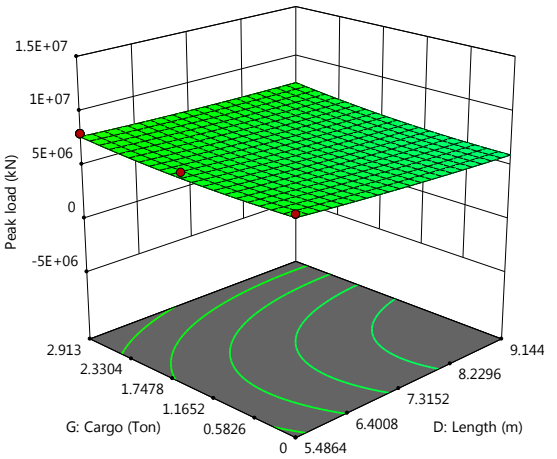

(q) D:F

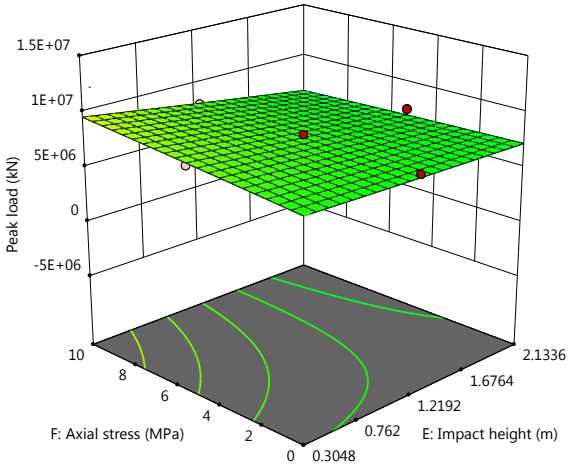

(r) D:G

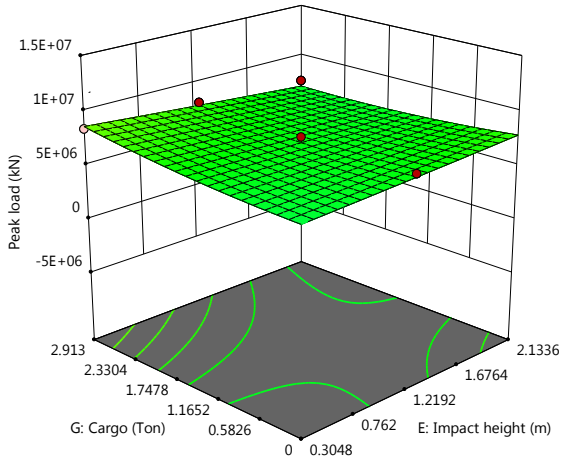

(s) E:F

(t) E:G

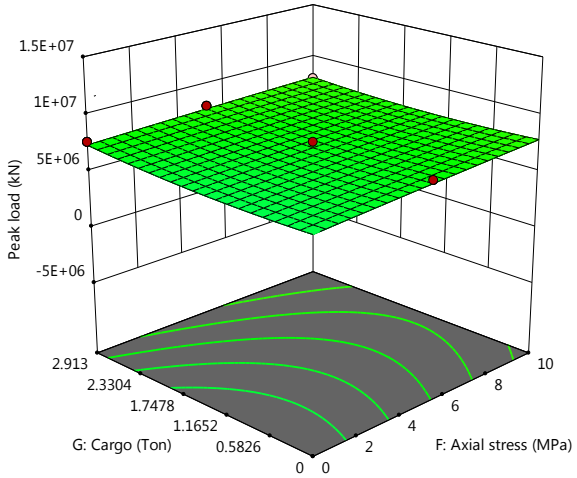

(u) F:G

Figure 6-16 3D response surface plot of peak dynamic load of F800

(Basic parameters: A=100km/h, B=27.58MPa, C=0.9144m, D=5.4864m, E=1.2192m, F=5MPa, G=2.913 ton)

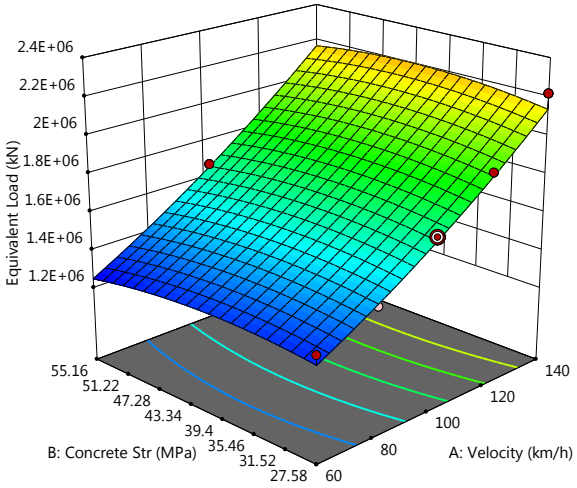

(a) A:B

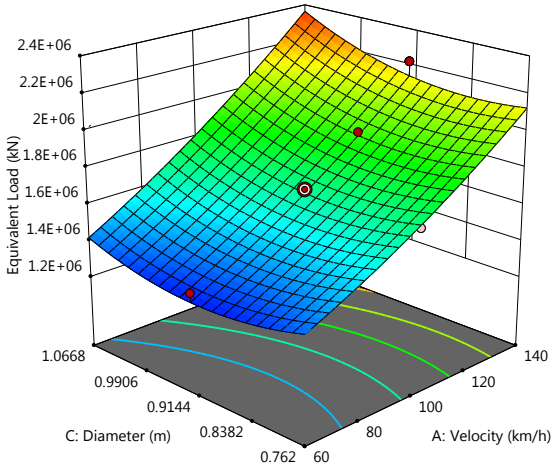

(b) A:C

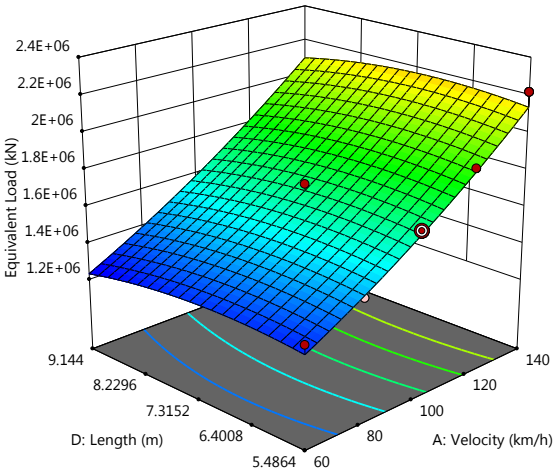

(c) A:D

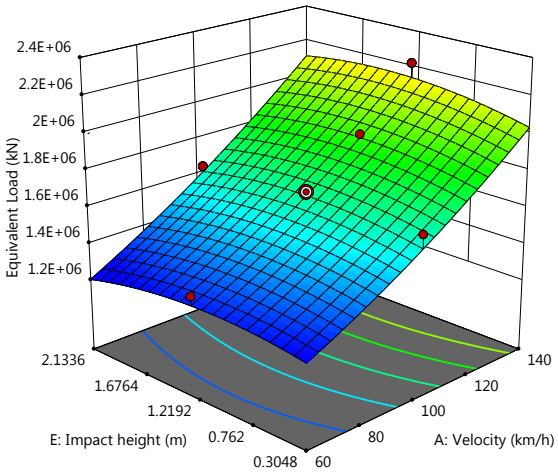

(d) A:E

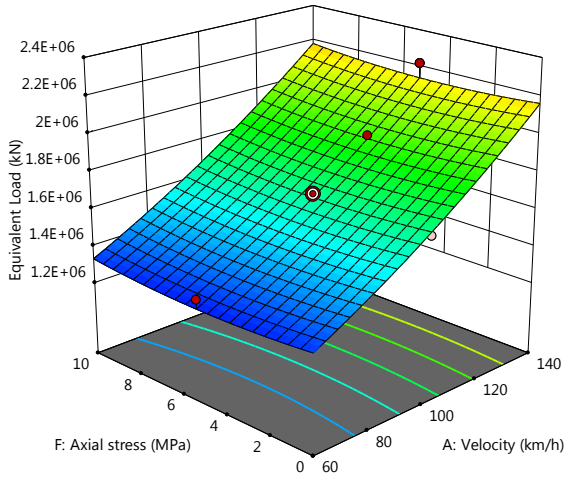

(e) A:F

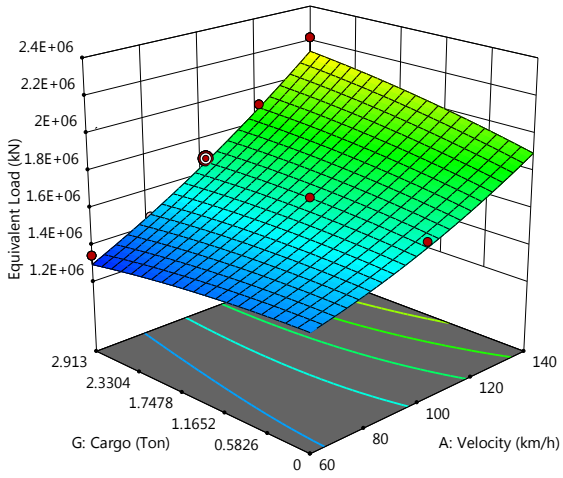

(f) A:G

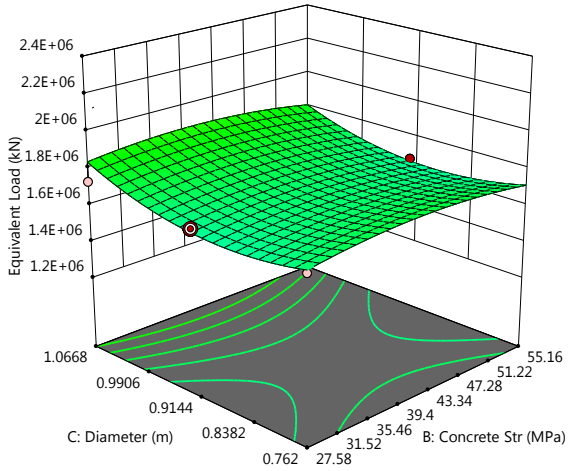

(g) B:C

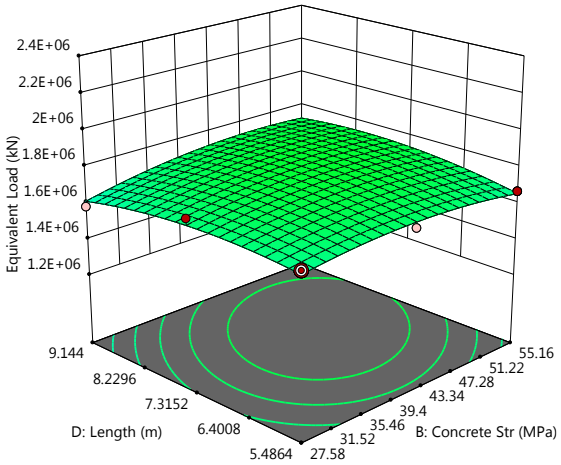

(h) B:D

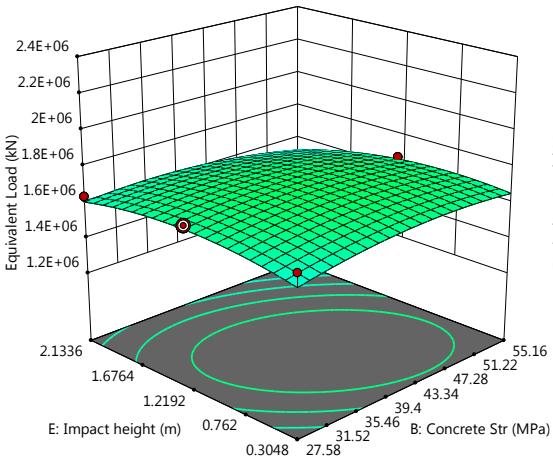

(i) B:E

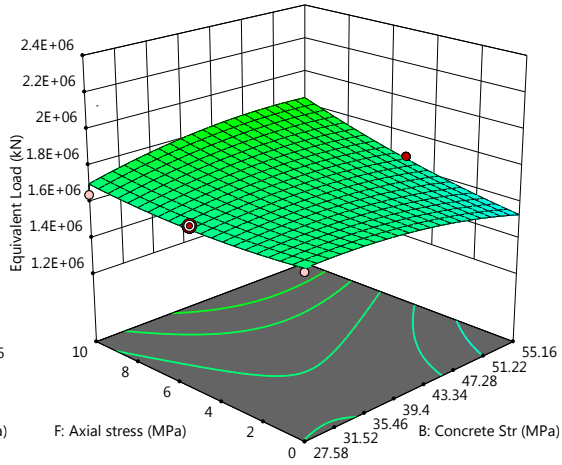

(j) B:F

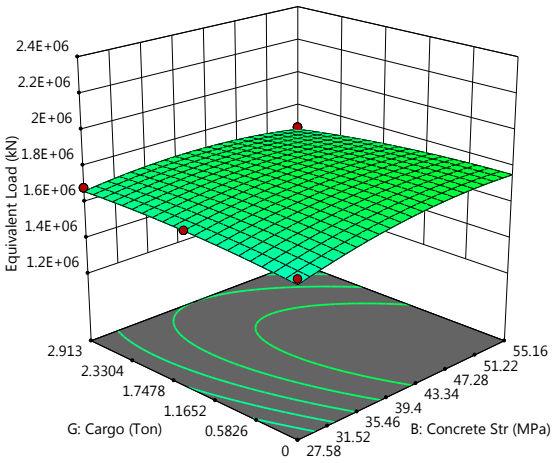

(k) B:G

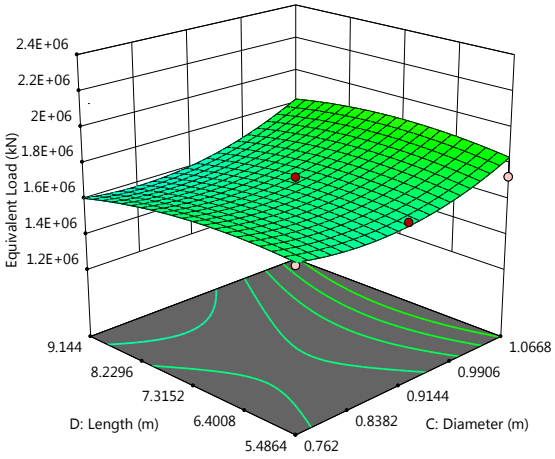

(l) C:D

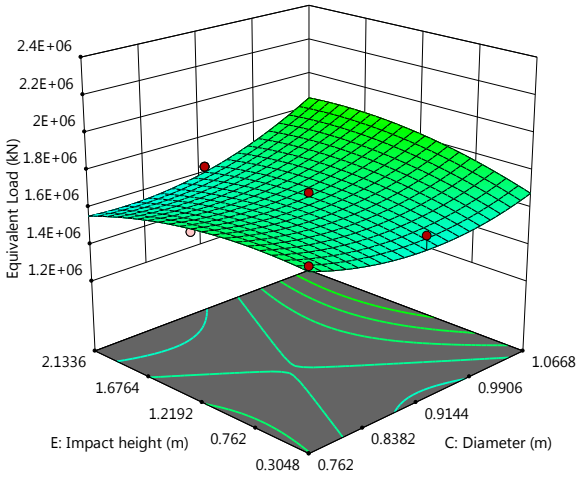

(m) C:E

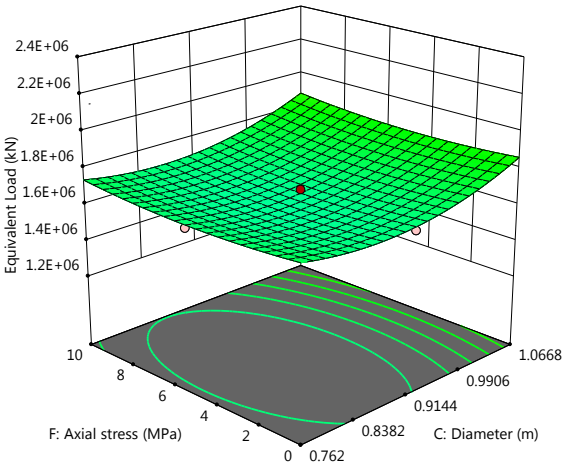

(n) C:F

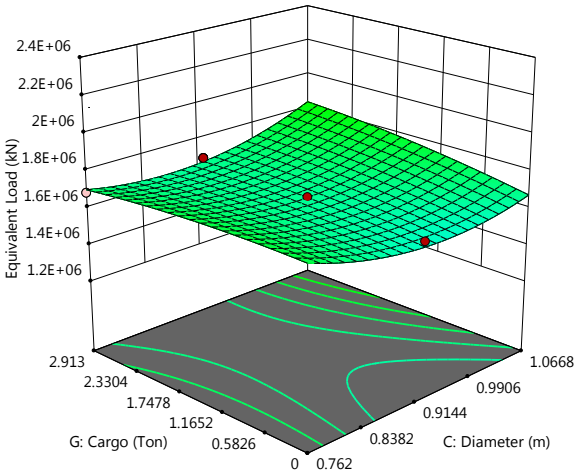

(o) C:G

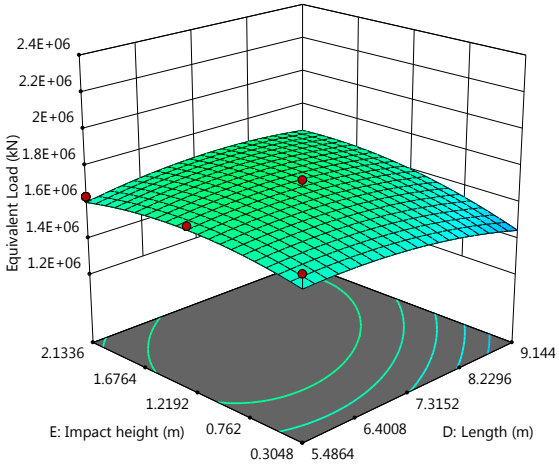

(p) D:E

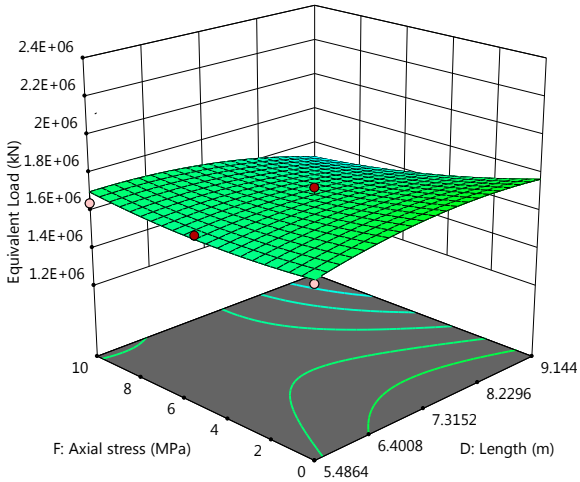

(q) D:F

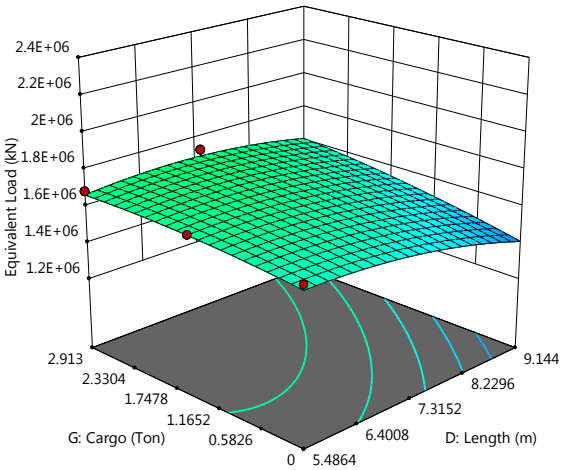

(r) D:G

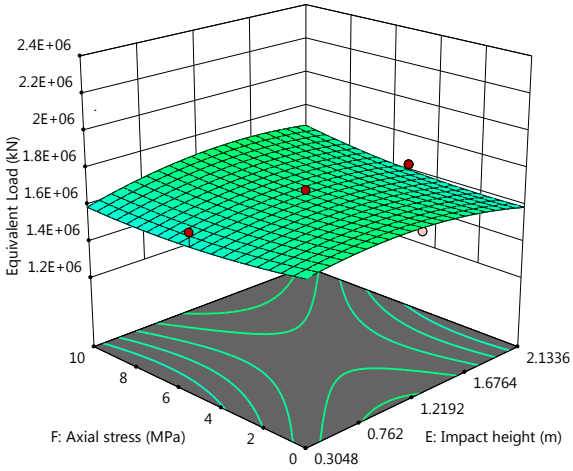

(s) E:F

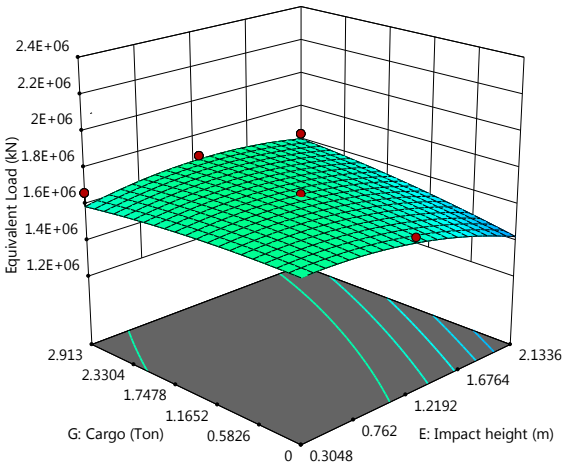

(t) E:G

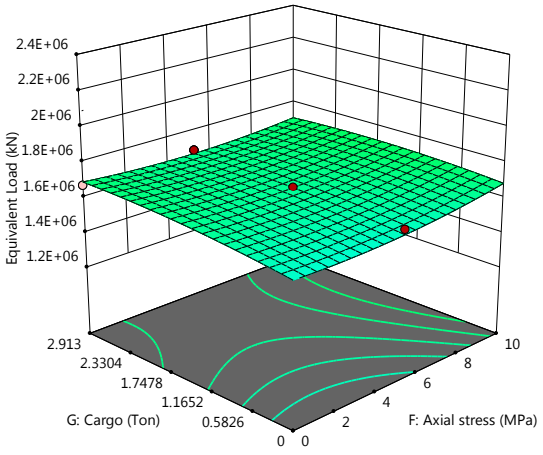

(u) F:G

Figure 6-17 3D response surface plot of equivalent static load of F800

(Basic parameters: A=100km/h, B=27.58MPa, C=0.9144m, D=5.4864m, E=1.2192m, F=5MPa, G=2.913 ton)

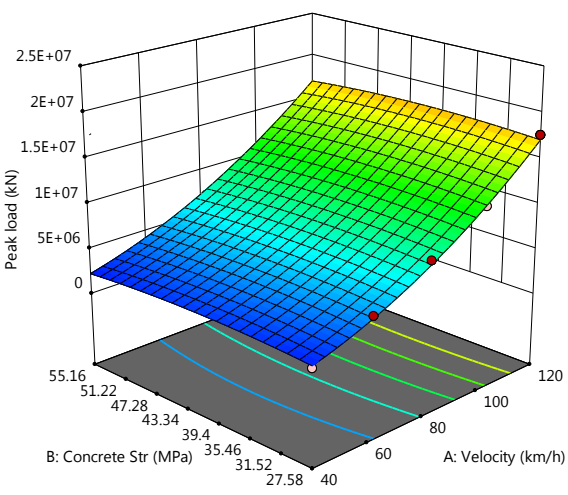

(a) A:B

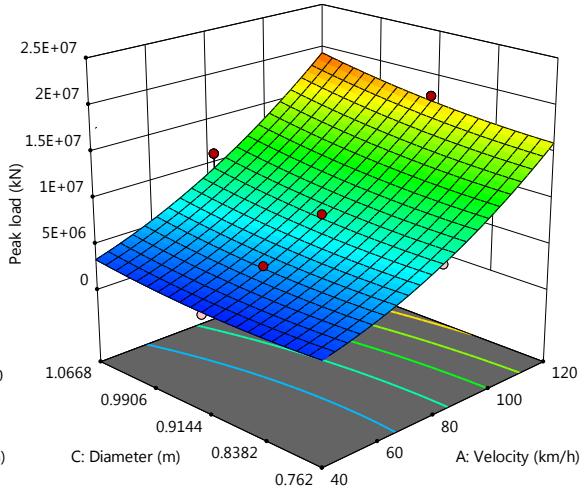

(b) A:C

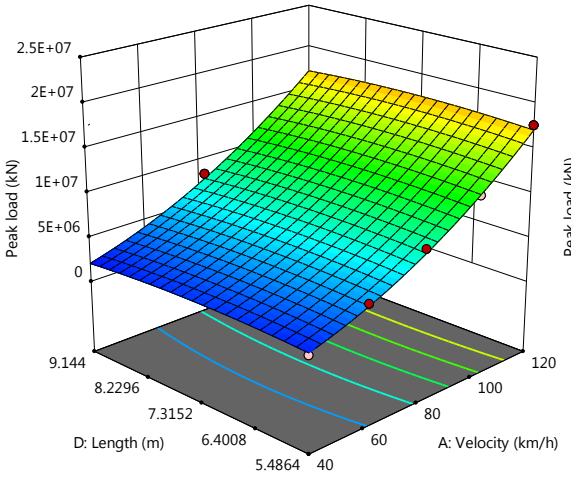

(c) A:D

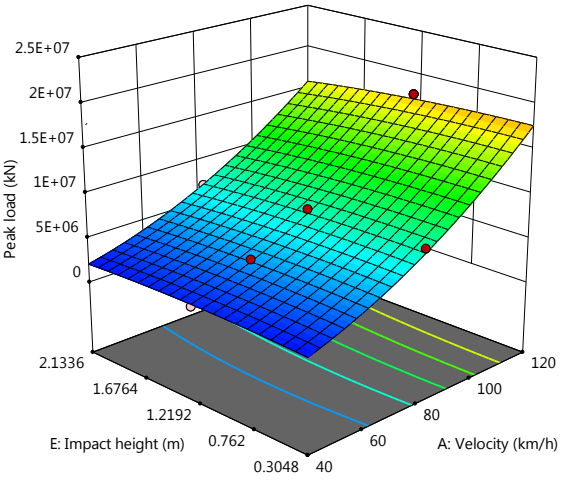

(d) A:E

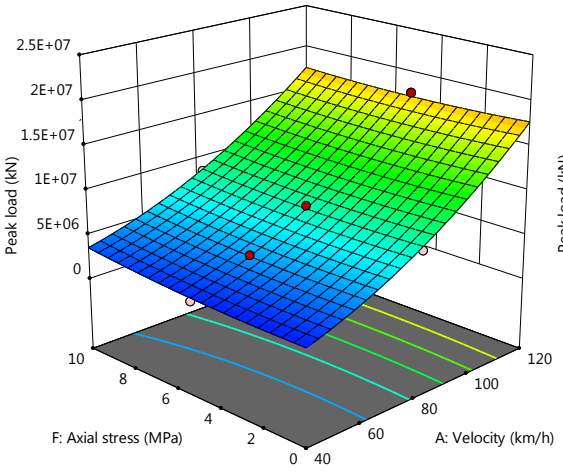

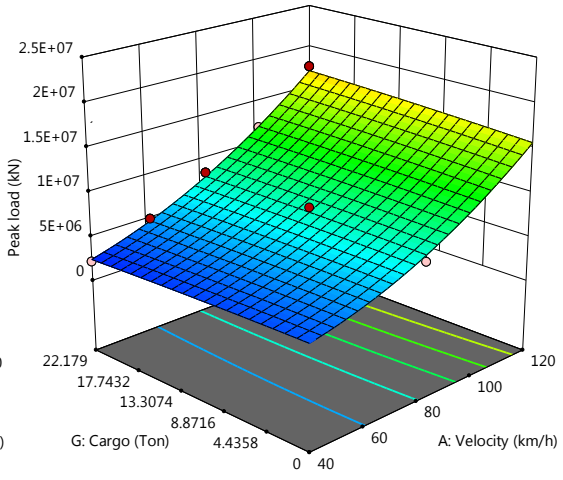

(e) A:F

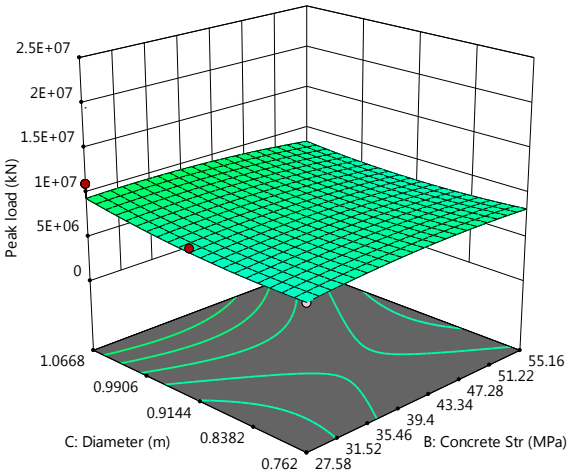

(f) A:G

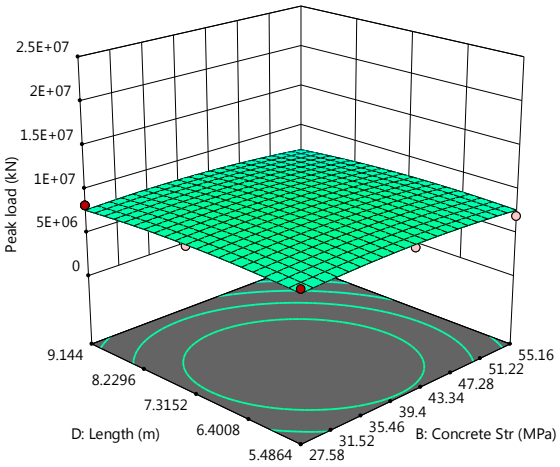

(g) B:C

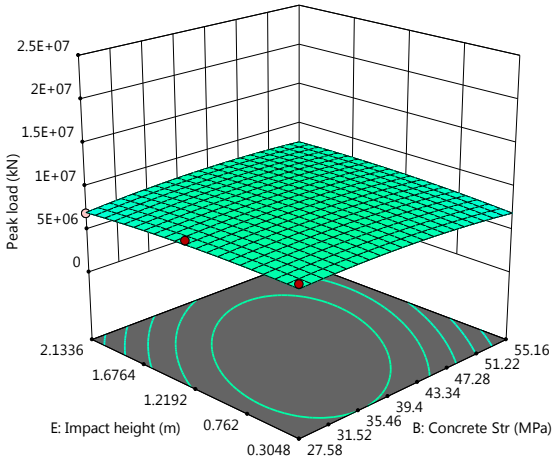

(h) B:D

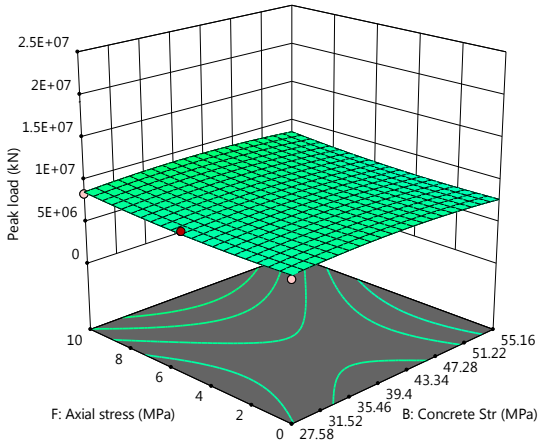

(i) B:E

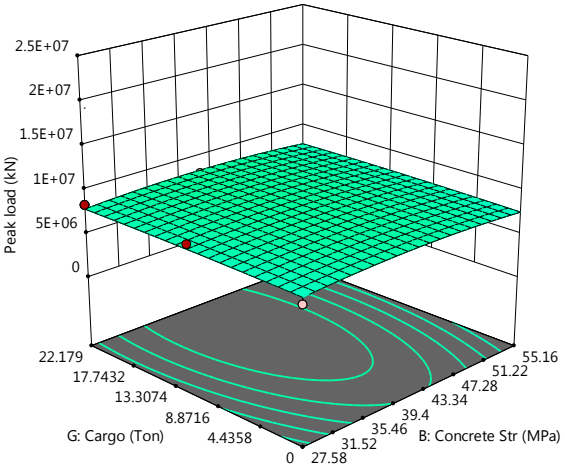

(j) B:F

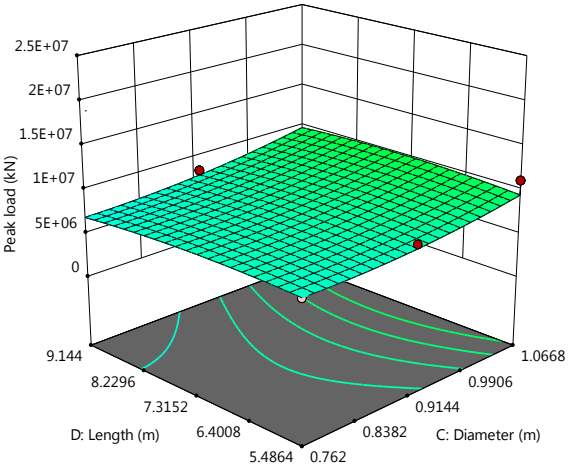

(k) B:G

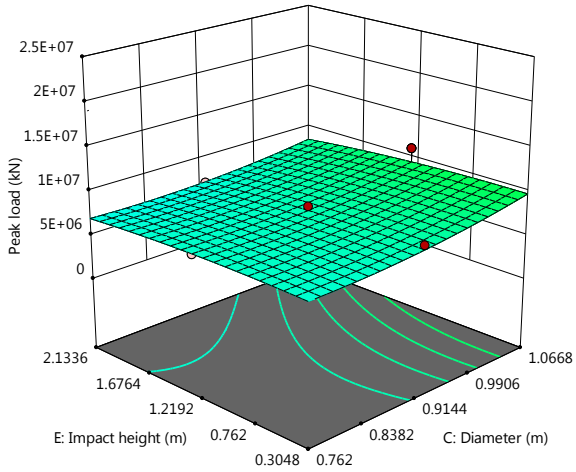

(l) C:D

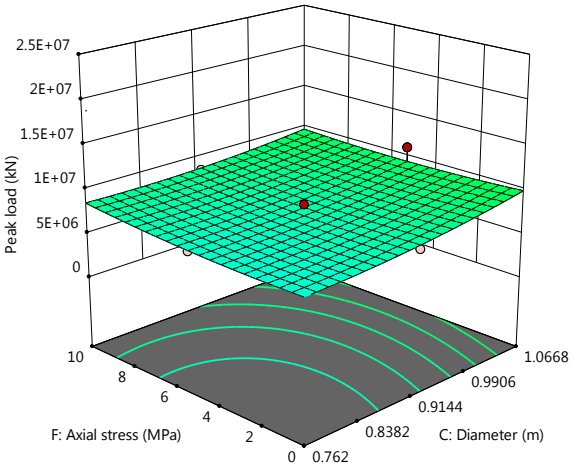

(m) C:E

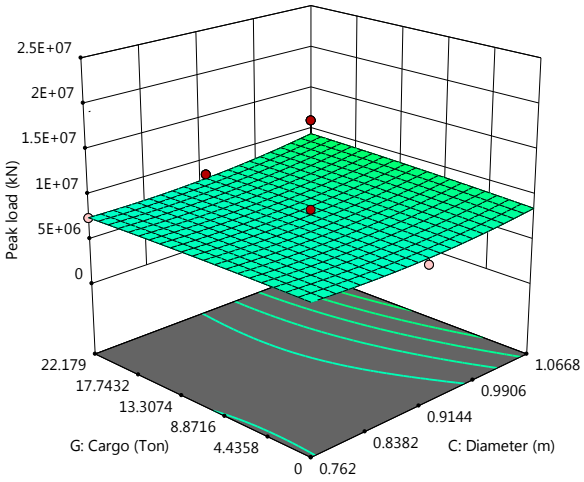

(n) C:F

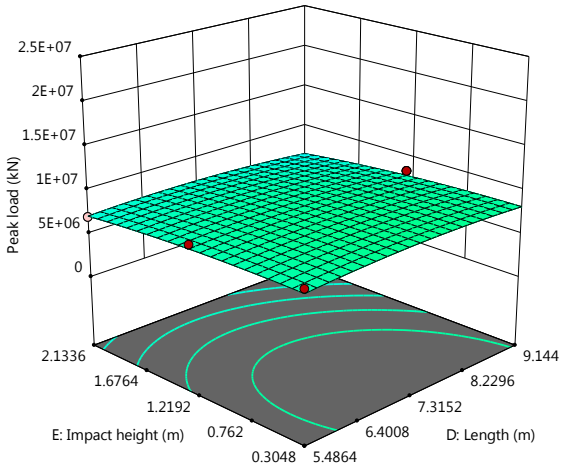

(o) C:G

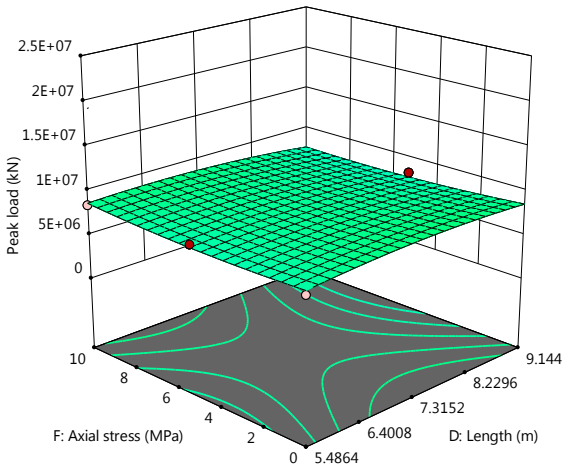

(p) D:E

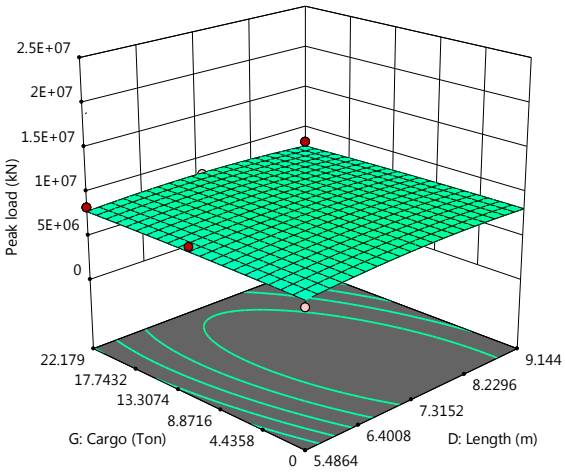

(q) D:F

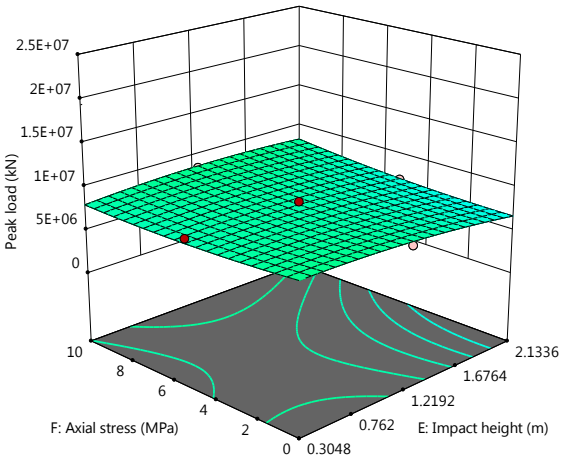

(r) D:G

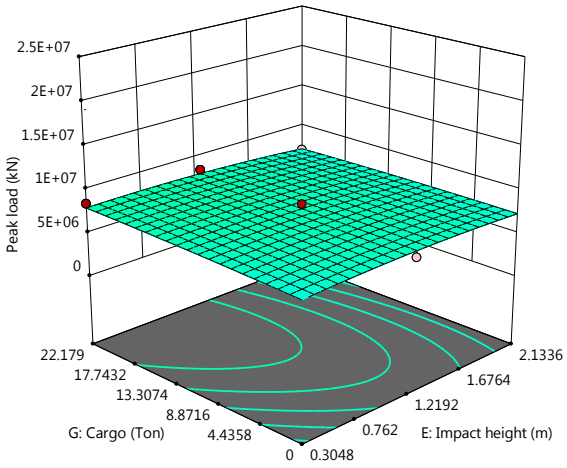

(s) E:F

(t) E:G

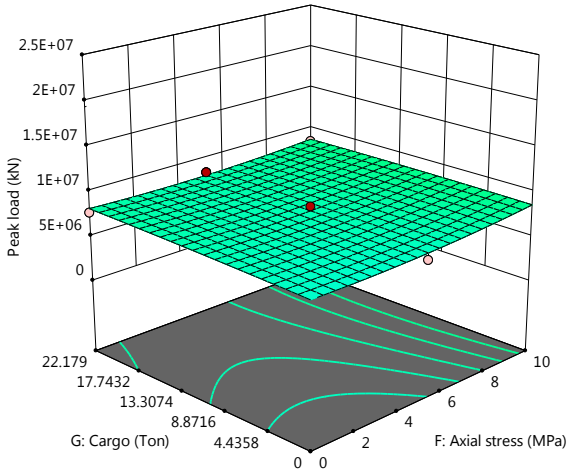

(u) F:G

Figure 6-18 3D response surface plot of peak dynamic load of tractor-trailer truck

(Basic parameters: A=100km/h, B=27.58MPa, C=0.9144m, D=5.4864m, E=1.2192m, F=5MPa, G=22.179 ton)

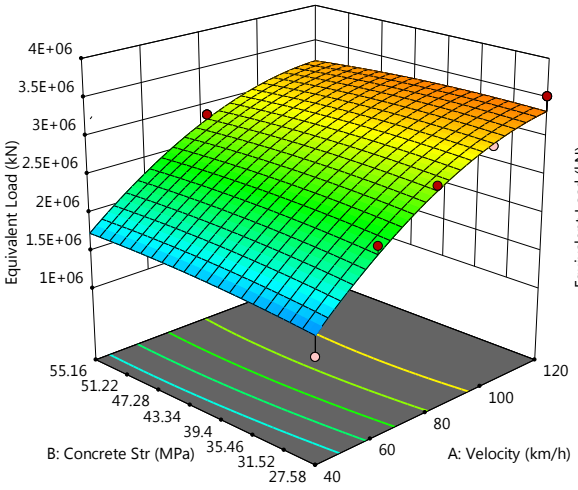

(a) A:B

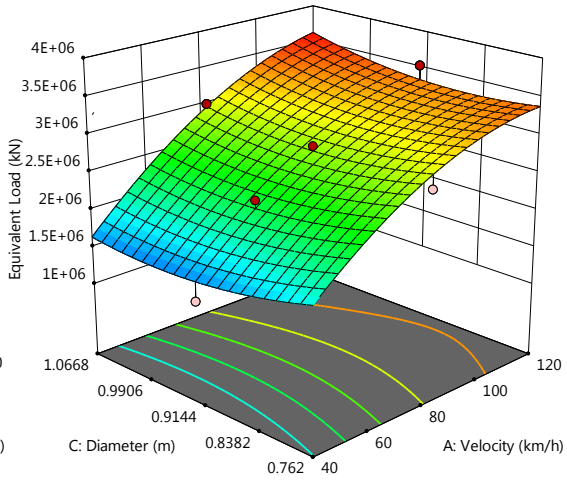

(b) A:C

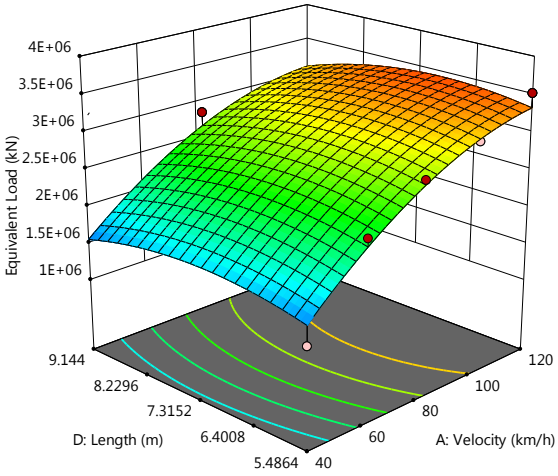

(c) A:D

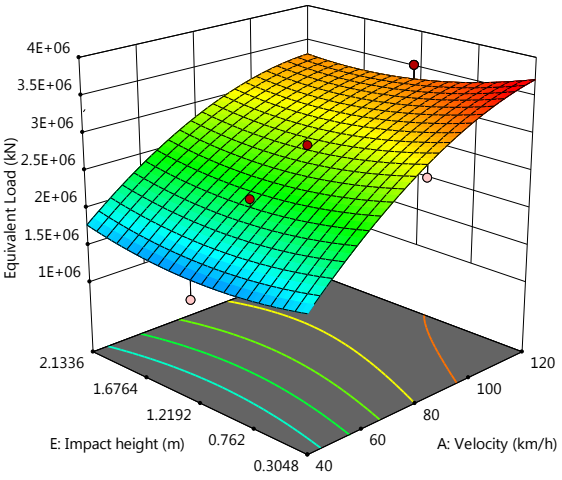

(d) A:E

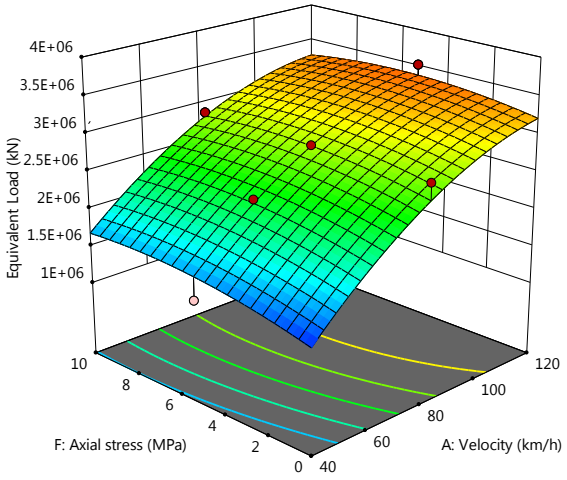

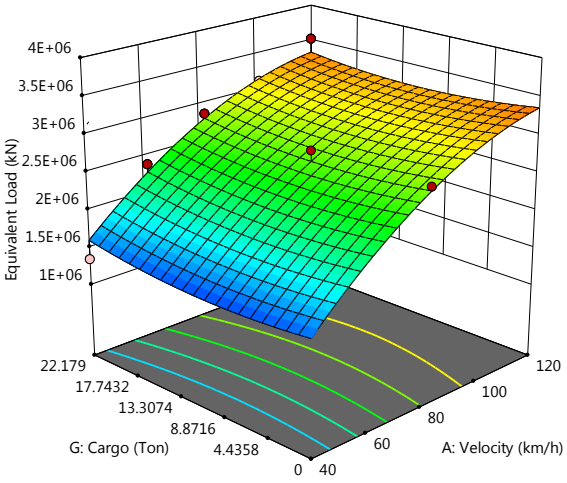

(e) A:F

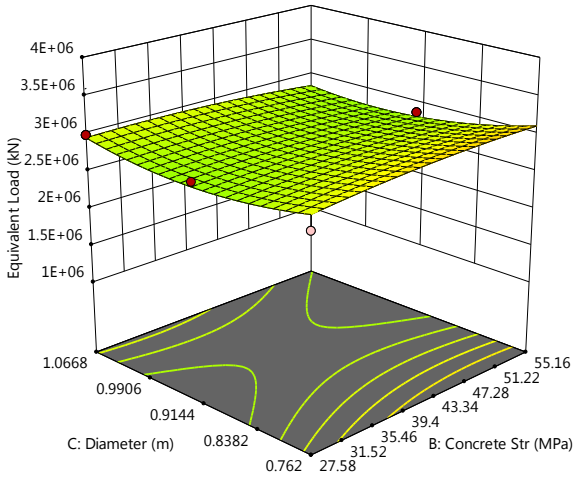

(f) A:G

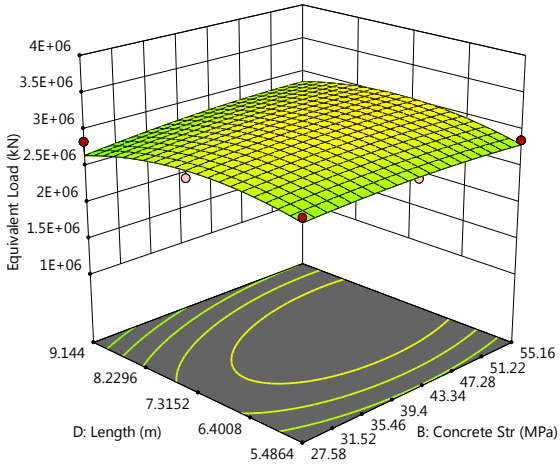

(g) B:C

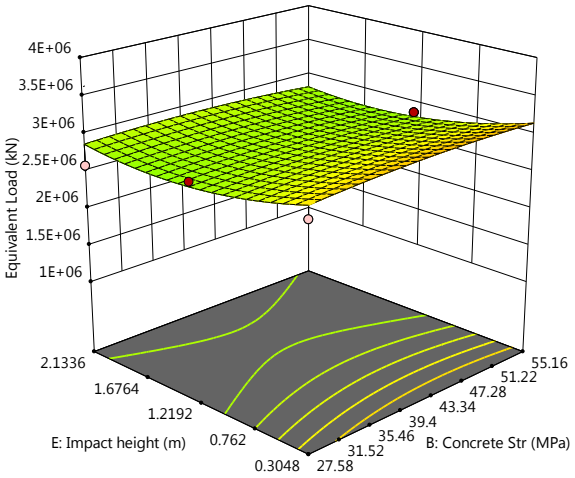

(h) B:D

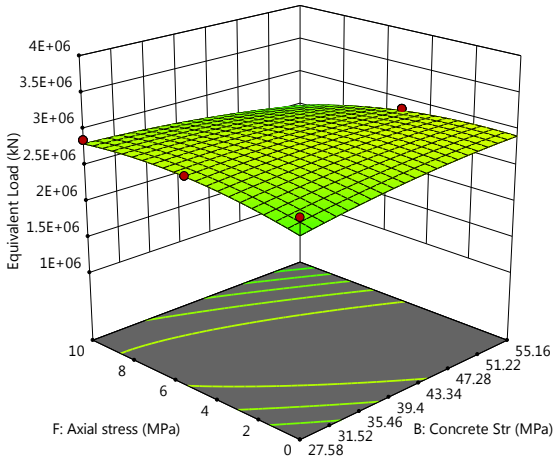

(i) B:E

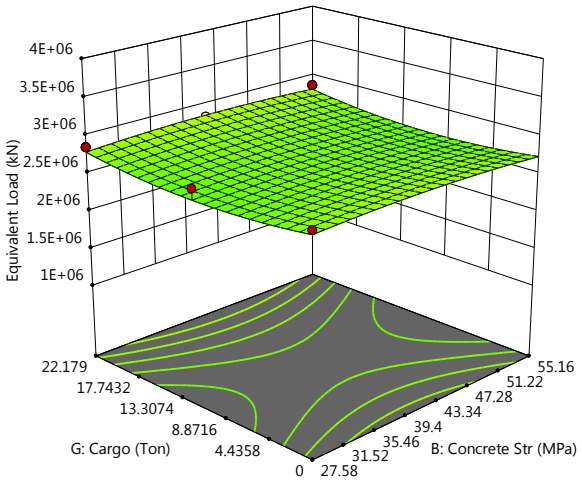

(j) B:F

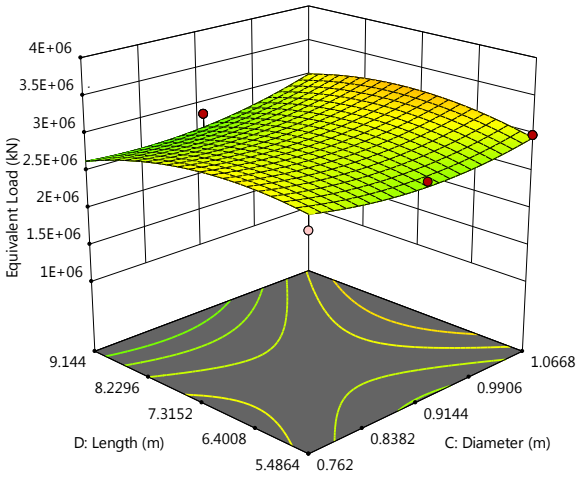

(k) B:G

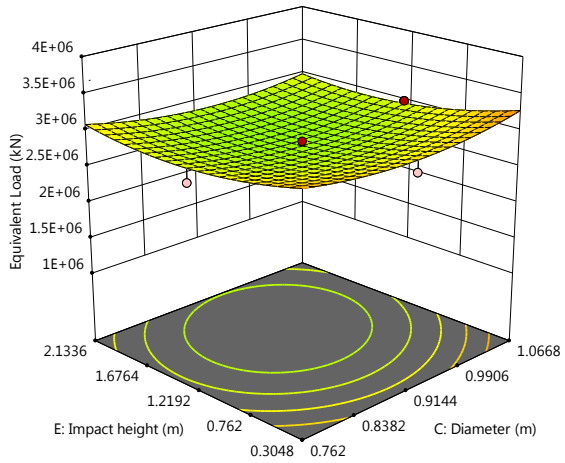

(l) C:D

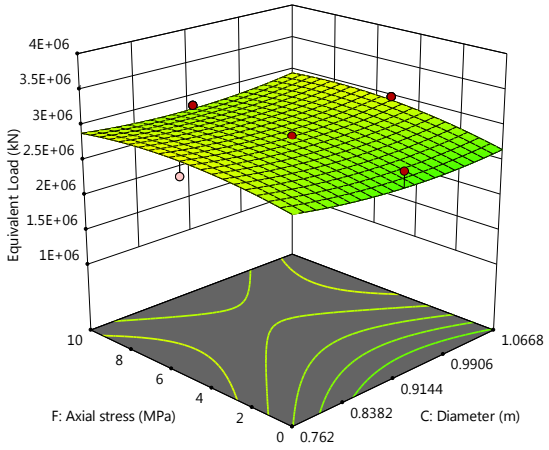

(m) C:E

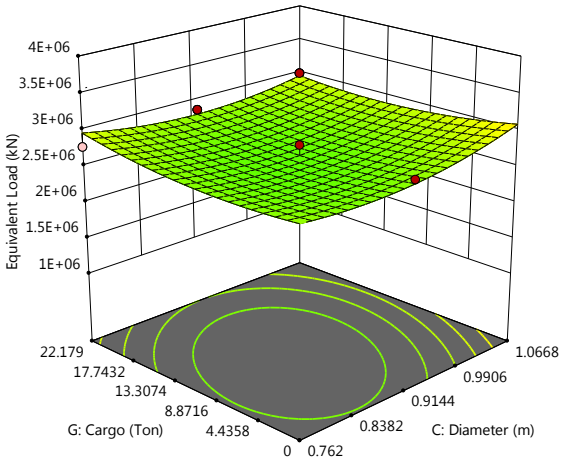

(n) C:F

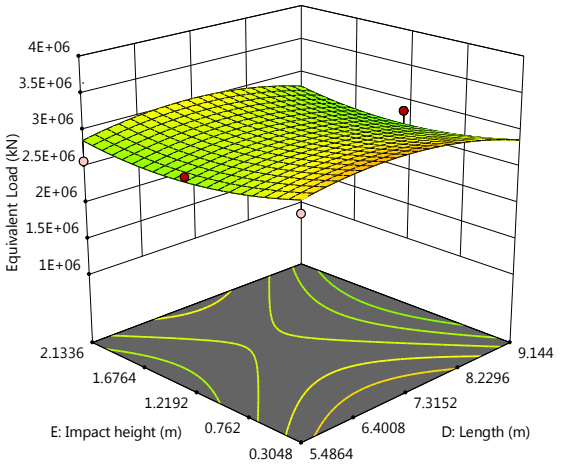

(o) C:G

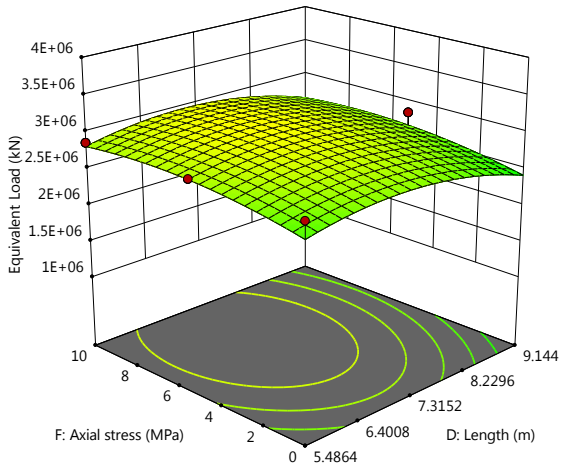

(p) D:E

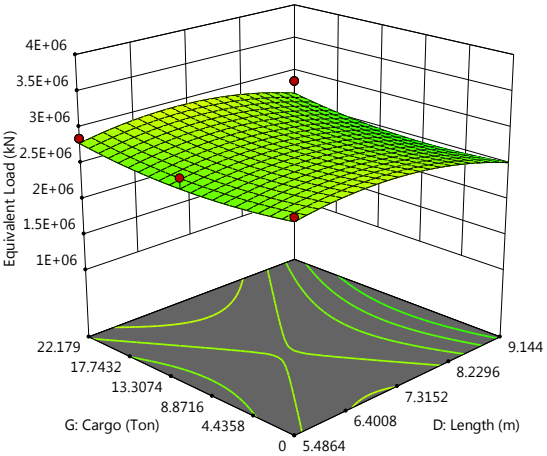

(q) D:F

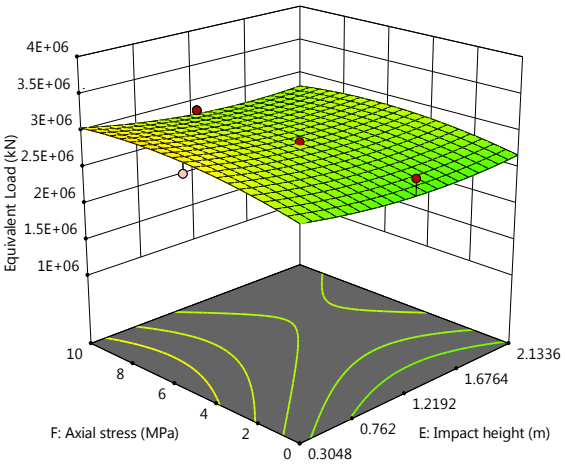

(r) D:G

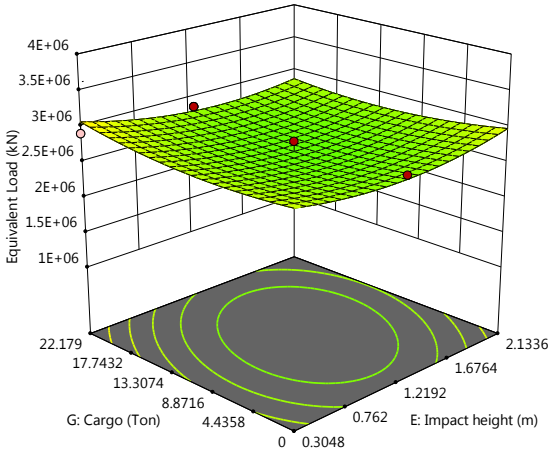

(s) E:F

(t) E:G

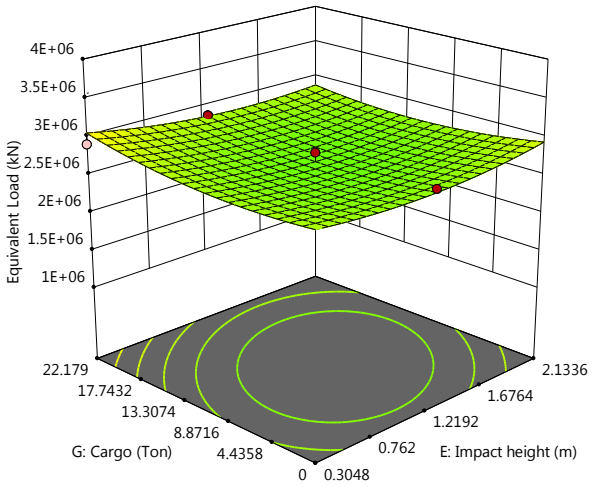

(u) F:G

Figure 6-19 3D response surface plot of equivalent static load of tractor-trailer truck

(Basic parameters: A=100km/h, B=27.58MPa, C=0.9144m, D=5.4864m, E=1.2192m, F=5MPa, G=22.179

Chapter 7 Reliability study of cantilever piers under vehicle impact load based on the simplified impact load model

The reliability of cantilever single column is studied in this chapter to assess the safety of a bridge subjected to the vehicle impact load with different parameters. The impact in this chapter is categorized as intentional impact, which means the impact event is deterministic. The reliability will be assessed by the probability of failure of the bridge under one deterministic impact event with uncertain parameters. Monte Carlo Simulation (MCS) technique is used in this chapter to estimate the failure probability of the structural system under the impact load.

7.1 Theoretical background

7.1.1 Monte Carlo Simulation

In the Monte Carlo simulation, samples of the basic correlated variables are randomly drawn according to their corresponding probabilistic characteristics and fed into the performance function, which in this study is expressed as that the structural strength minus the load effect, as shown in Eq. 7.1 and Eq 7.2 (Ayyub & McCuen,2011):

$$Z_M = M_{rd} - M_e \quad \text{Eq. 7.1}$$

$$Z_S = S_{rd} - S_e \quad \text{Eq. 7.2}$$

where M_{rd} and S_{rd} are defined as the bending moment and shear strength of the pier; moment M_e and shear S_e are the load effects based on the equivalent static impact load from the impact load model. The failure event happens while it satisfies$Z_M < 0$ or $Z_S < 0$. Therefore, the probability of failure could be expressed as:

$$\overline{P_f} = P(Z_M < 0 \; or \; Z_S < 0) = \frac{N_f}{N} \quad \text{Eq. 7.3}$$

where N_f is the number of simulation cycles for which the failure event happens in total N cycles of a simulation. Based on the law of large numbers, the probability of failure approaches the true value when N approaches infinity. Therefore, to make the $\overline{P_f}$ close to the true value, a large number of cycles are required. In this study the total cycles $N = 10^5$ are used after the test of convergence.

By assuming the performance function following the normal distribution, the reliability can be also represented by the reliability index β. The relationship between the reliability index and failure probability can be expressed as:

$$P_f = \phi(-\beta)$$

where $\phi(-\beta)$ means the cumulative probability of standard normal distribution at $-\beta$. The reliability index and its corresponding probability of failure is shown in Table 7-1.

Table 7-1 Reliability index and corresponding probability of failure

β	0	1	2	3	4	5	6
P_f	0.5	0.158655	0.02275	0.00135	3.17e-5	2.87e-7	9.87e-10

7.1.2 Load effect function

The load effect functions, as well known as the demand function, in this study are defined as the moment and shear effects which are induced by the equivalent static impact load during the design of a bridge pier. The equivalent static load functions (Eq. 6.61, Eq. 6.62 and Eq. 6.63) are already obtained in Chapter 6 based on the response surface model respectively for light-weight, medium-weight, and heavy-weight trucks. For a cantilever pier, the load effects could be expressed as:

$$M_e = hf_{RS}(v, C, D, L, H, P, M)_e \quad \text{Eq. 7.4}$$

$$S_e = f_{RS}(v, C, D, L, H, P, M)_e \quad \text{Eq. 7.5}$$

where the $f_{RS}(v, C, D, L, H, P, M)_e$ is the equivalent static impact load obtained in response surface model as shown in Eq. 6.61, Eq. 6.62 and Eq. 6.63; v is the impact velocity; C is the strength of concrete; D is the diameter of the pier; L is the length of the pier; H is the height form the ground surface to the top of the pier foot; P is the axial stress in the pier from superior structures; M is the cargo mass; h is height from the impact location to the top of the pier foot.

$$h = H + dh \quad \text{Eq. 7.6}$$

where dh is the height from the impact location to the ground surface, which is related to the engine height of different vehicles. As shown in Figure 7-1, dh is assumed as the average height from the midpoint of the shear area failure to the ground based on the study of chapter 5. The dh values for different trucks are listed in Table 7-2

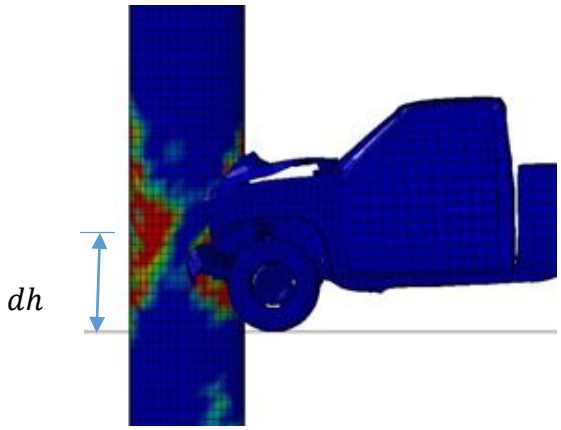

Figure 7-1 The height from the impact location to the ground surface

Table 7-2 Vehicle class, mass, and impact height

Vehicle	Mean Cargo Mass (Ton)	Impact height (m)
C2500	0.65	0.6
F800 Single Unit Truck	1.46	0.9
Tractor-trailer	11.09	1.2

7.1.3 Structural strength function

7.1.3.1 Bending moment strength

The structural strength functions, as well known as the demand function, are defined as the bending moment strength and shear strength M_{rd} and S_{rd} respectively.

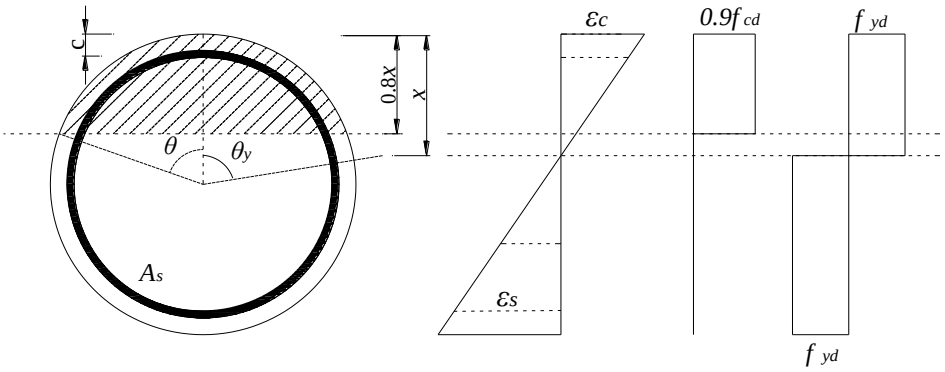

Figure 7-2 Diagrams for the analysis of circular cross-sections

For a circular section as shown in Figure 7-2.The bending moment strength of a RC circular section could be calculated by following equations (Cosenza, et al., 2011, and Trentadue, et al., 2016) :

$$M_{rd} = M_{rd,c} + M_{rd,s} = \frac{2}{3}R^3 sin^3\theta f'_{cd} + \frac{2}{\pi}(R-c)A_s sin\theta f_{yd} \qquad \text{Eq. 7.7}$$

where $f'_{cd} = 0.9f_{cd} = 0.9\frac{f'_c}{\gamma_c}$; $f_{yd} = \frac{f_y}{\gamma_s}$; $A_s = \rho\pi R^2$; f'_c is the specified compressive strength of concrete; f_y is the specified yield stress of steel; material safety factors γ_c and γ_s takes 1.5 and 1.15 respectively; $R = D/2$ is the radius of the circular cross section; ρ is the steel ratio of the cross section.

The value of θ which defines the compressive part of the cross section could be determined from the following equation by Newton's method:

$$f(\alpha) = \alpha(1+2\omega) - sin\alpha - 2\pi(\omega+\nu) = 0 \qquad \text{Eq. 7.8}$$

$$f'(\alpha) = (1+2\omega) - cos\alpha \qquad \text{Eq. 7.9}$$

where $\alpha = 2\theta$; $\omega = \frac{A_s}{\pi R^2}\frac{f_{yd}}{f'_{cd}}$; $\nu = \sigma_{Ed}\frac{1}{f'_{cd}}$; $\sigma_{Ed} = \frac{N_{Ed}}{\pi R^2}$; N_{Ed} is the axial force applied to the cross section.

7.1.3.2 Shear strength

For a circular section with hoop spaced maximum at 308.4mm (12in) with 90° to longitudinal reinforcement, the shear resistance of the section could be determined from the following equations based on AASHTO code:

$$S_{rd} = 0.9V_n = 0.9\min(V_c + V_s, 0.25f'_c b_v d_v) \quad \text{Eq. 7.10}$$

$$V_c = 0.0316\beta\sqrt{f'_c}\, b_v d_v \quad \text{Eq. 7.11}$$

$$V_s = \frac{A_v f_y d_v cot\theta}{s} = \frac{2A_h f_y d_v cot\theta}{s} \quad \text{Eq. 7.12}$$

$$\beta = \frac{4.8}{1 + 750\varepsilon_s} \quad \text{Eq. 7.13}$$

$$\varepsilon_s = \frac{\left|\frac{|M_u|}{d_v} + 0.5N_u + |V_u|\right|}{E_s A_s} \quad \text{Eq. 7.14}$$

$$d_v = 0.9d_e = \frac{D}{2} + \frac{D_r}{\pi} \quad \text{Eq. 7.15}$$

$$b_v = D \quad \text{Eq. 7.16}$$

where $M_u = M_e$; $N_u = N_{Ed}$; $V_u = S_e$; D is the external diameter of the circular section; D_r is the diameter of the circle passing through the centers of the longitudinal reinforcement; A_h is the area of the hoop section.

7.1.4 Assumption of probability distribution

To determine the probability distribution of the performance function, the probability distribution of variables in load effect function and structural strength function should be given. Following probability distributions of variables are assumed based on previous study by Steel and Sorensen (2014) as shown in Table 7-3.

Table 7-3 Probability distribution of variables

Variable	Units	Type	Mean	Standard Deviation (% of mean)
v	km/h	Lognormal	User input	15%
C	MPa	Lognormal	User input	5%
D	m	deterministic	User input	
L	m	deterministic	5486.4	
H	m	deterministic	User input	
h	m	Normal	Table 7.1	10%
P	MPa	Lognormal	User input	10%
M	Ton	Normal	Table 7.1	33%
fy	MPa	Lognormal	User input	5%
fyh	MPa	Lognormal	User input	5%
c	mm	deterministic	50.8	
p	1	Normal	User input	5%
Ah	mm^2	deterministic	User input	
s	mm	deterministic	User input	

7.2 Probability of failure analyses

Matlab is used for the Monte-Carlo simulation based on the response surface model in Section 6.2.2. The example MATLAB code is listed in Appendix B for the probability failure analysis of the pier under the impact of C2500 truck at the speed 120km/h with the different hoop spacing.

7.2.1 C2500 light-weight truck

The basic case has the parameters with concrete strength 27.58MPa, diameter 0.9144m, impact height 1.2192m, axial stress 5MPa, yield strength 413.7 MPa for both longitudinal and transverse reinforcements, steel ratio 2.5%, area of hoop section 127mm^2, spacing of hoop 76.2 mm.

From the variation of the probability of failure with the changes of concrete strength, it is learned that the failure probabilities are not significantly affected when the impact velocity is lower than 100 km/h. The failure probability is lower than 0.135% ($\beta > 3$). For the case with

impact velocity over 100km/h, higher concrete strength can greatly reduce the probability of failure induced by the impact of C2500 light-weight truck, as shown in Figure 7.3(a).

For the influence from the diameter of the pier, it shows that the minimum required diameter 0.762m (2.5 ft) specified in Maryland standard can hardly satisfy the strength requirement at high vehicular impact speed. For the section diameter of 0.9144m (3ft), when the vehicle impact speed under 120km/h, the failure probability keeps at very low level (lower or close to 0.135%) in Figure 7-3(b).

It depicts in Figure 7-3(c), increasing the impact height can greatly increase the failure probability at the same impact speed. To secure the safety of the pier, the foundation depth should be buried relative shallowly.

It shows in Figure 7-3(d), both too low and too high axial stress can result in high failure probability under the vehicular impact load. Low axial stress will lead to tensile failure due to the high bending moment, while high axial stress will cause compressive failure due to the bending moment.

Figures 7-3(e) and (f) show that Gr60 rebar (yield stress at 413.7MPa or 60ksi) could keep the probability of failure at low level (lower or close to 0.135%) for both longitudinal and transverse reinforcements. It is recommended the minimum grade should be Gr60, while lower grade steel could result in obvious increase in probability of failure.

In Figure 7-3(g), it can be referred that the steel ratio of 2.5% could grantee a low failure probability (lower or close to 0.135%) when the vehicular impact speed under 110km/h. For higher impact speed, the steel ratio should be 0.03 to reduce the failure probability.

The minimum requirement of transverse reinforcement #4 ($127mm^2$) in Maryland standard can ensure the safety of the pier with spacing at 76.2mm (3in) under the impact from lightweight truck when the truck impact speed does not exceed 110m/h. For higher impact speed, the larger size transverse reinforcement should be considered as shown in Figure 7-3(h). It can be also

known from Figure 7-3(i), the 76.2mm (3in) spacing for the transverse reinforcement is necessary. It is recommended to satisfy this spacing for the transverse reinforcement at the section under the impact location.

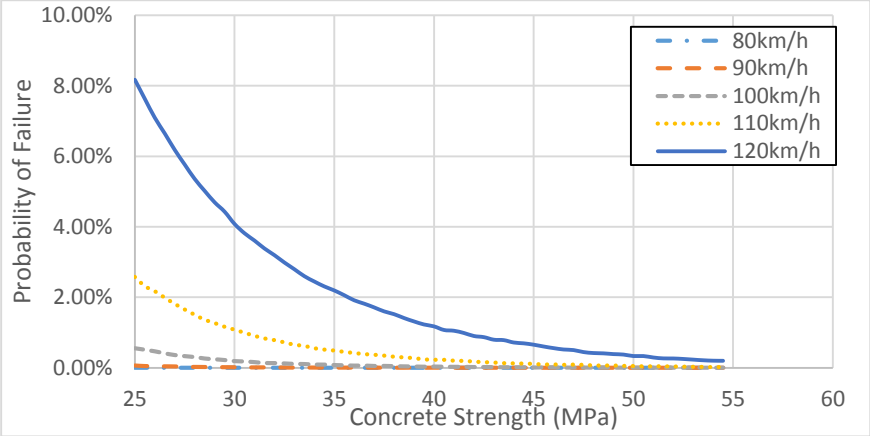

(a) Probability of failure with different concrete strength

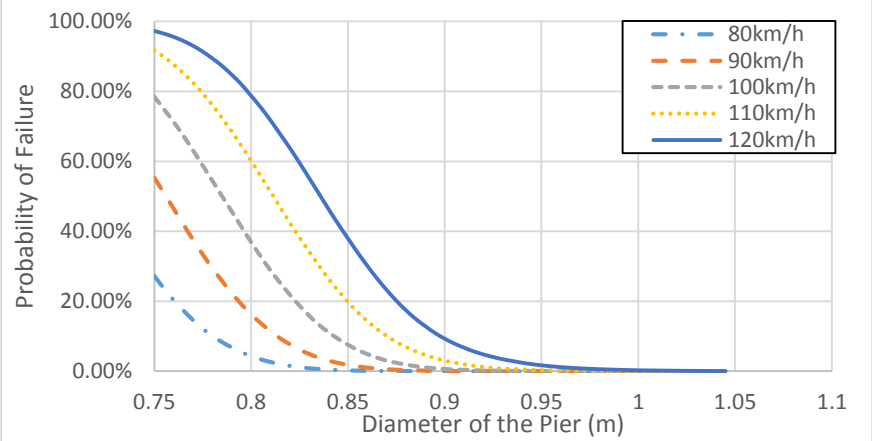

(a) Probability of failure with different pier diameter

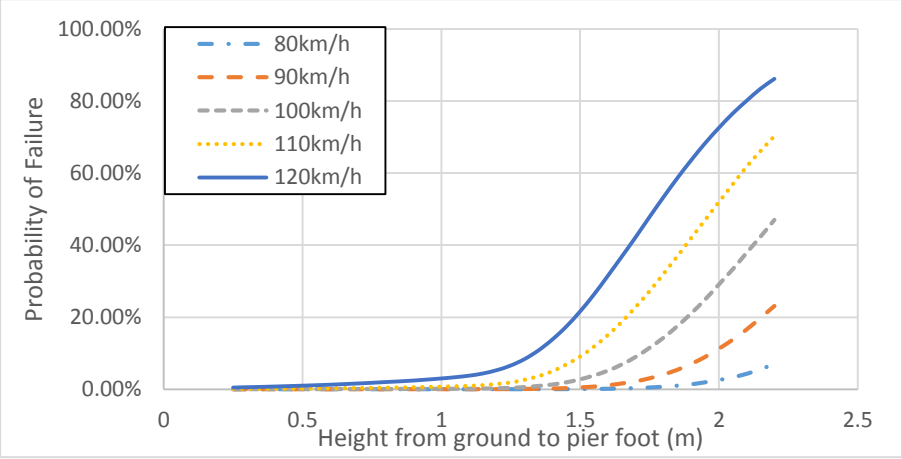

(c) Probability of failure with different impact height

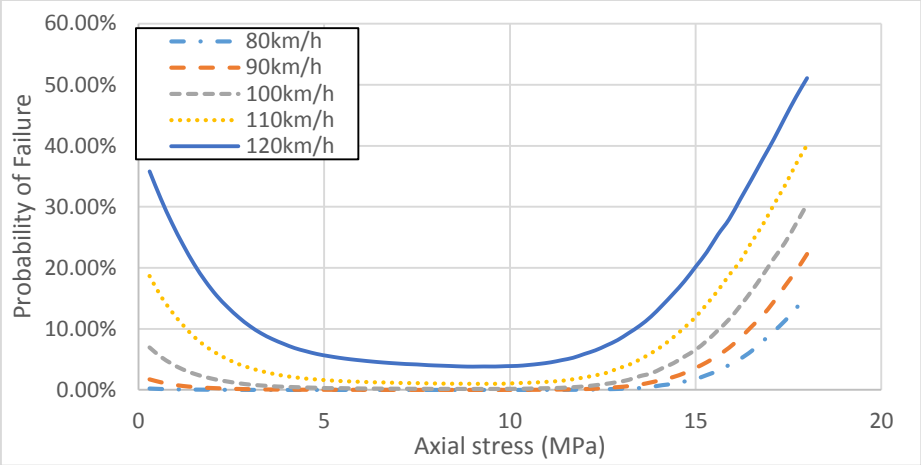

(d) Probability of failure with different axial stress

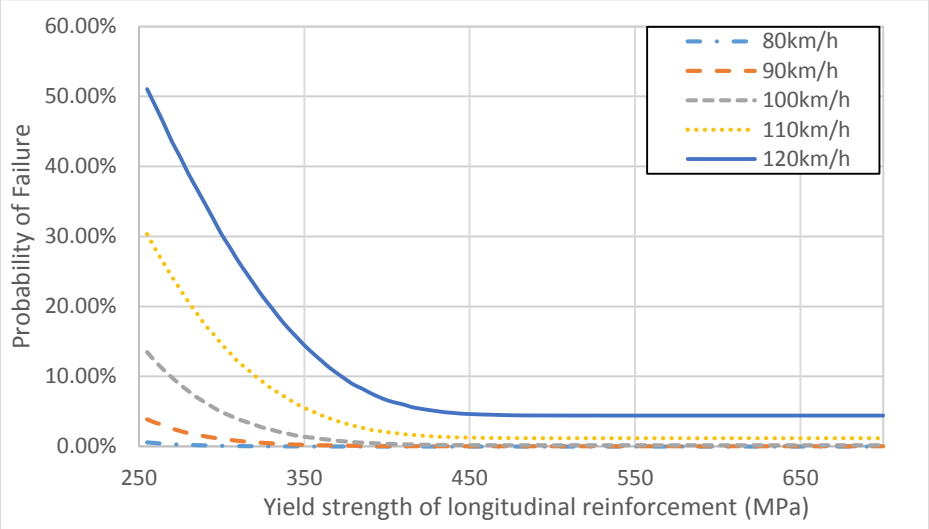

(e) Probability of failure with different yield strength of longitudinal reinforcement

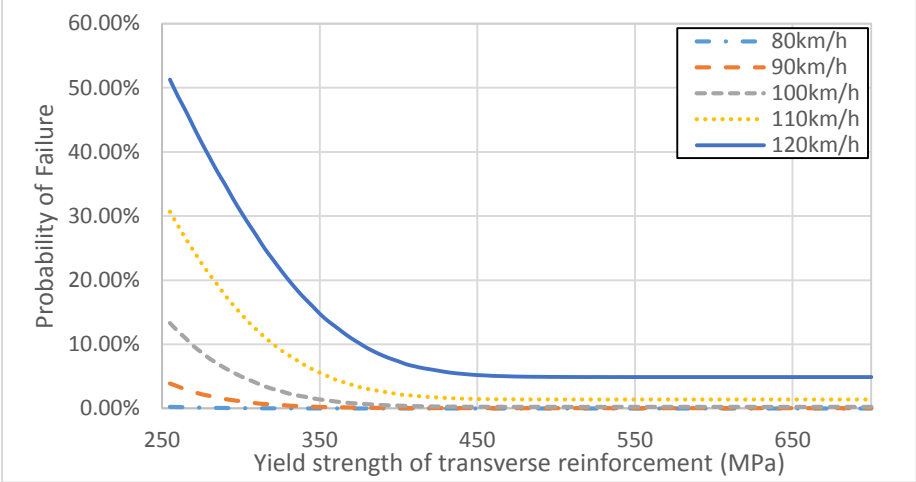

(f) Probability of failure with different yield strength of transverse reinforcement

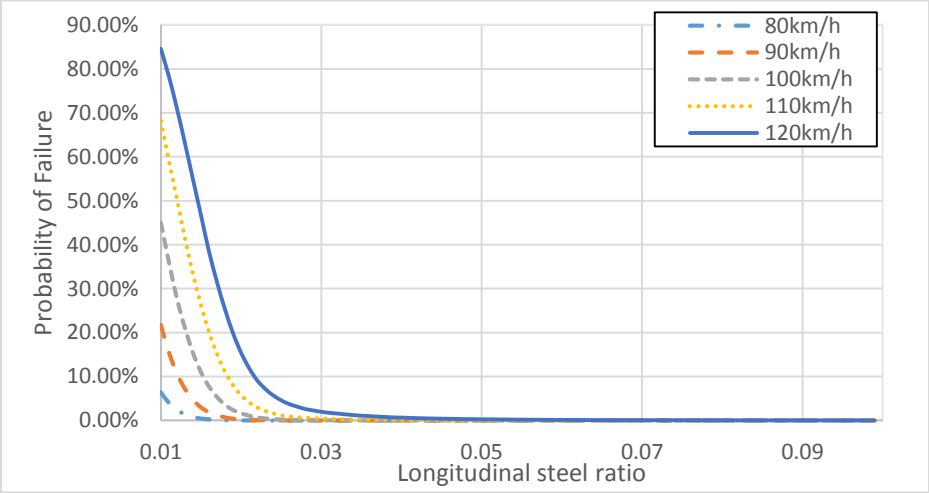

(g) Probability of failure with different steel ratio

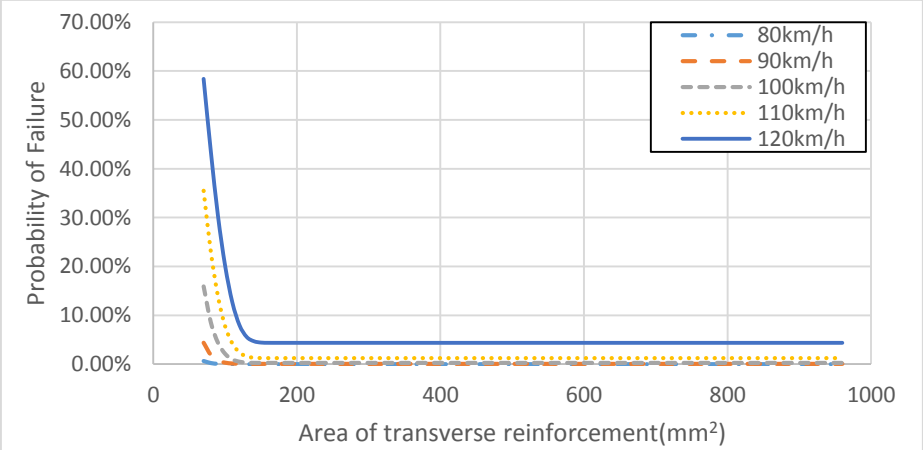

(h) Probability of failure with different cross-section area of hoop

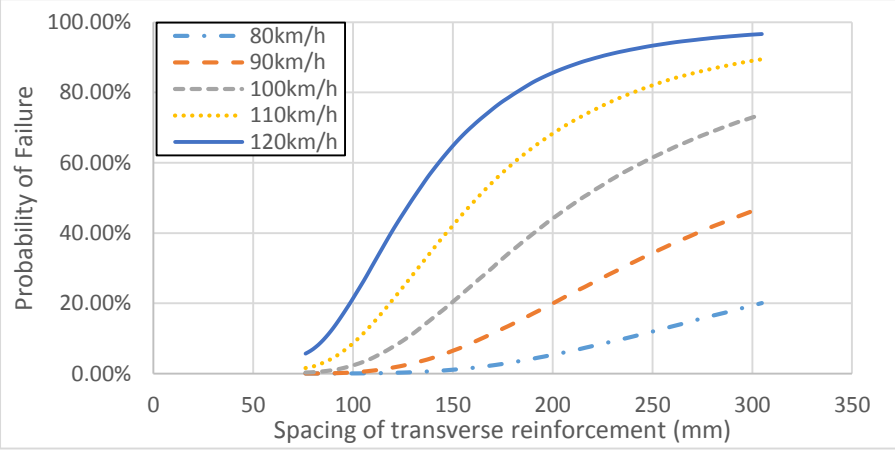

(i) Probability of failure with different spacing of hoop

Figure 7-3 Probability of failure with different impact velocity for C2500 light-weight truck

7.2.2 F800 medium-weight truck

The basic case has the parameters with concrete strength 27.58MPa, diameter 0.9144m, impact height 1.2192m, axial stress 5MPa, yield strength 413.7 MPa for both longitudinal and transverse reinforcements, steel ratio 5%, area of hoop section 284mm^2, spacing of hoop 76.2 mm.

Compared with the impact load induced by C2500, much higher resistances are required for both bending moment and shear force. Compared with the basic case, the failure probability of the pier could be controlled lower than 0.135% ($\beta > 3$) while the impact speed not exceeding 100km/h. By increasing the concrete strength from 25MPa to 55 MPa, the probability of failure could be lowered 60%, as shown in Figure 7-4(a).

As shown in Figure 7-4(b), the minimum required diameter 0.762m (2.5 ft) specified in Maryland standard can hardly satisfy the requirement even at impact speed at 80km/h. The failure will certainly happen when the pier with a diameter of 0.762m is under the impact by F800 truck. For the section diameter of 0.9144m (3ft), when the vehicle impact speed under 110km/h, the failure probability keeps at relative low level (P_f smaller than 0.135%). To ensure the safety while the speed at 120km/h, the diameter should be increase up to 0.95m.

It depicts in Figure 7-4(c), same as the cases of C2500, increasing the impact height can greatly increase the failure probability at same impact speed. To secure the safety of the pier, the height from the footing top surface to the ground with a value of 1.0 m could result in a low probability of failure of the pier ($P_f = 0.315\%$) even under the impact with a speed at 120km/h.

It shows in Figure 7-4(d), both too low and too high axial stresses can result in high failure probability under the vehicular impact load. Low axial stress will lead to tensile failure due to the high bending moment, while high axial stress will cause compressive failure due to the bending moment. The axial stress ranges from 5MPa to 10MPa could result in the lowest probability of failure.

Figure 7-4(e) shows that Gr60 longitudinal rebar (yield stress at 413.7MPa or 60ksi) could keep the probability of failure at low level when the impact speed under 110km/h (P_f smaller than, or close to 0.135%). It is recommended higher grade should be considered for the impact speed over 110km/h without increasing the steel ratio. Lower grade steel could result in obvious increase in probability of failure.

For the Gr60 transverse reinforcement, it can reduce the probability of failure to the minimum value even for the impact speed at 120km/h, as shown in Figure 7-4(f). When the speed under 110km/h, the probability of failure can be controlled lower than, or close to 0.137%. However, due to the bending failure, the failure probability is still at a high level compared with the failure probability under the impact load by C2500 truck, when impact speed reaches 120km/h with a probability of failure 3.073%.

In Figure 7-4(g), it can be referred that the steel ratio of 5% could grantee a low failure probability (lower than 0.137%) when the vehicular impact speed does not exceed 110km/h. For higher impact speed, the steel ratio should be higher to reduce the failure probability.

The size of transverse reinforcement #6 (284mm^2) is able to ensure the safety of the pier with spacing at 76.2mm (3in) under the impact from medium-weight truck, as shown in Figure 7-4(h). It can be also learned in Figure 7.4(i), the 76.2mm (3in) spacing for the

transverse reinforcement is necessary to increase the safety of the pier. It is recommended to satisfy this spacing for the transverse reinforcement at the section under the impact location.

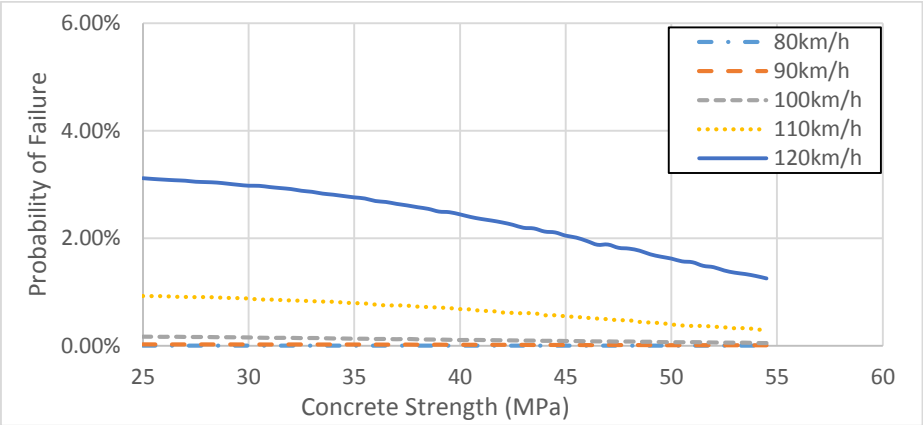

(a) Probability of failure with different concrete strength

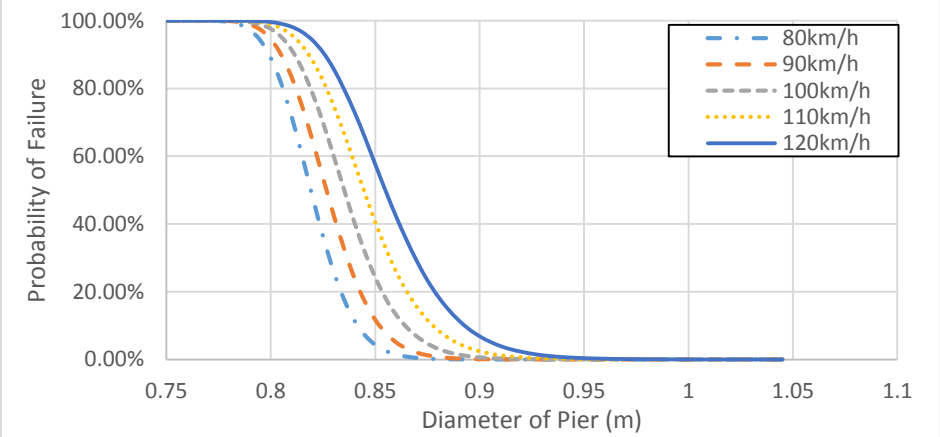

(b) Probability of failure with different diameter of pier

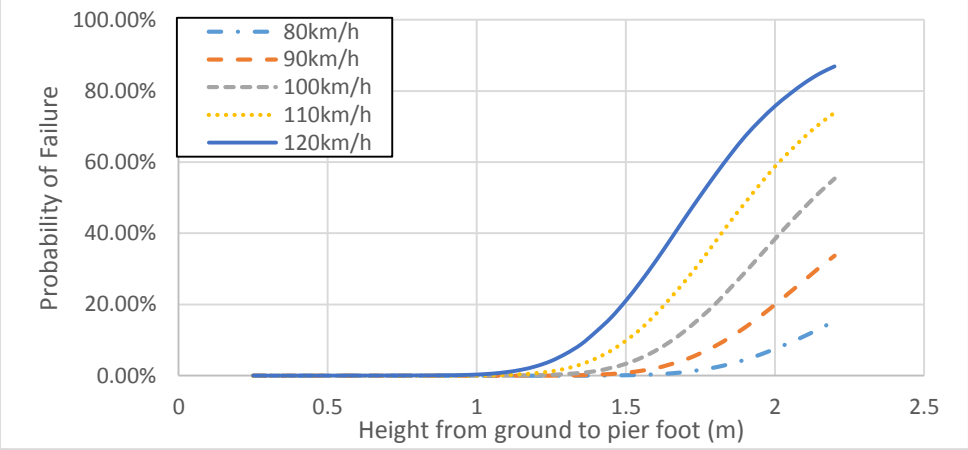

(c) Probability of failure with different impact height

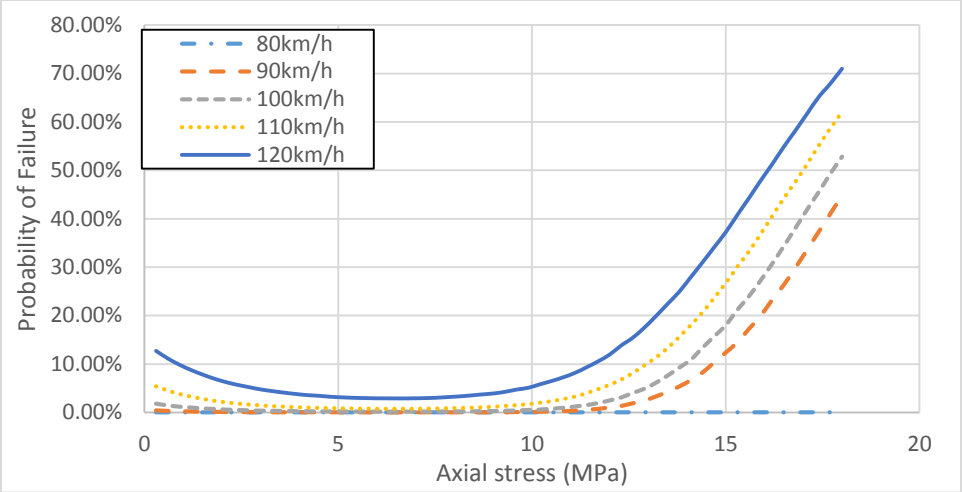

(d) Probability of failure with different axial stress

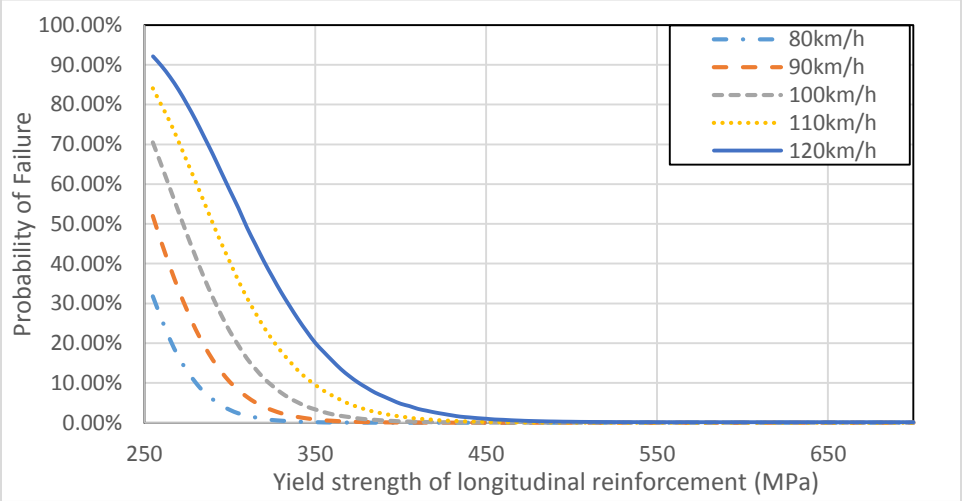

(e) Probability of failure with different yield strength of longitudinal reinforcement

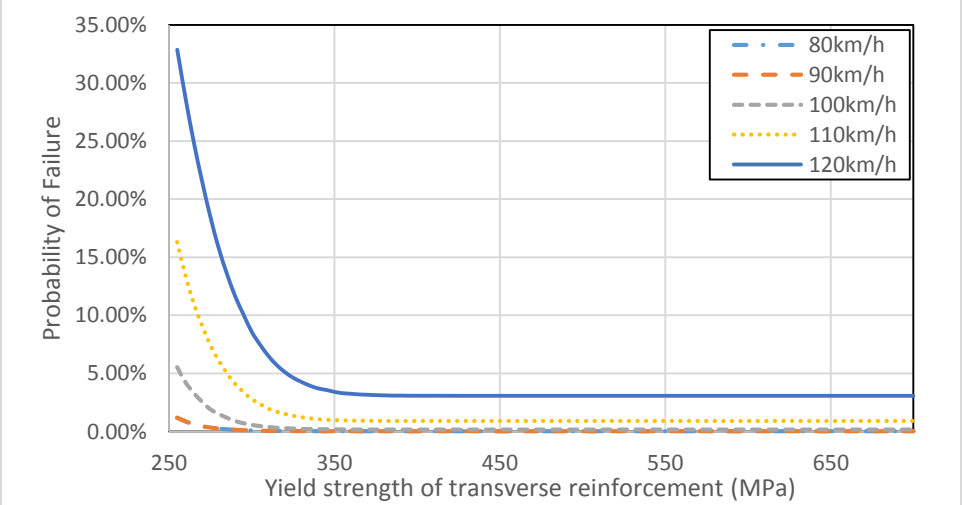

(f) Probability of failure with different yield strength of transverse reinforcement

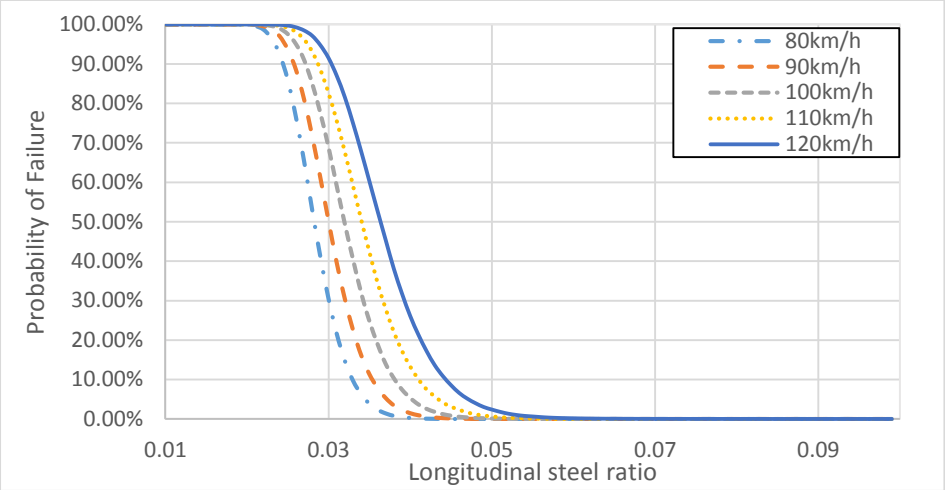

(g) Probability of failure with different steel ratio

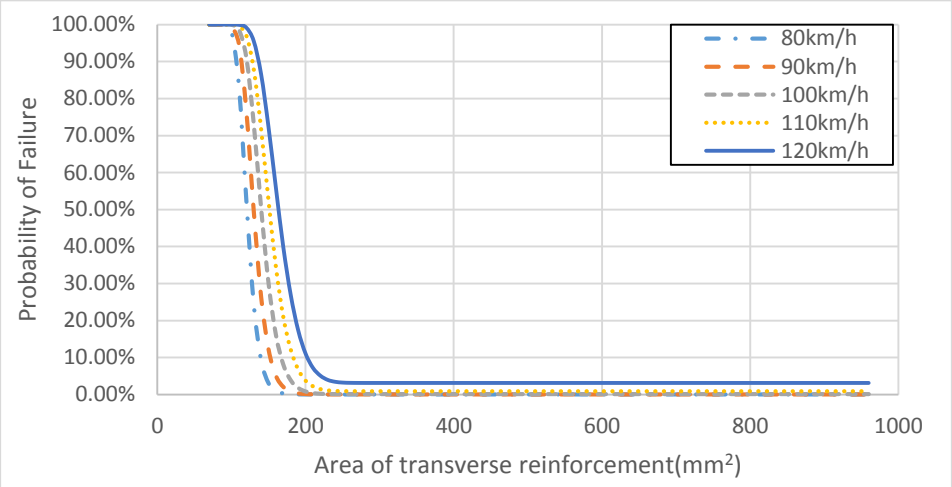

(h) Probability of failure with different cross-section area of hoop

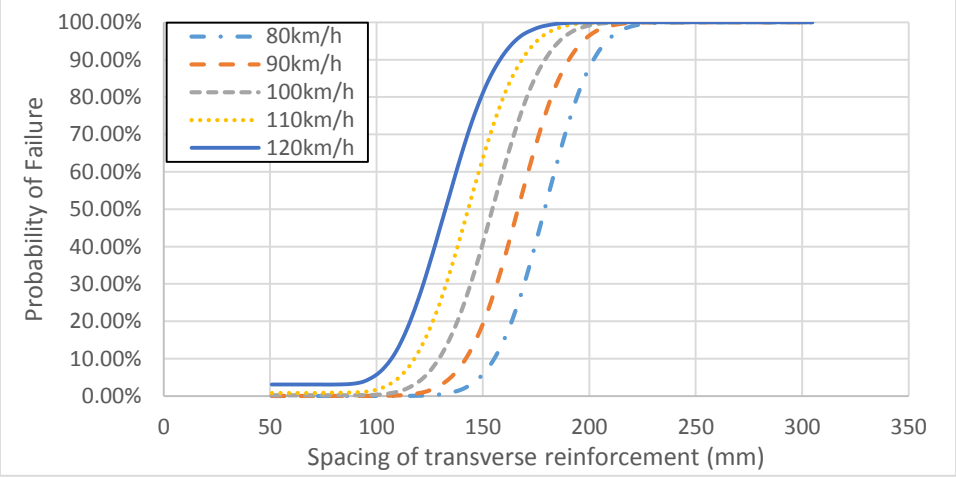

(i) Probability of failure with different spacing of hoop

Figure 7-4 Probability of failure with different impact velocity for F800 medium-weight truck

7.2.3 Tractor-trailer heavy-weight truck

The basic case has the parameters with concrete strength 27.58MPa, diameter 0.9144m, impact height 1.2192m, axial stress 5MPa, yield strength 413.7 MPa for both longitudinal and transverse reinforcements, steel ratio 5%, area of hoop section 387mm^2, spacing of hoop 76.2 mm.

Compared with the impact load induced by C2500 and F800, the impact load induced by tractor-trailer truck is so high that it is very hard to control the failure probability at very low level. Compared with the basic case, the failure probability of the pier could be controlled to 0.135% by increasing the concrete strength to 55MPa, while the impact speed under 80km/h, as shown in Figure 7-5(a).

As shown in Figure 7-5(b), the minimum required diameter 0.762m (2.5 ft) specified in Maryland standard can hardly satisfy the requirement even at impact speed at 60km/h. For the section diameter of 0.9144m (3ft), when the vehicle impact speed under 70km/h, the failure probability keeps at relative low level ($P_f < 1\%$). To ensure the safety while the speed at 100km/h, the diameter should be increase up to 1.0668m (3.5ft).

It depicts in Figure 7-5(c), the failure probability will first decrease slightly at small impact height, and will increase when the impact height increases over 1.2m. The height from the footing top surface to the ground with a value of about 1.0 m could help the failure probability drop to a relative small value.

It shows in Figure 7-5(d), high axial stress could reduce the probability of failure, because that the tensile failure due to bending moment, induced by large impact load, governs the failure.

Figure 7-5(e) shows that Gr60 longitudinal rebar (yield stress at 413.7MPa or 60ksi) could keep the probability of failure at low level when the impact speed under 80km/h. It is recommended higher grade should be considered for the impact speed over 80km/h without increasing the steel ratio. The Gr60 transverse reinforcement is sufficient to reduce the probability of failure to the minimum value, as shown in Figure 7-5(f). However, due to the bending failure, the failure probability is still at a high level.

In Figure 7-5(g), it can be referred that the steel ratio of 8% could reduce the failure probability to a relative low level. However, it still leads to the high failure of probability because of the large shear force.

The size of transverse reinforcement #7 ($387mm^2$) is able to ensure the safety of the pier with spacing at 76.2mm (3in) under the impact load from heavy-weight truck, as shown in Figure 7-5(h). It can be also learned in Figure 7-5(i), the 76.2mm (3in) spacing for the transverse reinforcement is necessary to increase the safety of the pier. It is recommended to satisfy this spacing for the transverse reinforcement at the section under the impact location.

In general, the failure probability is hard to be reduced to a relative low lever at high impact speed by the tractor-trailer truck. Other protection method, such as the steel jacket and protection barrier, is recommended to increase the safety of the pier under impact load.

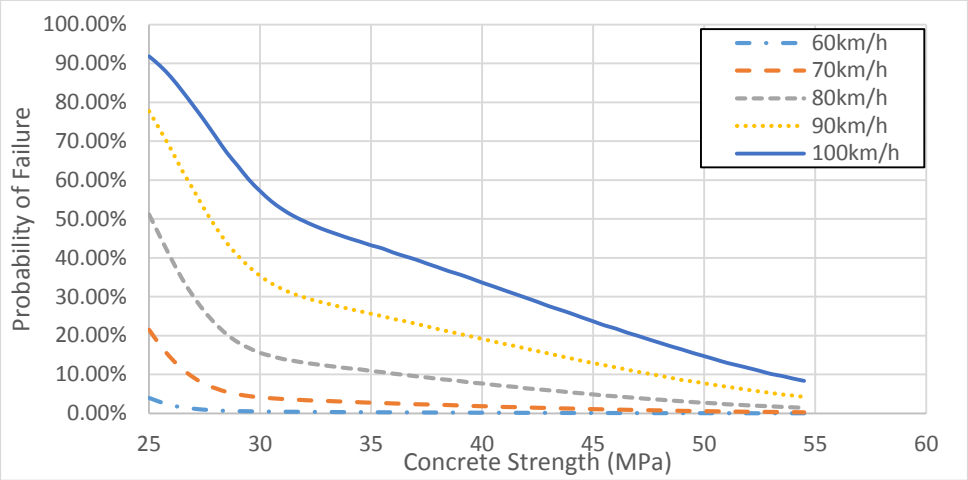

(a) Probability of failure with different concrete strength

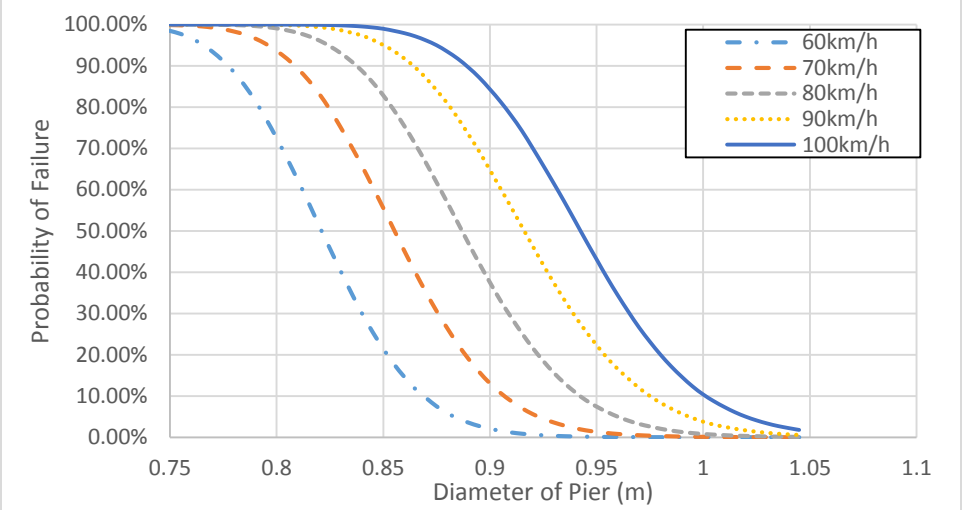

(b) Probability of failure with different diameter of pier

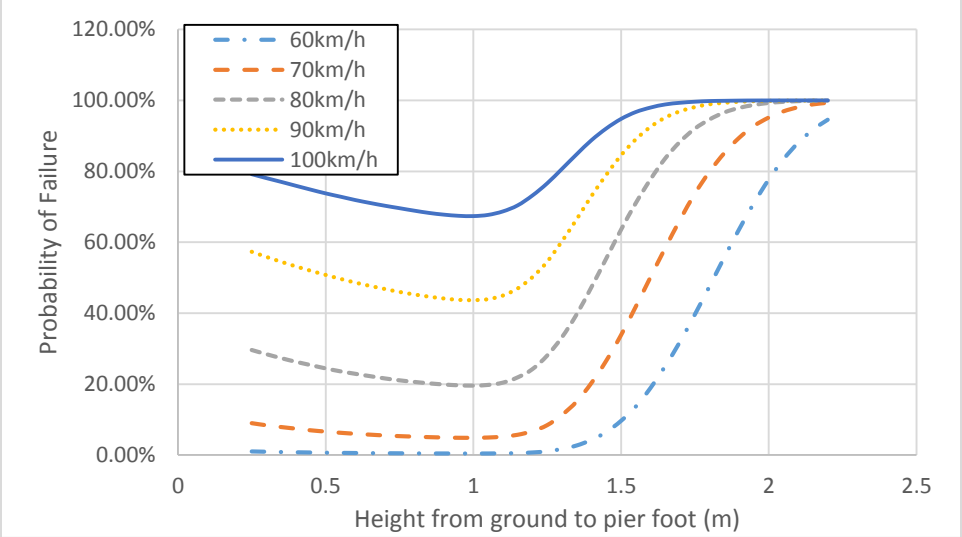

(c) Probability of failure with different impact height

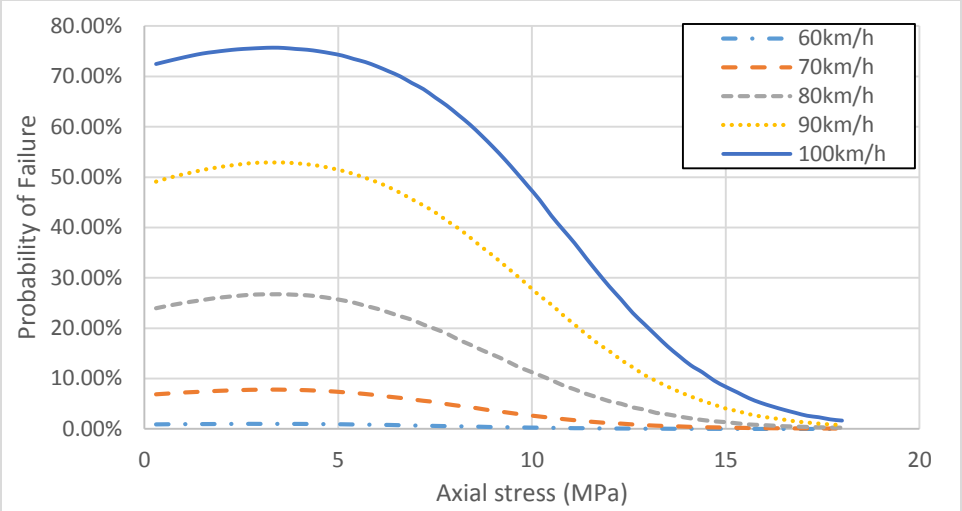

(d) Probability of failure with different axial stress

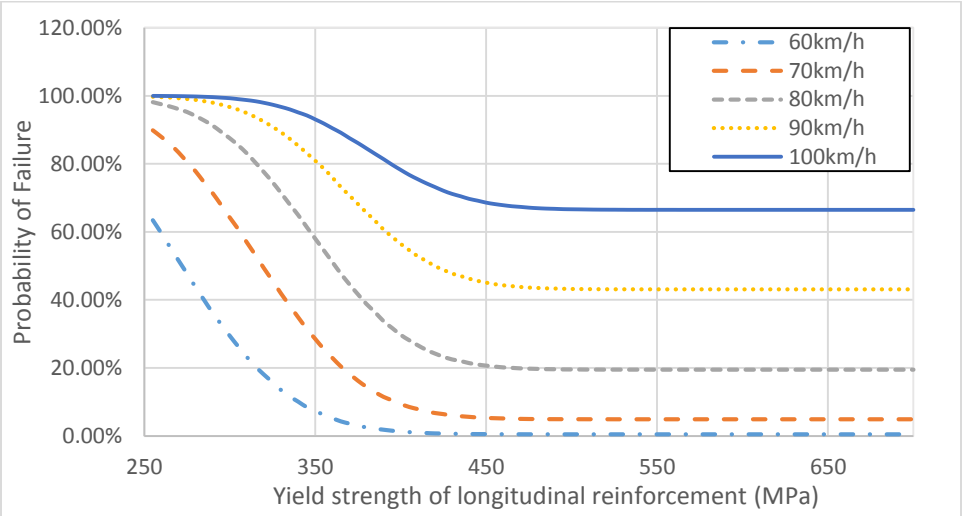

(e) Probability of failure with different yield strength of longitudinal reinforcement

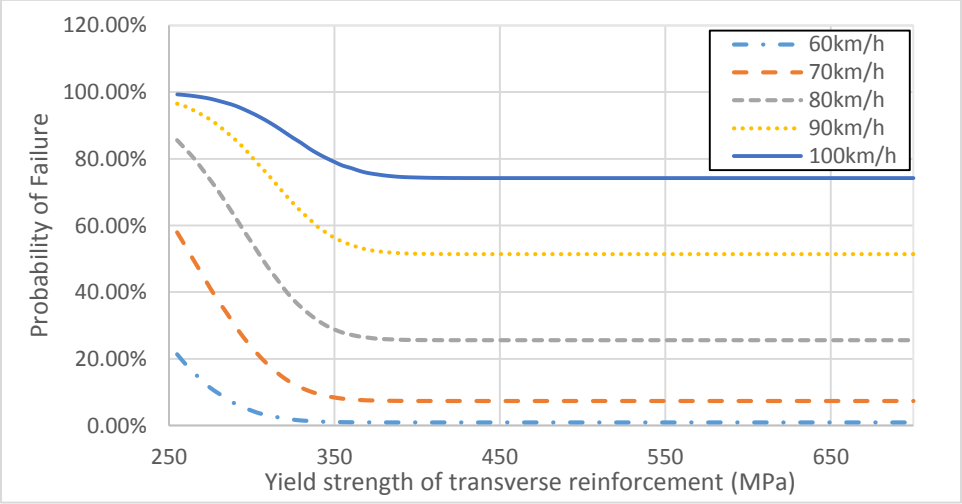

(f) Probability of failure with different yield strength of transverse reinforcement

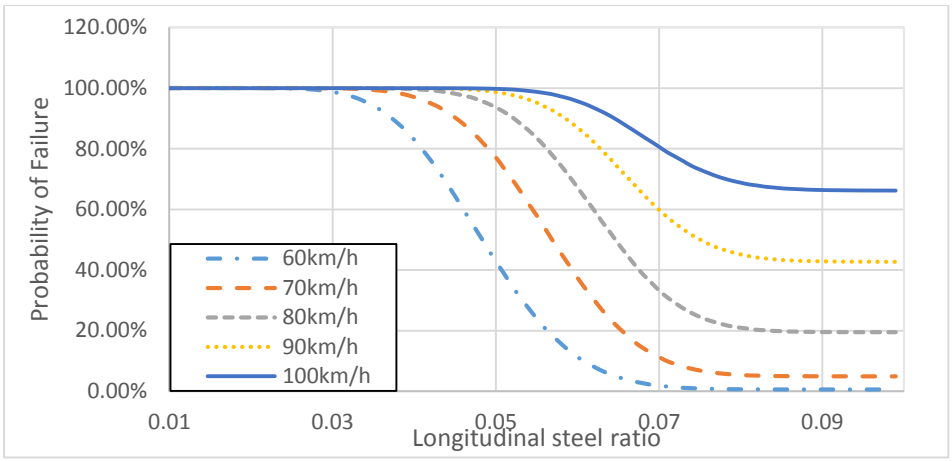

(g) Probability of failure with different steel ratio

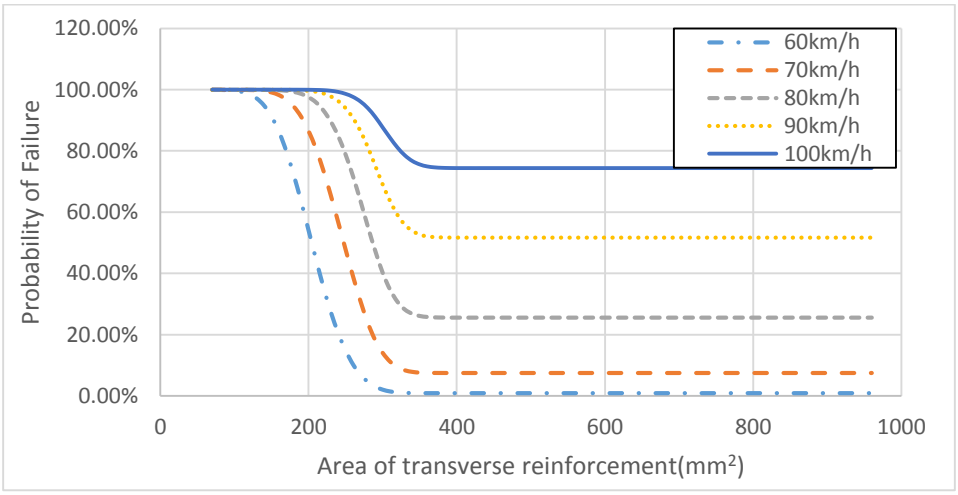

(h) Probability of failure with different cross-section area of hoop

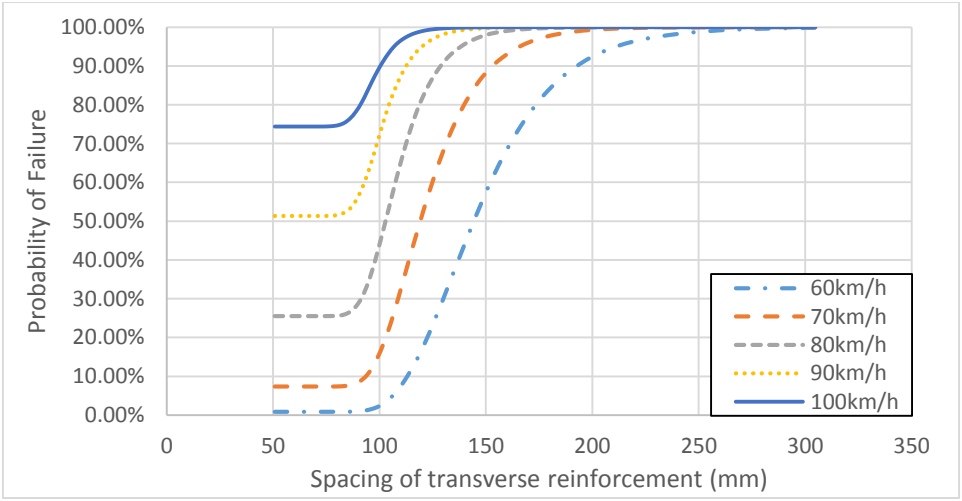

(i) Probability of failure with different spacing of hoop

Figure 7-5 Probability of failure with different impact velocity for tractor-trailer heavy-weight truck

7.3 Summary

This chapter discussed the failure probability of the pier under different impact loads with uncertainty of parameters based on Monte-Carlo simulation. For the light-weight or medium-weight truck, by increasing the resistance of pier or reducing load effect, the probability of failure can be controlled under 0.137% for the impact speed not exceeding 100km/h. However, it will not be economically efficient to reduce the probability of failure to such a small value when the pier is subjected to the heavy-truck impact with a speed over 80km/h.

Both the bending failure and shear failure may govern. To minimize the probability of failure, increasing the concrete strength, the diameter dimension, steel rebar strength and size, area of rebar could help to increase the resistance of the pier, while reducing the impact height and impact speed could help to reduce the impact effect.

When taking the impact load induced by tractor-truck at high impact speed into consideration, it is recommended to take the measure of steel jacket under the impact location to largely increase the resistance of the pier. Another efficient way is to reduce the impact speed, by setting barrier between the road and pier, or leaving enough distance between the pier and road curb to help driver to decelerate before the impact.

Chapter 8 Conclusion

According to an overall review of previous studies on the vehicle induced impact load on the pier, it is found that pier failures due to vehicle impact occurred in many states, while the study on the influence on the impact load is insufficient. However, there is limitation on full-scale tests due to economic issues. With the assistance of the explicit dynamic finite elemental software and high performance computer, variety of influence parameters on the impact load and the performance of the pier could be efficiently studied through a large amount of numerical analyses. Following conclusion could be made according to this study.

Conclusions

1. Based on the finite elemental simulation on previous experimental and numerical studies, it shows the validation of numerical analyses by the finite elemental software LS-DYNA in impact study. The results of FEM simulation could well match the results of previous experimental studies for both rigid impact of a hammer on the beam, and truck-to-pier impact.

2. The impact loads on a circular pier induced by light-weight, medium-weight, and heavy-weight truck are studied to investigate the influence of different parameters, related to the impact velocity, strengths of concrete and steel, boundary conditions, axial loads, the impact location, cargo masses, as well as steel ratios in both longitudinal and transverse directions. It is concluded that the peak dynamic load is sensitive to factors including impact velocity, concrete strength, pier diameter, pier length, impact height, axial force, and cargo mass. Besides, the current AASHTO design impact value

is found conservative for the impact induced by light-weight truck, medium-weight trucks, as well as the heavy truck with the impact speed under 80km/h. However, for a heavy truck with an impact speed over 80km/h, the code underestimates the impact load.

3. For the failure mechanism, local failure, bending failure and shear failure could be observed based on different parameters. The shear failure, considered brittle type of failure, is the most fatal which could lead to collapse of the pier, while the bending failure is more ductile. Additional attention should be paid to the impact induced by tractor –truck with the speed over 80km/h, which could result in shear failure with high probability. Measures should be taken to reduce the impact speed, or increase resistance of the pier.

Contributions

1. Two simplified impact load models are proposed in this study for improving the design value of the impact load based on the parametric study:

1) Simplified mass-spring model: It is suitable to obtain the time history of the impact force. However, appropriate assumption must be made for the spring stiffness and damper. Also case-by-case explicit analyses are necessary to obtain the impact load.

2) Response surface model: It can directly give the impact load function based on the chosen variables. To obtain the approximation function, a large number of mathematic experiments are required to increase the precision of the fitting function. It is an efficient way to obtain the key value, such as the peak dynamic load and equivalent static impact

load. However, the response surface cannot develop the time history, and the response may lack in fitting if the response shows large discreteness with the chosen variables.

2. The MATLAB codes for explicit dynamic analyses of the impact load are developed for the simplified mass-spring model. The fiber model of pier section is applied in the explicit dynamic analyses to involving the plastic behavior of the pier under large impact load. The codes are listed in the appendix, and can be further modified to take different truck-to-pier impact events into consideration.

3. Six second-order polynomial fitting functions for both peak dynamic impact load and equivalent static impact load are developed based on the response surface model. These fitting functions can be applied directly to the estimation of impact load for different truck-to-pier impact events.

4. Based on the response surface model and Monte-Carlo simulation, the reliability study shows it is possible to control the probability of failure, induced by impact loads of light-weight and medium-weight trucks, to a low level (i.e. P_f = 0.137%, reliability index β equal to 3) by appropriately increase the resistance of the pier. However, when the pier is subjected to the impact induced by heavy-weight truck with the impact speed over 80km/h, it is hard to satisfy the resistance requirement by regular methods. Only by lowering the impact speed or largely increasing the resistance, it is able to reduce the failure probability during the impact.

5. Overall, this study contributes to a comprehensive parametric study on the influence on impact load and failure mechanism of the pier. On the other hand, two simplified methods are proposed in the study, and are proven to be feasible in obtaining the impact

load by skipping commercial finite elemental software. Besides, two methods provided the alternative impact load value other than the conservative impact load value in the AASHTO specification for a more reasonable impact design. At last, the failure probability analyses based on the response surface model provided the way to improve the reliability of the pier with every different load cases and dimensions.

Future Studies

For future studies, following topics are suggested:

1. the influence of different shape of the section could be further discussed on the impact load.
2. Besides, the eccentric impact with the different incoming angle of the truck is another topic.
3. The spring-mass simplified model could be further improved by considering the shear deformation.
4. Response surface model could gain its robust by increasing the volume of data.
5. A more detail investigation on how to improve the reliability of the pier by active or passive ways could be further conducted, especially for heavy-truck induced impact.

Appendix A

MATLAB code for explicit dynamic analysis of truck-to-pier impact based on fiber elemental method for the truck F800 at 100km/h initial velocity

1) Main File

```
%%%% equivalent SDOF mass
fco=27.579;
E=5000*fco^0.5;
d=914.4;
I=pi*d^4/64;
l=6705.6;
dx=67.056;
As=819*20;
Ac=pi*d^2/4;
dm=As*7.89e-9+Ac*2.4e-9;
Limp=814.7+1219.2;
Pp=1;
for i=1:100
    x(i)=i*dx-dx/2;
def(i)=cantilever_def(x(i),Limp,Pp,l,E,I);
end
 deff=def/cantilever_def(Limp,Limp,Pp,l,E,I);
Me=dm*dx*deff*deff';
```

```
%%% end
 %%%%%% concrete pier properties
s=304.8;        %%spacing
ds=812.8;       %%core section diameter
d=12.7;         %%stirrup diameter
dc=914.4;       %%gross section diameter
dr=32.26;       %%longtudinal rebar diameter
n=20;           %%number of rebar
fyh=413.8;      %%yeld strength of steel stirrup
fco=27.579;     %%unconfined concrete strength
%%%end
%%%%% coefficients for confined concrete
Asp=pi*d^2/4;       %%stirrup area
As=pi*dr^2/4*n;     %%Area of rebar
Ac=pi*ds^2/4;       %%Area of core section
pcc=As/Ac;      %%ratio of area of longitudinal reinforcement to area of core of section
ps=4*Asp/ds/s;      %%ratio of the volume of transverse confining steel
ke=(1-(s-d)/2/ds)^2/(1-pcc);    %%confinement effectiveness coefficient
fl=0.5*ke*ps*fyh;       %%effective lateral confining stress
 fcc=fco*(-1.254+2.254*(1+7.94*fl/fco)^0.5-2*fl/fco);    %%confined concrete strength
epscc=0.002*(1+5*(fcc/fco-1)); %%yield strain
%%%%end
 %%location of reinforcement
```

```
degree=2*pi/20;

Ass=pi/4*32.26^2;

Ast(1)=Ass;Ast(2:10)=2*Ass;Ast(11)=Ass;

for i=1:11

X(i)=406.4*cos(degree*(i-1)); %%20rebars in 11 layers

end

%%% end

%%location of concrete fiber

r=457.2;rc=406.4;

for i=1:36

Y(i)=(18.5-1*i)*25.4;

Z(i)=2*(r^2-Y(i)^2)^0.5;

if rc^2-Y(i)^2<0

   Zc(i)=0;

else

   Zc(i)=2*(rc^2-Y(i)^2)^0.5;

end

Acov(i)=25.4*(Z(i)-Zc(i));  %%cover concrete in 36 layers

Acor(i)=25.4*Zc(i);        %%core concrete in 36 layers

end

%%%% end

 Mcar=0.607;

MM=[Mcar 0;0 Me];
```

```
dt=1e-5;

DE=493;

k1=190310;


V=27.78e3; %% speed 100km/h

D=1.3423e6; %% Constant damping force

U(:,1)=[-V*dt;0];   %% U-1 of car

U(:,2)=[0;0];       %% U0 of car

DC=2.43e5;


Kt=MM/dt^2;

 KK=[k1, -k1;-k1,k1];

%%pier initial compression stress

Ag=pi/4*dc^2;

N=5*Ag;

eps_m=0.000193;

epsun=zeros(1,36);epsun1=zeros(1,36);epsun2=zeros(1,36);

fun=zeros(1,36);fun1=zeros(1,36);fun2=zeros(1,36);

eps_c0=ones(1,36)*eps_m;

eps_s0=ones(1,11)*eps_m;

sigmas0=2e5*eps_s0;

%%%end
```

```
%%% dynamic increase factor
DFC=1.5
DFS=1.3
 for i=1:10000
%%%%%%%%%%%% calculate Fe=ke*Ue of the pier at dt(i+1)
  fai(i+1)=U(2,i+1)*3/Limp^2;
 %%first try
  eps_c=eps_m+fai(i+1)*Y;
  eps_s=eps_m+fai(i+1)*X;
  for j=1:36
     if eps_c(j)<eps_c0(j) %%% unloading
        epsun1(j)=max(epsun(j),eps_c0(j));
        fun1(j)=confined_stress_strain(epscc,fcc,fco,epsun1(j));
        sigmac(j)=confined_stress_strain_unloading(epscc,epsun1(j),fun1(j),fco,eps_c(j));
        sigmau(j)=unconfined_stress_strain_unloading(epsun1(j),fun1(j),fco,eps_c(j));
     end
     if eps_c(j)>=eps_c0(j) %%% loading
         sigmac(j)=confined_stress_strain(epscc,fcc,fco,eps_c(j));
         sigmau(j)=unconfined_stress_strain(fco,eps_c(j));
     end
  end
  for j=1:11
     sigmas(j)=steel_stress_strain1(fyh,sigmas0(j),eps_s0(j),eps_s(j));
```

```
end
F(1)=DFC*Acor*sigmac'+DFC*Acov*sigmau'+DFS*Ast*sigmas';
M(1)=DFC*Y*(Acor.*sigmac)'+DFC*Y*(Acov.*sigmac)'+DFS*X*(Ast.*sigmas)';
eps_c1=eps_c;
eps_s1=eps_s;
sigmas1=sigmas;
error(1)=abs(N-F(1));
if N-F(1)<=0
   deps=-0.000001;
else deps=0.000001;
end
%%second try
eps_m=eps_m+deps;
eps_c=eps_m+fai(i+1)*Y;
eps_s=eps_m+fai(i+1)*X;
for j=1:36
   if eps_c(j)<eps_c0(j) %%% unloading
      epsun2(j)=max(epsun(j),eps_c0(j));
      fun2(j)=confined_stress_strain(epscc,fcc,fco,epsun2(j));
      sigmac(j)=confined_stress_strain_unloading(epscc,epsun2(j),fun2(j),fco,eps_c(j));
      sigmau(j)=unconfined_stress_strain_unloading(epsun2(j),fun2(j),fco,eps_c(j));
   end
   if eps_c(j)>=eps_c0(j) %%% loading
```

```
            sigmac(j)=confined_stress_strain(epscc,fcc,fco,eps_c(j));
            sigmau(j)=unconfined_stress_strain(fco,eps_c(j));
        end
    end
    for j=1:11
        sigmas(j)=steel_stress_strain1(fyh,sigmas0(j),eps_s0(j),eps_s(j));
    end
    F(2)=DFC*Acor*sigmac'+DFC*Acov*sigmau'+DFS*Ast*sigmas';
    M(2)=DFC*Y*(Acor.*sigmac)'+DFC*Y*(Acov.*sigmac)'+DFS*X*(Ast.*sigmas)';
    eps_c2=eps_c;
    eps_s2=eps_s;
    sigmas2=sigmas;
    error(2)=abs(N-F(2));
%% loop to find neutral axis
 while error(2) < error(1)
     error(1)=error(2);
     F(1)=F(2);
     M(1)=M(2);
    eps_c1=eps_c2;
    eps_s1=eps_s2;
    sigmas1=sigmas2;
    epsun1=epsun2;
    fun1=fun2;
```

```
eps_m=eps_m+deps;
eps_c=eps_m+fai(i+1)*Y;
eps_s=eps_m+fai(i+1)*X;
for j=1:36
   if eps_c(j)<eps_c0(j) %%% unloading
      epsun2(j)=max(epsun(j),eps_c0(j));
      fun2(j)=confined_stress_strain(epscc,fcc,fco,epsun2(j));
      sigmac(j)= confined_stress_strain_unloading(epscc,epsun2(j),fun2(j),fco,eps_c(j));
      sigmau(j)=unconfined_stress_strain_unloading(epsun(j),fun2(j),fco,eps_c(j));
   end
   if eps_c(j)>=eps_c0(j) %%% loading
       sigmac(j)=confined_stress_strain(epscc,fcc,fco,eps_c(j));
       sigmau(j)=unconfined_stress_strain(fco,eps_c(j));
   end
end
for j=1:11
   sigmas(j)=steel_stress_strain1(fyh,sigmas0(j),eps_s0(j),eps_s(j));
end
F(2)=DFC*Acor*sigmac'+DFC*Acov*sigmau'+DFS*Ast*sigmas';
M(2)=DFC*Y*(Acor.*sigmac)'+DFC*Y*(Acov.*sigmac)'+DFS*X*(Ast.*sigmas)';
error(2)=abs(N-F(2));
eps_c2=eps_c;
eps_s2=eps_s;
```

```
  sigmas2=sigmas;
 end
 %%output
Moment(i+1)=M(1);    %%moment
Fe(i+1)=Moment(i+1)/Limp;
eps_c0=eps_c1;      %%strain of concrete fiber
eps_s0=eps_s1;      %%strain of steel fiber
sigmas0=sigmas1;    %%stess of steel fiber
epsun=epsun1;       %%unloading strain
%%fun=fun1;          %%unloading stress
%%%%%%%%%%% END
 DU(i+1)=U(1,i+1)-U(2,i+1);
if DU(i+1)>DE
    F1(i+1)=(DU(i+1)-DE)*k1;
else F1(i+1)=0;
end
if DU(i+1)>DU(i)
P(:,i+1)=[-DC;D];
else P(:,i+1)=[DC;D];
end
%explicit analysis at i
FS(:,i+1)=[F1(i+1);-F1(i+1)+Fe(i+1)];
U(:,i+2)=inv(Kt)*(P(:,i+1)-MM/dt^2*U(:,i)+2*MM/dt^2*U(:,i+1)-FS(:,i+1));
```

```
Impact(i+1,2)=(F1(i+1)+P(2,i+1))/1000;

Impact(i+1,1)=i*dt;

i %show the current step during analysis

end

plot(Impact)
```

2) Functions

a)

```
%% function for stress-strain relationship of confined concrete
function [sigma] = confined_stress_strain(epscc,fcc,fco,eps)
Esec=fcc/epscc;              %%sec-ela modula
Ec=5000*fco^0.5;             %%tangent modula
if eps>=0
%%confined concrete stress-strain
   x=eps/epscc;
   r=Ec/(Ec-Esec);
   sigma=fcc*x*r/(r-1+x^r);
else
   sigma=0;
end
```

b)

```
%% function for stress-strain relationship of confined concrete during unloading
function [sigma] = confined_stress_strain_unloading(epscc,epsun,fun,fco,eps)
Ec=5000*fco^0.5;             %%tangent modula
a=max(epscc/(epscc+epsun),0.09*epsun/epscc);
epsa=a*(epsun*epscc)^0.5;
epspl=epsun-(epsun+epsa)*fun/(fun+Ec*epsa);
```

```
b=max(fun/fco,1);
c=min((epscc/epsun)^0.5,1);
Eu=Ec*b*c;
Esec=fun/(epsun-epspl);
r=Eu/(Eu-Esec);
x=(eps-epsun)/(epspl-epsun);
if eps>=epspl
sigma=fun-fun*x*r/(r-1+x^r);
else
   sigma=0;
end
end
```

c)

```
%% function for stress-strain relationship of unconfined concrete
function [sigmau] = unconfined_stress_strain(fco,eps)
esp=0.005;
Ec=5000*fco^0.5;
ru=Ec/(Ec-fco/0.002);
xu=eps/0.002;
if eps<=0
   sigmau=0;
end
```

```
if (eps>0 && eps<=0.004)
   sigmau=fco*xu*ru/(ru-1+xu^ru);
end
if (eps>0.004 && eps<=0.005)
   sigmau=(2*fco*ru/(ru-1+2^ru))*(esp-eps)/(esp-2*0.002);
end
if eps>0.005
   sigmau=0;
end
```

d)

```
%% function for stress-strain relationship of unconfined concrete during unloading
function [sigma] = unconfined_stress_strain_unloading(epsun,fun,fco,eps)
Ec=5000*fco^0.5;              %%tangent modula
%% unloading
a=max(0.002/(0.002+epsun),0.09*epsun/0.002);
epsa=a*(epsun*0.002)^0.5;
epspl=epsun-(epsun+epsa)*fun/(fun+Ec*epsa);
b=max(fun/fco,1);
c=min((0.002/epsun)^0.5,1);
Eu=Ec*b*c;
Esec=fun/(epsun-epspl);
r=Eu/(Eu-Esec);
```

```
x=(eps-epsun)/(epspl-epsun);
if eps>=epspl
sigma=fun-fun*x*r/(r-1+x^r);
else
   sigma=0;
end
end
```

e)

```
%% function for stress-strain relationship of steel
function [sigmas] = steel_stress_strain1(fyh,sigmas0,eps0,eps)
Es=2e5;
Est=2352;
epsy=fyh/Es;
sigmas1=sigmas0+(eps-eps0)*Es;
sigmas2=-fyh+Est*(eps+epsy);
sigmas3=fyh+Est*(eps-epsy);
if (sigmas1>=sigmas2 && sigmas1<=sigmas3)
sigmas=sigmas1;
end
if sigmas1<=sigmas2
sigmas=sigmas2;
end
```

```
if sigmas1>=sigmas3
sigmas=sigmas3;
end
end
```

f)

```
%% function for the deflection of the pier under concentrated load P at height a
function [y]=cantilever_def(x,a,P,l,E,I)
if (x<=a && x>=0)
    y=P*x^2/6/E/I*(3*a-x);
end
if (x>a && x<=l)
    y=P*a^2/6/E/I*(3*x-a);
end
end
```

Appendix B

MATLAB code for Monte-Carlo simulation in reliability study

1) Main File

```
clc;clear;
n=100000; %% sample number for mento-carlo
m=91;
%%%%% parameters input for impact force
 %%velocity input lognormal
mean_V=120;
stad_V=mean_V*0.15;
mu_V=log(mean_V/(1+stad_V^2/mean_V^2)^0.5);
sigma_V=(log(1+stad_V^2/mean_V^2))^0.5;
V=lognrnd(mu_V,sigma_V,n,1);  %%velocity input lognormal
%%concrete str  input lognormal
mean_C=27.58;
stad_C=mean_C*0.05;
mu_C=log(mean_C/(1+stad_C^2/mean_C^2)^0.5);
sigma_C=(log(1+stad_C^2/mean_C^2))^0.5;
C=lognrnd(mu_C,sigma_C,n,1);
%%concrete str  input lognormal
 %%diameter  input Deterministic
 mean_D=0.9144;
```

```
D=mean_D*ones(n,1); %%diameter  input Deterministic
%%length input Deterministic
mean_L=5.4864;
L=mean_L*ones(n,1);  %%length input Deterministic
%%impact height(foot top to ground) input deterministic
mean_H=1.2192;
H=mean_H*ones(n,1);  %%impact height input Deterministic
%%axial stress input lognormal
mean_P=5;
stad_P=mean_P*0.15;
mu_P=log(mean_P/(1+stad_P^2/mean_P^2)^0.5);
sigma_P=(log(1+stad_P^2/mean_P^2))^0.5;
P=lognrnd(mu_P,sigma_P,n,1);  %%axial stress input lognormal
%%cargo mass input normal
mean_M=0.65;
stad_M=mean_M*0.33;
M=normrnd (mean_M,stad_M,n,1);  %%cargo mass input normal
%%%%%% parameters input for resistance
%% longi steel yield str
mean_fy=413.7;
stad_fy=mean_fy*0.05;
fy=normrnd (mean_fy,stad_fy,n,1);  %% longi steel yield str
%% trans steel yield str
```

```
mean_fyh=413.7;
stad_fyh=mean_fyh*0.05;
fyh=normrnd (mean_fyh,stad_fyh,n,1);  %%trans steel yield str
%%cover depth input deterministic
mean_c=50.8;
c=mean_c*ones(n,1);%%cover depth
%%Impact height(ground to impact location) input normal
mean_dh=0.6;
stad_dh=mean_dh*0.1;
dh=normrnd (mean_dh,stad_dh,n,1);
h=H+dh;   %%Impact height
%% rebar ratio input normal
mean_p=0.025;
stad_p=mean_p*0.05;
p=normrnd (mean_p,stad_p,n,1); %% rebar ratio input normal
%% area of hoop deterministic
mean_Ah=129;
Ah=mean_Ah*ones(n,1); %% area of hoop
%% spacing of hoop
for j=1:m
mean_s=76.2+(j-1)*2.54;
s(:,j)=mean_s*ones(n,1); %% hoop spacing
end
```

```
%%%%%%%% end
%% random impact force and resistance based on response surface model
for j=1:m
n_fail=0;
for i=1:n
Impact(i,1)=C2500(V(i),C(i),D(i),L(i),H(i),P(i),M(i)); %%  random impact force
[Mn(i,1),Vn(i,1)]=Resistance(P(i),Impact(i),C(i),fy(i),fyh(i),c(i),D(i),h(i),p(i),Ah(i),s(i,j))
; %% random resistance
Me(i,1)=Impact(i,1)*h(i,1)*1000;
Ve(i,1)=Impact(i,1);
Mp(i,1)=Mn(i,1)-Me(i,1);
Vp(i,1)=Vn(i,1)-Ve(i,1);
if Mp(i,1)<0 || Vp(i,1)<0
   n_fail=n_fail+1;
end
end
fail_prop(j,1)=n_fail/n; %% failure rate
j  %loop indicator
end
```

2) Functions

a)

```
%%%%%%%%% Response surface model for the impact load induced by C2500 truck
function [Impact]=C2500(V,C,D,L,H,P,M)
Var=[1,V,C,D,L,H,P,M,V*C,V*D,V*L,V*H,V*P,V*M,C*D,C*L,C*H,C*P,C*M,D*L,
D*H,D*P,D*M,L*H,L*P,L*M,H*P,H*M,P*M,V^2,C^2,D^2,L^2,H^2,P^2,M^2];
Con=[-10.953706;0.104349;-0.112126;16.733182;1.284919;-
0.930559;0.123752;1.978817;-0.000373;0.018037;0.000114;0.000026;-0.000715;-
0.009065;0.109325;0.006111;0.002760;-0.001030;-0.029361;-0.373185;0.108373;-
0.015978;0.055747;0.068892;-0.013615;-0.068609;0.074884;0.156628;-0.004960;-
0.000057;0.000118;-11.107849;-0.081679;0.017370;-0.003085;0.027913];
Impact=Var*Con*10^5;
```

b)

```
%%%%%%%%%%%%Resistance of the pier
%%%%%%%%%%%% Mn is the moment resistance; Vn is the shear resistance
function [Mn,Vn]=Resistance(N,Impact,fc,fy,fyh,c,D,h,p,Ah,s)  %% N=axial
stress;h=impact height;c=cover depth;p=ratio of reinforcement
D=D*1000;
h=h*1000;
%% moment resistance
R=D/2;
```

```
fcd=fc*0.9/1.5;

fyd=fy/1.15;

As=p*pi*R^2;

w=p*fyd/fcd;

v=N/fcd;

 alpha=pi; %initial value

i=0;% number of iteration

while i<= 100  %%iteration

alpha0=alpha-(alpha*(1+2*w)-sin(alpha)-2*pi*(w+v))/((1+2*w)-cos(alpha));% Newton

iteration

if abs(alpha0-alpha)>0.01; %convergence?

alpha=alpha0;

else break

end

i=i+1;

end

theta=alpha0/2;

Mn=2/3*R^3*(sin(theta))^3*fcd+2/pi*(R-c)*As*sin(theta)*fyd;

%%%%%end

%% shear resistance

V=Impact;

Es=210000;

M=V*h;
```

```
fci=fc*0.145;

Ec=1820*fci^0.5/0.145;

de=R+(R-c)/pi;

dv=de*0.9;

bv=D;

Av=2*Ah;

es=(M/dv+0.5*N+V)/(Es*As);  %%% calculate es

if es<0

   es=(M/dv+0.5*N+V)/(Es*As+Ec*pi*R^2);

end

beta=4.8/(1+750*es);

theta_s=(29+3500*es)/180*pi;

Vc=0.0316*beta*(fci^0.5)*bv*dv*6.89475727;

Vs=Av*fyh*dv*cot(theta_s)/s;

Vn=Vc+Vs;

Vn=0.9*min(Vn,0.25*fc*bv*dv);

%%%%%end

end
```

References

AASHTO(2007). *Load Resistance and Factor Design: Bridge Design Specifications*, Forth Edition, American Association of State Highway and Transportation Officials, Washington D.C.

AASHTO(2017). *Load Resistance and Factor Design: Bridge Design Specifications*, Eighth Edition, American Association of State Highway and Transportation Officials, Washington D.C.

Abdelkarim, Omar I., Mohamed A. ElGawady (2016). "Performance of Hollow-core FRP–concrete–steel Bridge Columns Subjected to Vehicle Collision", *Engineering Structures*, **123**, 517-531

ACI 318-11, 2011. *Building Code Requirements for Structural Concrete and Commentary*, American Concrete Institute, Detroit, Mich.

ASCE7-10(2010). *Minimum Design Loads for Buildings and Other Structures*, American Society of Civil Engineeris, Virginia.

Ayyub, Bilal M,. Richard H. McCuen (2011). *Probability, Statistics, and Reliability for Engineers and Scientists*, (3rd Edition), CRC press, Boca Raton, Florida.

Bala, S., and Day, J. (2003). "General Guidelines for Crash Analysis in LS-DYNA." Available at: https://awg.lstc.com/tiki/tiki-download_file.php?fileId=18

Bischoff, P.H., and S.H. Perry (1995). "Impact Behavior of Plain Concrete Loaded in Uniaxial Compression," *Journal of Engineering Mechanics*, **121**(6), 685–693.

Box, G. E. P. and Wilson, K.B. (1951) "On the Experimental Attainment of Optimum Conditions ", *Journal of the Royal Statistical Society*, 13(1):1–45.

Buth, C. Eugene, Michael S. Brackin, William F. Williams, Gary T. Fry (2011). "Collision Loads on Bridge Piers: Phase 2. Report of Guidelines for Designing Bridge Piers and Abutments for Vehicle Collisions", *Report FHWA/TX-11/9-4973-2*, Texas A&M University, Texas.

Buth, C. Eugene, William F. Williams, Michael S. Brackin, Dominique Lord, Srinivas R. Geedipally, and Akram Y. Abu-Odeh (2010). "Analysis of Large Truck Collisions with Bridge Piers: Phase 1. Report of Guidelines for Designing Bridge Piers and Abutments for Vehicle Collisions", *Report FHWA/TX-10/9-4973-1*, Texas A&M University, Texas.

Cao, Ran, Anil Kumar Agrawal, Sherif El-Tawil (2019). "Heavy Truck Collision with Bridge Piers: Computational Simulation Study", *Journal of Bridge Engineering*, **24**(6), 04019052.

Cao, Ran, Sherif El-Tawil, Anil Kumar Agrawal, Xiaochen Xu, Waider Wong (2019). "Behavior and Design of Bridge Piers Subjected to Heavy Truck Collision" *Journal of Bridge Engineering*, **24**(7), 04019057

Chatterjee, Samprit, Ali S. Hadi (2012). *Regression Analysis by Example*, (5th Edition), Wiley, New York, USA

Chen, Lin, Sherif El-Tawil, Yan Xiao (2016). "Reduced Models for Simulating Collisions between Trucks and Bridge Piers", *Journal of Bridge Engineering*, **21**(6), 04016020.

Chopra, A. K. (2000), *Dynamics of Structures: Theory and Applications to Earthquake Engineering*, (2nd Edition), Prentice Hall: Upper Saddle River, New Jersey, USA.

Cizmar, D., Mestrovic, D., & Miculinic, L. (2008). "Reliability of concrete columns under vehicle impact". *Structures Under Shock and Impact X*, **98**, 157-165.

Consolazio, Gary R., T David R. Cowan (2005). "Numerically Efficient Dynamic Analysis of Barge Collisions with Bridge Pier", *Journal of Structural Engineering*, **131**(8), 1256-1266

Cook, R. Dennis (1977). “Detection of Influential Observation in Linear Regression”. Technometrics, **19**(1), 15-18

Cosenza, Edoardo, Carmine Galasso, Giuseppe Maddaloni (2011). “A simplified method for flexural capacity assessment of circular RC cross-sections”, *Engineering Structures*, **33(**3), 942-946

Deficient Bridges by Highway System (2016). Available at: https://www.fhwa.dot.gov/bridge/nbi/no10/defbr16.cfm

Deficient Bridges by Highway System (2016). Available at: https://www.fhwa.dot.gov/bridge/nbi/no10/defbr16.cfm

Demartino, Cristoforo, Jiguang Wu, Yan Xiao (2017), “Experimental and Numerical Dtudy on the Behavior of Circular RC Columns under Impact Loading” *Procedia Engineering,* **199**, 2457-2462

Deng, Yaohua, C. Y. Tuan, Yan Xiao, “Flexural Behavior of Concrete-Filled Circular Steel Tubes under High-Strain Rate Impact Loading”, *Journal of Structural Engineering,* **138**(3), 449-456

Do, Tin V., Thong M. Pham, Hong Hao (2018), “A Dynamic responses and failure modes of bridge columns under vehicle collision”, *Engineering Structure*, **156**(1), 243-259

El-Tawil (2004). “Vehicle Collision with Bridge Pier”, *Report BC355_06*, University of Michigan, Michigan.

Eurocode 1: *Actions on structures–Part 1-1: General actions–Densities, self-weight, imposed loads for buildings*. Final Draft prEN 1991-1-1, Comité Europeo de Normalización, Julio 2001.

Eurocode 1: *Actions on structures–Part 1-7: General actions–Accidental actions.* Final Project Team Draft (Stage 34), Draft prEN 1991-1-7, Comité Europeo de Normalización, Marzo 2003.

Ferrer, B., S. Ivorra, E. Segovia, R. Irles (2010). "Tridimensional Modelization of the Impact of a Vehicle against a Metallic Parking Column at a Low Speed", *Engineering Structure*, **32**(8), 1986-1992

Fujikake, Kazunori, Bing Li, Sam Soeun(2009). "Impact Response of Reinforced Concrete Beam and Its Analytical Evaluation", *Journal of Structural Engineering*, **135**(8), 938-950.

Gendy, Samer Sabry F. Mehanny, Ashraf Ayoub (2018). "Explicit Fiber Beam-Column Elements for Impact Analysis of Structures", Journal of Structural Engineering, 144(7), 04018068

Gomez, Nevin L (2014). "Performance of Circular Reinforced Concrete Bridge Piers Subjected to Vehicular Collisions". Master Theses, University of Massachusetts - Amherst, Massachusetts.

I.E Harik, A. Shaaban, H. Gesund, G.Valli, S. Wang (1990). "United States bridge failures, 1951–1988", *Journal of Performance of Constructed Facilities*, **4**(4), 272-277

Kishi, N., H. Mikami, K.G. Matsuoka, T. Ando (2002). "Impact behavior of shear-failure-type RC beams without shear rebar", *International Journal of Impact Engineering*, **27**(9), 955-968.

Lee, G.C., S.B. Mohan, C. Huang and B.N. Fard (2008), "A Study of U.S. Bridge Failures (1980-2012)", *Report MCEER-13-0008*, University at Bufflo, State University of New York, New York.

Liu, Guangyong, "Behavior of bridge piers during vehicular impacts". PhD Dissertation, City University of New York, New York.

LSTC(2006), LS-DYNA Theory Manual. Available at: http://www.lstc.com/pdf/ls-dyna_theory_manual_2006.pdf

Mander, J.B., M. J. N. Priestley, R. Park. (1988). "Theoretical Stress‐Strain Model for Confined Concrete", *Journal of Structural Engineering*, **114**(8), 1804-1826.

Malvar, L. J., and Crawford, J. E. (1998). "Dynamic Increase Factors for Steel Reinforcing Bars." *Twenty-Eighth DDESB Seminar,* Orlando, Florida, August 1998

Mohammed, T. (2011). "Reinforced Concrete Structural Members Under Impact Loading." PhD Dissertation. University of Toledo, Ohio.

Murray, Yvonne D. (2007). "Collision Loads on Bridge Piers: Phase 2. Report of Guidelines for Designing Bridge Piers and Abutments for Vehicle Collisions", *Report FHWA-HRT-05-062*, APTEK Inc., Colorado.

NCAC. "1994 Chevy C2500 pick-up". Available at: https://www.ccsa.gmu.edu/capability/

NCAC. "F800 Single Unit Truck FEM Model for Crash Simulations with LS-DYNA". Available at: https://thyme.ornl.gov/FHWA/F800WebPage/downloads/downloads.html

NCAC. "FEM Models for Semitrailer Trucks" https://thyme.ornl.gov/fhwa/tractortrailer/download/download.cgi

NHTSA Vehicle Crash Test Database. Available at: https://www-nrd.nhtsa.dot.gov/database/veh/veh.htm

Popov, Valentin L. (2010), *Contact Mechanics and Friction*, Springer, Berlin, Germany.

Pukelsheim, Friedrich (2006). *Optimal Design of Experiments*, Society for Industrial and Applied Mathematics, Philadelphia, Pennsylvania

Ross, C.A., and J.W. Tedesco (1992), "Effects of Strain-Rate on Concrete Strength," *ACI 1991 Spring Convention*, Washington, D.C., March 1992.

Saatci,Selcuk, Frank J. Vecchio (2009). "Effects of Shear Mechanisms on Impact Behavior of Reinforced Concrete Beams", *ACI Structural Journal*, **106**(1), 78-86.

Sierakowski, R. L.; Chaturvedi, S. K. (1997). *Dynamic Loading and Characterization of Fiber-Reinforced Composite*, Wiley, New York, USA

Simo, J.C., J.W. Ju (1987). "Strain and Stress Based Continuum Damage Model," International *Journal of Solids and Structures*, **23**(7), 821-840

Steel, Kylie, Andrew D. Sorensen (2014). "Reliability Analysis of a Circular Bridge Pier Subject to Intentional Vehicular Impact" *Second International Conference on Vulnerability and Risk Analysis and Management (ICVRAM) and the Sixth International Symposium on Uncertainty, Modeling, and Analysis (ISUMA)*, Liverpool, England, July, 2014

Trentadue, Francesco, Giuseppe Quaranta, Giuseppe C.Marano (2016). "Closed-form approximations of interaction diagrams for assessment and design of reinforced concrete columns and concrete-filled steel tubes with circular cross-section", *Engineering Structures*, **127**, 594-601

Thilakarathna, H.M.I, D.P. Thambiratnam, M.Dhanasekar, N.Perera (2010). "Numerical simulation of axially loaded concrete columns under transverse impact and vulnerability assessment" *International Journal of Impact Engineering*, **37**(11), 1110-1112

US Department of Energy (2012). Maps and Data. Alternative Fuels Data Center. Available at: https://www.afdc.energy.gov/data/

Wardhana, Kumalasari, Fabian C. Hadipriono (1990). "Analysis of Recent Bridge Failures in the United States", *Journal of Performance of Constructed Facilities*, 17(3), 144-150

Wriggers, Peter (2002), *Computational Contact Mechanics*, (2nd Edition), Springer, Berlin, Germany.